MIT

PHYSICALLY-BASED PARAMETERIZATION OF SPATIALLY VARIABLE SOIL AND VEGETATION USING SATELLITE MULTISPECTRAL DATA

by
MICHAEL F. JASINSKI
and
PETER S. EAGLESON

RALPH M. PARSONS LABORATORY
HYDROLOGY AND WATER RESOURCE SYSTEMS

DEPARTMENT
OF
CIVIL
ENGINEERING

SCHOOL OF ENGINEERING
MASSACHUSETTS INSTITUTE OF TECHNOLOGY
Cambridge, Massachusetts 02139

Report Number 324

Prepared under the support of the
NASA Goddard Space Flight Center
Grant Nos. NAG 5-510 and NAGW-1696

September, 1989

R89–22

PHYSICALLY–BASED PARAMETERIZATION OF SPATIALLY VARIABLE SOIL AND VEGETATION USING SATELLITE MULTISPECTRAL DATA

by

MICHAEL F. JASINSKI

and

PETER S. EAGLESON

RALPH M. PARSONS LABORATORY

HYDROLOGY AND WATER RESOURCES

Report Number 324

Prepared under the support of the
NASA Goddard Space Flight Center, Greenbelt, Maryland
Grant Nos. NAG 5–510 and NAGW–1696

SEPTEMBER 1989

PHYSICALLY–BASED PARAMETERIZATION OF SPATIALLY VARIABLE SOIL AND VEGETATION USING SATELLITE MULTISPECTRAL DATA

Abstract

A stochastic–geometric landsurface reflectance model is formulated and tested for the parameterization of spatially variable vegetation and soil at subpixel scales using satellite multispectral images without ground truth. Landscapes are conceptualized as three–dimensional Lambertian reflecting surfaces consisting of plant canopies, represented by solid geometric figures, superposed on a flat soil background. Multiple scattering among landsurface components is neglected. The model is cast within the framework of an existing theoretical model of upwelling solar radiance for optically–thin atmospheres, as observed by a nadir–viewing satellite.

A computer simulation program is developed in order to investigate image characteristics at various spatial aggregations representative of satellite observational scales, or pixels. In particular, the evolution of the shape and structure of the red–infrared space, or scattergram, of typical semivegetated scenes is investigated by sequentially introducing model variables into the simulation. The correlation between canopy and shadow is identified as a principal mechanism contributing to the frequently observed tasseled cap of red–infrared scattergrams of semivegetated landscapes. A Sampling Scale Ratio is formulated as a quantitative criterion that identifies when that correlation occurs.

The analytical moments of the total pixel reflectance, including the mean, variance, spatial covariance, and cross–spectral covariance, are derived in terms of the moments of the individual fractional cover and reflectance components. The moments are applied to the solution of the inverse problem: The estimation of subpixel landscape properties on a pixel–by–pixel basis, given only one multispectral image and limited assumptions on the structure of the landscape. The inverse procedure involves the formulation of conditional moments for subsets of pixels that possess similar properties, and that can be identified through their common orientation in red–infrared scattergrams. The analysis is facilitated by assuming geometric similarity among canopy elements and by assuming a functional relationship between fractional covers in the case of large Sampling Scale Ratios.

The landsurface reflectance model and inversion technique are tested using actual aerial radiometric data collected over regularly spaced pecan trees, and using both aerial and Landsat Thematic Mapper data obtained over discontinuous, randomly spaced conifer canopies in a natural forested watershed. For the Landsat case, adjacency effects are neglected by assuming low interpixel contrast. Different amounts of solar backscattered diffuse radiation are assumed and the sensitivity of the estimated landsurface parameters to those amounts is examined.

Acknowledgements

The work in this report was sponsored principally by the NASA/Goddard Space Flight Center, Greenbelt, Maryland under contracts NAG 5–510 and NAG W–1696. Additional support was provided by the Edmund K. Turner Professorship.

The authors would like to thank Dr. Bhaskar J. Choudhury, NASA/Goddard Space Flight Center, and Professor Ronald G. Prinn, Department of Earth, Atmosphere and Planetary Sciences, M.I.T, for their useful comments.

The field work was facilitated through the support of Dr. Ray D. Jackson, Water Conservation Laboratory, Agricultural Research Service, U.S. Department of Agriculture, Phoenix, Arizona. M. Susan Moran, Water Conservation Lab, and David S. Ammon, Aerial Images, Tuscon, helped in the acquisition of the aerial data.

Mr. Edgar Work, Bureau of Land Management, Denver, and Mr. Robert Martinez, Taos Resources Area Office, provided the preprocessed satellite multispectral data and aerial photographs in order to conduct the preliminary analysis of the Taos Study Area in Appendix B.

Table of Contents

List of Figures

List of Tables

Notation

Symbol	Description
$a(\lambda)$	average specular reflectance of area adjacent to target pixel
b	geometric similarity parameter
d	distance between two points in a scene
$f(\lambda)$	bidirectional reflectance distribution
$f_i(\underline{x})$	fraction of pixel centered at $\underline{x}$ occupied with cover type i
g	fraction of total soil background (illuminated and shadowed) in pixel centered at $\underline{x}$
g_S	fraction of soil shadowed by vegetation cover in pixel centered at $\underline{x}$
g_I	fraction of illuminated soil background in pixel centered at $\underline{x}$
m	fraction of total vegetation in pixel centered at $\underline{x}$
m_I	fraction of illuminated vegetation in pixel centered at $\underline{x}$
m_s	fraction of shadowed vegetation in pixel centered at $\underline{x}$
$r_i(\lambda,\underline{u})$	reflectnce of point $\underline{u}$, given it possess cover type i
s	total canopy and soil shadow in pixel
A	area
$A_i(\underline{x})$	total area of pixel centered at $\underline{x}$ with cover type i
A_s	area of ground shadow associated with one plant
A_t	area of an individual plant
A_P	area of pixel
BI	Kauth–Thomas Brightness Index
COV[ ]	covariance
COV_x[ ]	spatial covariance

$E[\ ]$	expected value
$E(\lambda)$	irradiance, the total radiance impinging on a surface from all directions
$E_o(\lambda)$	intensity of total incoming radiation at the top of the canopy
GI	Kauth–Thomas Greenness Index
$J(\lambda)$	radiation source function
$L(\lambda)$	total radiance within a given interval in the spectrum
$L_a(\lambda)$	diffuse radiance scattered from the surounding vicinity into the column above the object pixel
$L_d(\lambda)$	diffuse radiance backscattered from the direct solar beam
$L_r(\lambda)$	direct beam of radiance from the target pixel
$L_s(\lambda)$	specular radiant energy flux per unit wavelength per unit solid angle per unit of projected area in a specified direction
$M(\lambda)$	radiant exitance emitted over the entire spherical angle
$M_i(\lambda)$	radiance emitted from cover type i in band λ
$M_g(\lambda)$	radiance emitted from soil in band λ
$M_m(\lambda)$	radiance emitted by vegetation in band λ
NDVI	Normalized Difference Vegetation Index
PVI	Perpendicular Vegetation Index
$P(\lambda)$	phase function
$P_M(\lambda)$	phase function due to Mie scattering
$P_R(\lambda)$	phase function due to Rayleigh scattering
$R(\lambda)$	specular reflectance
$R_i(\lambda,\underline{x})$	average bulk reflectance of cover type i in pixel centered at $\underline{x}$

$R_{g_S}(\lambda,\underline{x})$	average bulk reflectance of shadowed soil in band λ in pixel centered at $\underline{x}$
$R_{g_I}(\lambda,\underline{x})$	average bulk reflectance of illuminated soil backgroun in band λ in pixel centered at $\underline{x}$
$R_m(\lambda,\underline{x})$	average bulk reflectance of vegetation in band λ in pixel centered at $\underline{x}$
S_G	Sampling scale ratio for regular spatial distributions
S_P	Sampling Scale Ratio for Poission distributions
VAR[ ]	variance
α	slope of the soil line
β	inverse length scale of the covariance function
γ	intercept of the soil line
$\delta(\underline{u})$	delta function equal to 1 if point $\underline{u}$ is occupied by illuminated soil, 0 if it is not
ζ	leaf area index
η	solar–geometric similarity parameter
θ	angle with the vertical axis, or solar zenith angle
λ	wavelength
μ	cosine of the zenith angle, θ
ξ	zenith reflection angle
ρ	Poisson spatial density
σ	standard deviation of the soil reflectance distribution
τ	optical depth or thickness
τ_a	optical thickness due to absorption by gas molecules
τ_M	optical thickness due to Mie scattering
τ_R	optical thickness due to Rayleigh scattering

$\phi_s(\lambda)$	specular radiant flux in wavelength λ
ψ	angle with the x–axis in a clockwise manner when viewed from the bottom
Ω	solid angle

Chapter 1
INTRODUCTION

1.1 Objectives

The purpose of this research is to formulate and test a physically–based reflectance model that characterizes the spatial variability of multispectral images obtained over semivegetated landscapes. The immediate objective is to develop a flexible, physically–based algorithm for estimating the amount of subpixel vegetation cover (i.e. horizontal fractional cover) on a pixel–by–pixel basis using only one set of satellite multispectral data under clear–sky conditions, without ground truth, and without having to compute the numerous scattering and absorption parameters that govern atmospheric radiative transfer. The focus is on natural landscapes that exhibit random behavior in the size and location of individual plants, and in the soil background reflectance. The goal is to accomodate both the subpixel scales associated with the bulk physical properties of the plant canopy (overall geometry, height, and diameter) as well as the regional scales associated with the variability in soil background reflectance. The long–term objective is to provide a framework for the physically–based parameterization of mesoscale landsurface hydrology using remote multispectral observations.

1.2 Background

The physically–based parameterization of the large–scale coupled heat and moisture fluxes of semivegetated landscapes is a unsolved problem in hydrology (NASA, 1988). The principal difficulty arises from the complex spatial and

temporal heterogeneity of the interrelated hydrological, geophysical, and biological processes, as well as the many landsurface variables which define them. The hydrologic variables, including soil moisture, vegetation type and amount, hydraulic conductivity, and temperature, often exhibit random behavior and possess spatial scales of variation that are much smaller than the overall scale of the parameterization (mesoscale or greater). Such heterogeneity limits the fidelity of the usual homogeneous mathematical description of individual hydrologic processes (evapotranspiration, infiltration and runoff) and engenders the formidable logistical problem of how to acquire regionally representative hydrologic data in an efficient, cost–effective manner.

Most classical approaches to mesoscale investigations, such as flood forecasting, river basin management, and environmental impact assessment, rely on standard hydrometeorological data obtained at ground–based stations. Such stations, usually few in number, are often located at airports or agricultural research sites and almost never in remote watersheds. Regional surface fluxes are generally estimated using an area–weighted extension of point estimates calculated for the ground station data. However, since the ground stations do not necessarily capture all of the basinwide spatial variability in soil, vegetation and climate, and since the location of a station itself may be biased toward a particular hydrologic regime, the accuracy of that approach is highly uncertain.

The problem is more critical in global–scale hydrologic parameterizations, as modeled within atmospheric general circulation models (GCMs). Those models possess typical grid scales (100 km) which are much greater than the spatial scale of fluctuation of the hydrologic processes themselves (i.e. 1–100 km, See Smagorinsky, 1978). Although, traditionally, many GCMs prescribed simple surface flux models (i.e. Manabe, 1969; Washington and Parkinson, 1986), more

detailed algorithms have been recently proposed which include a large number of soil and vegetation properties (e.g. Dickinson, 1984; Rind, 1984; and Sellers et al, 1986). However, the practical benefit of those newer, more sophisticated parameterizations is not realized due to the lack of spatially detailed global landsurface hydrologic data.

A specific need for more detailed spatial landsurface data may be beneficial for estimating subsurface properties, through the application of a time–averaged one–dimensional statistical–dynamic representation of the climate–soil–vegetation system. Eagleson (1982) mathematically formulated three interrelated hypotheses describing the short, medium, and long–term equilibrium states of soil, vegetation, and climate for natural undisturbed systems. He argued that in water–limited systems, the short–term ecological pressure minimizes water demand stress through adjustment of vegetation canopy amount, the medium term pressure selects plant species for minimum water use, and in the long term, vegetation and climate modify soil properties in the root zone in a synergistic manner to reach a climatic–climax state such that biomass productivity is maximized. Limited testing of those hypotheses have been made on several catchments (Eagleson and Tellers, 1982) and on two savanna systems (Eagleson and Segarra, 1985).

Estimation of Soil Hydraulic Properties. Jasinski (1987) proposed to apply the equilibrium hypotheses to estimate soil hydraulic properties of natural water–limited systems, using vegetation density estimated from satellite data. A critical step in this analysis was the development of an algorithm for estimating spatially–variable fractional canopy cover, which controls the bounds of the rejection probability of the hypothesis. He collected extensive data for that investigation which is currently underway (See Jasinski and Eagleson, 1986; Eagleson and Jasinski, 1988).

1.3 Application of Satellite Radiometric Observations to Regional Hydrology

The critical need for detailed spatial and temporal knowledge of regional landsurface processes has led researchers to investigate the application of electromagnetic radiation data obtained from satellite platforms. Those data consist of instantaneous, spatially integrated observations of the electromagnetic radiation fluxes emitted or reflected from the earth's surface and atmosphere. The reasonableness of this approach rests not only in the relative facility of covering extensive areas in a matter of seconds, but also in the fact that many of the physical properties which describe the heat and moisture fluxes (i.e. landsurface and atmosphere composition, temperature) also govern radiative transfer. Unknown landsurface and atmospheric properties are theoretically determined by solving the inverse problem. That is, given a set of remote electromagnetic observations, one inverts the radiative transfer equation using a particular wavelength, or combination of wavelengths, so that the parameters of the reflecting surface and the medium can be retrieved. The challenge lies in carefully choosing specific wavelengths within the spectrum which respond to the presence (or absence) of the particular object or constituent under investigation.

Although the theoretical radiative transfer aspects of remote sensing are well understood (i.e. Chandrasekhar, 1960; American Society of Photogrammetry (ASP), 1983; Slater, 1980; Tsang et al, 1985), because of the variability and large number of landsurface and atmospheric parameters, and the limited number of satellite systems, the use of remotely sensed data alone has not been sufficient to estimate landsurface fluxes as of date. Successful retrieval of individual landsurface parameters has been achieved (See ASP, 1983), however, which can be incorporated into classical surface heat and moisture flux equations. For example,

the microwave portion of the spectrum has been shown to be sensitive to soil moisture content because of the large contrast between the dielectric properties of liquid water and dry soil (Schmugge, 1983). The visible and near–infrared portions of the spectrum are sensitive to vegetation amount due to the contrast in reflectance behavior between soil and healthy green vegetation (Colwell, 1974). Thermal infrared wavelengths have been shown to be sensitive to surface and atmospheric temperature (Chahine, 1983). The published results of those investigations are too numerous to mention, although an excellent summary of the response of different wavelengths to particular landsurface properties is provided in ASP (1983).

Most evapotranspiration investigations which have been reported typically combine one or more remotely sensed landsurface variables, such as albedo and temperature, with ground based meteorological data, and apply them to classical sensible and latent heat flux terms in the energy balance equation. Several studies over relatively homogenous agricultural areas have employed either airborne or hand–held radiometers. Camillo et al (1983) developed an energy and moisture balance model of the upper soil and lower atmosphere for use with remotely sensed surface temperature and soil moisture and standard meteorological data, and applied the model over bare soil. A similar approach was later used by Gurney and Camillo (1984) over wheat and barley. Van de Griend and van Boxel (1989) extended the approach to include multilayer canopy representation, and tested the model over maize. Reginato et al (1985) combined remotely sensed reflected solar radiation and surface temperatures using airborne sensors, with ground meteorological data to calculate net radiation and sensible heat flux over wheat.

Theoretically, the same approach as above can be used for investigating surface fluxes using satellite–based sensors. However, practical application has

been limited due to complexities arising from atmospheric effects and the problem of characterizing landsurface heterogeneity, especially with regard to vegetation and soil moisture. Most hydrologic studies using remote sensing data limit the study area to spatially homogeneous landscapes, or they assume spatial homogeneity. Price (1982) applied visible and thermal infrared data from the Heat Capacity Mapping Mission (HCMM), to the energy balance equation to estimate landsurface thermal inertia and moisture availability over principally grassland areas in Washington and Oregon. Similar approaches have been used by Carlson (1986) using GOES data over grasslands in Kansas, and by Taconet et al (1986) using AVHRR data over wheat, and by Pierce and Congalton (1988) using simulated TM data over mixed conifer forests in California.

While it is evident from above that significant progress has been achieved in the analytical treatment of satellite data for regional hydrologic investigations, there is substantial need for additional research. Ongoing programs within the International Satellite Land–Surface Climatology Project (ISLSCP), such as the First ISLSCP Experiment (FIFE) (Sellers et al, 1988; Hall et al 1989) and the Hydrological Atmosphere Pilot Experiments (HAPEX) (Andre, 1986) are currently bringing into focus the current limitations, and research needs, for applying satellite data to the study of landsurface hydrological processes. Research areas include developing methods to improve extraction of all the information hidden in the multispectral data, as well as rethinking the basic structure of classical energy and moisture balance equations to accommodate the particular characteristics of satellite data.

A recurrent problem identified by many of the above studies is the characterization of the spatial variability of vegetation amount, whether it be fractional cover, biomass, or leaf area. Knowledge of vegetation cover is

hydrologically important with regard to the partitioning of bare soil evaporation and transpiration, as with its influence on albedo, moisture storage, and surface temperature. Currently, however, no physically–based technique exists for estimating vegetation amount for large areas using only multispectral data. Most estimation procedures are empirical, involving ratios, differences, or transformations of signals in red and near infrared bands (Perry and Lautenschlager, 1984). Such indices respond to changes in vegetation amount primarily due to i) the relatively high radiation absorption capacity of chlorophyll in the red band, and ii) the high reflectance properties of the leaf structure in the near infrared band, as compared to soil. Despite that sensitivity to vegetation amount, however, vegetation indices provide only limited understanding of the physical structure of the scene. They generally require a large number of training samples and can exhibit inordinate scatter for equivalent amounts of vegetation.

1.4 Physically–Based Estimation of Subpixel Vegetation Cover

The physically–based characterization of spatially variable plant cover, using satellite multispectral data, is a critical constraint to hydrologic parameterization in many semivegetated landscapes. An important example is the natural semiarid region of most of the southwest United States, which typically consists of a random distribution of different size tree or shrub canopies interspersed with a mixture of grasses and bare soil. Also important are agricultural lands during early growth stage, in which the crops are more uniform in size and spacing, and separated primarily by bare soil.

One of the major problems in trying to use satellite multispectral data in semivegetated regions is that the plant canopy or size typically varies at

characteristic scales (several meters) much smaller than the spatial resolution of current satellite pixels (several tens of meters). At the same time, soil background reflectance varies over a wide range of length scales (meters to several thousand meters) due to geoclimatic factors affecting its physical structure and chemical composition. Since satellite observations integrate the reflectance of all elements within the pixel, subpixel information such as fractional cover, leaf area, surface roughness, is apparently lost. Thus, techniques are needed to disaggregate the individual subpixel components, while accounting for the variations in both soil and vegetation reflectance.

The above problem of estimating subpixel vegetation cover can be graphically illustrated using Figures 1.1 through 1.4. Figure 1.1 depicts a hypothetical landscape viewed through a red filter, in which the plants appear as dark circular disks of constant reflectance and of random size and distribution. The plants are superimposed on various soils which can possess different reflectances as indicated by the different shading on the figure. Also drawn on the scene is the outline of nine satellite pixels, each of which contains any number of trees or any type of soil background.

Figure 1.2 illustrates the remotely–sensed image of the scene in Figure 1.1 using the same red filter. Only one reflectance value exists for each pixel, obtained through the sensor's spatial integration of the reflectances of all the elements in the pixel. Thus, the subpixel information (size, number and distribution of the trees, distribution of soil reflectance) can not be discerned.

The same scene as viewed in the near infrared spectrum is depicted in Figure 1.3. In that band the plants generally appear brighter than the soil. The soil reflectance, although brighter than in the red region, possesses approximately the same spatial distribution. The remotely–sensed image of the near infrared scene also averages out the components of the pixel, as shown in Figure 1.4.

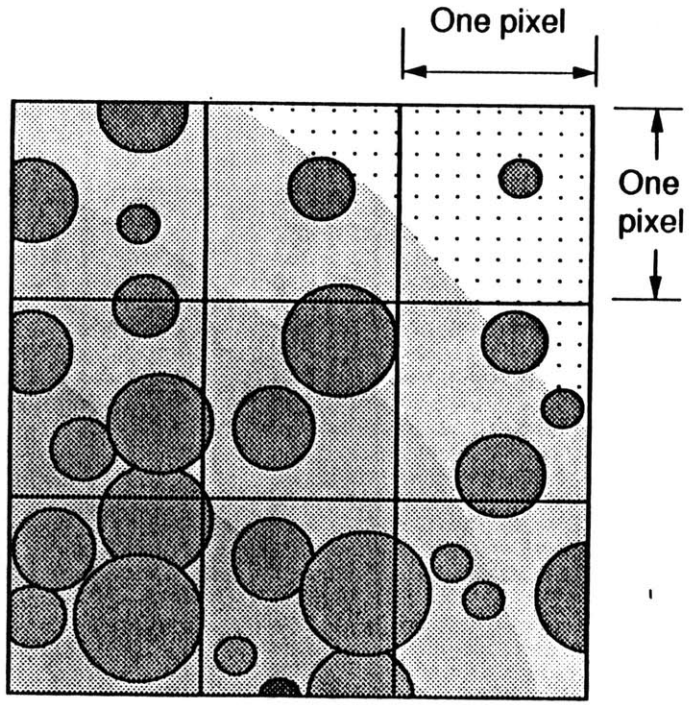

Figure 1.1 Hypothetical semivegetated scene viewed through red filter.

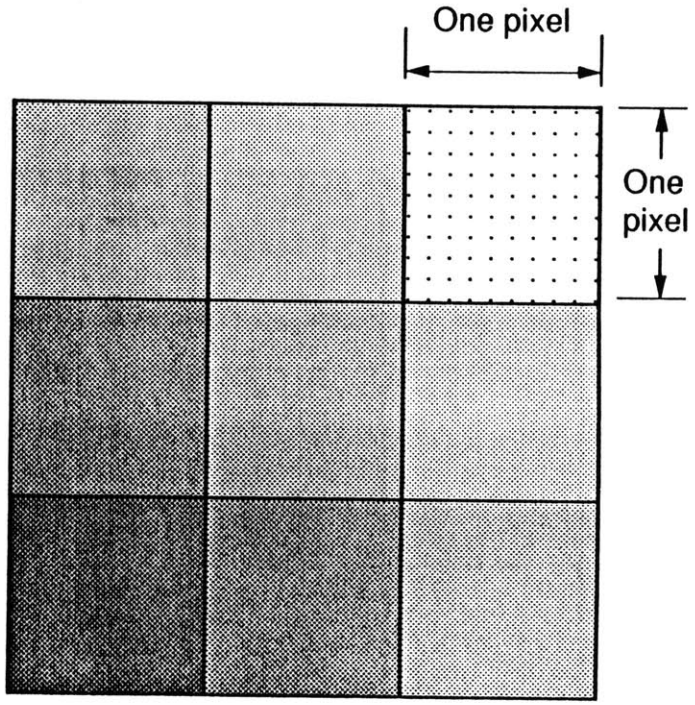

Figure 1.2 Remotely-sensed image of scene in Figure 1.1.

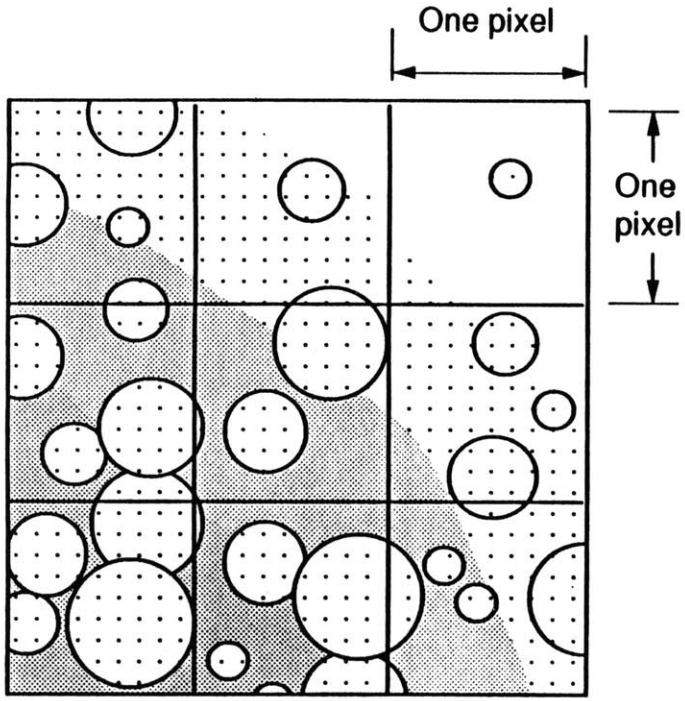

Figure 1.3 Hypothetical semivegetated scene viewed through near-infrared filter.

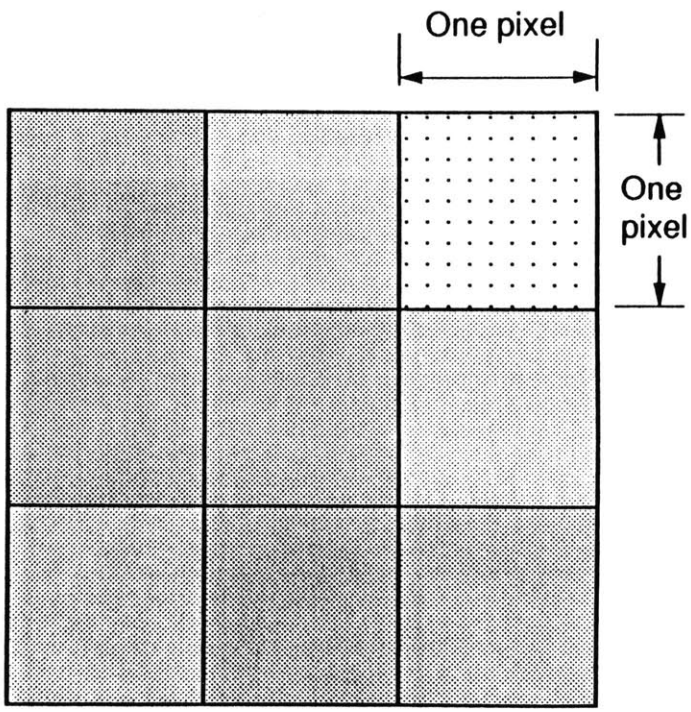

Figure 1.4 Remotely-sensed image of scene in Figure 1.3.

The inverse problem can be summarized in the following questions. Given only the two remotely–sensed images, to what extent can the subpixel properties of the original scene be retrieved? Can a physically–based inverse method be developed that exploits the true multispectral nature of the data (i.e. two observations per pixel), by incorporating cross spectral correlations? Are there assumptions with regard to the geometry or spatial distribution of the plants and the soil, which may be useful toward the solution? Also, are there particular relationships between the soil and vegetation which preclude certain solutions, such as the relationship between soil reflectance and vegetation amount, or vegetation amount and shadow? Those questions need to be considered to adequately address this problem.

In the real world, the problem is still more complex than the preceding example, especially for large–scale parameterizations. In addition to subpixel variations, one encounters many regional–scale variations in soil and vegetation reflectance due to a variety of geoclimatic factors. For instance, changes in slope and aspect induce corresponding changes in scene reflectance through an effective altering of the illumination and viewing angles. Changes in elevation, slope, and aspect also cause scene variability through their indirect influence on such properties as soil moisture, and vegetation species and density. Vegetation reflectance can change with plant size and density, and with changes in underlying soil reflectance. In such regions the stochastic nature of the vegetation and soil properties must be accommodated. Thus, the problem consists of trying to discern, through the interpretation of multispectral data, not only the small–scale (i.e. subpixel) variability, but also the regional–scale correlations that might exist.

The ability to estimate regionally variable subpixel vegetation cover would be invaluable to the solution of the large–scale parameterization problem.

Successful development of such an algorithm has potential utility for investigating not only vegetation amount but also other surface geophysical properties requiring subpixel resolution.

1.5 Physical Basis of Red–Infrared Scattergrams: Preliminary Analysis

A common attribute of the red–infrared data spaces of vegetated images is that they often take on a triangular shape, or tasseled cap. The physical basis of this shape was first investigated by Kauth and Thomas (1976) using the Suits model (1972) applied to a homogeneous layer of crops. They explained the seasonal progression of the tasseled cap in terms of the growth, maturation, and senescence of crops.

It was shown during the initial stages of this research that individual images of many natural semivegetated landscapes also exhibit triangular shapes when plotted in the red–infrared space (Jasinski, 1987). Three such scattergrams, constructed using three segments of Bands 2 and 4 of a Landsat 2 Multispectral Scanner (MSS) image in the vicinity of Taos, New Mexico, are shown in Figures 1.5 through 1.7. The first triangular scattergram, Figure 1.5, consists of a plot of the red–infrared data pairs of all the pixels in a segment covering about 400 square kilometers. The region contains a variety of semivegetated landscapes, ranging from bare soils, grasses shrubs along the flat lands in the valley, to pinyon–juniper in the foothills, to ponderosa pine and douglas firs in the mountains. The resulting characteristic triangular plot is generally flat at the base, but curved along the top. Figure 1.6 contains a smaller segment of pixels covering about 25 square kilometers, located principally in the foothills region dominated by pinyon–juniper trees. The resulting shape is also triangular in form,

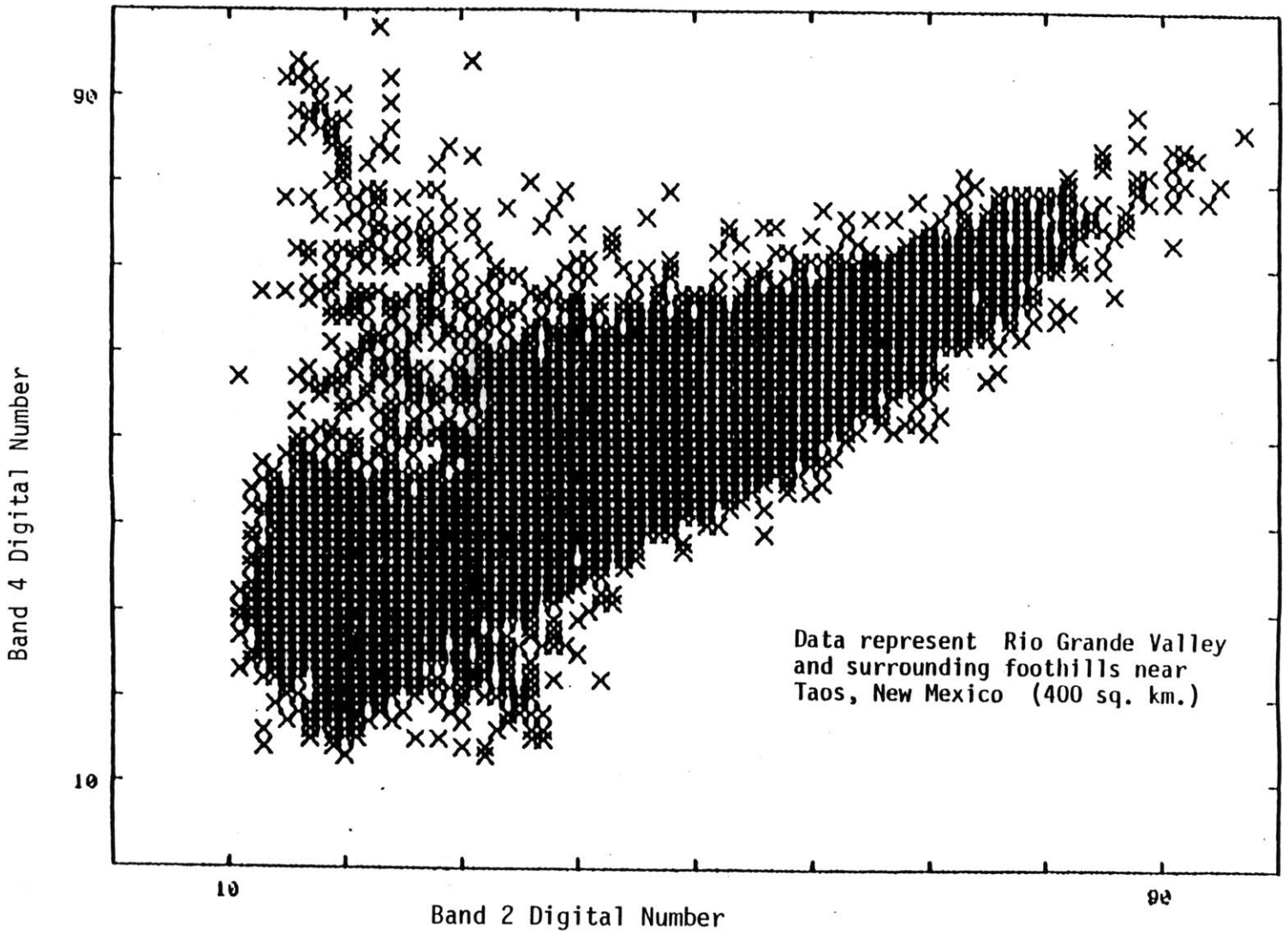

Figure 1.5 Plot of MSS Band 4 versus Band 2: Entire Taos Study Area (40,000 pixels).

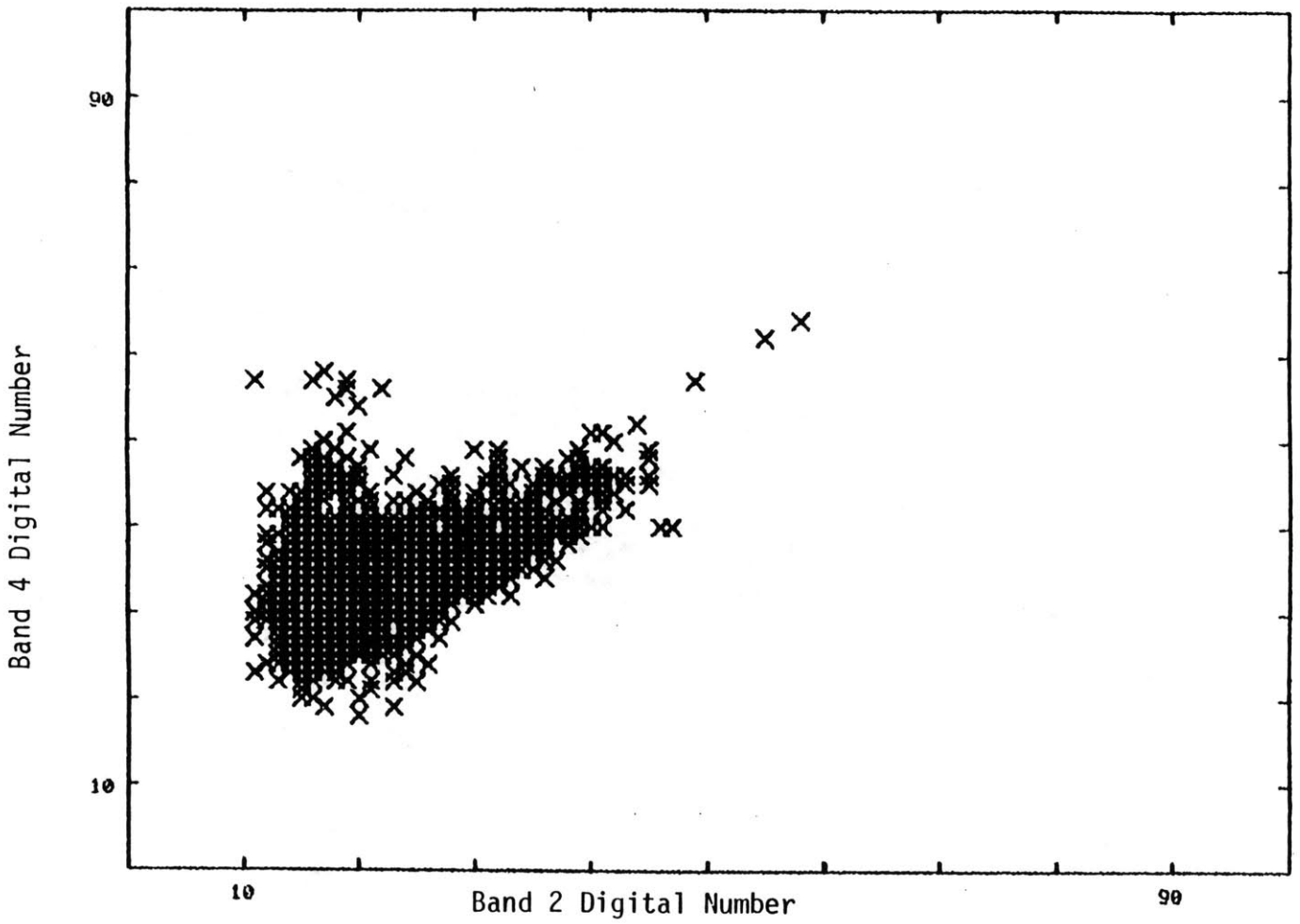

Figure 1.6 Plot of MSS Band 4 versus Band 2: Segment of foothills region in Taos Study Area (2250 pixels).

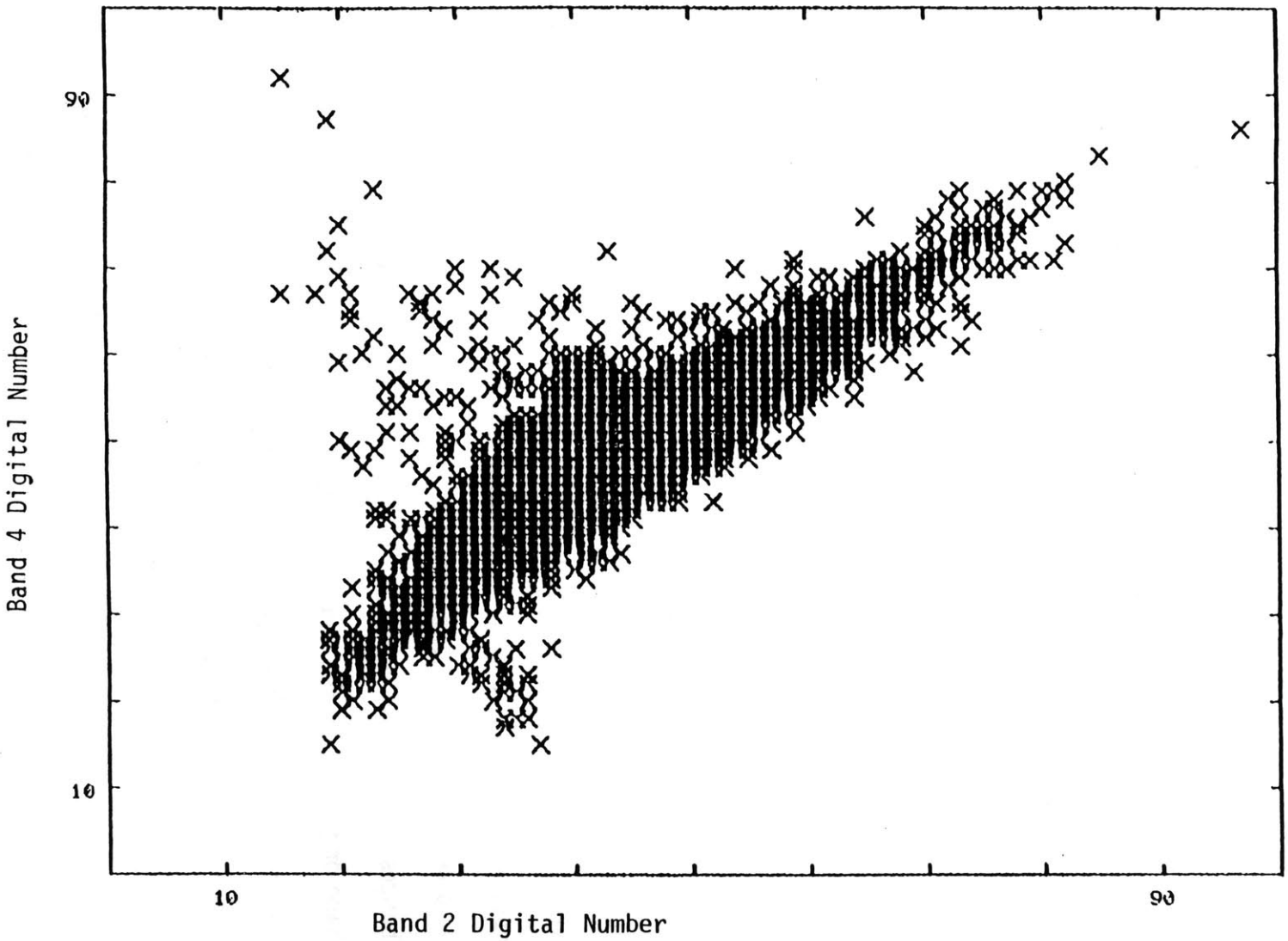

Figure 1.7 Plot of MSS Band 4 versus Band 2: Segment of valley region of Taos Study Area (8,000 pixels).

but much smaller than in Figure 1.5 and with data pairs exhibiting overall lower values. Finally, Figure 1.7 possesses pixels obtained primarily over 80 square kilometers of grasslands. The scattergram again exhibits a triangular shape, but with a wider base than from the foothills region.

Although triangular in shape, the above scattergrams possess many features not present in the Kauth–Thomas investigation. For example, they were constructed from natural vegetated regions and from only one MSS image. Further, individual pixels of the scene possessed different amounts of vegetation species, cover, soil and topography. Thus, the physical mechanisms which lead to those triangular shapes can not be explained simply in terms of the season growth of plants as noted by Kauth and Thomas.

Using a simple area–weighted combination of vegetation and soil reflectances, it was demonstrated that the characteristic triangular shapes of red–infrared scattergrams could be explained in terms of percent canopy cover, variable soil and vegetation reflectance, and shadows (Jasinski, 1987). For instance, using typical values of vegetation and soil reflectance, the hypothetical data space of a landscape possessing constant vegetation reflectance, variable soil reflectance, and variable canopy cover is, in fact, a triangle (see Figure A1.1). The effect of changes in either the vegetation or soil reflectances causes an equal response in the shape or position of the triangle (Figures A1.2 and A1.3). The inclusion of shadows cast by conical figures causes the triangle to take on a tasseled cap (Figure A1.4). By assuming a linear relation between vegetation reflectance and percent cover, the data space takes on curved sides (Figure A1.5). Other variations in plant or soil parameters, such as leaf area index and soil moisture, can be shown to cause similar effects on the red–infrared scattergram.

The above exercise demonstrated that a key to solving the inverse problem lay in an understanding of the physical basis of the red–infrared scattergram. It

further showed that the problem of estimating subpixel vegetation cover was inherently tied to the distribution of other landscape properties as well, in particular, soil background reflectance and shadows. That early discovery provided impetus to the direction of the methodology followed in this thesis.

1.6 Elaboration of Goals and Methodology

The research in this report addresses the parameterization of vegetation and soil of natural semi–arid regions using multispectral data, for application in large–scale hydrology. Specific goals and methodology are summarized below.

The first step is the formulation of a physically–based canopy–soil reflectance model that characterizes the spatial variability of multispectral images of semivegetated landscapes at both subpixel and regional scales. A stochastic–geometric reflectance model is developed for that purpose, as it is flexible enough to represent the possible stochastic nature of the distribution of vegetation and soil, but not so detailed as to render its practical application infeasible. The landsurface reflectance model is cast within the framework of an existing theoretical model of upwelling radiance observed by a nadir–viewing satellite.

The second step is the development of an understanding of the shape and structure of red–infrared scattergrams in terms of the physical properties of the landscape. That is achieved through computer simulations of idealized semivegetated landscapes using the above canopy–soil reflectance model. The principal mechanisms that contribute to the evolution of the triangular shape of red–infrared scattergrams are identified through the sequential altering of a given variable in the model.

Next, an inverse method is developed for estimating fractional (i.e. subpixel) canopy cover on a pixel–by–pixel basis using only multispectral data without ground truth. The inverse procedure chosen for the analysis is the method of moments in which the theoretical moments of the canopy–soil reflectance model are derived and equated to the actual moments of the multispectral image. The procedure makes use of the understanding of the shape and structure of the red–infrared scattergram, as it requires writing conditional moments for portions of the scattergram where the pixels are assumed to possess one or more similar attributes. The inverse procedure is further facilitated by assuming geometric similarity among the plant and shadow geometry, and through the formulation of a functional relationship among the fractional covers based on the similarity parameter and an assumed spatial distribution of the plants. A Sampling Scale Ratio is developed, based on the relative scales of the cover components relative to the scale of the pixel, which quantifies when the correlation among fractional covers exists.

After testing the inverse method on the simulated images to determine its effectiveness, the inverse procedure is then tested on actual aerial and satellite multispectral data. The field sites include one agricultural area and one natural forested scene, both in Arizona. Other properties of the landscape, such as the spatial distribution of soil reflectance, are also examined at that time.

Chapter 2

RADIANCE OBSERVED BY SATELLITE

This chapter briefly reviews existing fundamental radiative transfer theory related to remote sensing of landsurface properties from a satellite platform. The purpose is to provide an analytical framework, using an existing model of surface–reflected and atmospheric–scattered radiance, into which the canopy–soil reflectance model developed in Chapter 4 can be incorporated. While the principles in the present chapter generally apply to all wavelengths and media, the emphasis is on visible and near–infrared wavelengths interacting in the earth's atmosphere. Particular characteristics relevant to Landsat Multispectral Scanner (MSS) and Thematic Mapper (TM) sensors are reviewed.

2.1 Radiative Transfer Theory

2.1.1 Definitions and Nomenclature

The propagation of electromagnetic energy of a particular wavelength, λ, is described in terms of the specular radiance, $L_s(\lambda)$, defined as the specular radiant energy flux per unit wavelength per unit solid angle per unit of projected area in a specified direction. A graphical illustration of radiance emerging from an elemental area, dA, centered at P(x,y,z) is drawn in Figure 2.1. The sketch depicts a portion of specular radiant flux, $d\phi_s(\lambda)$, that emerges from dA and that is confined within the solid angle, $d\Omega$. The flux makes an angle θ with the vertical z axis, and an angle ψ with the x axis in a clockwise manner when viewed from the bottom.

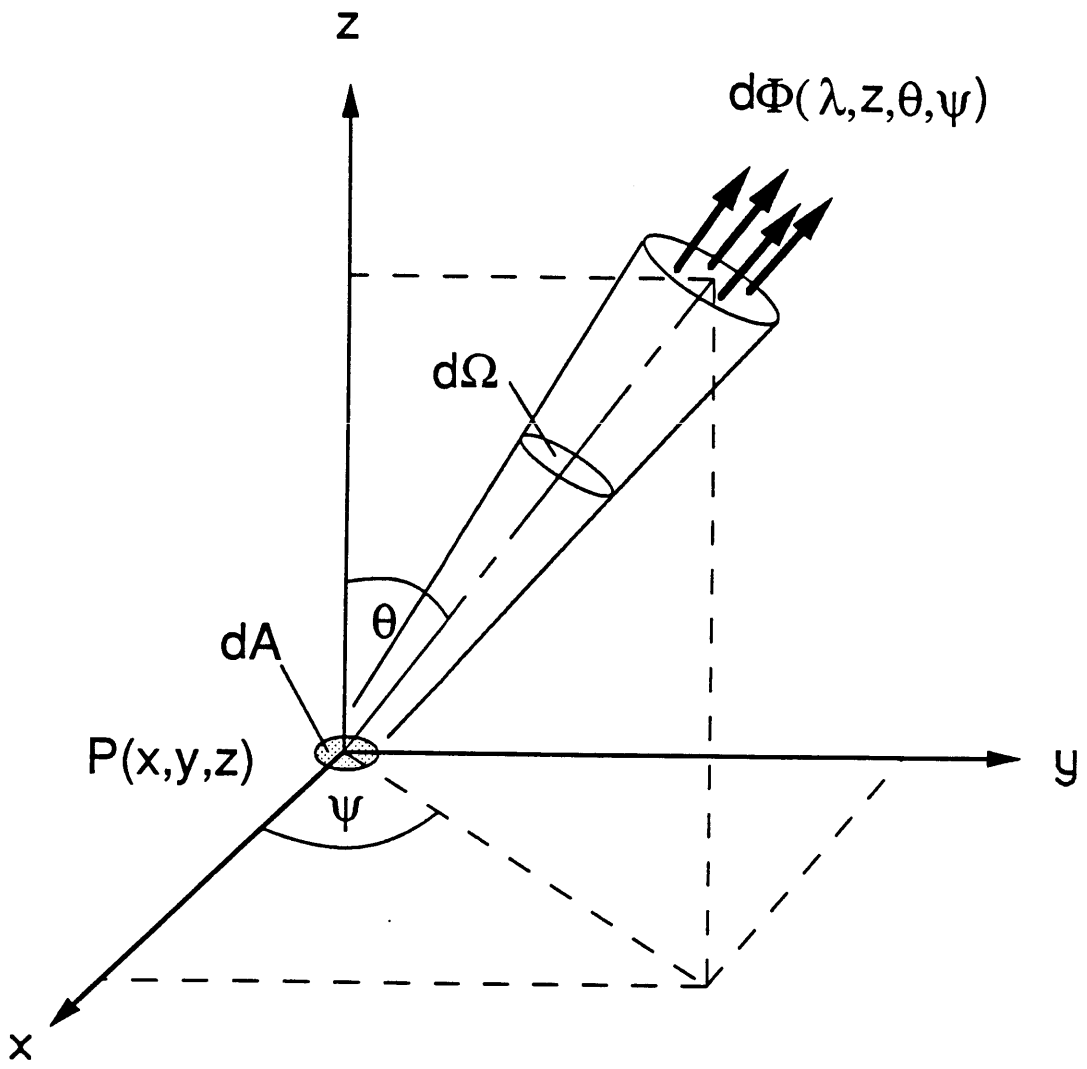

Figure 2.1 Graphical illustration of radiance.

Mathematically, the relation between specular radiance and radiant flux is given by,

$$L_s(\lambda) = \frac{d^2\phi(\lambda)}{d\Omega dA\cos\theta} \tag{2.1}$$

where the units of radiant flux are Watts per micrometer (W μm^{-1}) and those of radiance are Watts per square meter per steradian per micrometer (W m^{-2} $sr^{-1}\mu m^{-1}$).

Integration of the specular radiance over a finite bandwidth yields the total radiance within that interval of the spectrum, or

$$L(\lambda) = \int_{\lambda_1}^{\lambda_2} L_s(\lambda')d\lambda' \tag{2.2}$$

where now λ represents the center of the band, and the units are Watts per square meter per steradian (W m^{-2} sr^{-1}). While this measure is also specular in the sense that it represents the radiation only within a particular bandwidth, for simplicity, the adjective "specular" is deleted as the wavelength dependency is adequately represented by the nomenclature.

The integration of the radiance emitted from dA over the entire spherical angle is termed radiant exitance, $M(\lambda)$, or

$$M(\lambda) = \int_{2\Omega} L(\lambda)\cos\theta\, d\Omega \tag{2.3}$$

It possesses units of Watts per square meter per micrometer (W $m^{-2}\mu m^{-1}$).

The total radiance impinging on a surface from all directions can be defined in an analogous manner and is termed irradiance, $E(\lambda)$, having the same units.

A beam of radiation impinging on a surface at a given angle can be reflected, absorbed, and transmitted. The relative amounts of each component, as well as the direction of the reflected radiation, depend on the properties of both the incident beam (i.e. wavelength, angle of incidence) and the properties of the surface (i.e. roughness and chemical composition, etc.). Figure 2.2 illustrates the geometry describing reflectance due to a source beam, $L'(\lambda;\theta',\psi')$ impinging on dA, as viewed from an observer located at (θ,ψ). The observed beam, $dL(\lambda;\theta,\psi)$ represents only a portion of the total radiation reflected from the surface, as radiation is simultaneously being scattered in other directions. This angular dependent reflectance, due to a single source, is termed bidirectional reflectance, $dR(\lambda;\theta',\psi';\theta,\psi)$. It is a dimensionless quantity and is mathematically defined,

$$dR(\lambda;\theta',\psi';\theta,\psi) = \frac{dL(\lambda;\theta,\psi)\cos\theta\, d\Omega}{L'(\lambda;\theta',\psi')\cos\theta' d\Omega'} \tag{2.4}$$

When the incident radiation arrives from sources throughout the entire hemispherical angle, a useful quantity is the bidirectional reflectance distribution function (BRDF), or

$$f(\lambda;\theta',\psi';\theta,\psi) = \frac{dL(\lambda;\theta,\psi)}{dE(\lambda;\theta',\psi')} \tag{2.5}$$

with units of inverse steradians (sr^{-1}) (Slater, 1980).

When the reflected radiation is independent of angle, the surface is described as Lambertian. In many practical remote sensing investigations over natural landscapes, surface reflectance can often be assumed as Lambertian, especially at

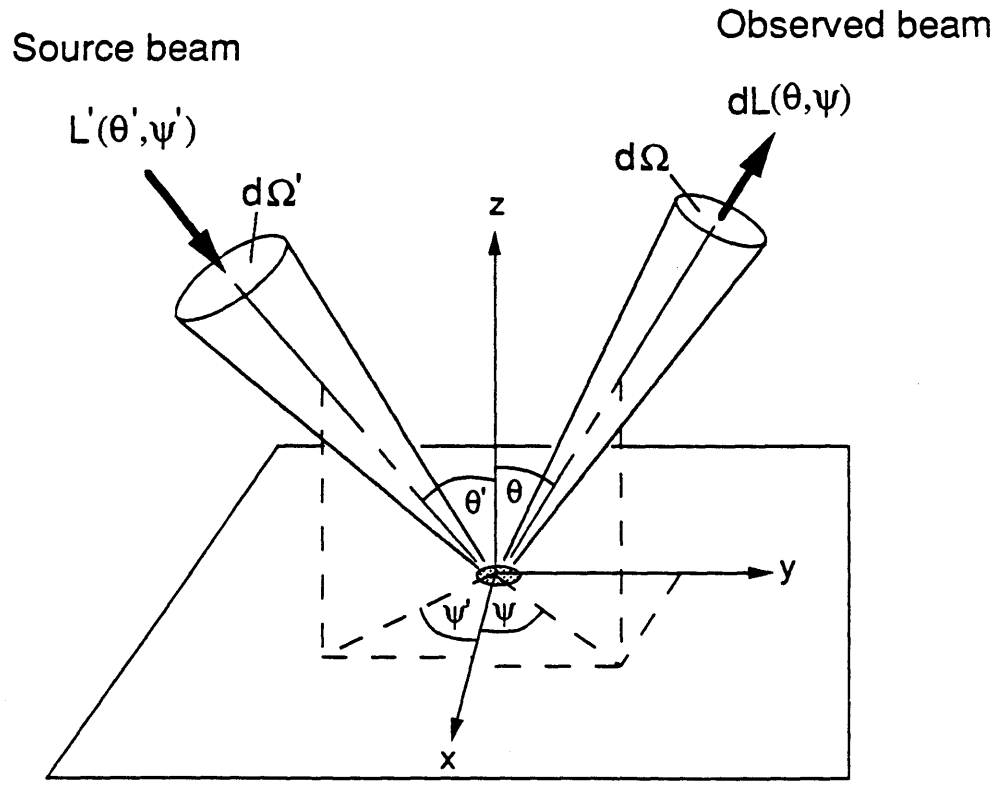

Figure 2.2 Geometry of surface reflectance
(After Slater, 1980).

low zenith angles (Slater, 1980). One exception is water which exhibits bidirectional reflectance. The specular reflectance, $R(\lambda)$, of a Lambertian surface is simply,

$$R(\lambda) = \frac{\pi L(\lambda)}{E(\lambda)} \tag{2.6}$$

(Slater, 1980). It is also a dimensionless quantity.

2.1.2 Radiative Transfer Equation

A beam of radiation traversing a medium can be attenuated due to absorption and scattering, or enhanced by emission and multiple scattering, as it interacts with the medium. A graphical sketch of this process is shown in Figure 2.3. For atmospheric applications, it is often sufficient to assume a plane–parallel medium in which the stratification lies along the z axis (vertical). In such cases the radiative transfer equation in its most general form is,

$$\mu \frac{\partial}{\partial} \frac{L(\lambda,\tau;\mu,\psi)}{\tau} = L(\lambda,\tau;\mu,\psi) - J(\lambda,\tau;\mu,\psi;P) \tag{2.7}$$

where J represents the source function (W $m^{-2}sr^{-1}\mu m^{-1}$), μ equals $\cos\theta$, and τ is the optical thickness (dimensionless). The source function characterizes all the scattering and emission from external sources which enhance the intensity of the beam. The optical thickness normalizes the path length with respect to the different scattering and absorption processes that the beam encounters. The quantities J and τ are functions of both the wavelength of the beam and the composition of the medium.

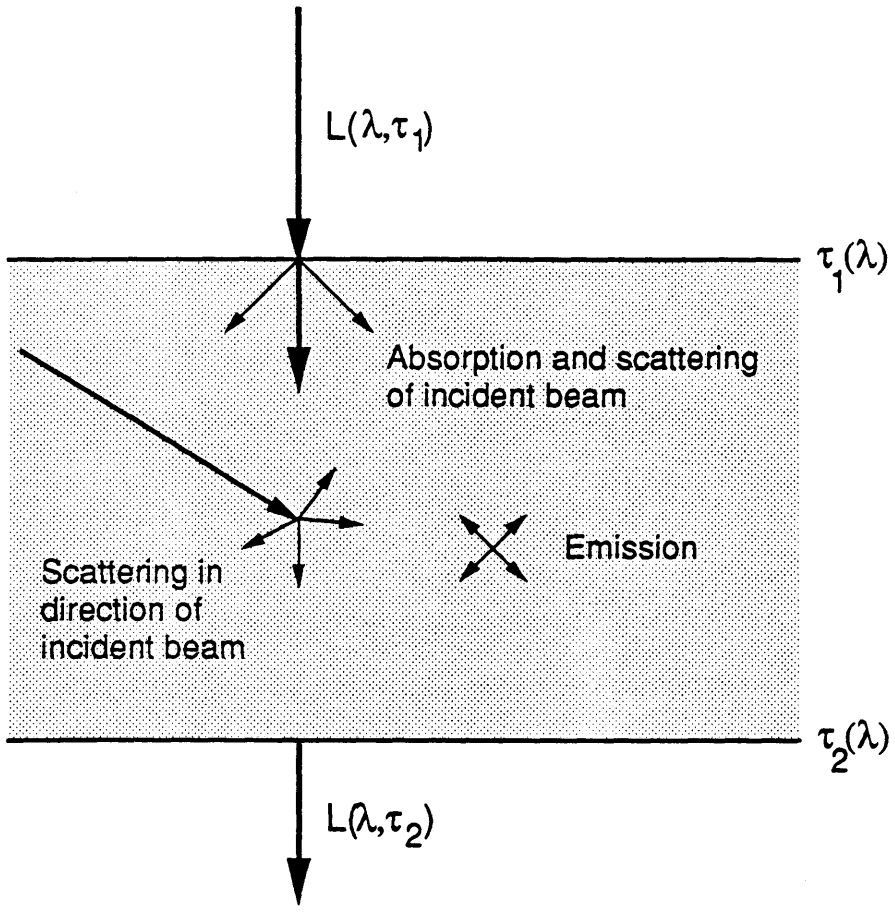

Figure 2.3 Graphical illustration of scattering, absorption, and emission.

The angular distribution of the scattered radiation is described by the phase function, $P(\lambda;\theta,\xi)$, where θ is the direction of the incoming radiation, and ξ is the direction of the scattered radiation. It is incorporated into the radiative transfer equation through the source function, J. The exact form of the phase function depends on both the wavelength and the size and shape of particles of the medium.

The formal solution of the radiative transfer equation is obtained by integrating it over the interval (τ_1, τ_2), or,

$$L(\lambda;\tau_2;\mu,\psi) = L(\lambda;\tau_1;\mu,\psi)e^{-(\tau_2 - \tau_1)} + \int_{\tau_1}^{\tau_2} J(\lambda;\tau';\mu,\psi;P)e^{-(\tau_2 - \tau')/\mu}\, d\tau'/\mu \tag{2.8}$$

(Chandrasekhar, 1960). The solution consists of two terms. The first term on the right hand side represents the direct beam which is attenuated in accordance with the optical thickness. The second term represents an augmentation in intensity due to external scattering and emission into the beam. The actual solution requires knowledge of the behavior of τ and J throughout the medium.

2.2 Radiance Observed by Nadir–Viewing Satellite

2.2.1 Scattering and Absorption Mechanisms of a Clear Atmosphere

It is useful to examine the principal scattering, absorption, and emission mechanisms which govern radiative transfer at visible and near–infrared wavelengths (0.4 – 1.3 μm) in the earth's atmosphere under clear–sky conditions. Clear atmospheres consist principally of gaseous molecules, particle aerosols (dust), water droplets and ice crystals. Gas molecules are the smallest constituent,

generally much less than 0.1 μm in diameter. Their spatial and temporal distribution depend on the specific gas. Many of the principal gases, such as nitrogen, oxygen, and argon, exhibit relatively constant vertical distributions with time. Other important gases, such as ozone, carbon dioxide, and sulfur dioxide, are variable with time. Water vapor can show significant horizontal and vertical spatial variability over time intervals as short as hours (Liou, 1980).

Aerosols include solid particulates and haze water droplets that range in size from 0.1 μm to 1.0 μm. The largest atmospheric particles include cloud water droplets and ice crystals with mean sizes between 1.0 μm and 10 μm. The aerosols are also highly variable in time and space (Iqbal, 1980).

All the above atmospheric constituents scatter solar radiation. The amount and direction of scatter depends on the relative scale of the incident wavelength as compared to the size and shape of the particle, as well as the volume density of the particles. When the size of the particles is much smaller than the size of the wavelength, scattering can be represented by Rayleigh scattering. Most gas molecules in the atmosphere contribute to scattering in the visible and near–infrared wavelengths approximately according to that mechanism (Slater, 1980), although for clear skies, the greatest scatter occurs at the shorter wavelengths (i.e. 0.4μm). When the particle sizes are comparable to or larger than the wavelength, the scattering is termed Mie scattering. Aerosols, cloud droplets, and ice crystals scatter solar radiation according to the Mie mechanism (Liou, 1980).

Absorption due to transitions in molecular energy levels occur throughout the visible and near–infrared spectrum, although the greatest effect is observed in the near–infrared region. Diatomic oxygen has three weak absorption bands centered at 0.63, 0.69, and 0.76 μm (Iqbal, 1983). Ozone absorbs from 0.45 to

0.77 μm. Water vapor absorbs at 0.72, 0.81, 0.94, 1.10, 1.38, and 1.87 μm. Carbon dioxide exhibits weak absorption bands 1.4, 1.6, and 2.0 μm (Liou, 1980).

Although the integrated effects of all the different types of scattering and absorption are a complex phenomenon, the solution to the radiative transfer equation is facilitated by treating many of the processes in an additive manner. An important quantity to which this applies is the optical thickness. For the atmosphere, $\tau(\lambda)$ can be treated as a sum of optical thicknesses due to Rayleigh scattering by gas molecules, $\tau_R(\lambda)$, Mie scattering by aerosols, $\tau_M(\lambda)$, and absorption by gas molecules, $\tau_a(\lambda)$ (Liou, 1980), or

$$\tau(\lambda) = \tau_R(\lambda) + \tau_M(\lambda) + \tau_a(\lambda) \tag{2.9}$$

Practically, the total optical thickness of clear skies (low aerosol density and water content) is much less than 1.0. For example, observations over southern Arizona during the dry season typically range from about 0.5 at 0.4 μm to less than 0.1 at 1.5 μm (Slater, 1980), with perturbations occurring at the principal absorption bands of water vapor. The decreasing trend is principally due to the decrease in Rayleigh scatter with increasing wavelength. Cloudy, aerosol–laden skies can possess optical thicknesses greater than 10 (Chahine, 1983).

2.2.2 Upwelling Radiance at the Top of the Atmosphere Under Clear Skies

The radiance leaving the top of the atmosphere depends on numerous complex factors including the solar zenith angle, ground reflectance and topography, and atmospheric composition. Despite the complexity, analytical solutions for the theoretical nadir radiance observed by a satellite for the case of a cloudless sky have been derived by several authors (See for example, Kaufman,

1982; Dave, 1980; Otterman and Fraser, 1979, Otterman et al, 1980; and Otterman, 1978, 1981). The general approach in most of those models is to assume single scattering and to treat the total outgoing radiance as the sum of direct and diffuse components. The single scattering assumption has been shown to be appropriate for small optical thicknesses (i.e. less than about 0.5) (Bugnolo, 1960).

The purpose of this section is not to review the merits of the above referenced models, but to select and describe one of them for the purpose of providing a framework for incorporation of the stochastic landsurface reflectance model presented in Chapter 4. Although any one of the models could be selected, the formulation by Otterman and Fraser is presented because it incorporates many of the atmospheric processes identified above, as well as the reflectances of the target pixel and surrounding pixels.

Otterman and Fraser (1979) developed an analytically attractive theoretical expressions for the nadir radiance as measured by a satellite, for the case when the target pixel possesses a different reflectance than the surrounding area. Their concern was to account for adjacency effects, that is, the contribution of light scattered from areas surrounding of the target pixel into the sensor's field of view.

The authors' approach was to treat the total nadir radiance observed by the satellite as the sum of three components as depicted in Figure 2.4. First, the direct beam component, $L_r(\lambda)$, represents the portion of solar irradiance reflected vertically from the target pixel that is attenuated by atmospheric effects, or

$$L_r(\lambda) = R(\lambda)E(\lambda)\exp[-\tau(\lambda)]/\pi \qquad (2.10)$$

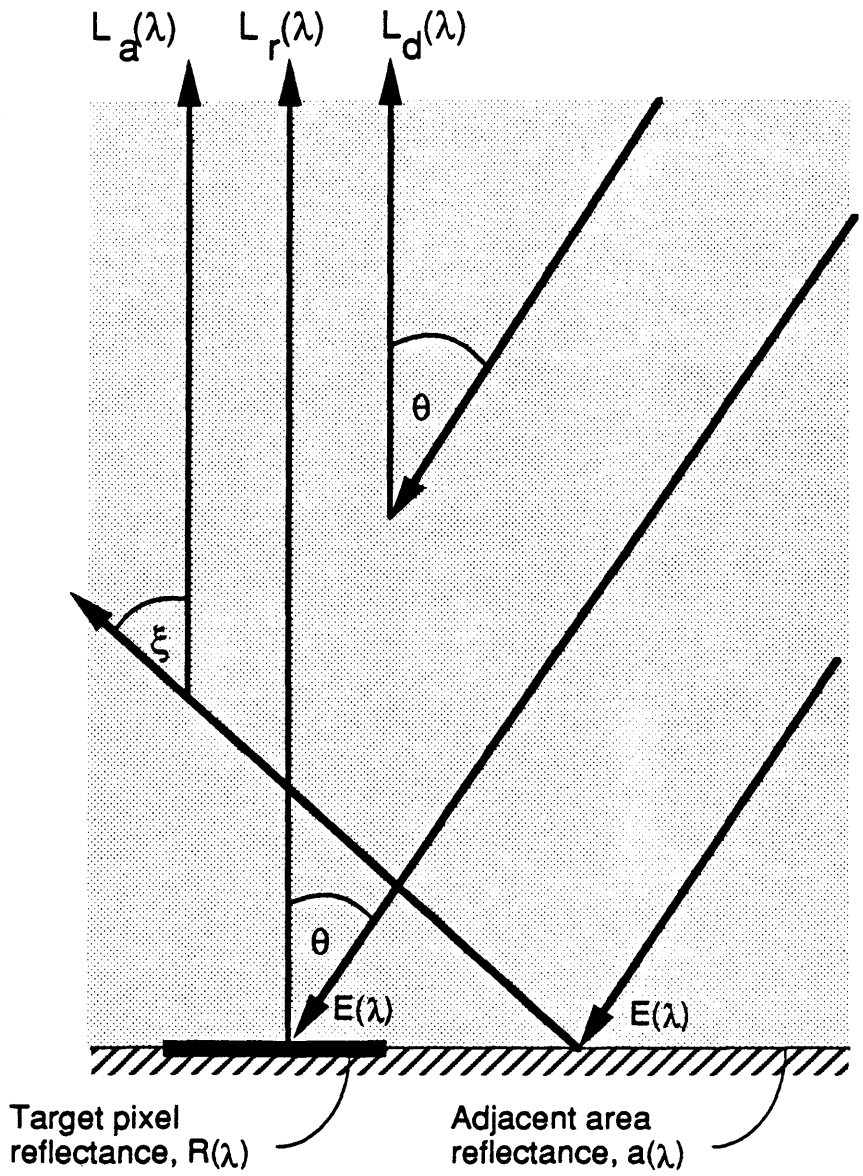

Figure 2.4 Graphical illustration of direct and scattered diffuse components of radiance at the zenith (After Otterman and Fraser, 1979).

where $R(\lambda)$ is the reflectance of the target pixel, assumed Lambertian, and $E(\lambda)$ is the global surface irradiance on the object pixel (Otterman, 1978).

A second term, $L_a(\lambda)$, accounts for adjacency effects, or more specifically, the portion of diffuse radiance scattered from the surrounding vicinity into the column above the object pixel. It is expressed,

$$L_a(\lambda) = [a(\lambda)E(\lambda)/\pi\tau(\lambda)]\int_0^{\pi/2}\left[1-\exp[-\tau(\lambda)/\cos\xi]\right]\cos\xi[\tau_R(\lambda)P_R(\lambda,\xi) + \tau_M(\lambda)P_M(\lambda,\xi)]2\pi\sin\xi\, d\xi \quad (2.11)$$

where

$a(\lambda)$ = average reflectance of the adjacent area,

P_R, P_M = phase functions associated with Rayleigh and aerosol (Mie) scattering, respectively, and

ξ = zenith reflection angle.

The size of the area surrounding the target pixel that contributes to this diffuse term is discussed by Otterman and Fraser (1979).

Finally, the third component, $L_d(\lambda)$, describes the radiance scattered from the direct solar beam into the direction of the satellite due to atmospheric effects, or

$$L_d(\lambda) = \frac{\mu\{1 - \exp[-\tau(\lambda)(1 + \sec\theta)]\}\ [\ \tau_R(\lambda)\,P_R(\lambda;180^\circ - \theta) + \tau_M(\lambda)P_M(\lambda;180^\circ - \theta)]}{\tau(\lambda)(\ 1 + \mu\ )} \quad (2.12)$$

where θ is the solar zenith angle.

The total radiance observed by a nadir–viewing satellite is the sum of the direct and two diffuse terms, or

$$L(\lambda) = L_r(\lambda) + L_a(\lambda) + L_d(\lambda) \tag{2.13}$$

For the case of optically thin atmospheres, and for clusters of pixels which do not exhibit highly contrasting reflectances, the direct beam constitutes the major portion of the observed radiance. Exact percentages are difficult to quantify since, as indicated by (2.10) through (2.13), their relative proportions are functions of numerous variables including surface reflectance, optical thickness, and solar angle. Further, most field studies have been conducted over oceans which possess low surface reflectance (Chahine, 1983), and thus, they provide limited insight on problems over landsurfaces. However, investigations by Otterman and Fraser (1979) and Chahine (1983) suggest that the relative magnitude of the direct beam ranges from approximately 70 percent of the total nadir radiance for an optical thicknesses of about 0.1 and surface reflectance of about 0.4, to as much as 95 percent for an optical thickness of 0.02 and the same surface reflectance. The direct beam percentage decreases with increasing optical thickness and decreasing surface reflectance.

2.3 Characteristics of Landsat Sensors

Five Landsat satellites were launched between 1972 and 1986 for the purpose of investigating earth resources. The technical specifications of the Multispectral Scanner System (MSS) and the Thematic Mapper (TM) aboard those satellites are well documented (See, for example Freden and Gordon, 1983; Lillesand and Kiefer, 1987). Several important features relevant to this thesis are summarized below.

The MSS sensors on Landsats 1, 2, and 3 are line–scanning devices covering 185 km swaths in four spectral bands. Those include two in the visible spectrum at 0.5–0.6 μm (green) and 0.6–0.7 μm (red), and two in the near–infrared at 0.7–0.8 μm and 0.8–1.1 μm. The satellite orbits are sun–synchronous, crossing the equator at 9:42 a.m. local sun time. The instantaneous field of view (IFOV) is square with a ground resolution of 79 meters on a side. The total field of view of the scan is 11.6 degrees and the quantization range of the sensor is 64 digital numbers (DN). The return period of the sensor for the same area is 18 days.

The TM sensors on Landsats 4 and 5 have a total of seven bands that possess greater sensitivity, finer ground resolution and narrower bandwidths than their MSS counterparts. The spectral bandpasses include three in the visible region at 0.45–0.52 μm (blue), 0.52–0.60 μm (green), and 0.63–0.69 μm (red), and four in the infrared at 0.76–0.90 μm, 1.55–1.75 mm, 10.4–12.5 μm (thermal), and 2.08–2.35 μm. The TM data are collected at 30 meter ground resolution at a quantization of 256 DNs. The orbit is sun–synchronous with an equatorial crossing at 11:00 a.m. local sun time, and with a 16 day return period.

Chapter 3

VEGETATION AND SOIL REFLECTANCE

3.1 Reflectance of Homogeneous Canopies

The radiation reflected from horizontally homogeneous canopies results from the scattering and reflectance properties of the plant components and soil background. These properties are both geometric and biophysical in nature and thus depend on the species, maturity and overall health of the plant, and on the structure and composition of the underlying soil. Geometric plant properties include plant architecture, total leaf area, and leaf structure, orientation and distribution. Biophysical properties allocate the radiative energy absorbed by the plant to important metabolic processes including photosynthesis, respiration, and transpiration. Those biophysical properties are manifested in terms of leaf color, transparency, temperature, and shape and orientation. Plant properties can vary daily and seasonally, in response to soil moisture and nutrients, and to meteorologic and climatic conditions.

3.1.1 Spectral Distribution

A typical spectral distribution of healthy green vegetation, as compared to soil, is shown in Figure 3.1. In the visible spectrum, vegetation reflectance is characterized primarily by the absorption of light by chlorophyll in the leaves. Strong absorption bands are centered at 0.45 μm (blue) and 0.67 μm (red), resulting in a local peak reflectance at about 0.54 μm that corresponds to the green portion of the spectrum. In the near–infrared region, vegetation reflectance is dominated principally by scattering properties of the internal structure of the

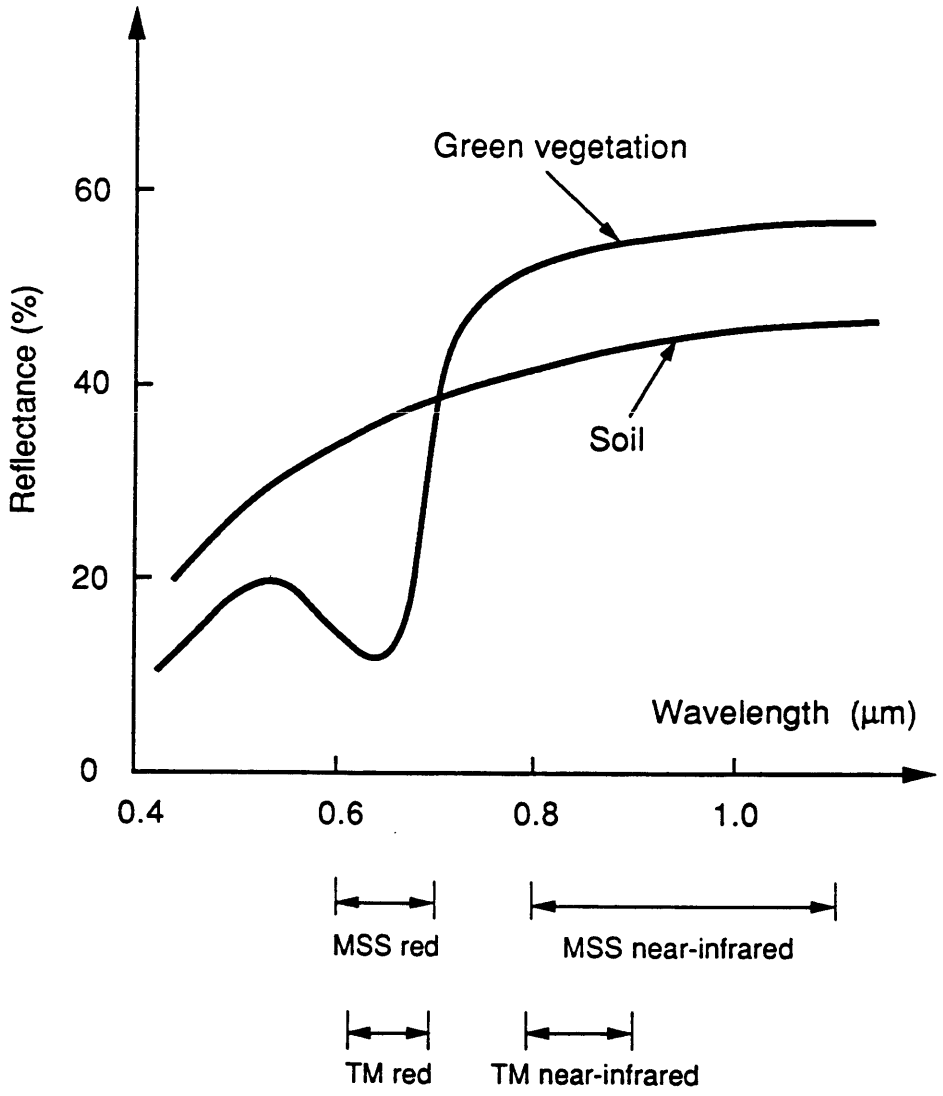

Figure 3.1 Typical spectral reflectance functions of vegetation and soil.

plant, such as the spongy mesophyll of leaves. High scattering in this region results in comparatively high overall reflectance by the plant.

Actual reflectances of plants in the visible and near infrared are well documented, especially for crops (Smith, 1983; Myers, 1983). It is typically low in the visible spectrum (< 30%) and higher in the near infrared region (40 – 50%). Canopy reflectances are generally much lower than those measured for individual leaves (Dickinson, 1983). Kondratyev (1969), Gates (1980), Ross (1981) and Iqbal (1983) provide summaries of reflectances for various vegetation types.

In contrast to vegetation, soil reflectance generally exhibits increasing reflectance with wavelength, as shown in Figure 3.1. Overall magnitudes are governed by grain size distribution, soil moisture, organic content, etc. (Myers, 1983). Some of the important factors are examined later in this chapter.

3.1.2 Reflectance Models

Numerous radiative transfer models for horizontally homogeneous canopies have been developed in terms of various plant properties and background soil reflectance. Typically, homogeneous canopies have been modeled as a diffusing medium with absorbing and scattering properties. Excellent reviews of these models are provided by Smith (1983) and Ross (1981). Suits (1972) envisioned a plant canopy as an infinitely extended plane–parallel medium with homogeneous geometric properties. Verhoeff and Bunnik (1981) extended the Suits model to include the effect of leaf angle distribution. Dickinson (1983) applied the two–stream approximation for radiation transfer in the atmosphere (Meador and Weaver, 1980) to plant canopies employing the leaf area index as a measure of the optical depth. Recent literature has increased the sophistication of those earlier models to include the modeling of bidirectional reflectance (Camillo, 1987;

Walthall et al., 1985; Chen, 1985; Simmer and Gerstl, 1985; Vanderbilt and Grant, 1985; Strebel et al., 1985; Gerstl and Zardecki, 1985; and Reyna and Badhwar, 1985).

Semiempirical formulas for the total radiation fluxes have been proposed for practical applications. The attenuation of radiation as it passes through a plant stand has been typically described in terms of some form of Bouguer's Law such as that proposed by Monsi and Saeki (1953), or

$$E(\lambda;\zeta) = E_o(\lambda) \exp[-\mu(\lambda)\zeta] \tag{3.1}$$

where

$E_o(\lambda)$ = intensity of incoming radiation at top of canopy

$E(\lambda;\zeta)$ = intensity of radiation at a penetration level associated with leaf area index, ζ

$\mu(\lambda)$ = experimentally determined extinction coefficient

When the upwelling radiance from the canopy represents only the backscattered solar radiation from the plant (i.e. no soil effects), then the plant reflectance, $R_m(\lambda;\zeta)$, is defined

$$R_m(\lambda;\zeta) = 1 - e^{-\mu(\lambda)\zeta} \tag{3.2}$$

Other semiempirical formulas which account for the partitioning of transmitted, scattered, and absorbed radiation, have been proposed (Ross, 1981).

Attention has also been focused on the invertibility of reflectance models of homogeneous canopies for estimating plant parameters such as leaf area index,

biomass, and leaf angle distribution (Goel and Strebel, 1983; Goel et al., 1984; Goel and Thompson, 1984a, 1984b, 1984c; Lang et al., 1985). Goel and Thompson (1984c) have shown that such parameters can, in principle, be estimated using multispectral data at approximately 25 combinations of solar zenith angle and viewing angle.

3.2 Reflectance of Discontinuous Canopies

Most natural landscapes will vary both horizontally and vertically in species and/or vegetation density. Modeling this situation has received considerably less attention than that for homogeneous canopies. Statistical techniques have been employed for classifying landscapes based on their similar spectral signatures (See summary by Lillesand and Kiefer, 1987). However, such methods require the identification of training samples and therefore can not be adopted for natural landscapes in which all target pixels possess unique spectral characteristics.

Radiative transfer models for non–homogeneous canopies have been developed by extending homogeneous canopy models and including three–dimensional scattering functions (Ross, 1981; Kimes et al, 1985). Such models can be solved in a few cases where plant distribution is periodic, such as for sown crops (Suits, 1985). Inversion of such models, using only multispectral observations, also require a large number of data at different angles (Goel and Thompson, 1984c).

For regional scale investigations of natural systems, the application of the above radiative transfer models, using Landsat data or any other current satellite multispectral sensor (i.e SPOT, AVHRR), is clearly infeasible. The first constraint is simply that any of those systems provides only one observation per overpass. Additionally, however, the regional–scale heterogeneity in plant species,

size and architecture would prohibit making any assumptions on the distribution of plant parameters.

3.2.1 Proportion Models

In many regional scale hydrologic investigations, it is generally sufficient to know only the amount of vegetation and the outgoing radiance at its surface, and not the complex architecture within the plant. In such cases the pixel has been described in terms of its bulk components, that is vegetation, soil, and shadow.

A simple approach has been to assume that the surface reflectances of individual plant clusters and soils within a pixel are constant, and that the total spectral response is a linear combination of the individual spectral responses of its components (Horwitz et al., 1971; Nalepka et al., 1972; Work, 1974; McCloy, 1980; Dozier, 1981; Ungar and Bryant, 1981; Chhikara, 1984, Lenningtion et al, 1984). The total radiance emitted from a pixel, $M(\lambda)$, containing n cover types can be expressed

$$M(\lambda) = \sum_{i=1}^{n} f_i M_i(\lambda) \tag{3.3}$$

where

f_i = fraction of area covered by type i, and

$M_i(\lambda)$ = radiance emitted from cover type i in band λ.

For the simple case of vegetation and soil cover, Equation (3.3) becomes:

$$M(\lambda) = mM_m(\lambda) + (1 - m)M_g(\lambda) \tag{3.4}$$

m = percent vegetation cover

$M_m(\lambda)$,$M_g(\lambda)$ = radiances emitted from vegetation and soil, respectively, in band λ.

Perhaps the earliest development of proportion estimation can be attributed to Horwitz et al. (1971) and Nalepka et al. (1977) who also termed the method "mixtures estimation". One of its first applications was in identifying subpixel scale ponding and wet marshes in glaciated prairies (Work, 1974).

McCloy (1980) later proposed that under conditions of negligible canopy transmission or multiple reflection, the response proportions of the various land covers will closely approximate the physical proportions of each type of cover. He suggested that up to four sub–pixel categories be used including three levels of vegetation greenness cover and one soil background cover. Ungar et al. (1981) reported limited success delineating forest canopy types in Maine using a similar approach which they termed the "Fanning algorithm". The fractional area was determined by minimizing the error between observed and theoretical radiances.

3.2.2 Geometric Models

In an extension to the linear proportion model described above, some investigators have considered the shadow cast by vegetation as an additional component to the total radiance. These models abstract clumps of vegetation as three–dimensional geometric shapes on flat horizontal surfaces with constant reflectances (Otterman, 1981, 1984; Otterman and Weiss, 1984; Strahler and Li, 1981; Li and Strahler, 1985). The distribution of the elements themselves can be geometric, as in the case of row crops, or statistical, as for natural vegetated landscapes. In most cases, the surfaces are assumed Lambertian and scattering between vegetation and soil is neglected.

Geometric models have been successfully used to describe much of the variability of semivegetated landscapes by altering the shape and density of the geometric elements. Otterman (1981, 1984) and Otterman and Weiss (1984) envisioned forests and desert vegetation as thin vertical cylinders. They accounted for the shadowing effects of vegetation, but assumed that the horizontal area of the plants was negligible. That model is thus not directly applicable to the determination of fractional vegetation cover.

Richardson et al (1975) modeled crop canopies as rectangular rows, neglecting scattering between the crop and soil. Jackson et al (1979) extended the above model to include shadowed canopy effects.

Strahler and Li (1981) and Li and Strahler (1985) modeled conifer forests as randomly located cones of similar shape and random height. They determined from simple geometry the shadow cast by the cones on the soil background or on other cones. The total radiance emitted by a pixel was assumed to consist of four components: illuminated background, illuminated cones, shadowed background and shadowed cones. Vegetation parameters including percent cover and average tree height were then estimated using assumed values of component reflectances.

3.3 Spatial Pattern of Vegetation

The application of geometric models to natural watersheds generally requires assumptions on the statistical distribution of plant spacing. Several authors (see, for example, Whittaker, 1975; Diggle, 1983) have focused on the problem of fitting stochastic models to spatial point patterns of natural (undisturbed) vegetation. Diggle (1983) found that the most appropriate stochastic representation for a given

situation was species dependent, with several forest species following a Poisson distribution or a Poisson cluster process.

Significant progress in incorporating statistical spatial distributions into the analysis of remotely sensed data has only recently been achieved (Strahler and Li, 1981; Li and Strahler, 1985; Woodcock, 1985). Li and Strahler (1985) and Strahler and Li (1979) assumed a homogeneous Poisson distribution of conifer tree locations. Woodcock (1985) used a similar model to examine the relation among the scale of pixel components, resolution size, and two indicators of spatial correlation: the variogram and the local variance.

3.4 Soil Reflectance

Soil background reflectance often exhibits high variability in semivegetated scenes. It varies over a wide range of length scales due to changes in the physical structure and chemical composition of the near surface soil. Small–scale perturbations (meters or less) occur with changes in mineral content, water and organic matter content, particle size, soil texture and surface roughness. Numerous experimental investigations have examined the relationship between bare soil reflectance and those parameters (for a summary, see Myers, 1983).

Soil reflectance also varies at larger geophysical scales. For example, the presence of hills will change soil reflectance due to an effective altering of the illumination and viewing angles. Changes in elevation, slope, and aspect will influence soil moisture and organic matter content. Subsurface variations in geologic formations will affect mineral content. Those geophysical factors impose a spatial correlation to soil reflectance at scales of 10 to 10^3 meters.

In addition to spatial correlations, soil reflectance can also be cross–correlated at different wavelengths. These wavelength dependent correlations are manifested in multispectral scattergrams of real scenes through the preferred location and orientation of bare soil pixels (see, for example, Kauth and Thomas, 1976; Richardson and Wiegand, 1977; Huete et al, 1985). For red–infrared scattergrams of typical semivegetated scenes, the data often take on the form of a triangle whose base consists of a straight line emanating from approximately the origin. Researchers have identified that base line, consisting primarily of pixels containing bare soil and dry vegetation, as the "soil line".

Analysis of previously published theoretical and experimental studies (for example Cierniewski, 1987; Smith, 1983; Bowers and Hanks, 1965; Skidmore et al, 1975) indicates that for a given type of soil variability, the soil reflectance at one wavelength is often functionally related to the reflectance in another wavelength. In many cases, the relation can be approximated by a simple linear expression

$$R(\lambda_2) = \alpha R(\lambda_1) + \gamma \tag{3.5}$$

where the slope, α, and intercept, γ, are coefficients dependent on both the wavelength and the type of variability. Thus, variability of any one soil parameter can lead to a representative "line" in a two–dimensional scattergram.

For instance, Figure 3.2 contains three hypothetical visible–infrared scattergrams, representing three different scenes, in each of which only one soil parameter is allowed to vary. In Scene 1 only the amounts of two minerals are allowed to vary, while all other soil parameters such as surface roughness, moisture, etc. are held constant. The resulting scattergram forms a "soil mineral line" in which the end points approach the respective reflectances of the pure minerals. The shape

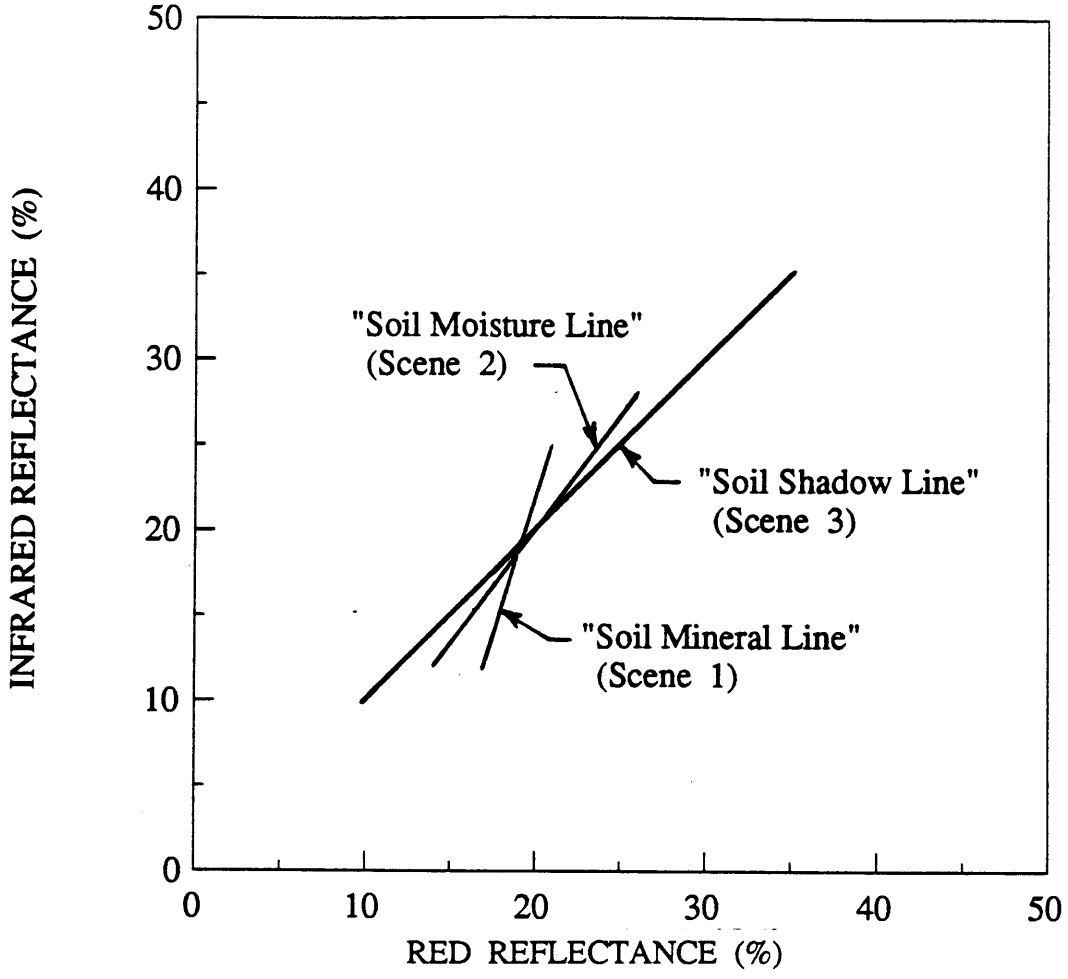

Figure 3.2 Hypothetical soil lines.

and orientation of the line may be linear (as drawn) or nonlinear, and are determined by the location of the end points and the nature of the mixing of the two mineral types (Smith et al, 1985). Pixels lying between the end points will contain mineral amounts proportional to their distance along the line.

Scene 2 contains hypothetical pixels in which only soil moisture is allowed to vary. Soil moisture increases the radiation absorption capacity of the soil in the visible and near infrared regions. Analysis of published experimental data (Bowers and Hanks, 1965; Skidmore et al, 1975) indicates that, for many soil types, equation (3.5) is applicable. Thus the locus of points for Scene 2 pixels should form a "soil moisture line" as indicated in Figure 3.2 with the pixels along the left portion of the line containing higher soil moisture than those to the right.

Finally, Scene 3 contains pixels in which only surface roughness varies. Soil reflectance generally decreases with increased surface roughness due to the increase in shadow cast by the soil particles and aggregates onto itself (Myers, 1983, Cierniewski, 1987). The resulting "soil shadow line" is approximately linear with an intercept of near zero. The linearity occurs since the amount of shadow caused by the soil aggregates is practically the same for the range of wavelengths being considered. In fact, a near zero intercept for straight soil lines of real scenes (with low diffuse radiation) may be an indication that soil shadow induced by its physical structure is the dominant source of soil reflectance variability.

In actuality, real soil scenes contain a composite of several types of variability. The corresponding soil line is generally linear in the mean although considerable scatter can exist (Kauth and Thomas, 1976; Richardson and Wiegand, 1977) A unique soil line will exist only if either 1) one dominant type of soil variability is occurring or 2) the scatter due to the different types of soil variability act in the same direction.

3.5 Empirical Indicators of Vegetation Amount

Numerous vegetation indices have been proposed in recent years as qualitative indicators of green vegetation. The purpose has been to reduce the several multispectral bands to one value to estimate vegetation parameters such as biomass, leaf area index, or percent cover. The relationship among vegetation indices and the plant physical properties was investigated by Choudhury (1987) using a two–stream approximation. The effect of soil background reflectance was examined by Huete (1988). Perry and Lautenschlager (1984) summarize the many different vegetation indices and describe their relationship to each other. Three such indices are the normalized vegetation index, the perpendicular vegetation index, and the Kauth–Thomas Greenness index.

3.5.1 Normalized Difference Vegetation Index

Of the many indices proposed, the normalized vegetation index (NDVI) has evolved as a practical popular choice for use in regression with vegetation parameters. It is of the form

$$\mathrm{NDVI} = \frac{R(NIR) - R(VIS)}{R(NIR) + R(VIS)} \tag{3.6}$$

where R(NIR) and R(VIS) represent the pixel reflectances or the digital numbers (DNs) in the near–infrared and visible (red) ranges, respectively. Low NDVI indicates low vegetation amount, whereas high NDVI indicates either high vegetation amount or high productivity (Curran, 1980). Sellers (1985) discussed the functional relationship between the NDVI and several vegetation parameters, including the leaf area index. Tucker et al. (1983) correlated the NDVI

(computed from NOAA's AVHRR data) to actual biomass obtained from field sampling in a semi–arid region of Senegal, West Africa. The effect of soil background on NDVIs computed from hand–held or airborne radiometer data was investigated by Elvidge and Lyon (1985) and Huete et al. (1985).

3.5.2 Perpendicular Vegetation Index

Richardson and Wiegand (1977) proposed the perpendicular vegetation index (PVI) as a measure of plant development. Application of this index first requires the establishment of a background soil line by linear regression of MSS bands 2 and 4 using bare soil pixels. The soil line is thus a straight line stemming from near the origin. The PVI is the perpendicular distance from the soil line to the actual data point which contains vegetation, and is defined,

$$PVI = [(R_{g2} - R_{p2})^2 + (R_{g4} - R_{p4})^2]^{1/2} \qquad (3.7)$$

where R_{g2}, R_{g4} = reflectances of soil background in bands 2 and 4, respectively, corresponding to the data point.

R_{p2}, R_{p4} = reflectances of data point in bands 2 and 4, respectively, perpendicular to R_{g2} and R_{g4} on the soil line.

Richardson and Wiegand (1977) regressed PVI with percent cover of sorghum with a correlation coefficient of 0.57. Theis et al. (1984) studied the effect of vegetation and soil moisture on PVI. Rosenthal et al. (1985) recently used the PVI to investigate crop height and biomass.

3.5.3 Kauth–Thomas Greenness Index

Kauth and Thomas (1976) applied Gram-Schmidt orthogonalization to the original four Landsat bands resulting in a new four–dimensional space termed "tasseled cap". The procedure, which is similar to principal components except in the order of calculations, essentially rotates the data so that most of the variability can be explained in terms of four indices: greenness (GI), brightness (BI), yellowness (YI), and nonsuch (NI). The first two of these indices are defined,

$$BI = 0.332\ DN1 + 0.603\ DN2 + 0.676\ DN3 + 0.263\ DN4 \qquad (3.8)$$

$$GI = -0.283\ DN1 - 0.660\ DN2 + 0.577\ DN3 + 0.388\ DN4 \qquad (3.9)$$

where DN1, DN2, DN3, and DN4 represent the digital counts of the three visible and one near infrared bands of the MSS scanner, respectively. A similar set of equations has been developed for the Thematic Mapper (Crist, 1983; Crist and Cicone, 1984).

The Kauth–Thomas Transformation has been used by numerous investigators to model various crop parameters including crop development, moisture stress, yield and crop classification (Ezra et al., 1984). Huete et al. (1984, 1985) in a series of small scale experiments of wooden boxes filled with soil, showed high correlation of GI with percent cover. Musick (1984), however, using Landsat MSS data over New Mexico, was unable to achieve consistent differentiation between arid rangeland cover changes using GI.

Chapter 4

A STOCHASTIC–GEOMETRIC LANDSURFACE REFLECTANCE MODEL FOR SATELLITE REMOTE SENSING

This chapter describes a stochastic–geometric landsurface reflectance model that can be incorporated into the theoretical nadir radiance model described in Section 2.2.2. The goal is to provide a framework for investigating the conditions under which subpixel variability is represented in satellite–observed radiance. The first part of this chapter presents a stochastic canopy–soil reflectance model for describing regional landsurface variability. The reflectance model is then coupled to the radiance model through the reflectance term.

4.1 Stochastic–Geometric Canopy–Soil Reflectance Model

Many semivegetated landscapes are characterized not only by variations in plant size and density, but also by complex variations in the physical properties controlling the reflectance of the plant–soil medium. The complexity arises principally from the highly random nature of many subpixel scale properties of the plant (e.g. species, plant geometry, leaf area, shape, and orientation) and the soil (e.g. surface roughness, texture, organic matter content, and moisture content). Such variations, induced by changes in topography and climate, can have a significant influence on the interpretation of scenes and therefore must be recognized when applying canopy reflectance models to regional scale problems.

One approach for accommodating the random subpixel fluctuations in plant and soil properties, while keeping the number of model parameters to a minimum,

is to conceptualize the semivegetated landscape as a stochastic–geometric reflecting surface. This approach is similar to the geometric models described in Section 3.2.1 in that the landscape is represented by the bulk plant and soil properties that dominate scene reflectance, that is, fractional cover, plant geometry, and plant and soil reflectance. However, it extends those models by treating any one of the bulk properties as a potential random variate. Treating the properties as random variables provides a flexible means of characterizing the scene without having to prescribe an inordinate number of detailed vegetation and soil parameters (e.g., leaf area and orientation, soil roughness, etc.). Such an approach is practical in many mesoscale hydrologic investigations in which detailed description of the surface is not necessary, nor is it feasible with current satellite sensors.

4.1.1 Plant and Shadow Geometry

The geometric aspects of the reflectance model include both the plant geometry and the spatial distribution of the plants. Since the plants are represented as solid three–dimensional objects, they can cast shadows onto themselves, onto the soil, and onto adjacent plants, according to their shape and spatial distribution, and to the solar angle.

The four principal reflecting surfaces of the model are the illuminated green canopy, the shadowed green canopy, the illuminated soil background, and the shadowed background. All surfaces are assumed to be Lambertian and scattering among geometric elements is neglected. The term "soil background" denotes that the landsurface between the green plants includes not only bare soil, but also a mixture of sparse grasses and senesced vegetation.

The geometry of the plant canopy and its shadow is shown in Figure 4.1 for the particular case of cones. Li and Strahler (1985) has shown that, assuming a plant diameter D, and height H, the portions of the illuminated plant, A_{t_I}, and shadowed plant, A_{t_S}, are respectively,

$$A_{t_I} = [\pi/2 - \chi]D^2/4 \tag{4.1}$$

$$A_{t_S} = [\pi/2 + \chi]D^2/4 \tag{4.2}$$

where

$$\chi = \sin^{-1}[D/H\tan\theta] \tag{4.3}$$

Geometric relationships for other shapes, such as cylinders and spheres, are provided in Section 6.2.3 and Table 6.1.

4.1.2 Reflectance of a Pixel

Depending on its size, an individual pixel can possess any number of plants and shadows, or fractions of plants and shadows. The total reflectance of an individual pixel, $R(\lambda,\underline{x})$, is assumed to consist of an area weighted linear combination of the average reflectances of the four landscape components. Mathematically,

$$R(\lambda,\underline{x}) = \sum_i f_i(\underline{x})R_i(\lambda,\underline{x}) \tag{4.4}$$

where,

λ = wavelength,

$\underline{x}$ = spatial coordinate of the center of the pixel,

$R_i(\lambda,\underline{x})$ = average bulk reflectance of cover type i in pixel centered at $\underline{x}$.

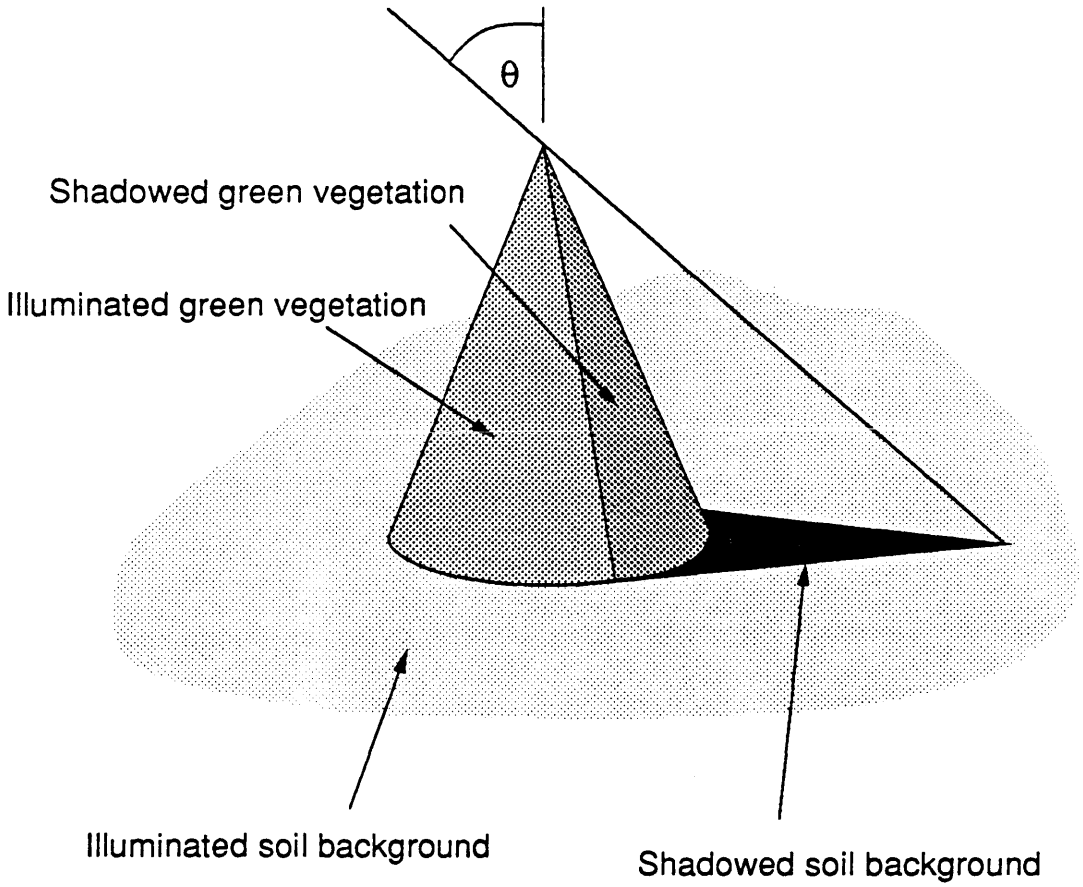

Figure 4.1 Geometry of canopy-soil reflectance model for the case of cones.

$f_i(\underline{x})$ = fraction of pixel centered at $\underline{x}$ possessing the cover type i as follows

i = 1 designates illuminated green vegetation,

i = 2 designates shadowed green vegetation,

i = 3 designates illuminated soil background, and,

i = 4 designates soil background shadowed by green vegetation.

The percent covers are constrained by,

$$\sum_i f_i(\underline{x}) = 1 \quad . \tag{4.5}$$

Average bulk reflectances and percent covers are defined as follows,

$$R_i(\lambda,\underline{x}) = \frac{1}{A_i(\underline{x})} \int_{A_i(\underline{x})} r_i(\lambda,\underline{u})\, d\underline{u} \tag{4.6}$$

$$f_i(\underline{x}) = \frac{A_i(\underline{x})}{A_P} \tag{4.7}$$

where,

$r_i(\lambda,\underline{u})$ = reflectance of point $\underline{u}$, given it possesses cover type i,

$A_i(\underline{x})$ = total area of the pixel with cover type i, and

A_P = total area of a pixel,

Equations (4.4) through (4.7) are applicable for any pixel in the scene.

4.1.3 Spatial and Spectral Distribution of Scene Variables

The equations representing total pixel reflectance, (4.4) through (4.7), are completely general in that they do not specify whether the scene variables are deterministic or random. The quantities $f_i(\underline{x})$ and $R_i(\lambda,\underline{x})$ can thus represent constants, deterministic variables, or random variables depending on the nature of the scene. For instance, the shape and spatial distribution of agricultural plants can often be prescribed by a regular geometry, such as rectangular rows. In natural areas, however, plant height and regional distribution can more appropriately be represented by random functions as noted in Section 3.3. Plant and soil reflectance may also be deterministic or random as noted above.

When one or more of the scene variables are random, the reflectance model takes on a stochastic nature in that the values of $f_i(\underline{x})$ and $R_i(\lambda,\underline{x})$ can become correlated in a number of possible ways. For instance, there may exist i) spatial correlations in plant and soil reflectance, ii) cross–spectral correlations between plant reflectance and soil reflectance, and iii) cross–correlations between fractional covers (i.e. vegetation and shadow). Some of those correlations are examined further in Chapters 6 through 8. The stochastic nature of the reflectance model thus provides a mechanism for solving the inverse problem as described later in Chapters 6 and 7.

4.2 Coupled Landsurface–Atmosphere Radiative Transfer Model

The landsurface reflectance model described in (4.4) is coupled to the atmospheric radiance model through the target reflectance parameter, $R(\lambda)$, in the direct beam equation (2.10), and through the adjacent area reflectance parameter,

$a(\lambda)$, in the diffuse scattered equation (2.11). For instance, inserting (4.4) into (2.10) yields,

$$L_r(\lambda,\underline{x}) = \sum_i f_i(\underline{x})R_i(\lambda,\underline{x})E(\lambda)\exp[-\tau(\lambda)]/\pi \tag{4.8}$$

The diffuse radiance scattered from the surrounding vicinity can be written,

$$L_a(\lambda,\underline{x}) = \left[\sum_i f_i'(\underline{x})a_i(\lambda,\underline{x})E(\lambda)/\pi\tau(\lambda)\right]\int_0^{\pi/2}\left[1-\exp[-\tau(\lambda)/\cos\xi]\right]\cos\xi[\tau_R P_R(\lambda,\xi) + \tau_M(\lambda)P_M(\lambda,\xi)]2\pi\sin\xi\, d\xi \tag{4.9}$$

where $f_i'(\underline{x})$ represents the average amount of cover type i in the area surrounding the target pixel located at $\underline{x}$, and $a_i(\lambda,\underline{x})$ represents the average reflectance of cover type i in that same area. The backscattered solar radiance, $L_d(\lambda)$, described in (2.12), contains no landsurface parameters and is thus unaffected by the nature of the landscape.

Since the focus of this report is on the landsurface cover, it is useful to separate the landsurface properties from those of the atmosphere. Equations (4.8) and (4.9) can be rewritten,

$$L_r(\lambda,\underline{x}) = \left[\sum_i f_i(\underline{x})R_i(\lambda,\underline{x})\right]L_r'[\lambda,E,\tau] \tag{4.10}$$

$$L_a(\lambda,\underline{x}) = \left[\sum_i f_i'(\underline{x})a_i(\lambda,\underline{x})\right]L_a'[\lambda,E,\tau,P_R,P_M,\xi] \tag{4.11}$$

where L_r' and L_a' represent the expressions in (2.10) and (2.11), respectively,

without the reflectance terms. The total radiance observed by the satellite is thus,

$$L(\lambda,\underline{x}) = \left[\sum_i f_i(\underline{x})R_i(\lambda,\underline{x})\right]L_r'(\lambda) + \left[\sum_i f_i'(\underline{x})a_i(\lambda,\underline{x})\right]L_a'(\lambda) + L_d(\lambda) \tag{4.12}$$

4.3 Effect of Subpixel Variability on Observed Radiance

Equations (4.10) through (4.12) can be used, at least in a qualitative manner, to examine the theoretical relationship between fractional cover and satellite–observed radiance, given the limiting assumptions of both the landscape reflectance model and atmospheric radiance model. For instance, (4.10) indicates that the direct beam, the dominant component of the observed radiance for optically thin atmospheres, is linearly proportional to the amount of the individual fractional covers of the target pixel (i.e. the f_i's). However, that proportionality does not exist when the adjacency effects of (4.11) are included. The magnitude of adjacency effects will depend on both the amount of atmospheric scattering and on the relative contrast between the target pixel reflectance and the surrounding area reflectance (Otterman and Fraser, 1979).

Since the diffuse terms are small compared to the direct beam for clear skies, it can be argued from (4.12) that adjacency effects will not be important when the average reflectance of the surrounding pixels approximately equals the total reflectance of the target pixel, even though the distribution of ground cover in any cluster of pixels may differ. In such cases,

$$R(\lambda,\underline{x}) \cong a(\lambda,\underline{x}) \tag{4.13}$$

and the total observed radiance can be expressed,

$$L(\lambda,\underline{x}) = \left[\sum_i f_i(\underline{x})R_i(\lambda,\underline{x})\right][L'_r(\lambda) + L'_a(\lambda)] + L_d(\lambda) \qquad (4.14)$$

Since the satellite data provides observations in terms of DN values, equation (4.14) can be rewritten in the form,

$$DN(\lambda,\underline{x}) = \left[\sum_i f_i(\underline{x})R_i(\lambda,\underline{x})\right]l'_r(\lambda) + l'_d(\lambda) \qquad (4.15)$$

where $l'_r(\lambda)$ and $l'_d(\lambda)$ are calibration coefficients for a particular horizontally homogeneous atmosphere and satellite sensor. Further, since one is primarily interested in the landscape fractional cover, then (4.15) can be expressed,

$$DN(\lambda,\underline{x}) = \sum_i f_i(\underline{x})R'_i(\lambda,\underline{x}) + l'_d(\lambda) \qquad (4.16)$$

where $R'_i(\lambda)$ represents an "effective" reflectance, that is, the reflectance of component i multiplied by the coefficient $l'_r(\lambda)$. Equation (4.16) implies that for horizontally–homogeneous, optically–thin atmospheres, the satellite observed radiance is linearly proportional to subpixel fractional cover when the landscape reflectance does not possess sharp contrasts. That preliminary conclusion has important implications for the interpretation of scattergrams obtained from satellite data as discussed later in Chapter 8.

Chapter 5

SIMULATION OF RED–INFRARED SCATTERGRAMS OF SEMIVEGETATED LANDSCAPES

One application of the stochastic–geometric canopy reflectance model is the investigation of the structure, or physical basis, of red-infrared scattergrams of semivegetated landscapes. That is achieved by using the reflectance model presented in Section 4.1 with typical values to simulate different scenes, and then comparing the shape and common features of the corresponding red-infrared scattergrams. An understanding of the influence of a given random variable is obtained by altering one of its statistics (e.g., variance), while holding all others constant.

The following section presents the results of five different simulations in terms of the nadir reflectance model. Atmospheric effects are not considered and it is assumed that all areas of the scene are equally illuminated. The input values of the different reflectance variables are provided in Table 5.1. While those scenes represent only a few selected scenarios, they were chosen to demonstrate the important general relationship between the major landscape variables and their effect on the scattergram.

Scenes are generated as follows. A scene consists of eight segments, each 150 meters square with one meter square grids. Each segment within a scene is assigned an identical soil background reflectance distribution. Next, trees of fixed height (3.5 m), represented by square cylinders, are superposed on the soil background of each segment according to a Poisson distribution having a different arrival rate for each segment. The area of the canopy (or cylinder) is fixed at

Table 5.1
Summary
Input Parameters of Simulated Scenes

	Vegetation Reflectance Parameters */					Soil Reflectance Parameters						
	Red		Infrared		Covariance	Red		Infrared		Spatial	Covariance	
Case	Mean (%)	S.Dev. (%)	Mean (%)	S.Dev. (%)	Structure	Mean (%)	S.Dev. (%)	Mean (%)	S.Dev (%)	Distribn.	Structure	Shadow
I	15.0	0.0	40.0	0.0	none	20.0	0.0	25.0	0.0	uniform	none	No
II	15.0	0.0	40.0	0.0	none	15.0	2.3	20.0	2.3	normal	exponential β = 0.05 m	No
III	15.0	2.0	40.0	4.0	exponential β = 0.10 m	15.0	2.3	20.0	2.3	normal	exponential β = 0.05 m	No
IV	15.0	0.0	40.0	0.0	none	20.0	0.0	25.0	0.0	uniform	none	Yes**/
V	15.0	0.0	40.0	0.0	none	15.0	2.3	20.0	2.3	normal	exponential β = 0.05 m	Yes**/

*/Trees distributed according to a Poisson process with variable rate; tree height assumed to be 5 meters.

**/Solar angle assumed to be 30 degrees.

1 m^2. The shadowed portions of the scene are then determined based on the geometry of the tree and the solar zenith angle (θ = 30 degrees). Typical values of soil and vegetation reflectance are assumed (Ross, 1981; Myers, 1983; Smith, 1983) as indicated in Table 5.1. All surfaces are assumed to exhibit Lambertian properties. A graphical sketch of a typical pixel in the simulated scene is shown in Figure 5.1.

Once the scene is generated at the 1 meter grid level, it is then aggregated to pixel sizes of 5, 10, and 30 meters square by averaging the reflectance values of the components of the grid. A comparison of the pixel scales for the different levels of aggregation is shown in Figure 5.2. The latter two scales represent SPOT and Thematic Mapper satellite pixels, respectively. Information regarding subpixel variables is recorded at each level of aggregation. The computer code for the generation of scenes is provided in Appendix D.

The simulations are based on the reflectance equations described in (4.4) through (4.7). To facilitate the explanation of the individual cases, the notation is changed as follows,

m_I = fraction of illuminated vegetation cover in pixel centered at $\underline{x}$,

m_S = fraction of shadowed vegetation cover in pixel at $\underline{x}$,

g_S = fraction of soil shadowed by vegetation cover in pixel at $\underline{x}$,

g_I = fraction of illuminated soil background in pixel at $\underline{x}$,

$R_{m_I}(\lambda,\underline{x})$, $R_{m_S}(\lambda,\underline{x})$ = average bulk reflectance of illuminated and shadowed vegetation, respectively, in band λ, in pixel centered at $\underline{x}$,

$R_{g_I}(\lambda,\underline{x})$, $R_{g_S}(\lambda,\underline{x})$ = average bulk reflectance of illuminated and shadowed soil background, respectively, in band λ, in pixel centered at $\underline{x}$.

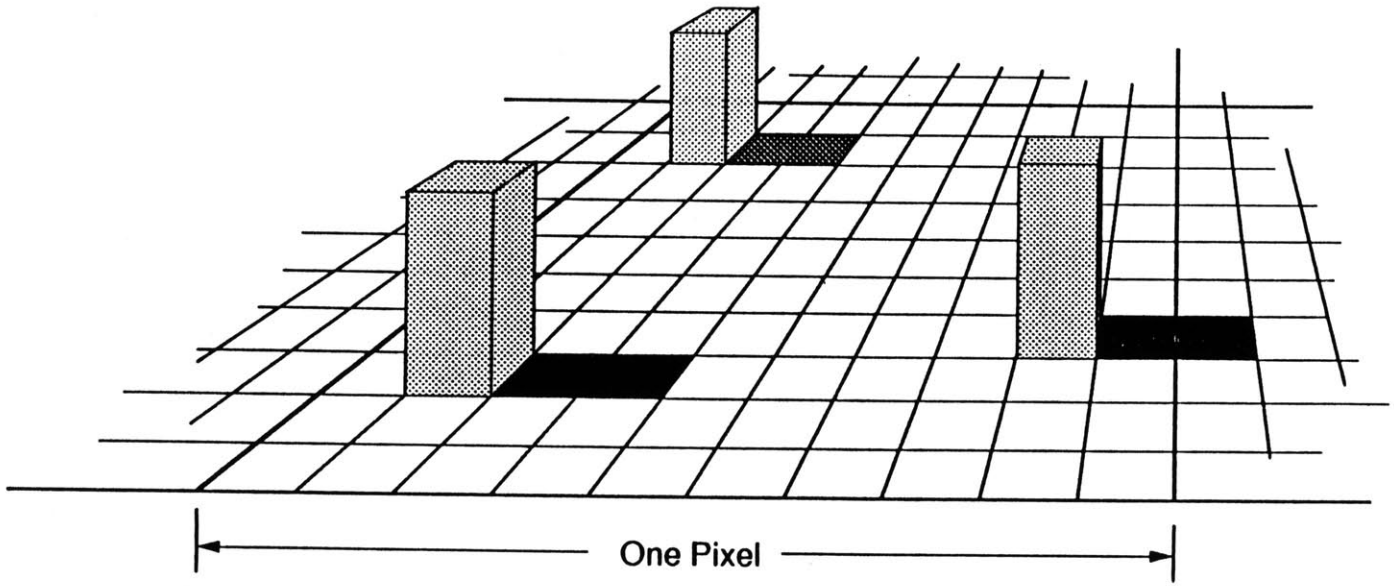

Figure 5.1 Graphical sketch of typical pixel in simulated scene.

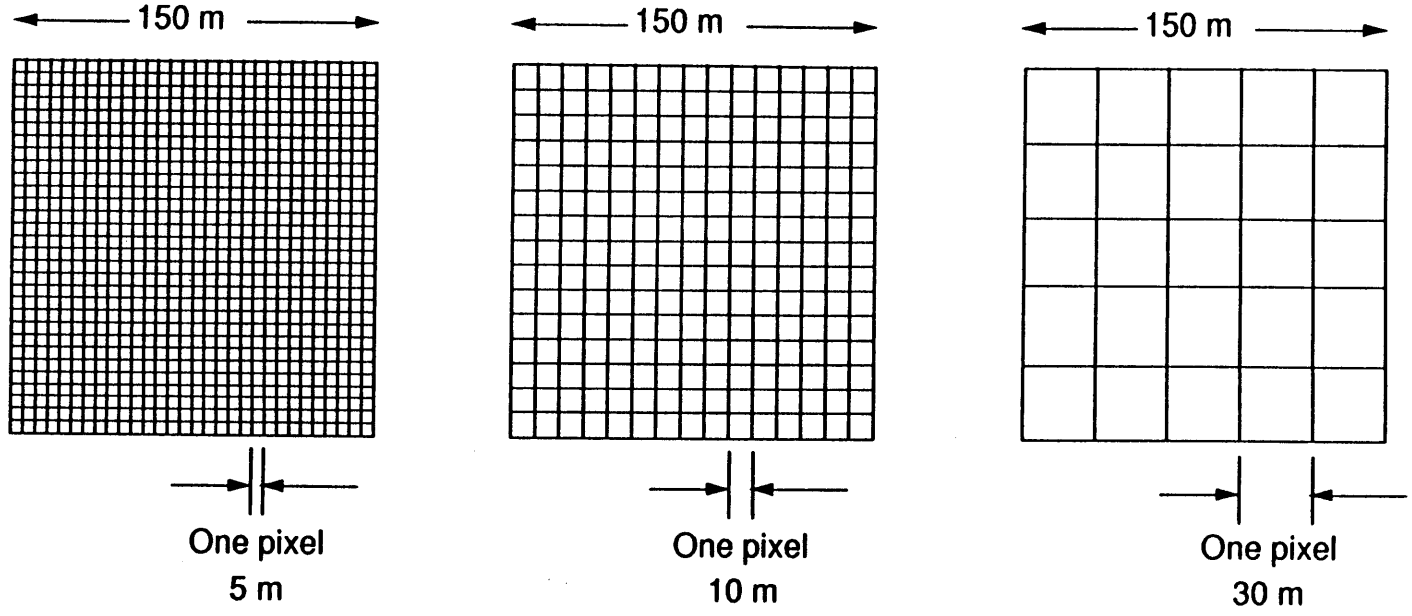

Figure 5.2 Comparison of pixel scales for different aggregations of simulated scenes.

The reflectance equation of an individual pixel given in (4.4) can be written in terms of the new notation as,

$$R(\lambda,\underline{x}) = m_I R_{m_I}(\lambda,\underline{x}) + m_S R_{m_S}(\lambda,\underline{x}) + g_I R_{g_I}(\lambda,\underline{x}) + g_S R_{g_S}(\lambda,\underline{x}) \qquad (5.1)$$

The average bulk reflectances are computed, for example, in the case of soil reflectance,

$$R_{g_I}(\lambda,\underline{x}) = \frac{1}{n}\sum_{n} r_{g_I}(\lambda,\underline{u})\delta(\underline{u}) \qquad (5.2)$$

where,

- n = the number of grids in the pixel centered at $\underline{x}$ occupied by illuminated soil,
- $r_{g_I}(\lambda,\underline{u})$ = illuminated soil reflectance at point $\underline{u}$, and
- $\delta g_I(\underline{u})$ = delta function equal to 1, if point $\underline{u}$ is occupied by illuminated soil, or 0 if it is not.

When the bulk reflectances are not spatially variable, that is, when they are only a function of wavelength, then for clarity, they will be written without the coordinate variable $\underline{x}$. For example, $R_{g_I}(\lambda,\underline{x})$ becomes $R_{g_I}(\lambda)$ when soil reflectance is not spatially variable.

The fractional cover of an individual pixel is defined,

$$g_I = \frac{A_{g_I}(\underline{x})}{A_p} \qquad (5.3)$$

where $A_{g_I}(\underline{x})$ is the total area of the pixel occupied by illuminated soil, and A_p is the area of the pixel. Expressions similar to (5.2) and (5.3) can be written for other components of the pixel. The total percent canopy cover, m, soil background, g, and shadow, s, in a pixel are, respectively,

$$m = m_I + m_s \tag{5.4}$$

$$g = g_I + g_s \tag{5.5}$$

$$s = m_s + g_s \tag{5.6}$$

where

$$m_I + m_s + g_I + g_s = 1 \tag{5.7}$$

5.1 Case I – Constant Reflectances, No Shadows

This case represents an idealized two–component situation in which the vegetation and soil each have a constant reflectance over the entire scene, and observations are from the nadir. The sun is near zenith resulting in no shadows in the field of view. Hence, the only random variable is percent cover. The equation expressing total reflectance from an individual pixel is taken from equations (5.1) through (5.7) with $m_s = g_s = 0$, or

$$R(\lambda,\underline{x}) = mR_{m_I}(\lambda) + (1 - m)R_{g_I}(\lambda) \tag{5.8}$$

The red–infrared scattergrams for the Case I simulation are shown in Figures 5.3–a,b,c for the levels 5, 10, and 30 aggregation. They indicate that all the data points fall on a straight line whose end points represent pixels containing the

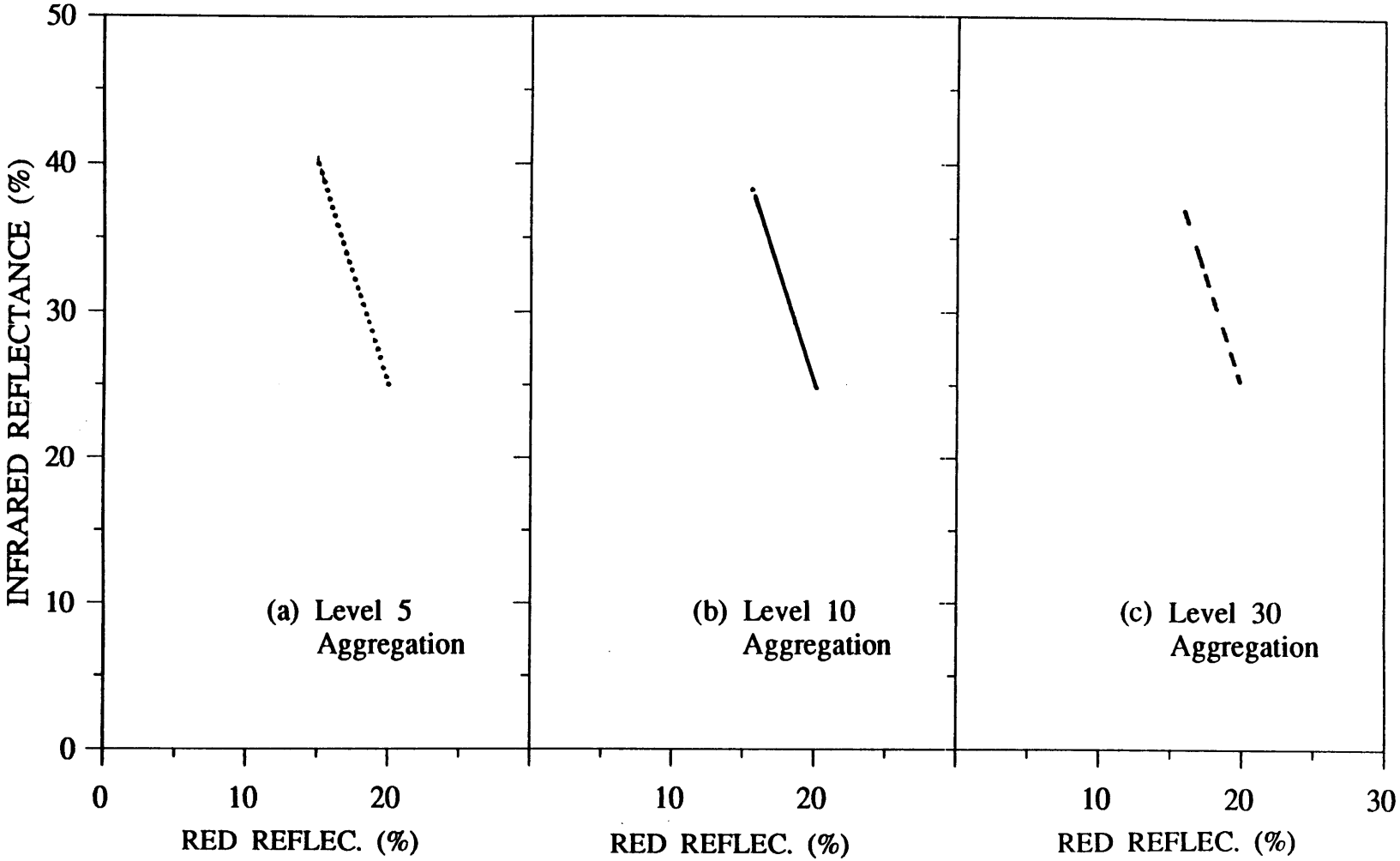

Figure 5.3–a,b,c Red–infrared scattergrams, Case I simulation: variable percent cover, constant soil and vegetation reflectances; no shadows.

maximum (upper left) and minimum (lower right) percent vegetation cover within the scene. The length of the line decreases with increasing aggregation since the standard deviation of the canopy density decreases as the pixel size increases. The percent cover of any pixel lying along the line is proportional to the distance between the end points.

5.2 Case II – Variable Soil Reflectance, No Shadows

In addition to changing vegetation cover, the Case II simulation includes the effect of spatial variability of soil reflectance. Both small scale (subpixel) and large scale (regional) variations are incorporated by treating soil reflectance as a two–dimensional random field with a prescribed covariance structure.

While various functional forms might be applicable, for demonstration purposes, the Case II simulation assumes that soil reflectance is normally distributed with an exponential covariance function. It is expressed

$$\mathrm{cov}(d) = \sigma^2 \exp(-\beta d) \tag{5.9}$$

where σ^2 = the variance of the soil reflectance distribution,

β = inverse length scale of the covariance function, and

d = distance between two points in the scene.

The simulated bare soil scene for the red band is shown in Figure 5.4. That scene, generated using the Turning Bands Method (Mantaglou and Wilson, 1982), contains a mean reflectance (0.15), standard deviation (0.023), and exponential covariance. A similar scene (not shown) was generated for the infrared band.

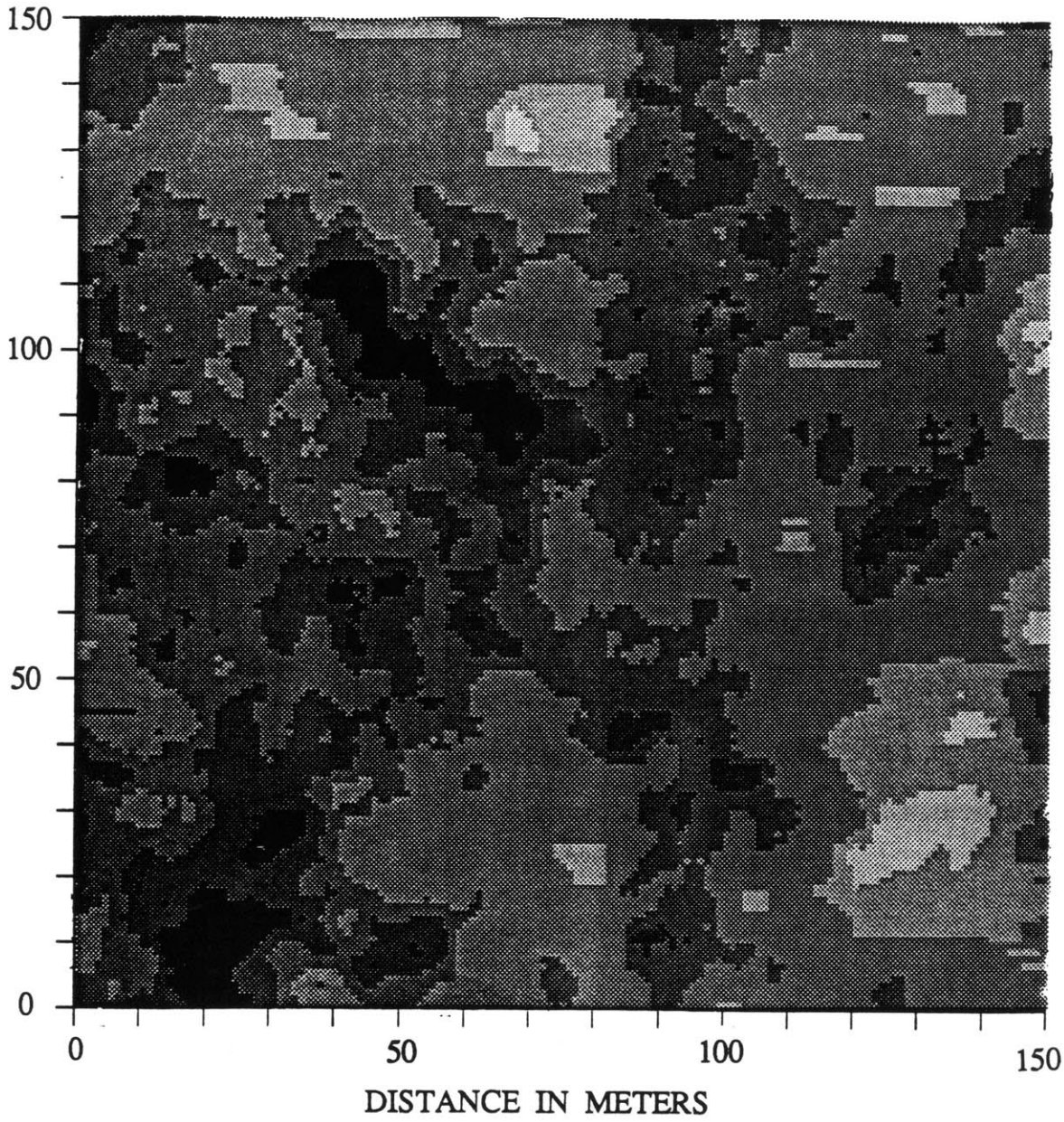

Figure 5.4 Hypothetical segment of bare soil scene, red band.

The mean and standard deviations of both scenes are based on the hypothetical soil reflectance curve shown in Figure 5.5, which indicates a typical range of reflectances for a soil with variable properties (e.g., soil moisture or surface roughness) (Myers, 1983).

The length scale of the exponential covariance function was chosen to be 20 meters. While that might represent some geophysical scale, for the present case, it was chosen for convenience. It is much larger than the grid scale of one meter, and the two smaller aggregations (5 and 10 meters), but smaller than the largest aggregation (30 meters). Thus, the choice of that scale allows one to examine the relation between covariance length scale and pixel size.

The total reflectance from a given pixel in the Case II simulation is,

$$R(\lambda,\underline{x}) = mR_{m_I}(\lambda) + (1 - m)R_{g_I}(\lambda,\underline{x}) \qquad (5.10)$$

The results of the Case II simulation for all three aggregations are shown in Figures 5.6–a,b,c. (Regular spaces in the scattergrams, especially at lower level aggregations, are due to finite increments in percent cover as limited by the level of aggregation. This effect occurs in subsequent cases as well.) They indicate that the red–infrared scattergram tends to take on the characteristic shape of a triangle. The top of the triangle represents full canopy cover, and the base represents the minimum vegetation cover in the scene. For areas in which it can be assumed that bare soil exists, the base of the triangle represents the classic "soil line."

While Case II is still a relatively simple example, it demonstrates the usefulness of the scattergram for explaining subpixel variability. For instance, all

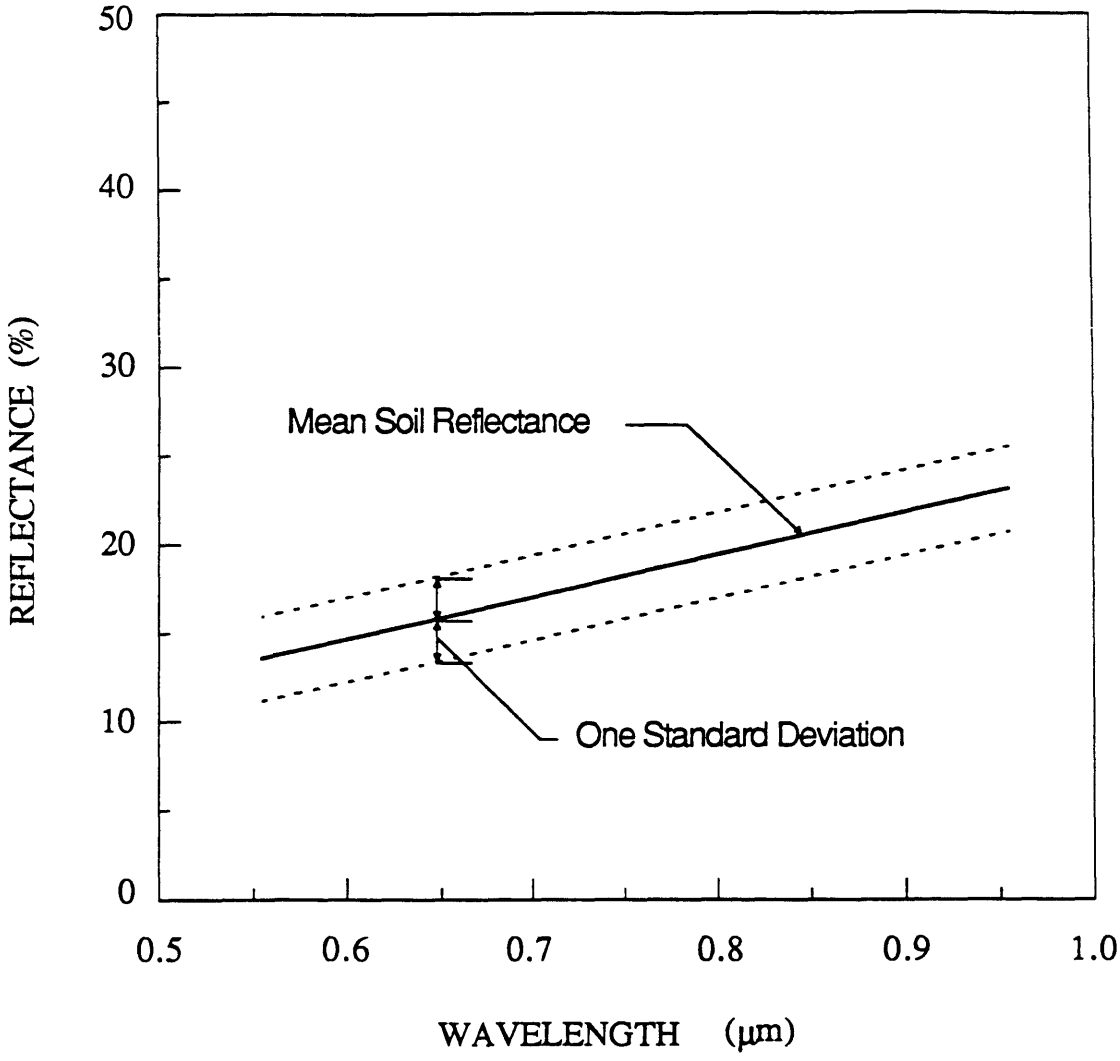

Figure 5.5 Hypothetical soil reflectance curve.

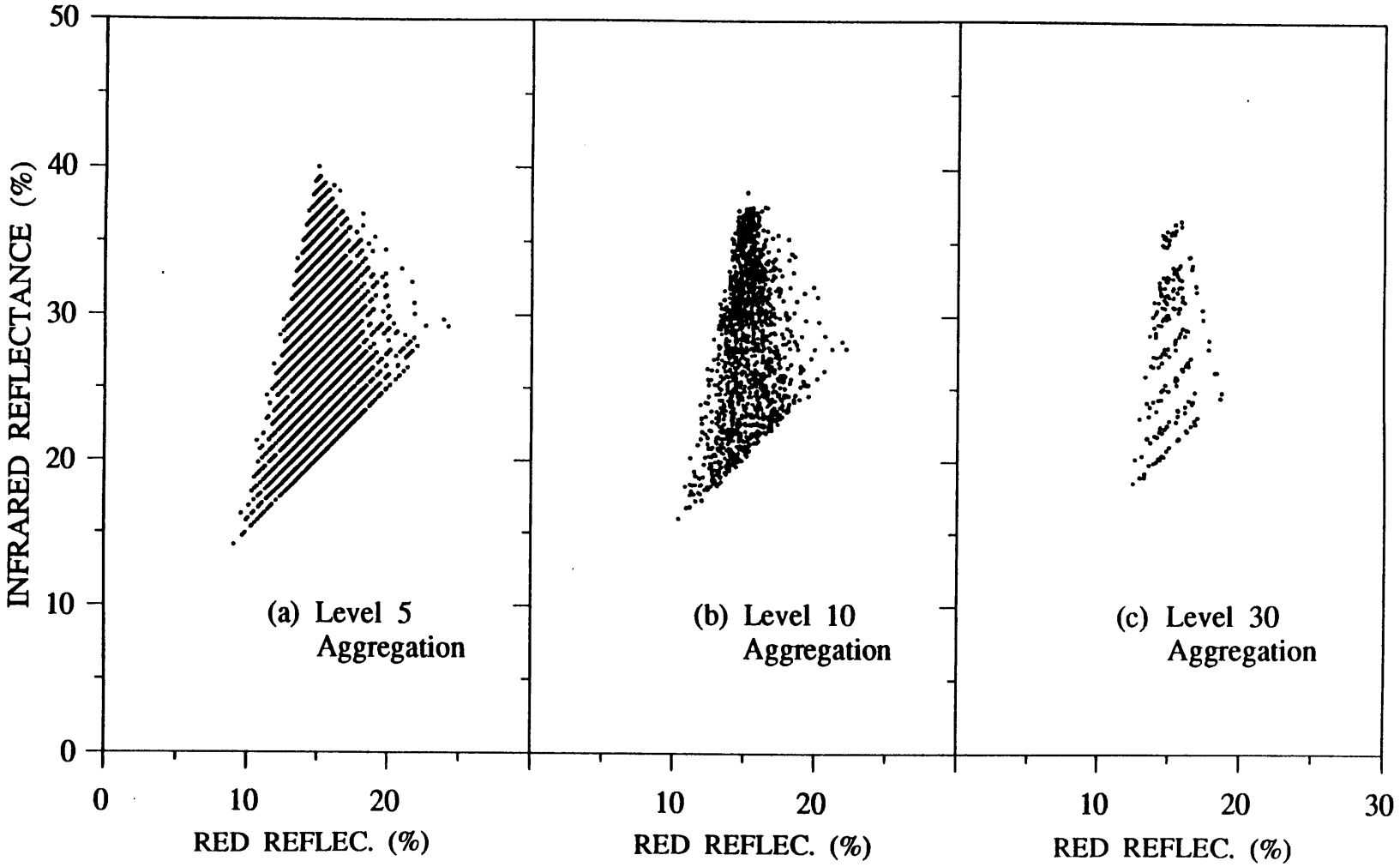

Figure 5.6–a,b,c Red–infrared scattergrams, Case II simulation: variable percent cover and soil reflectance, constant vegetation reflectance; no shadows.

pixels falling on a line parallel to the soil line will have the same percent vegetation. A second observation is that all pixels falling on a straight line extending from the top of the triangle to the soil line will have the same value of average soil reflectance. The above interpretations of the scattergram are indicated on Figure 5.7 (an expanded version of 5.6b) for the level 10 aggregation.

The importance of pixel scale relative to the covariance function is seen in the size of the triangles at different levels of aggregation. The scattergrams indicate that the length of the soil line and, hence, the width of the triangle decrease with increasing aggregation. Both the standard deviation and the covariance length scale contribute to that effect. Since scenes composed of large pixels average over a greater area than scenes with small pixels, statistically, one can expect the former case to have a lower standard deviation. However, that effect is mitigated by the covariance length scale. Scenes with small length scales (relative to pixel size) will exhibit short soil lines, while scenes with large length scales will exhibit long soil lines.

5.3 Case III – Variable Vegetation Reflectance, No Shadows

In addition to variable percent cover and variable soil reflectance, the Case III simulation introduces variable vegetation reflectance and examines its effect on the red–infrared scattergram. Vegetation reflectance will change at small and large spatial scales due to variations in a number of plant parameters, including plant species, leaf reflectance, growth stage, plant architecture, leaf orientation and distribution, leaf area, and plant stress (Ross, 1981). Regional scale variations in the pattern of natural vegetation and dominant species are influenced by elevation, gradient, and local climate (Whittaker, 1975).

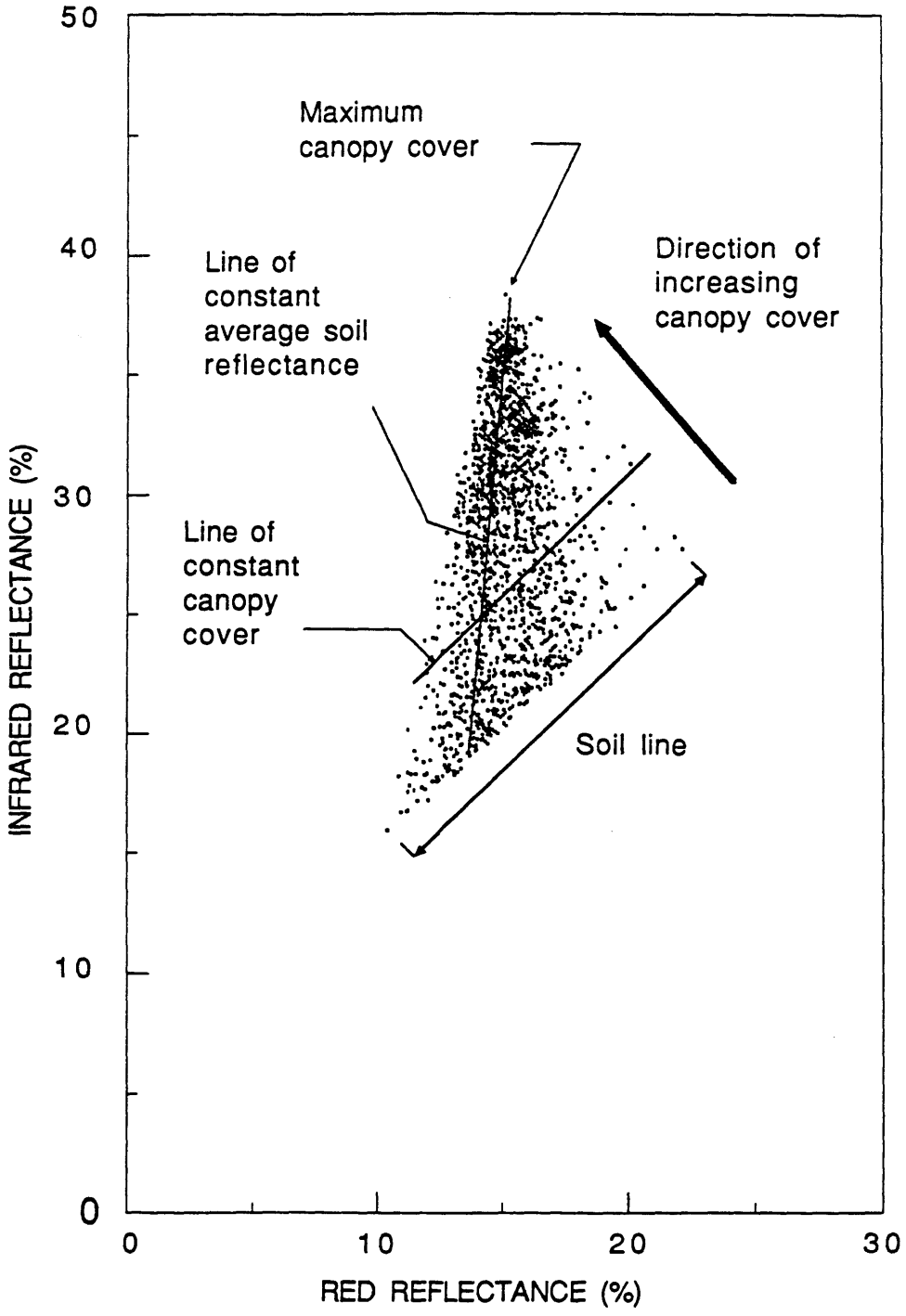

Figure 5.7 Interpretation of scattergram, Case II simulation level 10 aggregation: variable percent cover and soil reflectance, constant vegetation reflectance; no shadow.

As for soil, Case III treats the variation in vegetation reflectance as a normally distributed random variable with an exponential covariance structure. It further assumes that reflectances in the infrared and red bands are linearly related with negative slope. That relationship is not intended to represent all types of vegetation variability, but may be a simple approximation for some cases. For instance, increases in leaf area are generally associated with decreases in red reflectance and increases in infrared reflectance (see for example, Colwell, 1974; Hall, 1984).

For Case III, the total reflectance of a given pixel becomes

$$R(\lambda,\underline{x}) = mR_{m_I}(\lambda,\underline{x}) + (1 - m)R_{g_I}(\lambda,\underline{x}) \qquad (5.11)$$

where the three random variables are percent cover (m), vegetation reflectance (R_{m_I}) and soil reflectance (R_{g_I}).

The scattergram for Case III is presented in Figures 5.8–a,b,c for all levels of aggregation. The difference from Case II is that the top of the triangle has spread open, resulting in a quadrilateral data plot. An envelope curve along the top of the quadrilateral represents pixels of maximum vegetation cover. For scenes containing full canopy cover, that locus of points can be considered the "canopy line" analogous to the soil line at the base of the quadrilateral.

It is noted that for all three non shadowed cases (I, II, and III), neither plant geometry nor spatial distribution play a role in the shape of the scattergram or the relative location of a given pixel. Similar scattergrams could have been achieved using any plant geometry (e.g., spheres or cones) or spatial distribution (e.g., row crops with any orientation) as long as the distribution of the reflectances and the percentage of vegetation cover were the same.

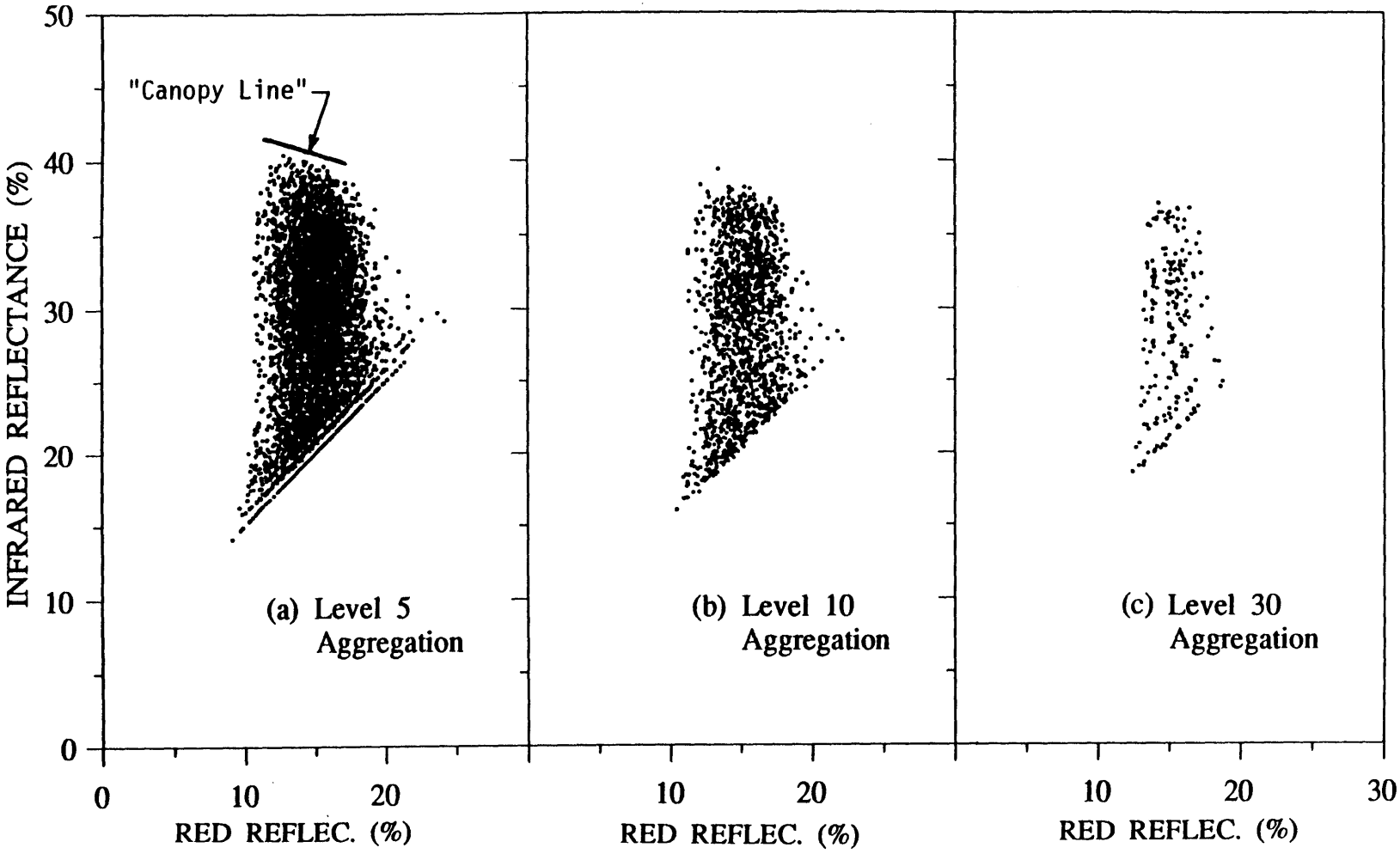

Figure 5.8–a,b,c Red–infrared scattergrams, Case III simulation: variable percent cover, soil and vegetation reflectances; no shadows.

5.4 Case IV – Shadowed Soil Background, Constant Vegetation and Soil Reflectance

Shadows cast by vegetation can be an important component of total pixel reflectance. Shadows change diurnally with the position of the sun and with the amount of diffuse solar radiation. Important seasonal changes occur both with the sun's migration and with changes in plant structure.

Case IV examines the effect of shadows cast by plants on soil. The solar and view angles are arbitrarily assumed to be 30° and 0°, respectively, and the reflectances are constant. The reflectance equation for a given pixel is

$$R(\lambda) = mR_{m_I}(\lambda) + g_I R_{g_I}(\lambda) + g_S R_{g_S}(\lambda) \qquad (5.12)$$

The scattergrams associated with the three aggregation levels for the Case IV simulation are shown in Figures 5.9–a,b,c. They reveal several interesting relations among percent cover and shadow, the level of aggregation, and the characteristic shape of the scattergram.

All the data pairs fall within a space defined by a triangle. This is illustrated using the level 5 aggregation as indicated in Figure 5.10 (an expanded version of 5.9a). The vertices of the triangle (labeled Points B, C, and D) correspond to the assumed pure spectra of the full shadow (reflectance = 0.0), full canopy, and pure soil, respectively, as indicated in Table 5.1.

Since pixels located within the triangle are linear mixtures of the three cover types, the exact percentage of any cover type can be determined on the basis of its location in the scattergram. For instance, the percent covers for an arbitrary pixel A shown on Figure 5.10 can be determined graphically as follows. First,

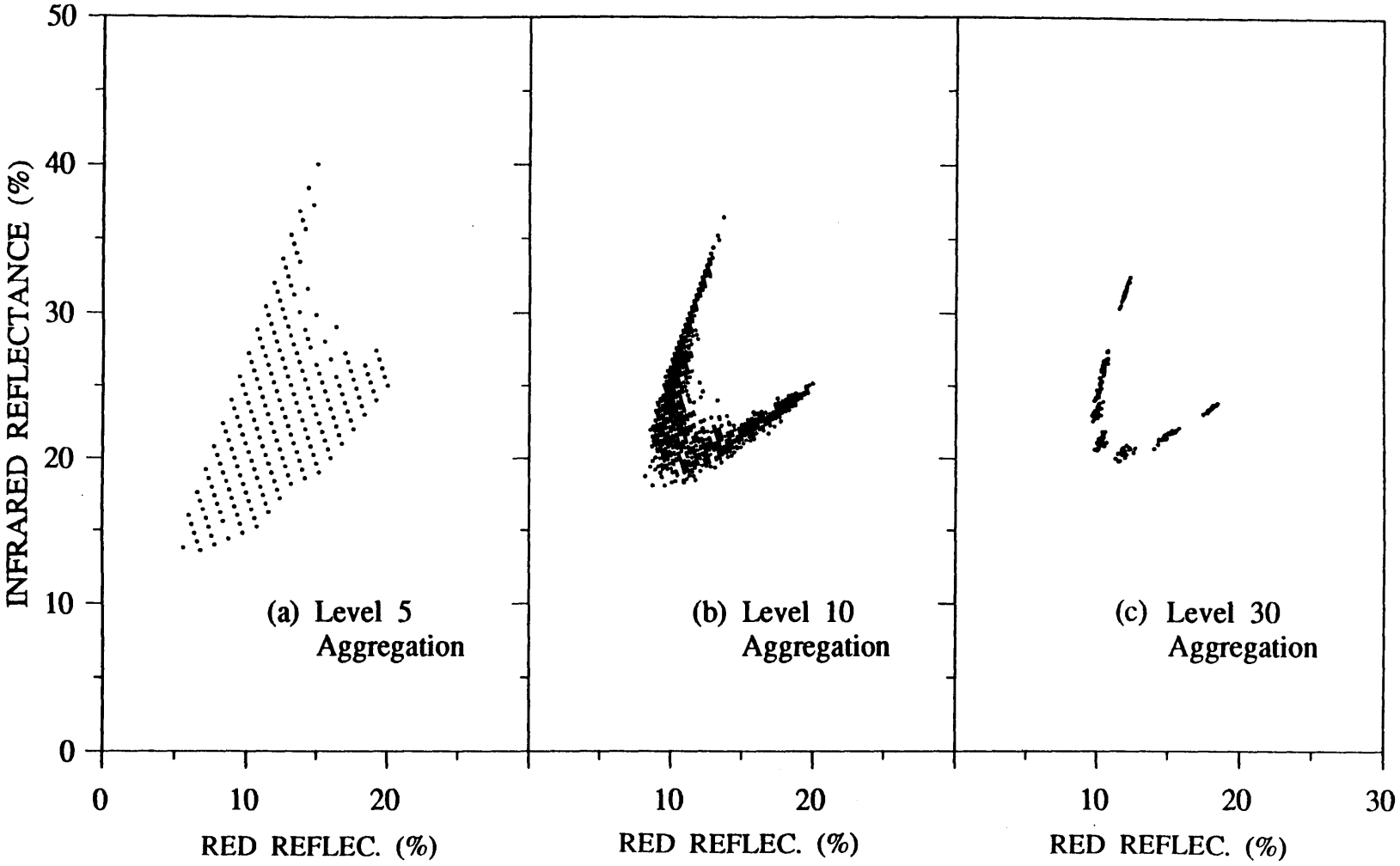

Figure 5.9–a,b,c Red–infrared scattergram, Case IV simulation: variable percent cover, constant soil and vegetation reflectances; shadowed soil background.

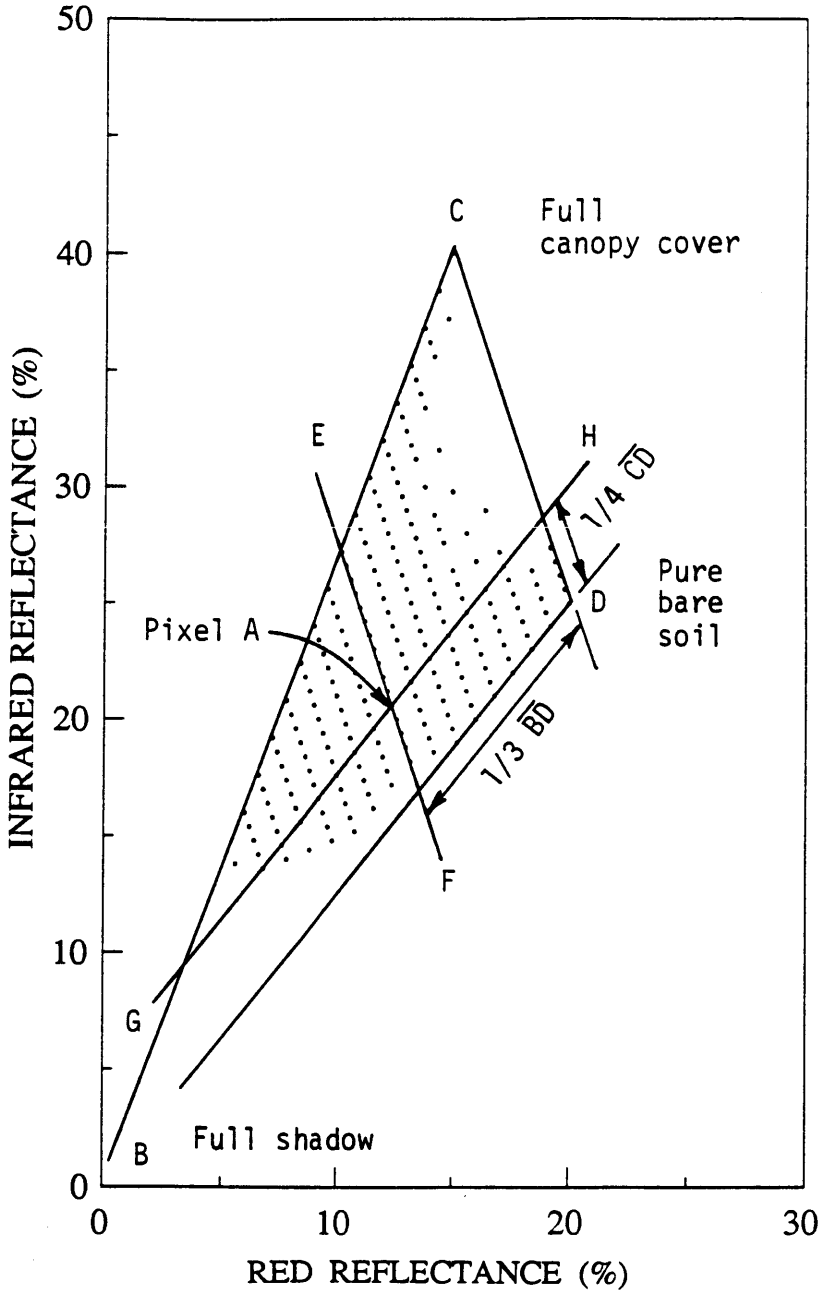

Figure 5.10 Interpretation of scattergram, Case IV simulation, level 5 aggregation: variable percent cover, constant soil and vegetation reflectances; shadowed soil background.

lines EF and GH are drawn through pixel A parallel to CD and BD, respectively. It is then noted that line EF is located about one–third of the distance between the line CD and point B. That indicates that pixel A contains 33 percent shadow. Line GH is situated about one–fourth the distance between the line BD and point C, indicating that pixel A has 25 percent vegetation cover. The remaining cover, 42 percent, is bare soil, which can be checked on the basis of pixel A's location between line BC and point D.

The above determination of the three cover types is simply a graphical illustration of an analytical solution applicable within the limits of the Case IV assumptions. It can be applied to any level of aggregation. The solution could also be achieved algebraically using equation (5.12) for both wavelengths (two equations) and equation (5.7).

The Case IV scattergrams also reveal an important relation between shadow length scale and pixel size. For instance, at the level 5 aggregation, since the length scale of the shadow is about the same as the pixel scale, there are numerous instances when the shadow of a tree in one pixel falls onto an adjacent pixel. The three components of the pixel (vegetation, shadowed soil and illuminated soil) are independent of each other in a majority of cases. As a result, pixels can occupy almost any space within the limits of the triangular scattergram given a large enough sample size.

As the level of aggregation increases, however, the length scale of the shadows becomes much smaller than the size of the pixel. As a result, shadows associated with a given tree fall increasingly within the same pixel and the amount of ground shadow becomes more and more correlated with the amount of vegetation cover. Mathematically, a covariance is generated among the three cover variables for the higher levels of aggregation which can be expressed,

$$g_S = g_S(m) \tag{5.13}$$

$$g_I = g_I(m) = 1 - m - g_S(m) \tag{5.14}$$

and equation (5.12) becomes

$$R(\lambda) = R[\lambda, m, g_I(m), g_S(m)] \tag{5.15}$$

A major consequence of the above relations is that it reduces the feasible region in the scattergram. Even at the level 5 aggregation (Figure 5.9a), that effect is manifested as a slight indentation in the upper right hand side of the triangular scattergram. At higher levels of aggregation, Equation (5.15) implies that there is only one position in the scattergram associated with a given canopy cover. As a result, one should expect the triangular scattergram observed at the level 5 aggregation to collapse to a single curved line when the shadow length scale becomes small relative to the pixel size. That is indeed shown to be true in a progressive manner by examining the sequential shapes of the scattergrams in Figure 5.9b (level 10 aggregation) and Figure 5.9c (level 30 aggregation).

5.5 Case V – Shadowed Soil Background, Variable Soil Reflectance

Case V is a more realistic version of the shadow model in which soil reflectance is assumed normally distributed as in Case II. The governing equation for an individual pixel is

$$R(\lambda,\underline{x}) = mR_{m_I}(\lambda) + g_I R_{g_I}(\lambda,\underline{x}) + g_S R_{g_S}(\lambda) \qquad (5.16)$$

The resulting scattergrams for the different levels of aggregation are shown in Figure 5.11.

The scattergrams of the Case V simulation represent a combination of the effects illustrated in Case II (constant vegetation reflectance, variable soil reflectance) and Case IV (shadow effects).

For instance, the scattergram of the level 5 aggregation, Figure 5.11a, exhibits a triangular shape overall, but with a pronounced indentation in the upper right portion due to the shadow effects. It can be regarded as a superposition of many triangular scattergrams, each for a homogeneous soil (constant background reflectance), similar to that of Case IV, level 5 aggregation (Figure 5.10). That is illustrated in Figure 5.12 (expanded version of 5.11a). Those triangles share two common vertices at 1) the point of pure shadow reflectance (point B), and 2) the point of pure vegetation reflectance (point C). The third vertex (labeled D_1, D_2, D_3, ... etc.) is unique for each triangle, representing the reflectivity of a particular soil which is homogeneous at that aggregation. The collection of all vertices, D, constitutes the true soil line.

In the particular example shown, the true soil line has an intercept greater than zero, and is thus situated slightly inside the boundaries of the overall scattergram, as indicated in Figure 5.12. It is also possible, however, that the shadowed soil reflectance lies above the soil line. Only in such cases will the bottom of the scattergram accurately represent the true soil line.

An important consequence of the level 5 aggregation is that pixels containing different mixtures of vegetation, shadow, and variable soil can occupy the same

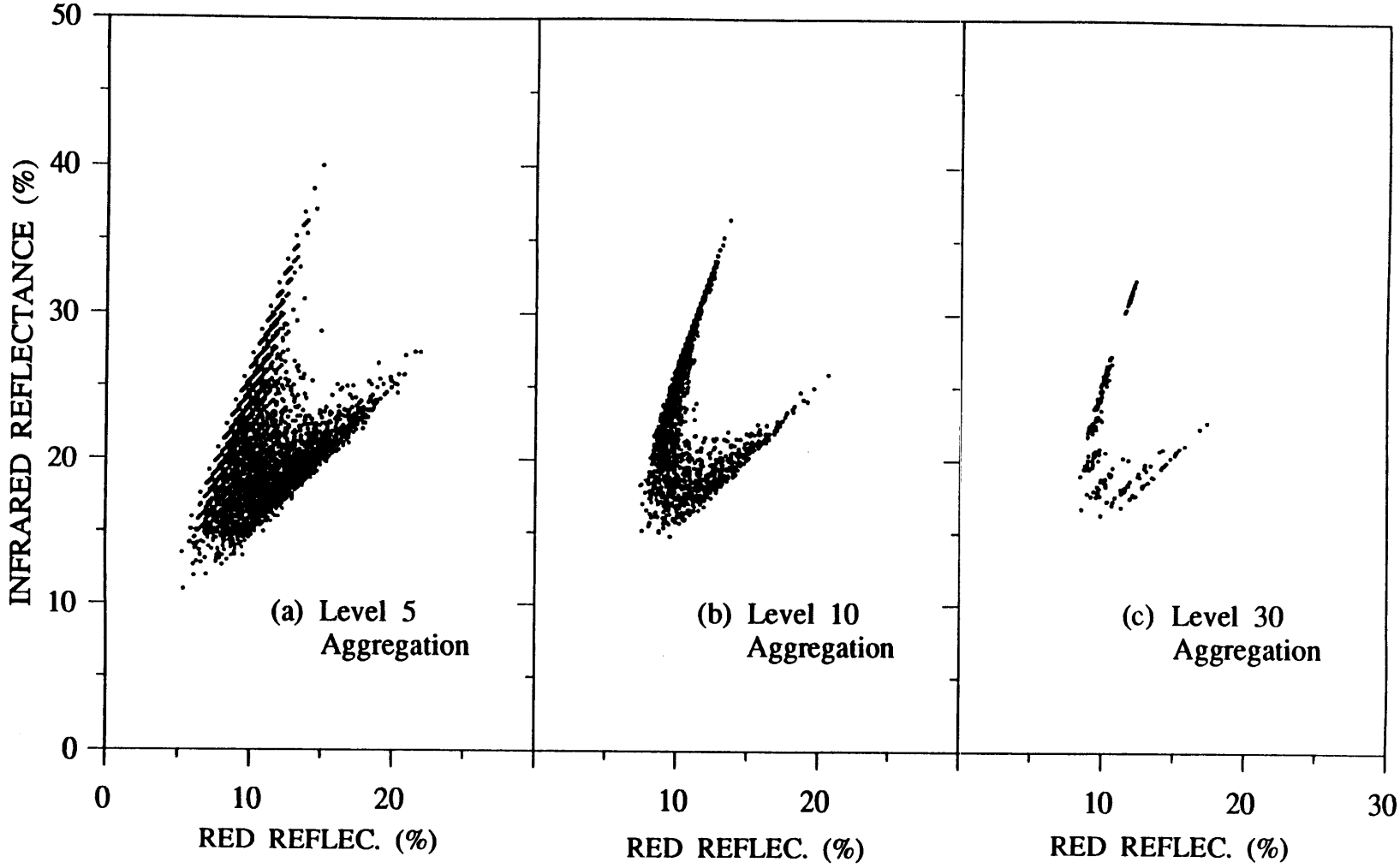

Figure 5.11–a,b,c Red–infrared scattergrams, Case V simulation: variable percent cover and soil reflectance, constant vegetation reflectance; shadowed soil background.

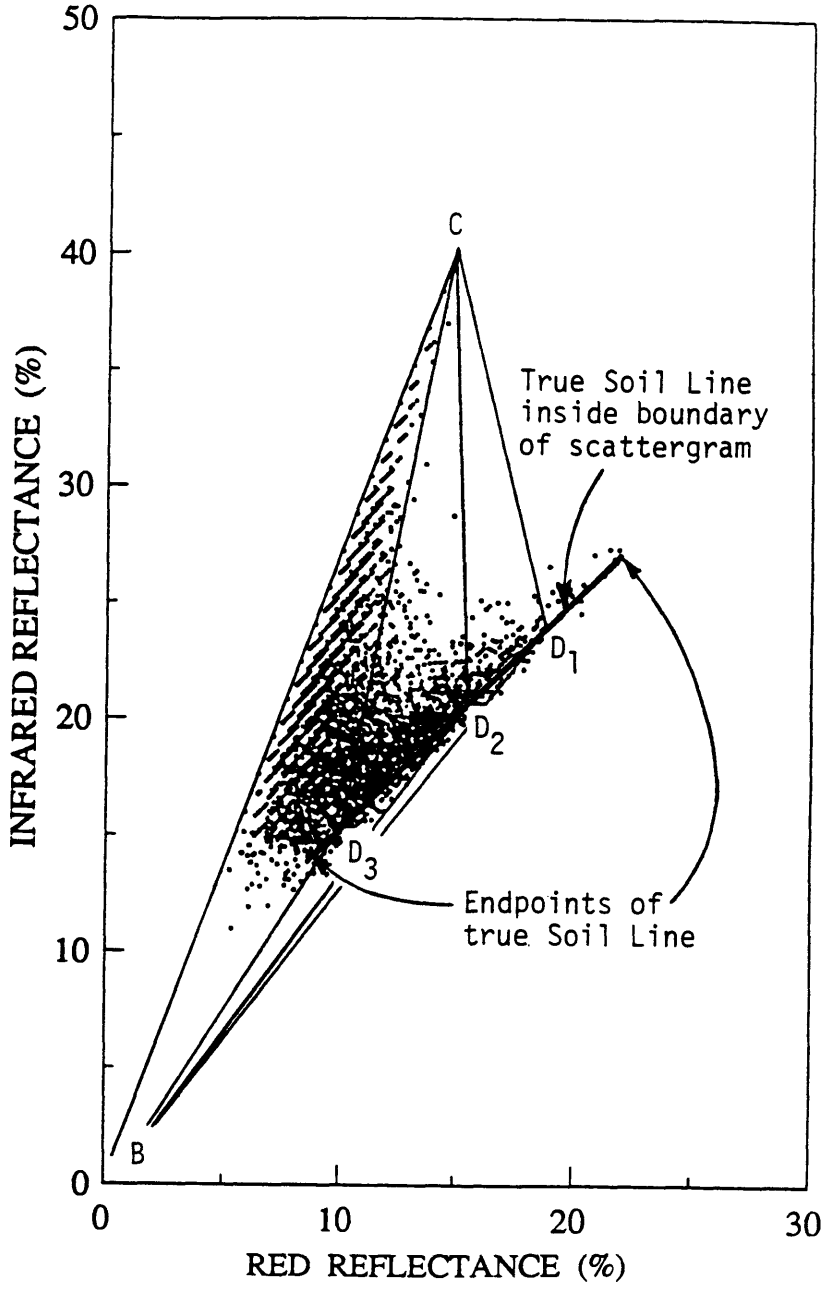

Figure 5.12 Interpretation of scattergram, Case V simulation, level 5 aggregation: variable percent cover and soil reflectances, constant vegetation reflectance; shadowed soil background.

location in the scattergram. As a result, the percent cover of individual pixels can not be determined explicitly as shown in previous examples.

The scattergrams of the levels 10 and 30 aggregation are shown in Figures 5.11b and 5.11c, respectively. As in Case IV, because of the unique relation between shadow and vegetation cover at this scale, the scattergrams collapse progressively to the shape of a "tasseled cap" (Kauth and Thomas, 1976). At the level 30 aggregation, the scattergram consists of a series of juxtaposed curved lines, each line possessing constant average soil reflectivity (similar to Case IV, level 30 aggregation, Figure 5.9c), extending from individual points on the true soil line to the tip of the tasseled cap. That is illustrated in Figure 5.13 (expanded version of 5.11c).

Unlike the level 5 aggregation, percent cover can be estimated for Case V, level 30 aggregation, in a manner similar to Cases II and IV. Percent cover is proportional to the distance between the soil line and the tip of the tasseled cap.

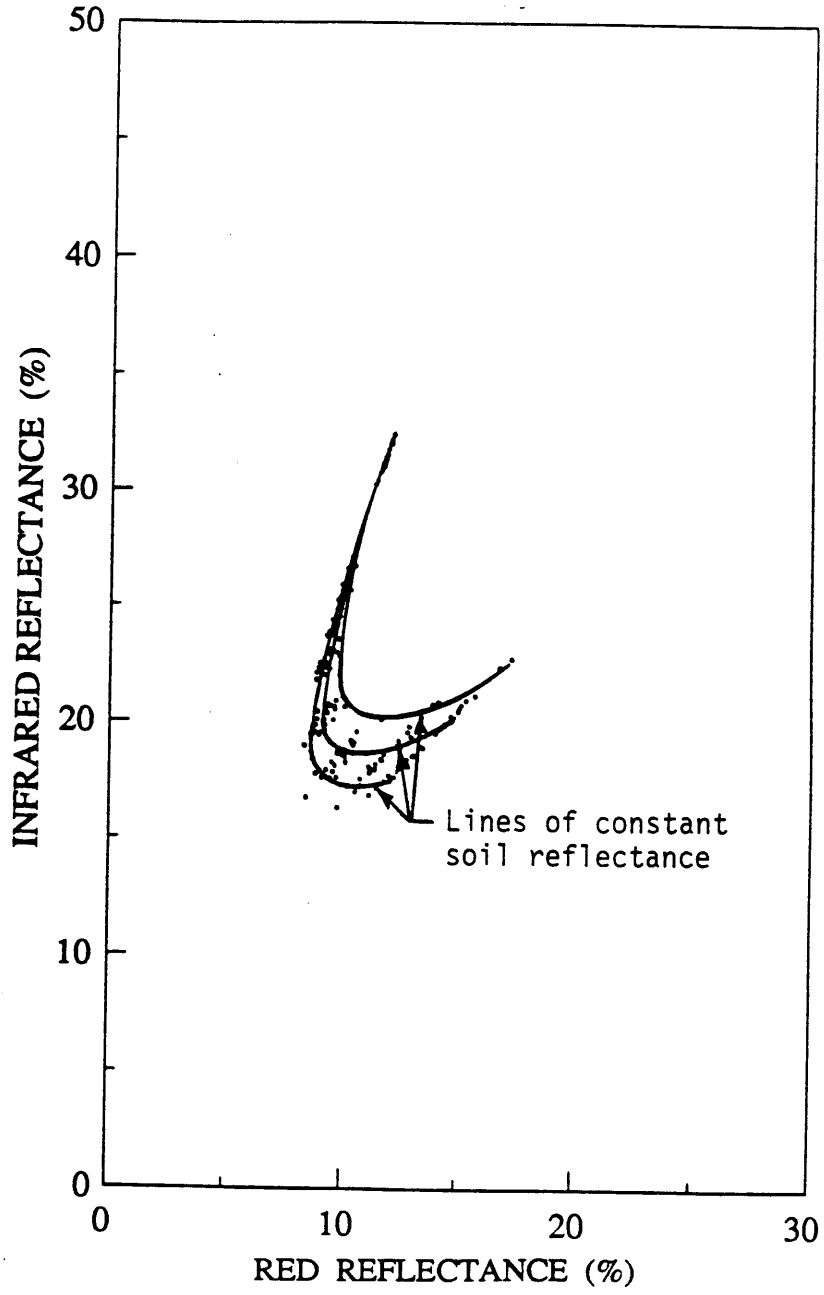

Figure 5.13 Interpretation of scattergram, Case V simulation, level 30 aggregation: variable percent cover and soil reflectance, constant vegetation reflectance; shadowed soil background.

Chapter 6

REFLECTANCE AND COVER MOMENTS

This chapter describes various moment equations applicable to the solution of the inverse problem described in Chapter 7. The moments include the mean, variance, cross–spectral covariance, and the spatial covariance of the reflectance equation. Conditional moments are formulated for portions of the scene where the pixels are assumed to possess one or more similar attributes, and which can be identified through ones knowledge of the scattergram. The geometric similarity and scaling criterion necessary for the application of the conditional moment equations are developed. A sampling scale ratio is developed as a quantitative scaling criterion to test when the fractional covers are functionally related.

6.1 General Moment Equations

When one or more of the terms of the reflectance model are considered random, then the moments of both (4.4) and (4.5) can be expressed in terms of the moments of the individual variates. Such expansions can be achieved by applying fundamental properties of random functions without prescribing the probability density functions of the variates. For instance, if one assumes i) all the terms of equation (4.4) to be random, ii) that the reflectance terms are statistically independent of the percent cover terms, reflectances of different cover types are statistically independent, a general set of moment equations as presented below can be obtained. The mathematical details and the assumptions underlying the moment equations are provided in Appendix C.

The expected value, or mean pixel reflectance is

$$E[R(\lambda,\underline{x})] = \sum_i E[f_i(\underline{x})]E[R_i(\lambda,\underline{x})] \tag{6.1}$$

where E[ ] designates the expected value. The variance of equation (4.4) can be written,

$$\begin{aligned} \text{VAR}[R(\lambda,\underline{x}))] = \sum_i \Big\{ & E[f_i(\underline{x})]^2 \text{ VAR}[R_i(\lambda,\underline{x})] + E[R_i(\lambda,\underline{x})]^2 \text{ VAR}[f_i(\underline{x})] \\ & + \text{VAR}[f_i(\underline{x})] \text{ VAR}[R_i(\lambda,\underline{x})] \Big\} \\ & + \sum_{i \neq j} \sum E[R_i(\lambda,\underline{x})] E[R_j(\lambda,\underline{x})] \text{COV}[f_i(\underline{x}),f_j(\underline{x})] \end{aligned} \tag{6.2}$$

where $\text{COV}[f_i(\underline{x}),f_j(\underline{x})]$ represents the covariance between cover type i and j in a given pixel. The summations in (6.1) and (6.2) occur over the four cover types. The cross spectral covariance of the reflectance between the two bands, λ_1 and λ_2, for a given pixel is written,

$$\begin{aligned} \text{COV}[R(\lambda_1,\underline{x}),R(\lambda_2,\underline{x})] = \sum_i \Big\{ & E[f_i(\underline{x})]^2 \text{COV}[R_i(\lambda_1,\underline{x}),R_i(\lambda_2,\underline{x})] \\ & + \text{VAR}[f_i(\underline{x})] E[R_i(\lambda_1,\underline{x})] E[R_i(\lambda_2,\underline{x})] \Big\} \\ & + \sum_{i \neq j} \sum E[R_i(\lambda_1,\underline{x})] E[R_j(\lambda_2,\underline{x})] \text{ COV}[f_i(\underline{x}),f_j(\underline{x})] \end{aligned} \tag{6.3}$$

Similarly, the spatial covariance of the total reflectance between any two pixels in one band is,

$$\begin{aligned}\mathrm{COV}_x[R(\lambda,\underline{x}),R(\lambda,\underline{x}')] = \quad & \sum_i \sum_j \Big\{ \Big[\mathrm{COV}_x[f_i(\underline{x}),f_j(\underline{x}')] + E[f_i(\underline{x})]\, E[f_j(\underline{x}')] \Big] \cdot \\ & \Big[\mathrm{COV}_x[R_i(\lambda,\underline{x}),R_j(\lambda,\underline{x}')] + E[R_i(\lambda,\underline{x})]\, E[R_j(\lambda,\underline{x}')] \Big] \\ & - E[f_i(\underline{x})]\, E[f_j(\underline{x}')]\, E[R_i(\lambda,\underline{x})]\, E[R_j(\lambda,\underline{x}')] \Big\}\end{aligned} \tag{6.4}$$

where $\underline{x} = (\underline{x}_1,\underline{x}_2)$ and $\underline{x}' = (\underline{x}_1',\underline{x}_2')$ represent two separate locations in the image and $\mathrm{COV}_x[R_i(\lambda,\underline{x}),R_j(\lambda,\underline{x}')]$ equals zero (by assumption) except for $i = j$.

The relationship among the moments of the cover variates can be established using equation (4.5). Those quantities are not assumed to be statistically independent but are related by the geometry and spatial distribution of the plants. The expected value is,

$$\sum_i E[f_i(\underline{x})] = 1 \tag{6.5}$$

and the variance is,

$$\sum_i \mathrm{VAR}[f_i(\underline{x})] + \sum_{i \neq j} \sum \mathrm{COV}[f_i(\underline{x}),f_j(\underline{x})] = 0 \tag{6.6}$$

Equations (6.1) through (6.6) constitute at least six moment equations which, theoretically, can be augmented if more than one wavelength is used. For instance, equations (6.1), (6.2) and (6.4) each represent two equations when written for both the red and infrared bands. The actual number of moment equations depends on several factors, including the nature of the scene, the number of random variables in the model, and the linear independence of the moment equations at different wavelengths.

6.2 Conditional Reflectance and Cover Moments

In some instances, conditional moments can be written for a portion of the pixels that possesses similar attributes. Examples include pixels possessing only bare soil, equal amounts of vegetation cover, or the same probability distribution describing plant spacing. The formulation of conditional moments for those cases generally reduces the complexity of the analysis provided that the appropriate set of pixels can be identified.

One approach for identifying a set of pixels with common attributes is through the interpretation of multidimensional scattergrams. The previous chapter demonstrated, through the use of simulated images, that the structure of semivegetated scenes manifests itself in the structure of red–infrared scattergrams. That knowledge of the structure of scattergrams provides a mechanism for identifying sets of pixels, not necessarily located within the same segment of the scene, for which conditional moments can be formulated.

6.2.1 Soil Line Conditional Moments

A relatively simple example of conditional moments is for the case of bare soil pixels. For many semivegetated scenes, bare soil pixels orient themselves along a preferred "soil line" at the base of triangular red–infrared scattergrams as described in Section 3.4, or,

$$R_{g_I}(\lambda_{IR}, \underline{x}) = \alpha\, R_{g_I}(\lambda_{RED}, \underline{x}) + \gamma \tag{6.7}$$

where α is the slope and γ the intercept. In terms of equation (5.7), the only fractional cover type is bare soil, or

$$g_I = 1 \tag{6.8}$$

By conditioning the mean and variance of the reflectance equations (6.1 and 6.2) along the soil line, then,

$$E[R(\lambda,\underline{x})\,|\,g_I = 1] \;=\; E[R_{g_I}(\lambda,\underline{x})] \tag{6.9}$$

$$VAR[R(\lambda,\underline{x})\,|\,g_I = 1] \;=\; VAR[R_{g_I}(\lambda,\underline{x})] \tag{6.10}$$

resulting in two additional conditional moment equations for a given wavelength. The soil reflectance moments are related by,

$$E[R_{g_I}(\lambda_{IR},\underline{x})] = \alpha\, E[R_{g_I}(\lambda_{RED},\underline{x})] + \gamma \tag{6.11}$$

$$VAR[R_{g_I}(\lambda_{IR},\underline{x})] = \alpha^2\, E[R_{g_I}(\lambda_{RED},\underline{x})] \tag{6.12}$$

6.2.2 Cover Moments for Statistically Homogeneous Spatial Distributions

In many natural semivegetated regions, the spatial distribution of vegetation follows particular patterns which can be analytically prescribed. The statistical analysis of such spatial patterns in botany, with emphasis on coniferous vegetation, is well documented (Diggle, 1983). Knowledge of those distributions can be useful for relating the cover moments to the spatial distribution and geometry of the vegetation elements.

One example is when a portion of the scene contains plants which can be assumed to follow a Poisson distribution in space. The mean of the fraction of illuminated vegetation for that segment of the scene can be written,

$$E[m\,|\,\text{Poisson}] \;=\; 1 \;-\; \exp[-\rho(A_t + A_S)] \tag{6.13}$$

where ρ is the Poisson spatial density, A_t is the average area of one plant canopy, A_S is the average area of the shadow cast by one canopy on the soil. The variance of the fraction of illuminated vegetation can be obtained in terms of m from the coverage problem derived empirically by Garwood (1947), or

$$\text{VAR}[m \mid \text{Poisson}] = \left[m^2 \left[\{1 - \frac{2.3}{k}\} m^{-A_t/A_p} - 1 \right] + \frac{2.3m}{k} \right]^{0.5} \qquad (6.14)$$

where A_t is the average area of the plant, A_p is the area of the pixel, and $k = (A_t/A_p)^{1.5}$. A graphical solution of (6.14) is provided in Figure 7.3 for the Case V simulation , level 10 aggregation, presented in Chapter 5.

6.2.3 Geometric Similarity

Many semivegetated landscapes possess only a few dominant species whose shapes can be represented by simple geometric figures, such as cylinders, cones, or spheres. The plants can be of different heights or sizes reflecting different stages of growth. In order to parameterize such shapes with a minimum number of variables, it is useful to assume that they are geometrically similar. Geometric similarity, employed in that sense, implies that the ratio of the plant height to some canopy width scale is a constant regardless of the size of the plant. In the case of conifer trees represented by cones, Li and Strahler (1985) assumed that the apex angle was constant. That assumption can be generalized to other geometric shapes as well. For instance, the similarity parameter of cylinders is the aspect ratio, b, defined as the ratio of the mean width, D, to mean height, H. For spheres, no similarity parameter is required, as the ratio of height to width is unity.

The geometric similarity assumption can be extended to include the solar angle, and thus, becomes particularly useful for establishing the analytical relationship between canopy area and shadowed area for different spatial arrangements. When no overlapping effects are considered, the shape of the plant's shadow is dictated precisely by the geometry of the plant itself and the solar zenith angle, θ. By defining η as the ratio of shadowed area, A_S, to plant area, A_t, or,

$$\eta = A_S/A_t \tag{6.15}$$

then for example, for square cylinders,

$$\eta = \frac{\tan\theta}{b} \tag{6.16}$$

Similarity parameters and corresponding η's for different geometric shapes are provided in Table 6.1. A graphical illustration of geometric similarity in the case of cones is presented in Figure 6.1.

The practical advantage of defining η is that it allows one to absorb all the geometric factors which relate canopy area to shadowed area into only one variable. Consequently, the landscape can often be parameterized without the limitation of having to specify cones, cylinders or another geometric shape.

As the vegetation density or the solar zenith angle increases, the shadow cast by one plant can extend far enough to be overlapped by the canopy of an adjacent plant. In such cases the amount of shadow is a function of the spatial distribution of the plants as well as of their geometry. Shadowing can occur when the plants are arranged in homogeneous deterministic spatial distributions, such as for row crops or orchards, or in stochastic distributions, as for natural vegetation.

Table 6.1

Similarity of Canopy Geometry

	Canopy Shape	Geometric Similarity Parameter	Solar–Geometric Similarity Parameter $\eta = A_s/A_t$
i)	Circular Cylinders	$b = D/H$	$\frac{4}{\pi}\frac{\tan\theta}{b}$
ii)	Square Cylinders	$b = D/H$	$\frac{\tan\theta}{b}$
iii)	Cone	$\phi = \tan^{-1}(D/H)$	$(\cot\chi - \frac{\pi}{2} + \chi)/\pi$
iv)	Sphere	none	$\tan\theta \sin\theta$

where D = mean canopy width
H = mean canopy height
θ = solar zenith angle
$\chi = \sin^{-1}(\tan\phi/\tan\theta)$

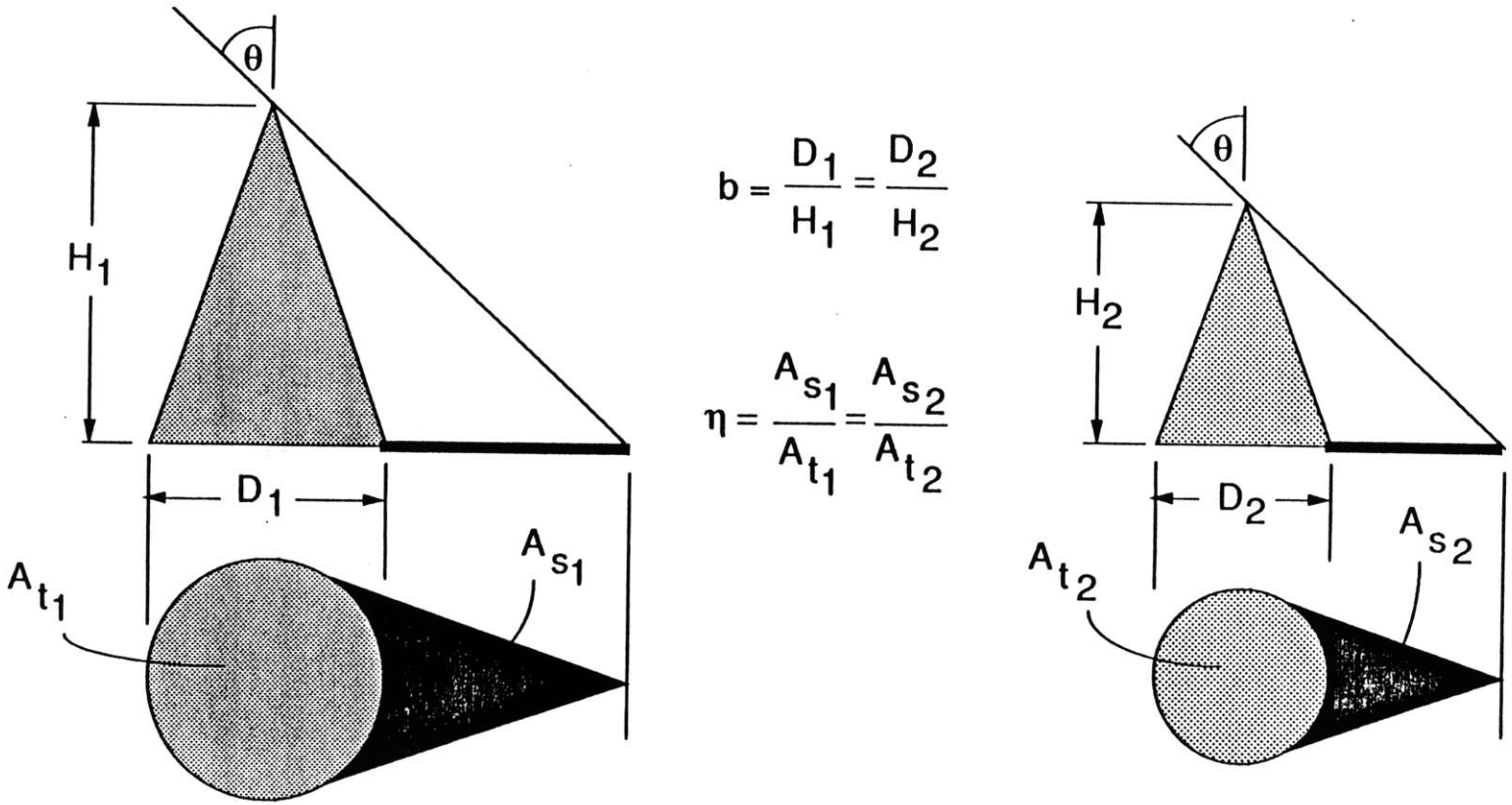

Figure 6.1 Concept of geometric similarity applied to cones.

For random spatial distributions, the relationship among cover types is more conveniently expressed in terms of their expected values. For example, in the particular case of Poisson distributed plants, equations (6.5), (6.13) and (6.15) can be combined to yield,

$$E[g_I] = \left\{1 - E[m]\right\}^{\eta + 1} \tag{6.17}$$

The derivation of equation (6.17) is provided in Appendix C.

6.2.4 Conditional Moments for Pixels with Constant Vegetation Cover

The soil line moment equations are, in fact, a special case of the conditional moments for pixels of constant vegetation cover. For example, it was empirically shown in Section 5.4 that when i) the only variables in the scene are the fractional covers (vegetation, shadow, and illuminated soil) and soil background reflectance, and ii) a unique functional relationship exists among the different cover types of the form

$$g_I = g_I(m, g_s) \tag{6.18}$$

then all pixels falling on a line parallel to the soil line possess equal amounts of vegetation cover. However, the distance of that line from the soil line was not linearly proportional to the amount of vegetation, but depended on the amount of vegetation and shadow, and the magnitude of the reflectances.

Along each parallel line, since m, g_I, and g_s are constant, the conditional mean and variance of the reflectance equations given in (6.1) and (6.2) become, respectively,

$$E[R(\lambda,\underline{x})|m] = mR_m(\lambda) + g_S R_{g_S}(\lambda) + g_I E[R_{g_I}(\lambda,\underline{x})] \quad (6.19)$$

$$VAR[R(\lambda,\underline{x})|m] = g_I^2 \; VAR[R_{g_I}(\lambda,\underline{x})] \quad (6.20)$$

The above formulation does not include the possible covariance between the soil reflectance and the amount of vegetation cover. Realistically, vegetation detritus changes soil reflectance by altering its organic and moisture content, and the resulting covariance must be considered in a more detailed analysis.

6.2.5 Sampling Scale Ratio

It is useful to develop a quantitative scaling criterion to test when the fractional covers are functionally related as in (6.18). One approach is to examine the relative scales of the shadow, as determined by the plant geometry and solar angle, and that of the pixel as determined by the field of view and altitude of the sensor. For instance, it can be reasoned based on the Case IV simulations, that as the scale of aggregation increases relative to the scale of the shadow, then, for homogeneous regions, a correlation develops among the different cover types. That correlation occurs since the variance in shadow cover is inversely proportional to pixel size. For very large pixels, the variance becomes so small that the fractional covers of each pixel approach the functional relationship in (6.18). The exact relationship depends on the geometry and spatial distribution of the plants, the solar angle, and the sensor characteristics.

The above reasoning can be examined quantitatively by comparing order of magnitude estimates of the standard deviation (square root of variance) in shadow and the amount of canopy cover as a function of canopy geometry and pixel size.

For instance, in order for (6.18) to exist, one criterion that must be true is

$$E[m] >> VAR[g_S]^{1/2} \tag{6.21}$$

From (6.6), (6.14), and (6.15) it can be shown empirically that

$$VAR[g_S]^{1/2} \sim \frac{\eta A_t}{A_p} \tag{6.22}$$

Thus, by combining (6.21) and (6.22), and noting that m is of the order of magnitude 10^{-1}, a sampling scale ratio for Poisson distributions, S_P, can be obtained of the form

$$S_P = \frac{A_p}{\eta A_t} >> 10 \tag{6.23}$$

For $S_P >> 10$, equation (6.18) is valid. When vegetation reflectances are also constant, then (6.19) and (6.20) can serve as approximations for the more complex expressions (6.1) and (6.2). For homogeneous Poisson distributions, large S_P implies that the partition of fractional covers in any given pixel approaches the mean relationship in (6.17), or

$$g_I \simeq (1 - m)^{\eta+1} \tag{6.24}$$

For regular geometric (non–statistical) spacings, variability in g_S occurs when the shadow associated with a given plant falls on a different pixel than that in which the plant is located. That situation is likely to occur when the scale of the plant is about the same or greater than the scale of the pixel. One criterion that avoids that situation is,

$$A_P >> \eta A_t \tag{6.25}$$

The sampling scale ratio for regular geometries is thus,

$$S_G = \frac{A_p}{\eta A_t} >> 1 \tag{6.26}$$

The importance of (6.23), (6.24) and (6.26) for the inverse problem will be demonstrated in Chapters 7 and 8.

6.3 Moments of Satellite Observed Radiance

It is useful to write the moments of the coupled landsurface–atmosphere radiation equations provided in Section 4.2 in order to examine the influence of the diffuse scattering terms on the moment equations. For instance, assuming horizontally homogeneous atmospheric conditions, the expected value of the satellite observed radiance given in equation (4.12) is

$$E[L(\lambda,\underline{x})] = \left[\sum_i E[f_i(\underline{x})]E[R_i(\lambda,\underline{x})]\right]L'_r(\lambda) + \left[\sum_i E[f'_i(\underline{x})]E[a_i(\lambda,\underline{x})]\right]L'_a(\lambda) + L_d(\lambda) \tag{6.27}$$

where the L' values, defined in Section 4.2, are treated as constants for a given wavelength. The variance of (4.12) can be written

$$\begin{aligned} VAR[L(\lambda,\underline{x})] = {} & L'^2_r(\lambda)VAR\left[\sum_i f_i(\underline{x})R_i(\lambda,\underline{x})\right] + L'^2_a(\lambda)VAR\left[\sum_i f'_i(\underline{x})a_i(\lambda,\underline{x})\right] \\ & + 2L'_r(\lambda)L'_a(\lambda)COV\left[\left[\sum_i f_i(\underline{x})R_i(\lambda,\underline{x})\right],\left[\sum_i f'_i(\underline{x})a_i(\lambda,\underline{x})\right]\right] \end{aligned} \tag{6.28}$$

where, for simplicity, the summed terms have not been expanded as in (6.2) and (6.3). Equations (6.27) and (6.28) indicate that the atmospheric scattered diffuse radiance, $L_d(\lambda)$, adds a constant term to the mean equation and has no influence on the variance. However, the diffuse radiance caused by adjacency effects can be significant, especially with regard to the variance, due to the introduction of cross–covariance terms. When the assumption that the surrounding area and target pixel reflectances are approximately equal, as given in (4.13), then the moments become

$$E[L(\lambda,\underline{x})] = \left[\sum_i E[f_i(\underline{x})]E[R_i(\lambda,\underline{x})]\right]L_r'(\lambda) + L_d(\lambda) \tag{6.29}$$

$$VAR[L(\lambda,\underline{x})] = L_r'^2(\lambda)VAR\left[\sum_i f_i(\underline{x})R_i(\lambda,\underline{x})\right] \tag{6.30}$$

In terms of the DN values recorded by the satellite,

$$E[DN(\lambda,\underline{x})] = \sum_i E[f_i(\underline{x})]E[R_i'(\lambda,\underline{x})] + l_d'(\lambda) \tag{6.31}$$

$$VAR[DN(\lambda,\underline{x})] = VAR\left[\sum_i f_i(\underline{x})R_i'(\lambda,\underline{x})\right] \tag{6.32}$$

where $R_i'(\lambda,\underline{x})$ is the effective component reflectance defined in Section 4.3. Thus, it is shown that for regions of low interpixel contrast, the moment equations for the observed radiance, (6.31) and (6.32), are very similar in form to those of the target reflectance defined in Sections 6.1 and 6.2. That conclusion is valid only within the assumptions of the radiance model for optically thin atmospheres provided earlier.

Chapter 7

GENERAL INVERSE PROBLEM: ESTIMATION OF SUBPIXEL PARAMETERS

In most remote sensing applications, only the spatially integrated multispectral observations are available, with limited knowledge concerning the physical structure of the scene. That is especially true in natural areas where ground truth (e.g. training samples or spectral signatures) is not regularly obtained.

The following sections present an approach for estimating the bulk physical parameters of the scene, with emphasis on subpixel vegetation cover, using the method of moments in the red and infrared bands. The method consists of equating the theoretical moments derived above for the two bands to the sample moments of the red and infrared images, and solving for the unknown parameters.

Several versions of the method are possible depending on the nature of the scene. In this chapter, the method is applied to two simulation cases presented in Chapter 5. Inversion is first applied to Case II as an introduction to the method on a relatively simple scene, without shadows, in which the Sampling Scale ratio for Poisson distributions, S_p, is zero. The inverse procedure is then applied to two different aggregations of the same landscape simulated in Case V. Different versions of the inverse procedure are used on each aggregation of Case V, as a direct consequence of the change in value of the Sampling Scale Ratio with pixel size.

The simulated images are analyzed primarily as a theoretical demonstration of the method for scenes in which the surface parameters are well known and can

be controlled. The analysis shows to what extent subpixel parameters, evidently lost through the aggregation process, can be retrieved.

7.1 Inversion of Case II

The parameters of the Case II image can be retrieved by employing the conditional moment equations to sets of pixels which possess similar attributes, as identified in the scattergram. More than one approach is possible, depending on which parameters are desired. This section demonstrates a version applicable for estimating the fractional vegetation cover on a pixel by pixel basis. The approach uses the knowledge that the sampling scale ratio, S_p, is very large, since in the case of no shadows, equation (6.15) yields $\eta = 0$ and equation (6.23) yields $S_p = \infty$. It also takes advantage of the knowledge that pixels of constant vegetation cover lie parallel to the soil line. Once a set of pixels has been identified, the solution can be obtained by writing conditional moments along those lines using either band.

The solution procedure is first, to locate the soil line in the scattergram, and then to calculate the sample mean and variance of those pixels. Equating those sample moments to the theoretical conditional moments of the soil line, equations (6.9) and (6.10), provides a direct estimate of the mean and variance of the soil reflectance at that scale. Next, a narrow band of pixels lying at an arbitrary distance from the soil line, but parallel to the soil line, is chosen and the sample moments of those pixels are calculated. The fractional vegetation cover of pixels in that band is estimated by equating the sample variances to the theoretical variances, and using (6.20) rewritten for Case II in which $m = 1 - g_I$, or

$$m = 1 - \left[VAR[R(\lambda,\underline{x})\,|\,m] / VAR[R_{g_I}(\lambda,\underline{x})] \right]^{1/2} \qquad (7.1)$$

By choosing another parallel line at a different distance from the soil line, another estimate of m can be obtained for a new set of pixels. The procedure is repeated until the desired number of pixels has been analyzed. The computer code for the solution of the inverse problem for Case II is provided in Appendix D.

The vegetation reflectance can be retrieved although it is not a prerequisite to estimate m. It is obtained by rewriting (6.19) specifically for Case II in which $g_s = 0$, or

$$R_m(\lambda) = \{E[R(\lambda,\underline{x})|m] - E[R_{g_I}(\lambda,\underline{x})]\}/m + E[R_{g_I}(\lambda,\underline{x})] \qquad (7.2)$$

The results of the Case II analysis using either the red or infrared band are shown in Figure 7.1 and Table 7.1. Figure 7.1 contains a plot of the estimated values of m versus the simulated values of each pixel in seven different parallel lines. The results indicate excellent retrieval for most values of m, with a standard deviation of error, s, equal to 0.026 for calculations using the red band and 0.028 for calculations using the IR band. The estimated reflectances also agree closely with the actual values for all values of m as can be seen in Table 7.1 for one arbitrary line at which m equals 40 percent.

It is noted that the above estimates of vegetation cover are made without introducing any assumptions on the geometry or spatial distribution of the trees. It is further noted that the variance of the soil reflectance computed above represents the variance of the aggregated process. The variance of the point process can be retrieved by applying the appropriate variance function to the results obtained at the aggregated level (Vanmarcke, 1983).

For homogeneous regions, the spatial correlation function of soil reflectance can also be retrieved using the covariance equation (6.4) which, in Case II, reduces to,

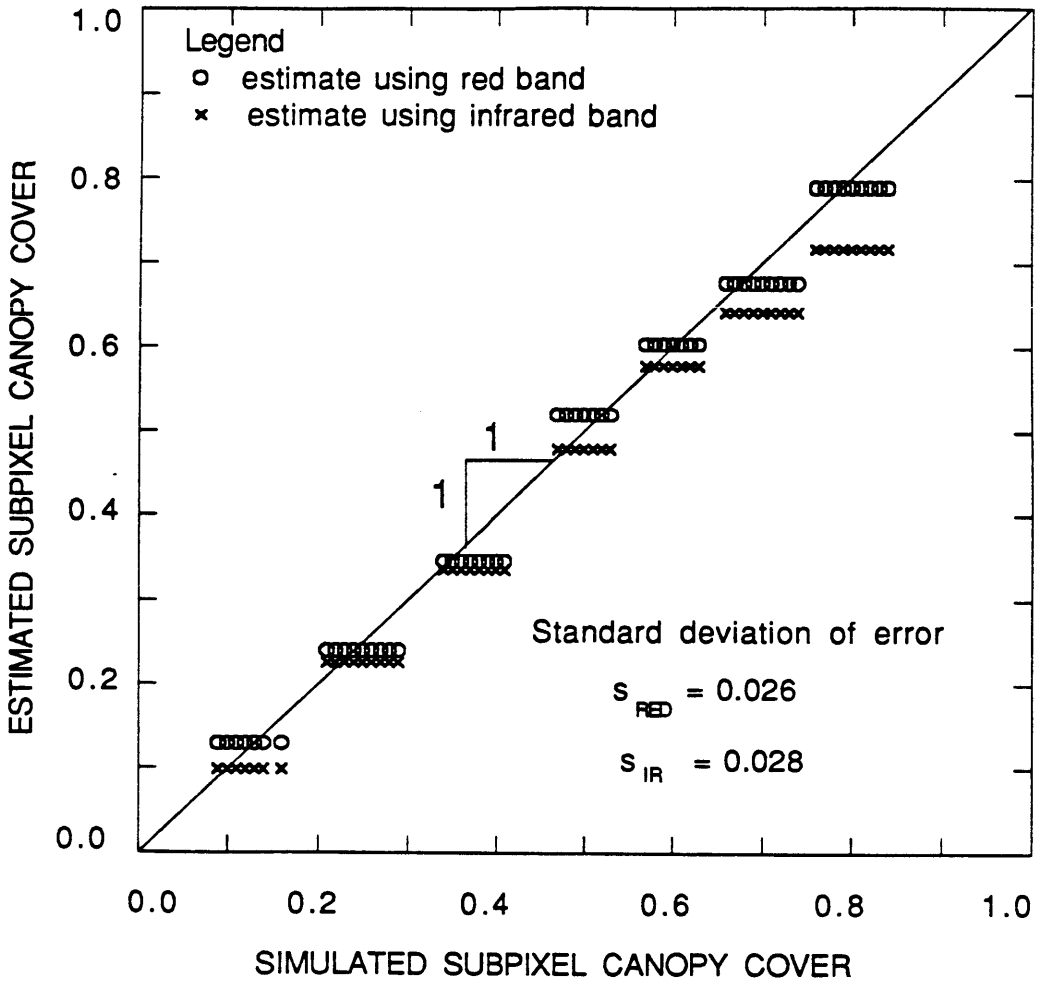

Figure 7.1 Estimated versus simulated canopy cover Case II simulation.

Table 7.1
Comparison of Simulated and Estimated Scene Parameters
Cases II and V, m = 0.40

Parameter	Units	CASE II Simulated Value	CASE II Estimated Value	CASE V Simulated Value	CASE V Estimated Values Method 1	CASE V Estimated Values Method 2
Reflectance Parameters						
$R_m(\lambda_{RED})$	%	15.0	15.7	15.0	22.2	14.8
$R_m(\lambda_{IR})$	%	40.0	40.6	40.0	51.3	39.8
$R_{g_s}(\lambda_{RED})$	%	....	....	0.0	0.0†	0.0†
$R_{g_s}(\lambda_{IR})$	%	....	....	0.0	0.0†	0.0†
$E[R_{g_I}(\lambda_{RED})]$	%	15.0	15.0	15.0	15.3	15.3
$E[R_{g_I}(\lambda_{IR})]$	%	20.0	20.0	20.0	20.3	20.3
$VAR[R_{g_I}(\lambda_{RED})]$, level 10	$\%^2$	4.8	5.3	4.8	3.3	...
$VAR[R_{g_I}(\lambda_{RED})]$, level 30	$\%^2$	....	....	3.0	....	3.0
$VAR[R_{g_I}(\lambda_{IR})]$, level 10	$\%^2$	4.8	5.3	4.8	3.3	....
$VAR[R_{g_I}(\lambda_{IR})]$, level 30	$\%^2$	....	....	3.0	....	3.0
Geometric Parameters						
Canopy Area, A_t	m^2	1.0	....	1.0	0.85	....
Similarity Parameter, η		0.0	....	2.0	2.2	2.0
Sampling Scale Ratio, S			∞		50	450
Soil Line Parameters						
Spatial Correlation Length Scale	m	20.0	21.0			
Soil Line Equation	%		$R_{g_I}(\lambda_{IR}) = 1.0\ R_{g_I}(\lambda_{RED}) + 5.0$			

†Assumed value

$$\text{COV}_x[R(\lambda,\underline{x}),R(\lambda,\underline{x}')] = \left[E[g_I]^2 + \text{VAR}[m]\right] \text{COV}_x[R_{g_I}(\lambda,\underline{x}),R_{g_I}(\lambda,\underline{x}')] + \text{VAR}[m]\left[R_m(\lambda) - E[R_{g_I}(\lambda,\underline{x})]\right]^2 \quad (7.3)$$

Two steps are required. First, the sample spatial covariance of soil reflectance, $\text{COV}_x[R_{g_I}(\lambda,\underline{x}),R_{g_I}(\lambda,\underline{x}')]$, must be determined by computing (7.3) at different lags, $\underline{x} - \underline{x}'$. The sample spatial correlation function is then obtained from

$$\rho_{R_{g_I}(\lambda)}(\underline{x} - \underline{x}') = \frac{\text{COV}_x\left[R_{g_I}(\lambda,\underline{x}),R_{g_I}(\lambda,\underline{x}')\right]}{\text{VAR}\,[R_{g_I}(\lambda,\underline{x})]} \quad (7.4)$$

to which an appropriate function can be fitted if an analytical relationship is desired.

The correlation function for Case II was estimated by applying the above procedure to the eight different segments (representing eight values of m) of the red and infrared scenes. The results are shown in Figure 7.2 and Table 7.2. Figure 7.2 shows a comparison of i) the sample correlation of the simulated bare soil reflectance in the red band at the 10–meter level of resolution and ii) the estimated soil reflectance correlations using (7.3) and (7.4) for a range of m's (14, 40, and 57%) at lags of 10, 20, 30 and 40 meters. The good agreement between the simulated and estimated correlations, as indicated in Figure 7.2, was typical for all values of m in the red band, but poor for the IR band for m greater than about 50%.

The estimated soil reflectance length scales for each value of m, assuming an exponential correlation, are shown in Table 7.2 for both the red and infrared bands. Overall, the estimated values compare favorably with the actual simulated

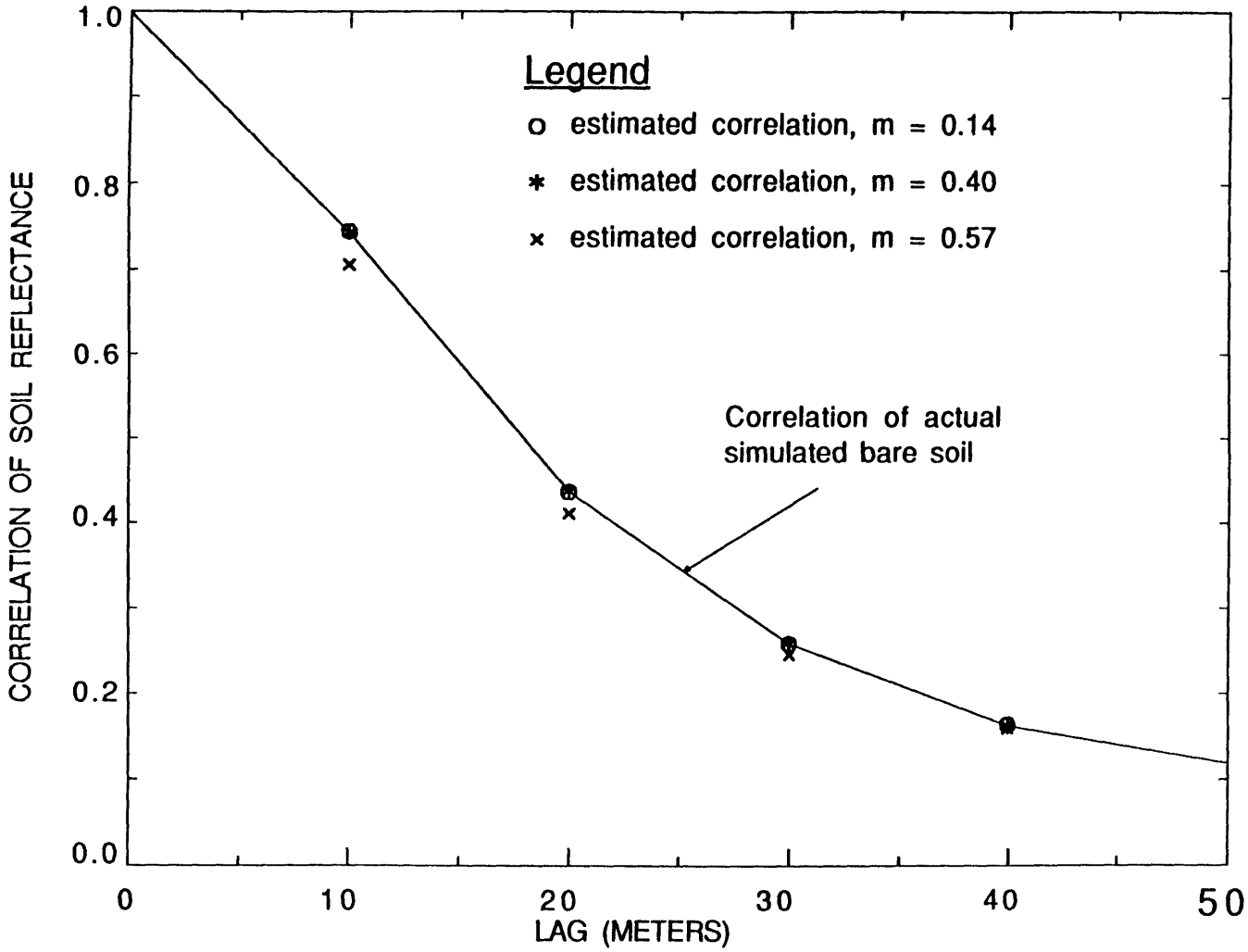

Figure 7.2 Estimated soil reflectance spatial correlation compared to sample soil reflectance correlation, Case II, red band, level 10 aggregation.

Table 7.2

Estimated Soil Reflectance Length Scale

Level 10 Aggregation

Simulated Length Scale = 20 m

Fractional Canopy Cover	Case II		Case V	
	IR	RED	IR	RED
	(m)	(m)	(m)	(m)
0.05	20.6	21.4	21.2	20.7
0.14	16.8	21.3	18.4	20.5
0.26	22.5	21.0	12.3	13.7
0.39	18.4	21.0	—	14.9
0.51	20.0	21.3	—	—
0.52	12.2	21.2	—	—
0.63	11.3	21.07	—	—
0.78	18.3	20.3	—	—

value (20 m), although the agreement is better for the red band. In the infrared band, the length scales are not retrieved as well at higher values of m. That is due to the greater difference in the reflectances of the vegetation and soil in the IR band, as compared to the red band.

7.2 Inversion of Case V

For the Case V simulation, equation (6.16) yields $\eta = 2.0$. Two different approaches are presented for estimating the Case V parameters, depending on the magnitude of the sampling scale ratio, S_p, defined in (6.23). A first approach (Method 1), applicable for all ranges of S_p, consists of solving the full set of moment equations simultaneously for different statistically homogeneous regions. The second procedure (Method 2), applicable only for large S_p in which (6.18) is true, utilizes a simpler approximate set of moment equations and one's knowledge of the structure of the scattergram.

7.2.1 Estimation of Parameters, Method 1: $S_p \gg 10$

The introduction of shadows in Case V adds to the complexity of inverse problem in several ways. First, it increases the number of cover types to three (e.g., illuminated canopy, illuminated soil background, and shadowed soil background) as well as the number of associated reflectance terms in both bands. Additionally, the covariance among the three cover types must be considered in the analysis.

At the level 10 aggregation, the sampling scale ratio, S_p, is only $\frac{100}{2 \cdot 1} \gg 10$. Since (6.24) is not valid for such small S_p, pixels with different amounts of vegetation cover can occupy the same location in the scattergram, previously shown in Figure 5.9b. The assumption of constant canopy cover for pixels

oriented parallel to the soil line does not apply (except for the soil line itself in which m = 0). Thus, unlike Case II, subsets of pixels required for the analysis can not be identified on the basis of the scattergram.

When segments of the scene can be assumed statistically homogeneous, however, the following conditional moments can be written for the set of pixels located in each region. The mean reflectance equation is,

$$E[R(\lambda,\underline{x})] = E[m]R_m(\lambda) + E[g_S]R_{g_S}(\lambda) + E[g_I]E[R_{g_I}(\lambda,\underline{x})] \qquad (7.5)$$

The variance equation now includes the variances and covariances of the individual cover types, or

$$\begin{aligned} VAR[R(\lambda,\underline{x})] &= E[g_I]^2 VAR[R_{g_I}(\lambda,\underline{x})] + R_m(\lambda)^2 VAR[m] + E[R_{g_I}(\lambda,\underline{x})]^2 VAR[g_I] \\ &+ VAR[g_I]VAR[R_{g_I}(\lambda,\underline{x})] + R_{g_S}(\lambda)^2 VAR[g_S] - 2R_m(\lambda)E[R_{g_I}(\lambda,\underline{x})] \cdot \\ &\left\{VAR[m] + COV[m,g_S]\right\} + 2R_m(\lambda)R_{g_S}(\lambda)\, COV[m,g_S] \\ &- 2E[R_{g_I}(\lambda,\underline{x})]R_{g_S}(\lambda)\left\{VAR[g_S] + COV[m,g_S]\right\} \end{aligned} \qquad (7.6)$$

The cross covariance between any two spectral bands is written,

$$
\begin{aligned}
\mathrm{COV}[R(\lambda_{RED},\underline{x}),R(\lambda_{IR},\underline{x})] &= \mathrm{VAR}[m]R_m(\lambda_{RED})R_m(\lambda_{IR}) \\
&+ E[g_I^2]\mathrm{COV}[R_{g_I}(\lambda_{RED},\underline{x}),R_{g_I}(\lambda_{IR},\underline{x})] \\
&+ \mathrm{VAR}[g_I]E[R_{g_I}(\lambda_{RED},\underline{x})]E[R_{g_I}(\lambda_{IR},\underline{x})] + \mathrm{VAR}[g_S]R_{g_S}(\lambda_{RED})R_{g_S}(\lambda_{IR}) \\
&- \left\{R_m(\lambda_{RED})\ E[R_{g_I}(\lambda_{IR},\underline{x})] + R_m(\lambda_{IR})E[R_{g_I}(\lambda_{RED},\underline{x})]\right\} \\
&\cdot \left\{\mathrm{VAR}[m] + \mathrm{COV}[m,g_S]\right\} \\
&+ \left\{R_m(\lambda_{RED})\ R_{g_S}(\lambda_{IR}) + R_m(\lambda_{IR})\ R_{g_S}(\lambda_{RED})\right\}\ \mathrm{COV}[m,g_S] \\
&- \left\{E[R_{g_I}(\lambda_{RED},\underline{x})]R_{g_S}(\lambda_{IR}) + E[R_{g_I}(\lambda_{IR},\underline{x})]R_{g_S}(\lambda_{RED})\right\} \\
&\cdot \left\{\mathrm{VAR}[g_I] + \mathrm{COV}[m,g_S]\right\} \qquad (7.7)
\end{aligned}
$$

The derivation of (7.5), (7.6), and (7.7) are given in Appendix C. The moments of the percent cover variates can be written,

$$E[m] + E[g_I] + E[g_S] = 1 \qquad (7.8)$$

$$\mathrm{VAR}[m] + \mathrm{VAR}[g_S] - \mathrm{VAR}[g_I] + 2\mathrm{COV}[m,\ g_S] = 0 \qquad (7.9)$$

for a total of seven conditional moment equations when (7.5) and (7.6) are written for two bands. The addition of the five soil line equations, i.e., (6.9) and (6.10) written for both bands, and (7.7) written for m = 0, brings the total to twelve. The unknowns include i) the means and variances of the three cover types plus $\mathrm{COV}[m,g_S]$, ii) the vegetation and shadowed reflectances written for both bands, iii) the mean and variance of the illuminated soil for both bands, and the illuminated soil reflectance spectral cross covariance. The number of unknowns is 16.

The solution procedure is, first, as in Case II, to obtain the four illuminated soil reflectance moments using (6.9) and (6.10). The cross covariance of the soil reflectance is also directly obtained from those moments or, equivalently, from conditioning (7.7) along the soil line.

Since there are still four more unknowns than equations, additional assumptions of i) Poisson spatial distribution and ii) geometric similarity of the plants are required. Those assumptions introduce two unknowns, η and A_t, but provide four additional equations, namely (6.14), (6.17), and

$$\text{VAR}[g_I \,|\, \text{Poisson}] = h_2\{E[g_I], \eta, A_t, A_P\} \tag{7.10}$$

and

$$\text{COV}[m, g_S] = h_3\{E[m], \eta, A_t, A_P\} \tag{7.11}$$

Graphs of h_1 (equation 6.14), h_2, and h_3, are shown in Figure 7.3 for the Case V simulation, level 10 aggregation.

The covariance between m and g_s was obtained in the following manner. It was observed during the simulations that the correlation between m and g_s could be approximated by a stepwise linear function of m, as shown in Figure 7.4. The expression for $\text{COV}(m, g_s)$ in (7.11) and Figure 7.3 was obtained by combining (7.9) and the definition of correlation, or

$$\rho_{m,g_S} = \frac{\text{COV}(m, g_S)}{[\text{COV}(g_S)\,\text{VAR}(g_I)]^{0.5}} \tag{7.12}$$

where

$$\begin{aligned}
\rho &= 1.00 - 0.50E[m] && \text{for } 0.00 < E[m] \leq 0.10 \\
\rho &= 1.28 - 3.27E[m] && \text{for } 0.10 < E[m] \leq 0.65 \\
\rho &= -0.57 - 0.43E[m] && \text{for } 0.65 < E[m] \leq 1.00
\end{aligned} \tag{7.13}$$

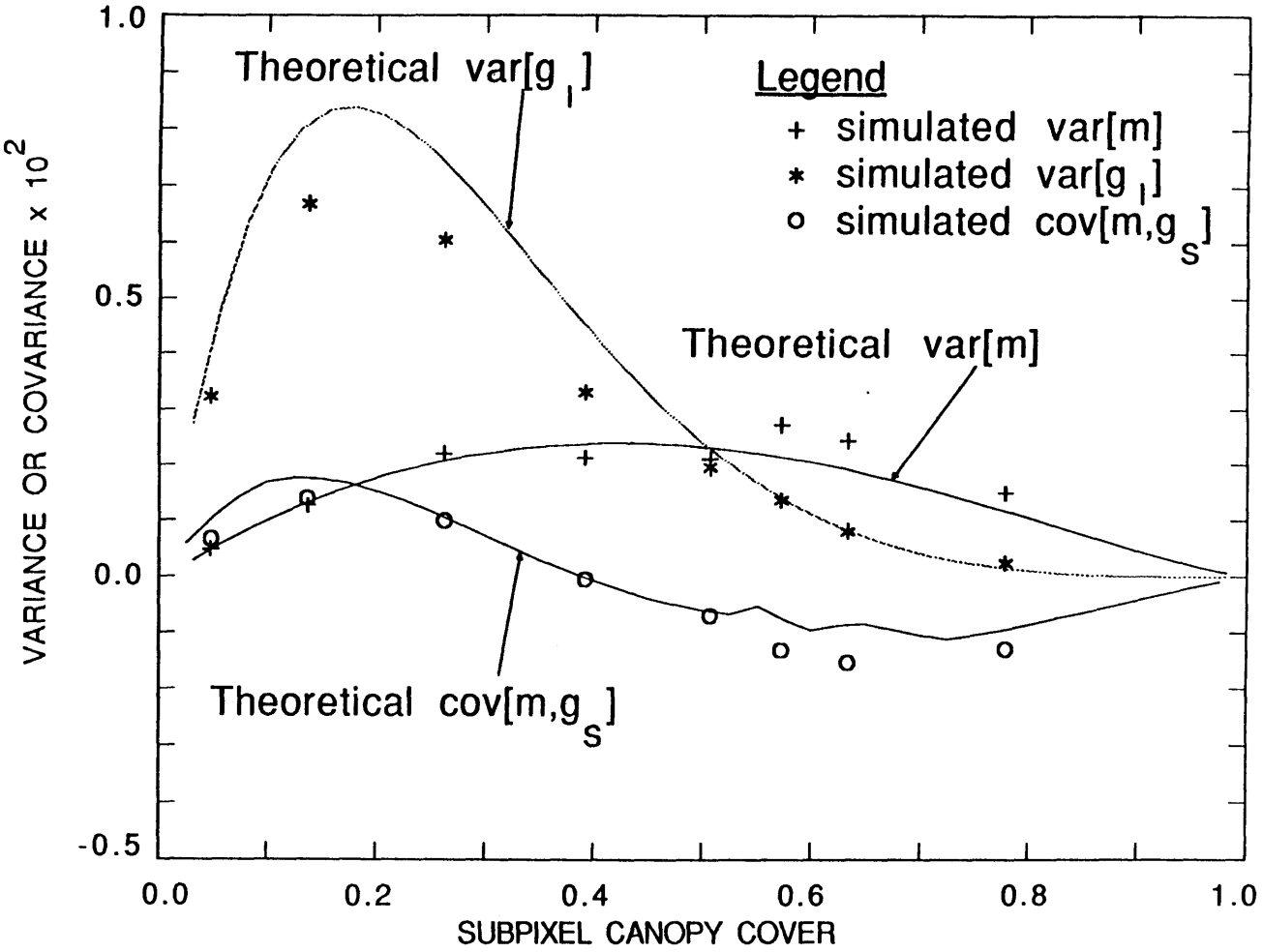

Figure 7.3 Graphs of empirical functions h_1(var[m]), h_2 and h_3 Case V simulation, level 10 aggregation.

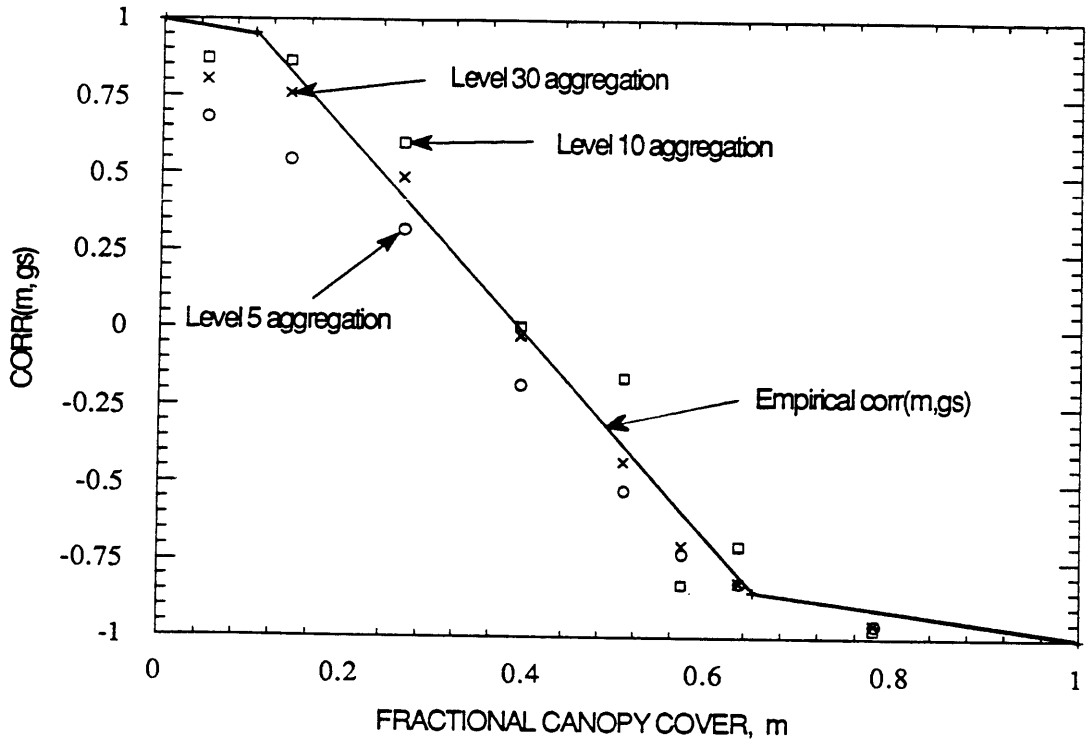

Figure 7.4 Functional relationship of ρ_{m,g_s} versus m for Case V simulation.

in order to yield the following semiempirical expression

$$0 = \frac{COV^2(m,g_s)}{2\rho\ VAR^2(m)} + cov(m,g_s) - \frac{VAR^2(g_I) - VAR^2(m)}{2} \tag{7.14}$$

which can be solved by iteration for $COV(m,g_s)$.

Since there are still two more unknowns than equations, the solution to the inverse problem can be obtained in one of two manners. One approach is to choose two different homogeneous regions, and to write conditional moment equations for those two regions. Each segment adds seven unknowns (the cover moments), but provides nine equations ((6.14), (6.17), and (7.5) through (7.9), with (7.5) and (7.6) written for two bands), for a net gain of two. Thus, theoretically, the parameters can be obtained by simultaneously solving 25 conditional moment equations simultaneously.

A second, more practical approach in some cases is to assume that $R_{g_S}(\lambda)$ in equations (7.5), (7.6) and (7.7) is negligible compared to the other terms. That assumption is only valid for i) relatively clear atmospheric conditions when the diffuse radiation is small, ii) low zenith angles (i.e., small η), and iii) bands in which the vegetation and illuminated soil reflectances are both much greater than the shadowed soil reflectance. The third condition is generally true for most red bands, and for near–infrared bands when the extinction due to leaf area is large. The solution can thus be obtained using one set of conditional moment equations applicable to one homogeneous region.

Due to the complexity of the equations, the solution to the Case V, Method 1 inverse problem can not be solved explicitly. Instead, it is obtained by minimizing the sum of the squared errors between the theoretical and sample

moments. The procedure involves iteration over E[m], A_t, and η until the minimum error is obtained.

Since the complete set of equations is non–linear, in order to avoid local minimum solutions, the global solution is obtained by solving the problem over a range of reasonable initial values and iteration steps. The computer code for the Case V, Method 1 inverse problem is provided in Appendix D.

The results of applying the second approach to the level 10 aggregation of Case V are shown in Figure 7.5 and Table 7.1. The procedure provides estimates of only the mean values for each statistically homogeneous area. The results indicate that the values of the estimated mean vegetation cover compare reasonably well to the simulated mean values (the standard deviation of error, s = 0.056). The reflectances are also fairly well recovered, although λ and A_t are not.

The length scales of the spatial correlation function of soil reflectance were also computed for Case V – Method 2 using (7.3) and (7.4) for various m's. The results, shown in Table 7.2 indicate that the retrieval of such length scales was only possible for low values of m. The poor retrieval is a result of the large amount of shadow which masks the soil background in this simulation at large m's.

7.2.2 Estimation of Parameters, Method 2: $S_P >> 10$

At the level 30 aggregation, S_P equals $\frac{900}{2 \cdot 1} >> 10$. At such large S_P, an approximate functional relation occurs among g_I, g_S and m as shown in (6.18). Since the simulated canopy reflectance is also constant, then pixels with different amounts of canopy cover will orient themselves parallel to the soil line as described in Sections 5.4 and 6.2.4, and shown in Figure 7.6. Thus, the inverse procedure for large S_P makes use of that knowledge by formulating approximate

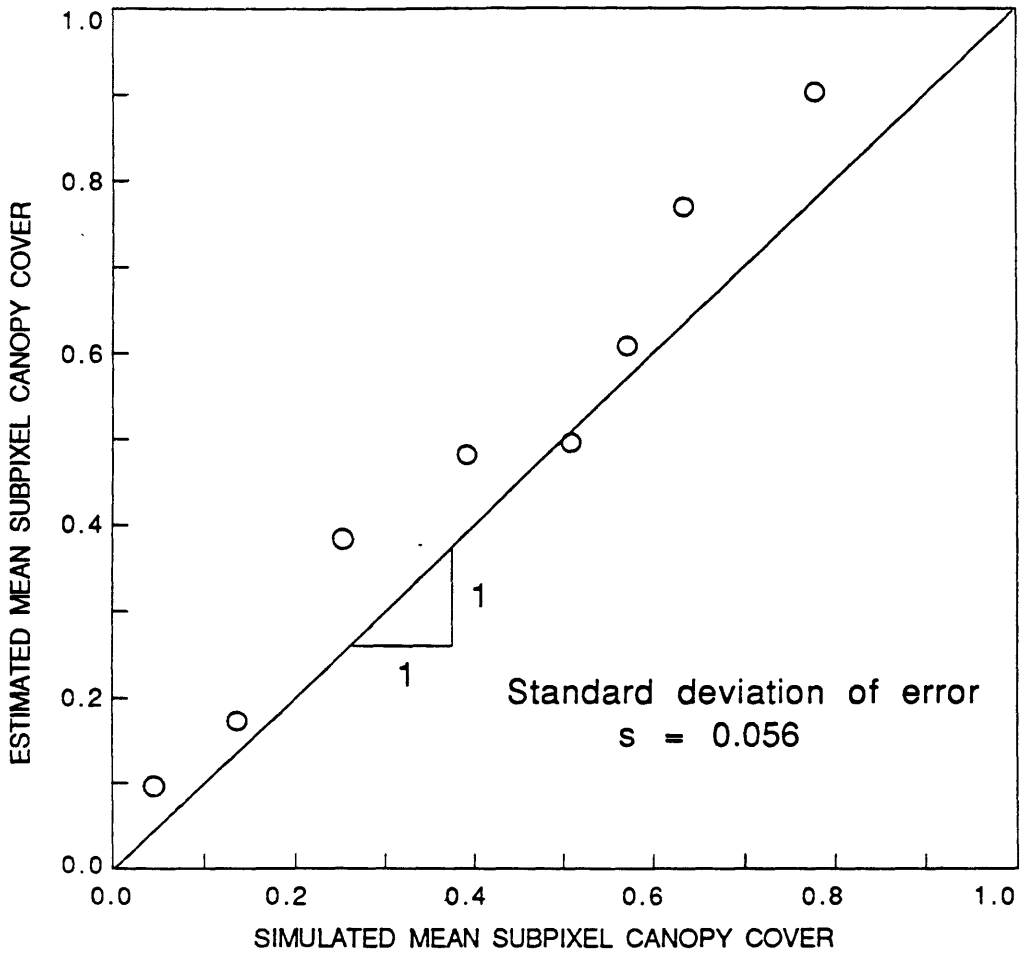

Figure 7.5 Estimated mean versus simulated mean subpixel canopy cover, Case V simulation, level 10 aggregation.

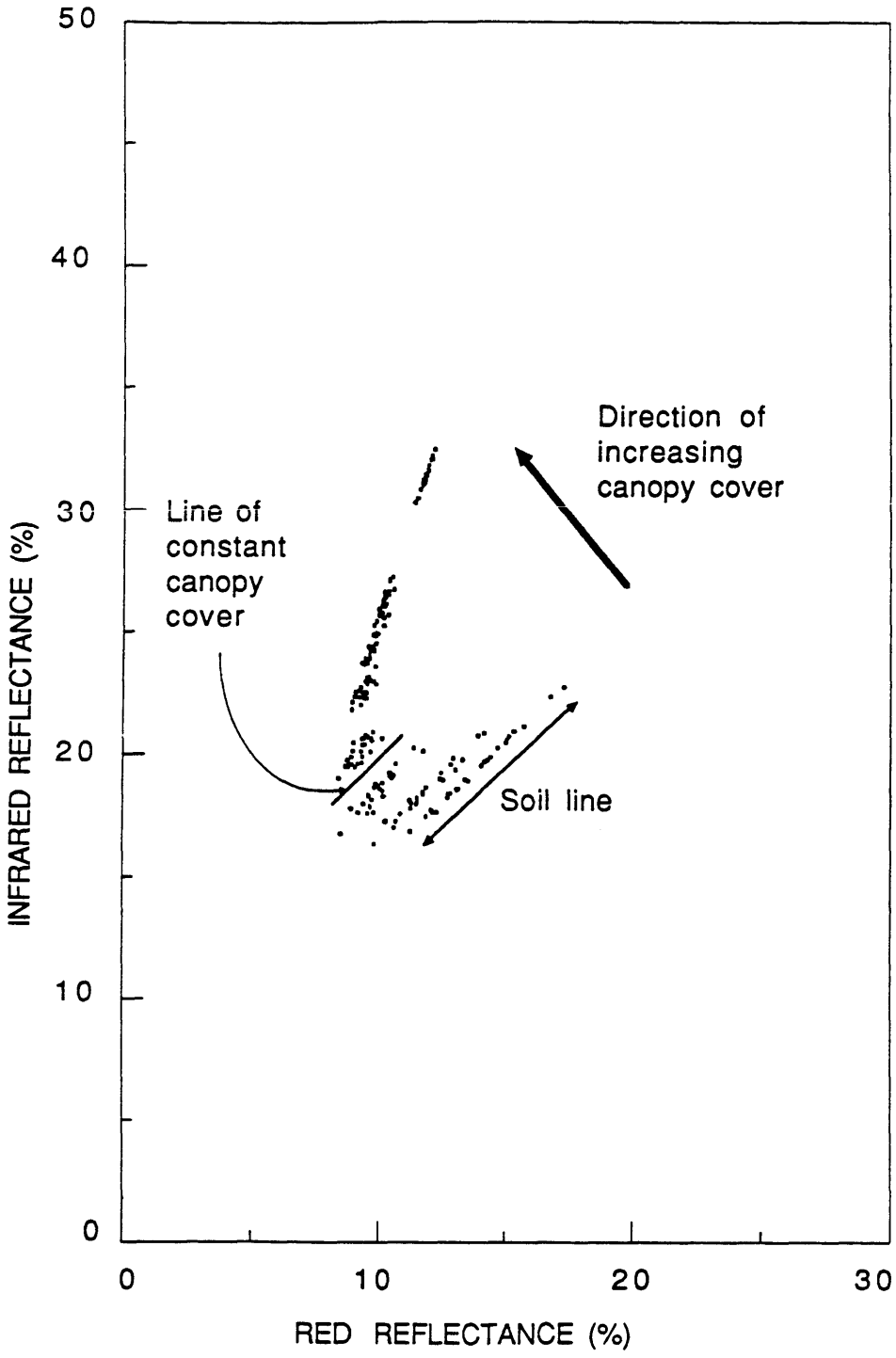

Figure 7.6 Indication of direction of increasing canopy cover, Case V simulation, level 30 aggregation (method 2).

conditional moments for individual subsets of pixels which lie along those parallel lines.

As in Case II, once the appropriate set of pixels needed for the conditional sample moments are determined from the scattergram, the parameter estimation can proceed using only one band. For each arbitrarily chosen parallel line, there are seven unknowns including i) the three fractional covers m, g_I, and g_S, ii) two constant reflectance terms, $R_m(\lambda)$, $R_{g_S}(\lambda)$, and iii) the mean and variance of the soil reflectance, $E[R_{g_I}(\lambda,\underline{x})]$, and $\mathrm{VAR}[R_{g_I}(\lambda,\underline{x})]$, respectively. The available conditional moment equations are i) the two soil line equations, (6.9) and (6.10), ii) the conditional mean reflectance, (6.19), and iii) the variance as provided in (6.20). It is noted that (6.20) is obtained directly from (7.6) by assuming that the variances of the fractional covers are negligible. In addition, the percent cover equation, (5.7), gives,

$$m + g_S + g_I = 1 \tag{7.15}$$

for a total of only five equations, two less than the number of unknowns. The above formulation only allows several terms to be retrieved. For instance, the soil line moments can be obtained as in the previous examples. Then, by selecting an arbitrary locus of pixels parallel to the soil line, g_I can be solved directly using (6.20). However, close examination of (6.19) reveals that m cannot be determined using only the above equations.

The remaining terms can be obtained by first assuming Poisson spatial distribution and geometric similarity of the plants. Those two assumptions permit one to use (6.24), for a total of six equations, although an additional unknown, η, is introduced. Since there are still two more unknowns than equations, the deficit

is made up in one of two ways. One approach is to arbitrarily choose two additional parallel lines (for a total of three) for which the above conditional moments apply. Each additional line introduces three new unknowns (m, g_S, and g_I), but augments the number of equations by four (equations (6.19), (6.20), (6.24), and (7.15)). Thus, m for each line is obtained by first solving for g_I for all three parallel lines using (6.20), and then solving the remaining moment equations simultaneously. While this approach is theoretically correct, its validity is limited to scenes which possess a large number of pixels in at least three different homogeneous regions.

As in Method 1, a second approach is to assume that the shadowed reflectance term in (6.19), $g_S R_{g_S}(\lambda)$, is negligible compared to the other two illuminated terms. That assumption eliminates the need to calculate $R_{g_S}(\lambda)$ and the analysis can be conducted using only two parallel lines.

The results of the second approach are summarized in Figures 7.7 and 7.8 and Table 7.1. Figure 7.7 contains plots of the estimated canopy cover versus the simulated values for each pixel contained in each of five conditional lines, using both the red and infrared bands. The standard deviation of error s, is 0.028 in the red band and 0.069 in the infrared band. Although the agreement is very good, Figure 7.7 indicates that the estimated values are generally lower than the simulated values, especially at higher values of m. That difference is due to the error associated with neglecting the cover variance terms in (7.6). The error is greater for estimates made using the infrared band since the magnitudes of the infrared reflectances are greater than those in the red band.

Figure 7.8 indicates equally good agreement between the simulated values of $g_I(m)$ and $g_S(m)$ and the theoretical curves using (6.24), (7.15) and the mean

estimated value of η. The simulated and estimated reflectance terms also compare favorably, as shown in Table 7.1.

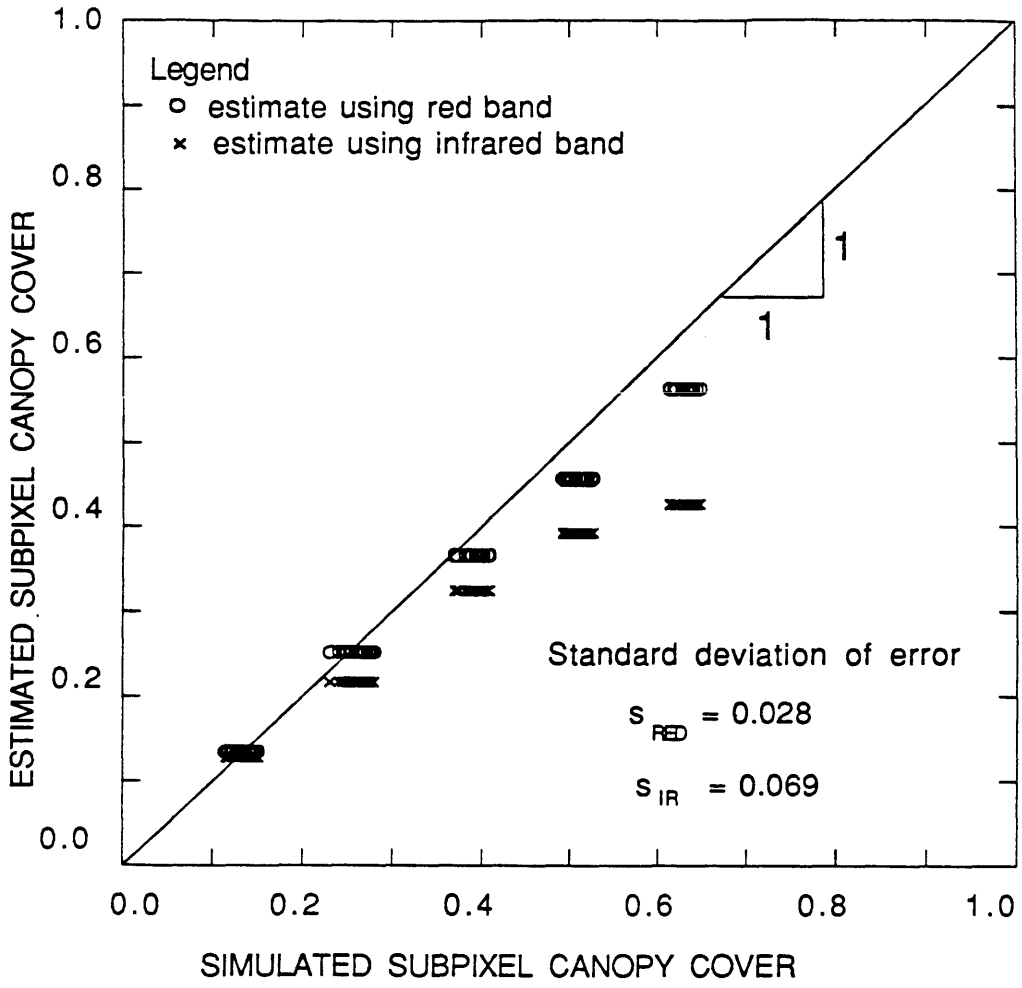

Figure 7.7 Estimated versus simulated subpixel canopy cover, Case V simulation, level 30 aggregation (method 2).

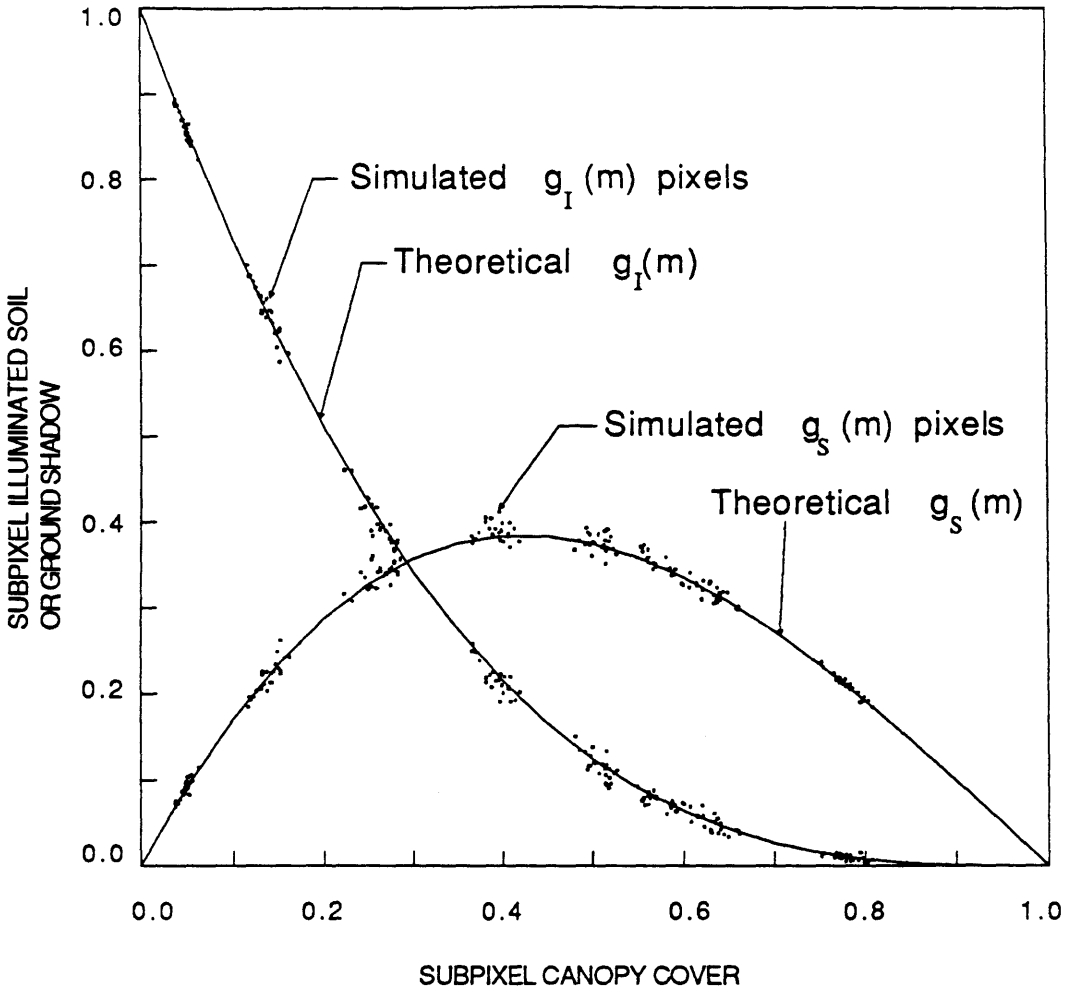

Figure 7.8 Comparison of simulated values of illuminated and shadowed soil fractional cover versus canopy cover, to the theoretical curves using equations (6.24) and (7.15), Case V simulation, level 30 aggregation.

Chapter 8

CASE STUDIES

This chapter examines the application of the canopy reflectance model to actual multispectral data obtained over two field sites. The first site is a pecan orchard in southern Arizona for which actual aerial radiometric data were obtained. The second site is a pinyon–juniper watershed in northern Arizona for which both aerial and satellite multispectral data (Landsat TM data) were obtained. Atmospheric effects on the subpixel estimates are examined using hypothetical values of backscattered solar diffuse radiation.

8.1 Scattergram of a Pecan Orchard

The pecan orchard represents a special case of the canopy reflectance model in which the trees are spatially distributed in a fixed geometric fashion and the only random property is the soil background reflectance. In this example, a visual comparison is made between the plots of the radiometric data in the red–infrared reflectance space, and a hypothetical scattergram constructed from ground truth measurements at the time of overflight. The moment analysis is not applied to the estimation of subpixel cover due to the limited number of pixels. Rather, a qualitative comparison of the theoretical and estimated canopy cover is made.

8.1.1 Site Description

The study site is located within a flat one mile square area near Maricopa, Arizona, about 40 km south of Phoenix. Aerial radiometric measurements were collected at an altitude of about 150 meters at 9:30 a.m. on June 12, 1988, as part

of the MAC (Maricopa Agricultural Center) III Experiment organized by the Water Conservation laboratory, Agricultural Research Service, Phoenix, Arizona. During the experiment, there were no clouds, and the air could be qualitatively described as clear and dry.

The orchard itself consisted entirely of pecan trees planted on a square grid in an east–west orientation, with center intervals of approximately 85 meters. The diameter of individual trees ranged from about 5 to 10 meters ($A_t \simeq 20 - 80$ sq.m.), with a height to depth ratio of about unity. Tree height was generally constant in any given section of the orchard, and thus, tree canopies were not significantly shadowed by adjacent trees. The size of the trees and, thus, the amount of canopy cover, could vary from pixel to pixel. Trees were interspersed with a combination of bare soil and senesced grasses.

8.1.2 Reflectance Data

Radiometric observations were made using an Exotech radiometer with Thematic Mapper red (0.62–0.69 μm) and infrared (0.78–0.90μm) filters at a ground resolution of about 40 meters ($A_p \simeq 1250$ sq.m.). The solar angle was estimated to be 43.5° at the time of overflight.

Radiometric observations over the pecan orchard were converted to reflectance factors (ratio of target reflectance to the reflectance of a Lambertian surface; See Jackson et al, 1987) by Moran (1988). The reflectance factors are proportional to and approximately equal to the target reflectance, and thus for simplicity, they will be termed reflectance throughout this section.

Ground truth values of the pecan canopy's bulk reflectance could not be easily obtained due to the large size of the trees. However, the aerial observations

over nearly continuous canopies indicate that the bulk canopy reflectance is about 2 – 4% in the red band and 45 – 55% in the IR band. The mid-points of those values (canopy red reflectance = 3.0%; canopy IR reflectance = 50%) were arbitrarily chosen as estimates of the canopy reflectances. Shadowed reflectances were assumed to equal 10% of the canopy reflectances.

Since no treeless pixels existed in the orchard itself, the soil reflectance and the soil line was obtained by sensing bare soil fields (Maricopa field No. 18, 27, 1nd 32) immediately adjacent to the orchard which contained a mixture of bare soil and senesced grasses. The soil line obtained from a red–infrared plot of the data is shown in Figure 8.1. The line exhibits a nearly linear relationship as described in equation (3.5). The mean, standard deviation, and covariance length scale (computed as the average e–folding distance of the empirical correlation function) of those soil pixels, together with the parameters of the soil line are provided in Table 8.1.

8.1.3 Fractional Cover Estimates

As a substitute for ground truth, independent estimates of fractional cover were made by analyzing the histograms of the digitized multispectral video images for each of four radiometric observations. Because the length scale of the canopy is several meters, and the length scale of the video pixel is only about one–half meter, a majority of the pixels will be approximately pure canopy, pure shadow, or pure illuminated soil pixels. As a result, if the reflectance of each cover type is unique, a histogram of the digitized video image should possess local modes corresponding to each of the different cover types. The percentage of pixels associated with each mode approximates the amount of a particular fractional

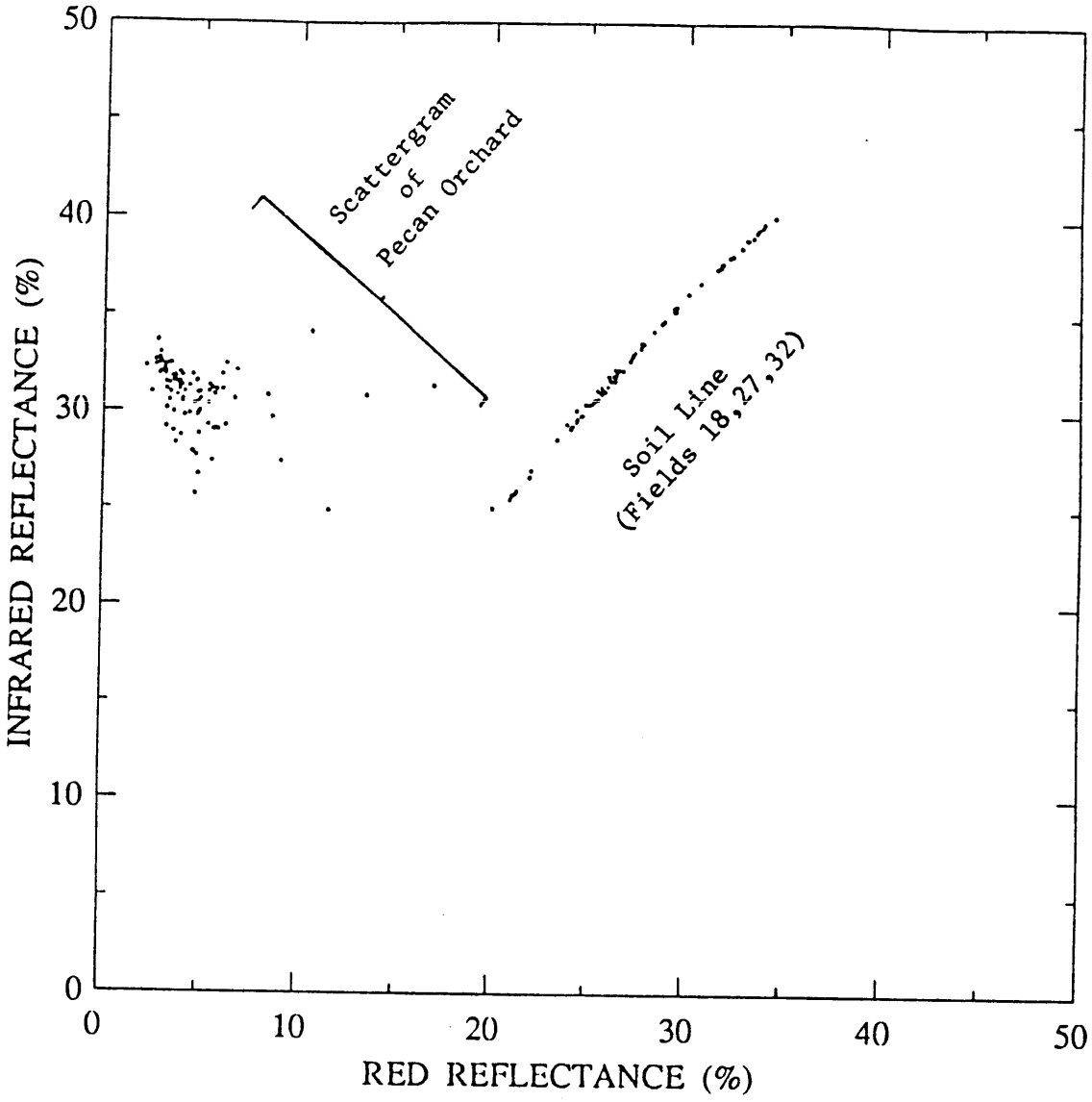

Figure 8.1 Red–infrared scattergram of pecan orchard and bare soil.

Table 8.1

Soil Line Parameters of Pecan Orchard

	Red TM Band (0.62– 0.69 μm)	Infrared TM Band (0.78– 0.90 μm)
Mean Reflectance (%)	27.3	32.8
Standard Deviation of Reflectance (%)	3.7	4.1

Soil Line Equation (%): $R_{g_I}(\lambda_{IR}) = 1.09\ R_{g_I}(\lambda_{RED}) + 3.06$

Covariance Length Scale $\simeq$ 200 meters

cover, depending on the wavelength.

For example, Figure 8.2 contains the red and infrared histograms of one video image (time = 9.3969 hours) for which a radiometric observation was simultaneously made. In the red image, trees and shadows appear very dark, while the soil is bright. The corresponding red histogram exhibits a strong bimodal shape, with a local minimum occurring at an intensity level of 89. Thus, intensity levels less than 89 (31 %) are assumed to represent pixels containing primarily vegetation and shadow. Pixels greater than 89 are assumed to represent illuminated soil (69 %).

For the infrared image, only the shadows appear dark while both trees and soil are bright. Since the amount of shadow is small, a strong bimodal effect is not observed in the histogram, although a slight trough is observed at an intensity level of about 128. As a result, pixels with intensity < 128 are assumed to represent shadow (12%), while pixels with intensity > 128 represent vegetation and illuminated soil (88%). Combining the results of the histogram analysis for both bands yields estimates of fractional cover for the vegetation (19%), shadow (12%), and illuminated soil (69%), for the single radiometric observation. Quantitative estimates obtained in the above manner were confirmed by visual examination of the video image.

8.1.4 Comparison of Actual and Hypothetical Scattergrams

The hypothetical scattergram is obtained by first conceptualizing the orchard as a stochastic geometric surface, in which the only variables are the fractional canopy cover and the soil reflectance. The hypothetical reflectance of a pixel was

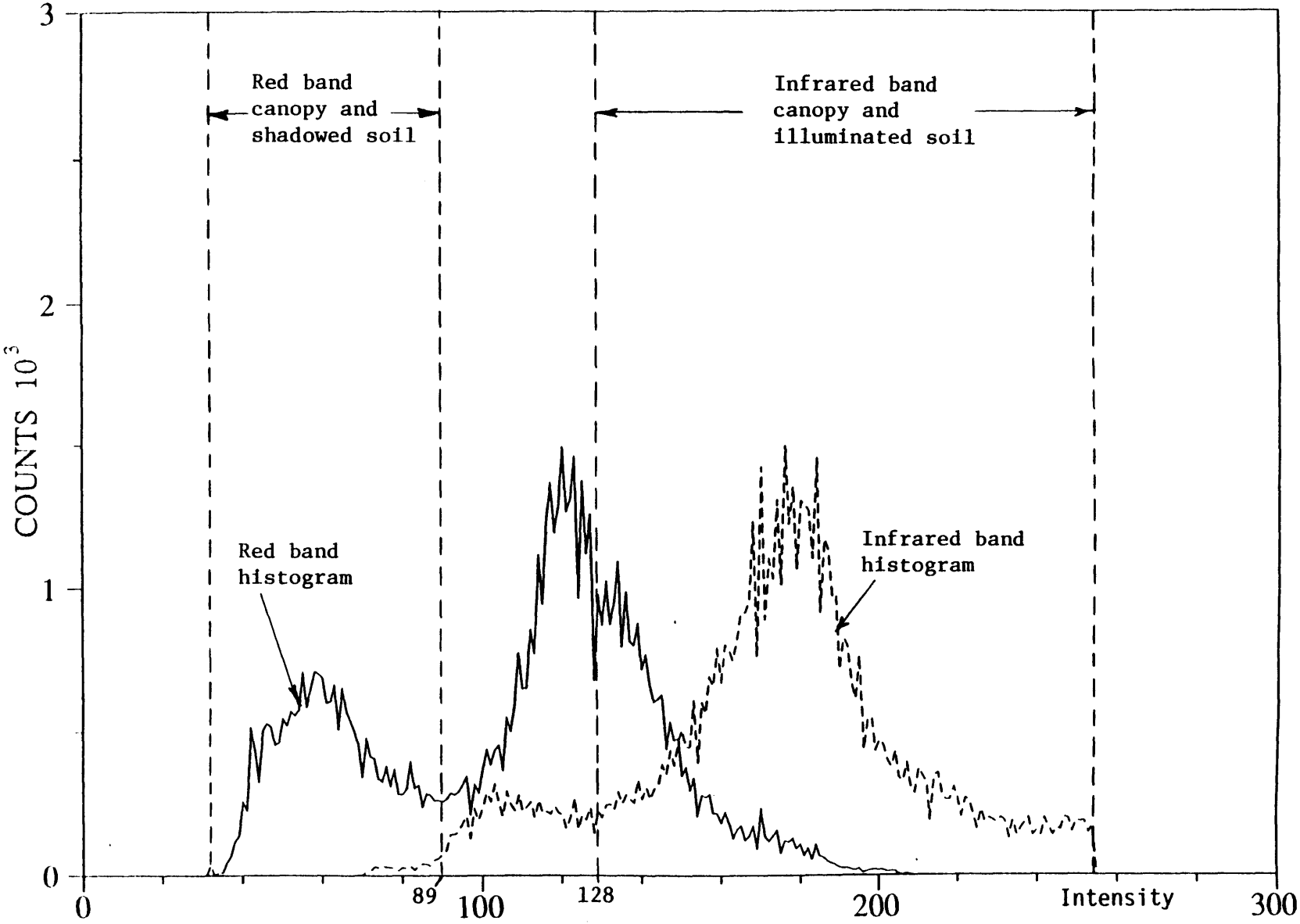

Figure 8.2 Histograms of red and infrared video images of identical area over pecan orchard, Day 164, 9.3.69 hours.

assumed to be

$$R(\lambda) = mR_m(\lambda) + g_s R_{g_s}(\lambda) + g_I R_{g_I}(\lambda,\underline{x}) \tag{8.1}$$

where $R_m(\lambda)$, $R_{g_s}(\lambda)$ and $R_{g_I}(\lambda,\underline{x})$ represent estimated ground truth reflectances of the illuminated canopy, shadowed soil, and illuminated soil, respectively.

The next step is the calculation of the sampling scale ratio for regular geometries, S_G, based on the similarity parameter. Visual observations at the time of the experiment indicated that the trees could best be represented by circular cylinders, and that they were approximately geometrically similar. From Table 6.1,

$$\eta = \frac{4H}{\pi D} \tan \theta \tag{8.2}$$

Inserting the parameters of the experiment (θ = 43.6 degrees, H/D $\simeq$ 1) into the above equation yields η = 1.21. The sampling scale ratio for geometric distributions is

$$S_G = A_p/\eta A_t \simeq 13 - 50 \tag{8.3}$$

Thus, based on the criterion given in (6.26) for geometric distributions, since $S_G >> 1$, the assumption of large Sampling Scale Ratio is made.

The assumption of i) geometric similarity and ii) large sampling scale allows one to formulate a unique analytical relationship among the fractional covers as described in Section 6.2.4. For the particular orchard described above, two

different shadow regimes can be identified. Regime I occurs when the trees are small and the entire shadow cast by a tree is observed. In this case the fractional shadowed area g_s is linearly related to the fractional canopy cover, m or

$$g_s = \frac{4\mu m}{\pi f} ;$$

$$\text{for} \quad 2\sqrt{\frac{m}{\pi}}\left[1 + \frac{\mu}{f}\right] - 1 < 0 \tag{8.4}$$

where μ equals the tangent of the zenith angle and f is a similarity parameter equal to the ratio of canopy diameter to tree height. Regime II occurs for larger trees when the shadow cast by one tree extends far enough as to be overlapped, in part, by the canopy of an adjacent tree. A second term is added to the above equation to account for that decrease in shadowed area, or

$$g_s = \frac{4\mu m}{\pi f} - 2\left\{\frac{m}{\pi}\cos^{-1}\left[\frac{1}{2}\sqrt{\frac{\pi}{m}} - \frac{\mu}{f}\right] - \left[\frac{1}{2} - \frac{\mu}{f}\sqrt{\frac{m}{\pi}}\right]\right.$$

$$\left. \cdot \left[\left[\sqrt{\frac{m}{\pi}}\left[1 + \frac{\mu}{f}\right] - \frac{1}{2}\right]\left[\sqrt{\frac{m}{\pi}}\left[1 - \frac{\mu}{f}\right] + \frac{1}{2}\right]\right]^{\frac{1}{2}}\right\} ;$$

$$\text{for} \quad 0 < 2\sqrt{\frac{m}{\pi}}\left[1 + \frac{\mu}{f}\right] - 1 \leq 2\sqrt{\frac{m}{\pi}} \tag{8.5}$$

In both regimes, the illuminated soil is constrained by

$$g_I = 1 - m - g_s \tag{8.6}$$

A sketch of both regimes is provided in Figure 8.3 The graphical forms of $g_S(m)$ and $g_I(m)$ are given in Figure 8.4. Also plotted on Figure 8.4 are the actual fractional cover estimates of several pixels obtained from aerial video. The plots indicate that the theoretical curves of the fractional shadow and illuminated soil agree reasonably well with the actual data.

Using (8.1) through (8.6), the scattergram of a hypothetical orchard scene was constructed by superposing canopy cover ranging from 10 to 70 percent onto each of the soil background pixels. The resulting scattergram based on that model is shown in Figure 8.5. It possesses many similarities to the simulated cases presented earlier, including a triangular shape with curved sides and a flat base.

Figure 8.5 also includes the plot of several radiometric data from Figure 8.1 for which the subpixel fractional covers were estimated. The orchard itself does not possess a wide range of vegetation cover needed to establish a complete triangular scattergram as in the simulations. However, a comparison of the actual data with the hypothetical scattergram indicates that their location is consistent with the predicted values. A summary of the actual and hypothetical fractional covers for four pixels is provided in Table 8.2. The good agreement achieved above serves as a preliminary confirmation of the validity of the canopy reflectance model for explaining how subpixel variations in cover type affect the relative location of pixels in a red–infrared scattergram.

8.2 Pinyon–Juniper Watershed: Aerial Radiometric Data

This example tests the canopy reflectance model and inverse procedure on an actual semivegetated watershed for which aerial radiometric data were obtained.

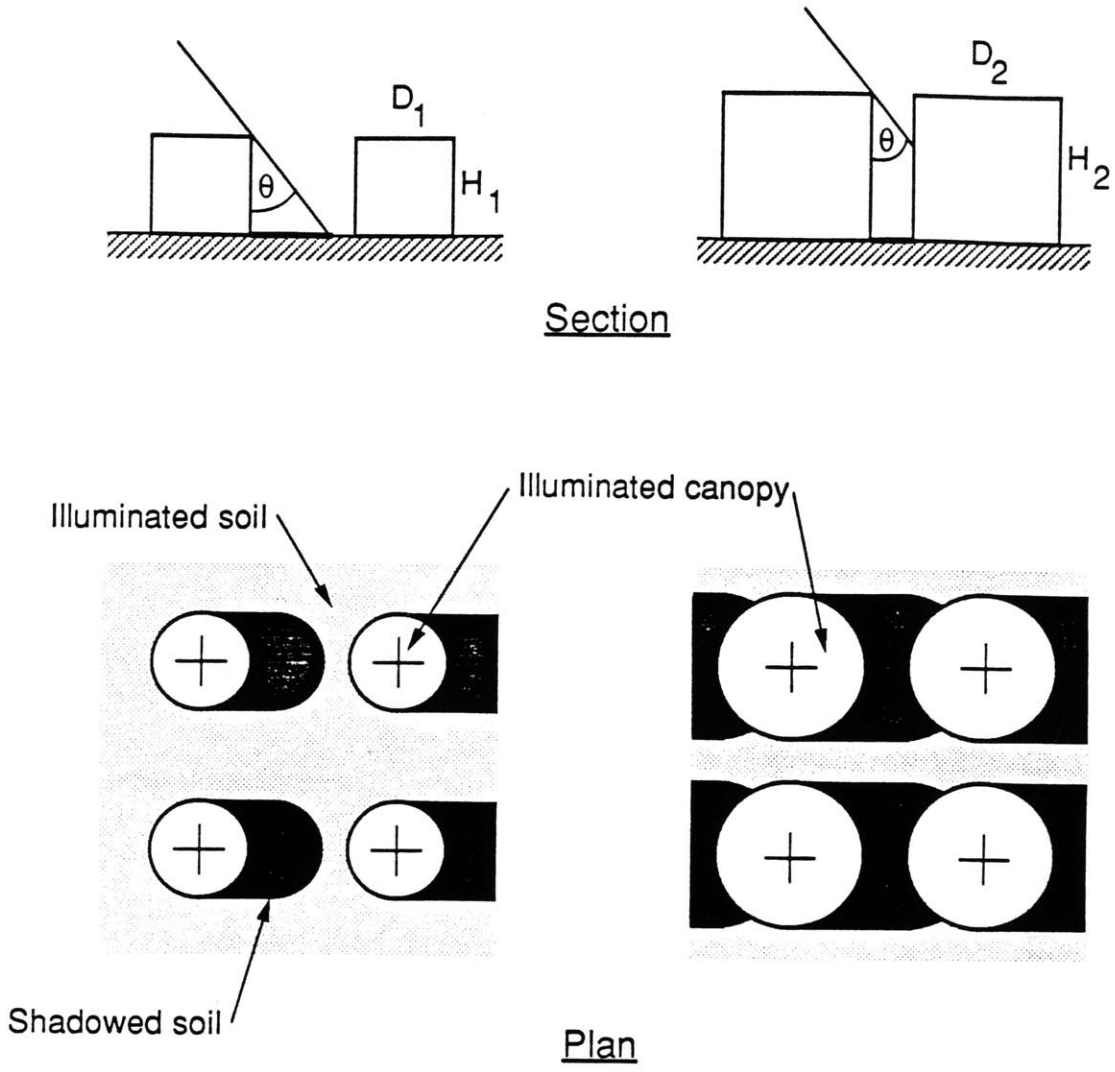

Figure 8.3 Hypothetical shadow regimes for pecan orchard.

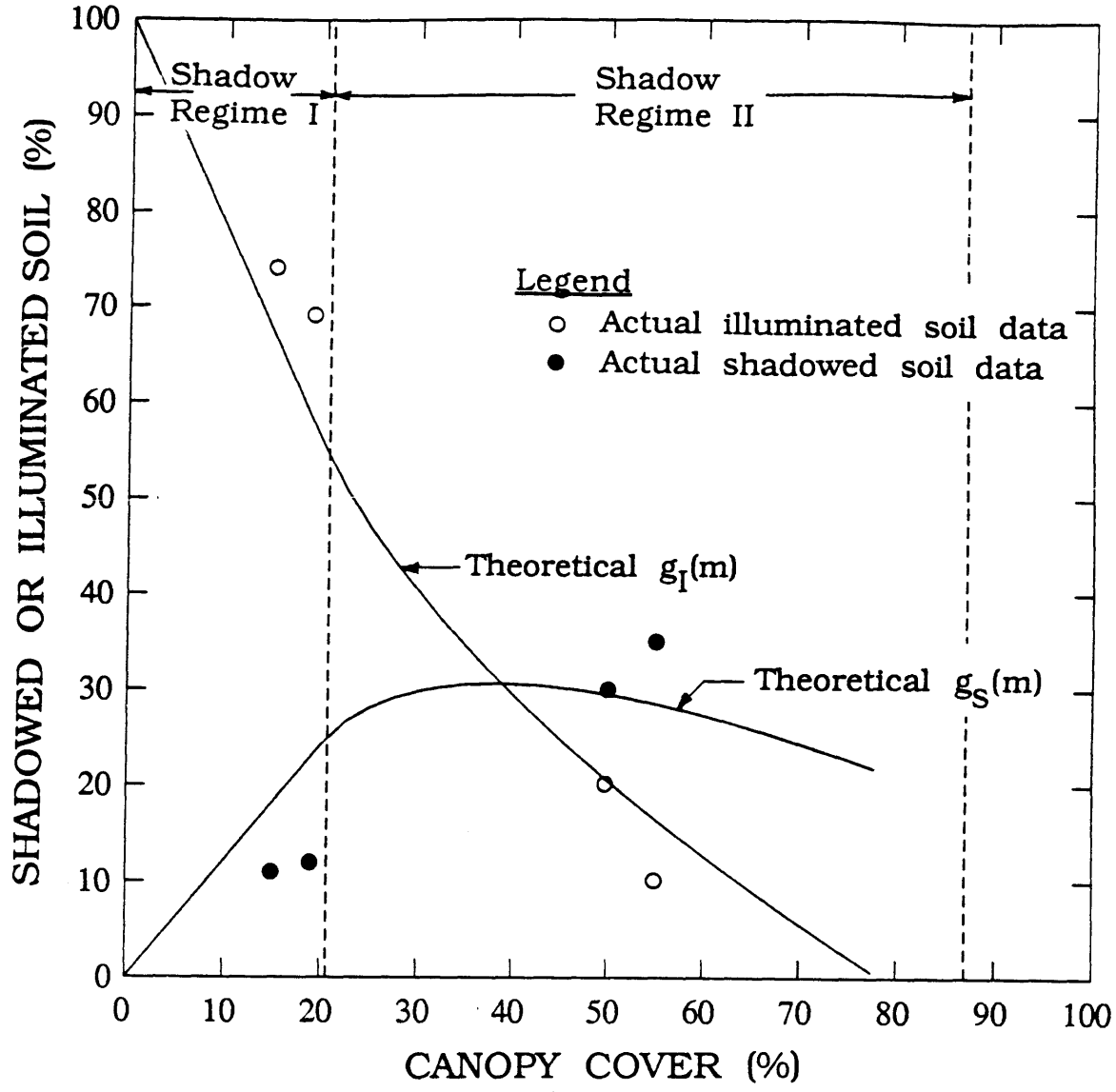

Figure 8.4 Theoretical relationship of percent illuminated soil, g_I, and percent shadowed soil, g_s, as a function of percent canopy cover, m, compared to actual data for a pecan orchard.

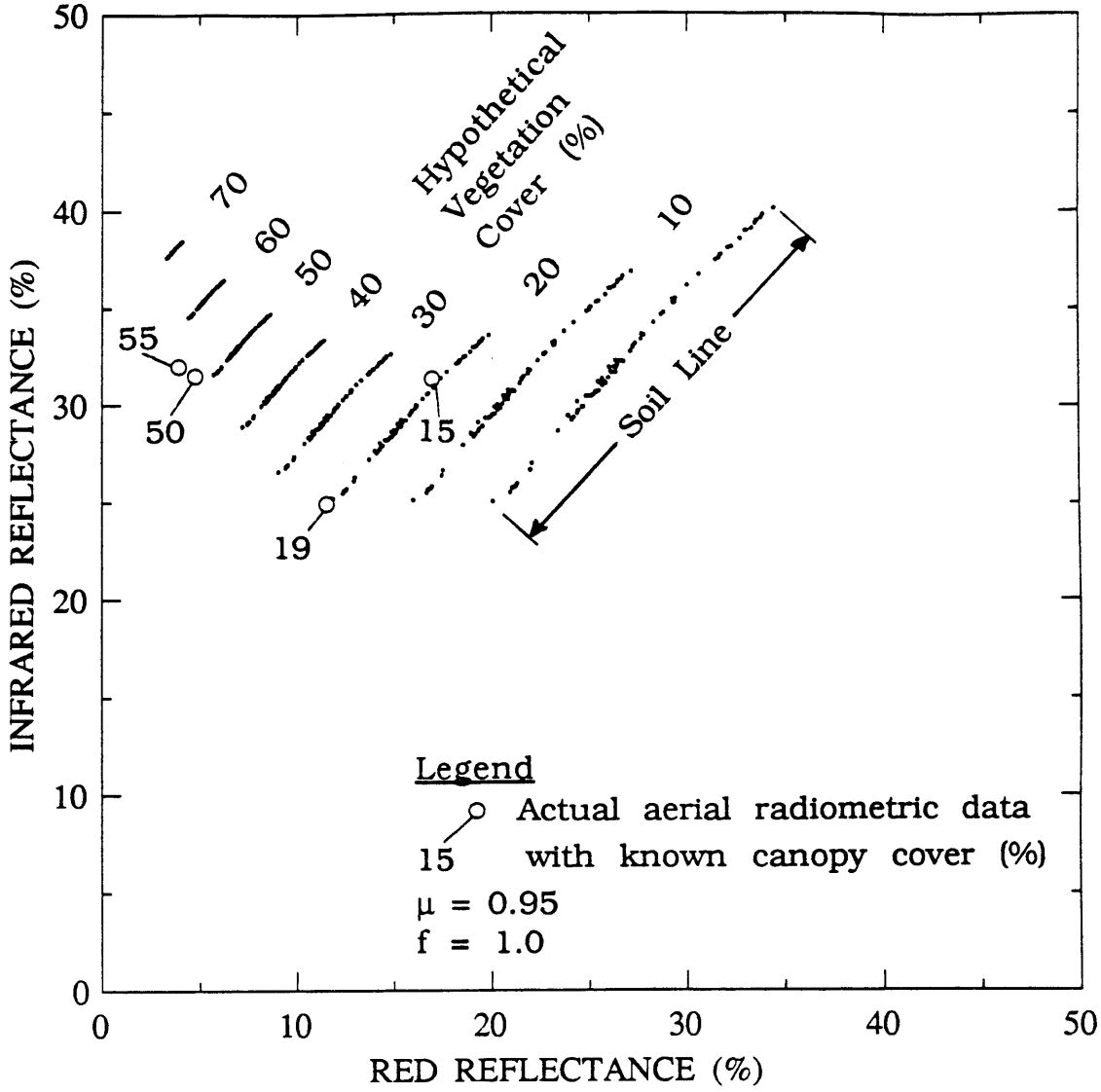

Figure 8.5 Hypothetical scattergram of pecan orchard compared with actual aerial radiometric data.

Table 8.2

Comparison of Actual and Hypothetical Fractional Covers for Pecan Orchard

Pixel Number	Total Canopy Cover (%)		Total Shadowed Soil Cover (%)		Total Illuminated Soil Cover (%)	
	Actual	Model	Actual	Model	Actual	Model
1	55	54	35	29	10	17
2	50	51	30	29	20	20
3	15	21	11	25	74	54
4	19	20	12	24	69	56

It also shows how the procedure can be adapted to situations in which the total number of pixels is small. In such cases, the red–infrared scattergram may not form a fully developed tasseled cap shape, as previously shown for the idealized simulated cases.

8.2.1 Site Description

The study site is a small, natural semivegetated watershed, about 0.8 km^2, located in the Beaver Creek Basin in the Coconino National Forest in north central Arizona, as shown in Figure 8.6. The area is relatively flat sloping 3.0 percent to the southwest at an average elevation of 1900 meters. The predominant tree species is alligator juniper (*Juniperus deppeana*), a short, egg–shaped evergreen with tiny scale–like leaves, ranging in height from 3 to 5 meters. Small amounts of Utah Juniper (*Juniperus osteosperma*), a tree similar in shape to the Alligator Juniper, and Ponderosa Pine (*Pinus ponderosa*), a taller, narrower evergreen with a rounded crown, also exist. The area between the trees is interspersed with a mixture of bare soil and a variety of sparse, relatively dry, semiarid grasses and shrubs. Field observations indicate that the fractional pinyon–juniper canopy cover ranges from about 0 to 70 percent, with a mean of about 25 percent. Soils are rocky and developed from volcanic materials, primarily basalts (Clary et al, 1974).

8.2.2 Acquisition of Radiometric Data and Ground Truth

Multispectral data were collected in a similar manner as for the pecan orchard experiment. The overflight occurred between 10:15 and 10:30 a.m. on June 23, 1988. at an altitude of about 150 m. using nadir–viewing instruments.

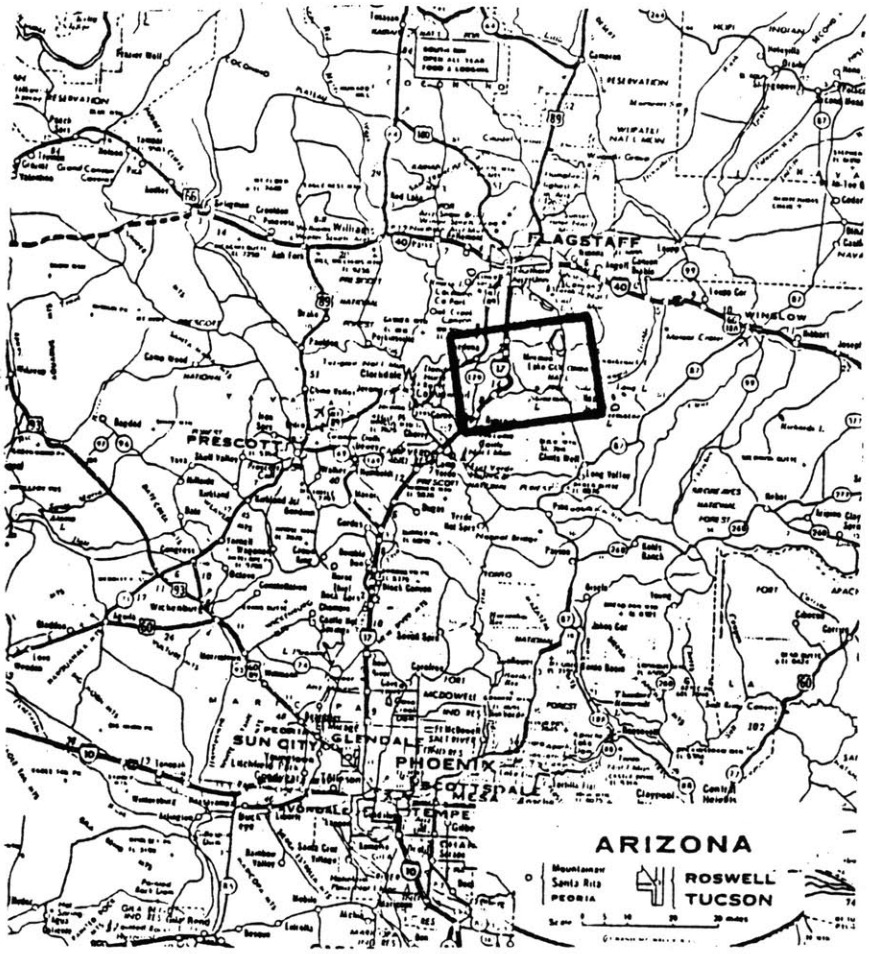

Figure 8.6 Location Map: Beaver Creek Watershed.

Approximately 200 radiometric observations were made using an Exotech radiometer with Thematic Mapper red (0.62–0.69 μm) and near infrared (0.78–0.90 μm) filters at a ground resolution of about 40 meters. Simultaneous multispectral video was also obtained.

Late June was chosen as the acquisition period as it was a relatively dry period when soil moisture was low and the grasses were in a somewhat senesced state, offering good contrast to the dark green evergreens. The solar zenith angle is relatively low compared to other seasons which minimizes the effect of shadows. Measurements were taken at 10:00 AM in order to conduct the analysis at the same time as a typical Landsat overpass, and to avoid further buildup of haze which was occurring during the morning of the overflight.

The radiometer data, recorded in terms of voltages, were not converted to reflectances, as it would have required additional ground–based instrumentation, not typically available in most remote sensing applications. Further, since the primary interest was in estimating fractional cover amounts, conversion to reflectances was not necessary. Sensor voltage is approximately linearly related to incoming radiance (Jackson et al, 1987). Thus, in the analysis which follows, voltage was used as a surrogate measure of reflectance. The analysis is valid as long as i) the time interval over which the data were collected was small (several minutes) in order to minimize the effect of changing solar zenith angle, ii) the solar irradiance on all target pixels was constant, and iii) diffuse atmospheric effects on the reflected radiance were minimal and constant over the region.

Estimates of fractional cover were made using the video data described in Section 8.1.3. The resulting histograms also exhibited a bimodal shape as for the pecan orchard, as shown in Figure 8.7 for one observation.

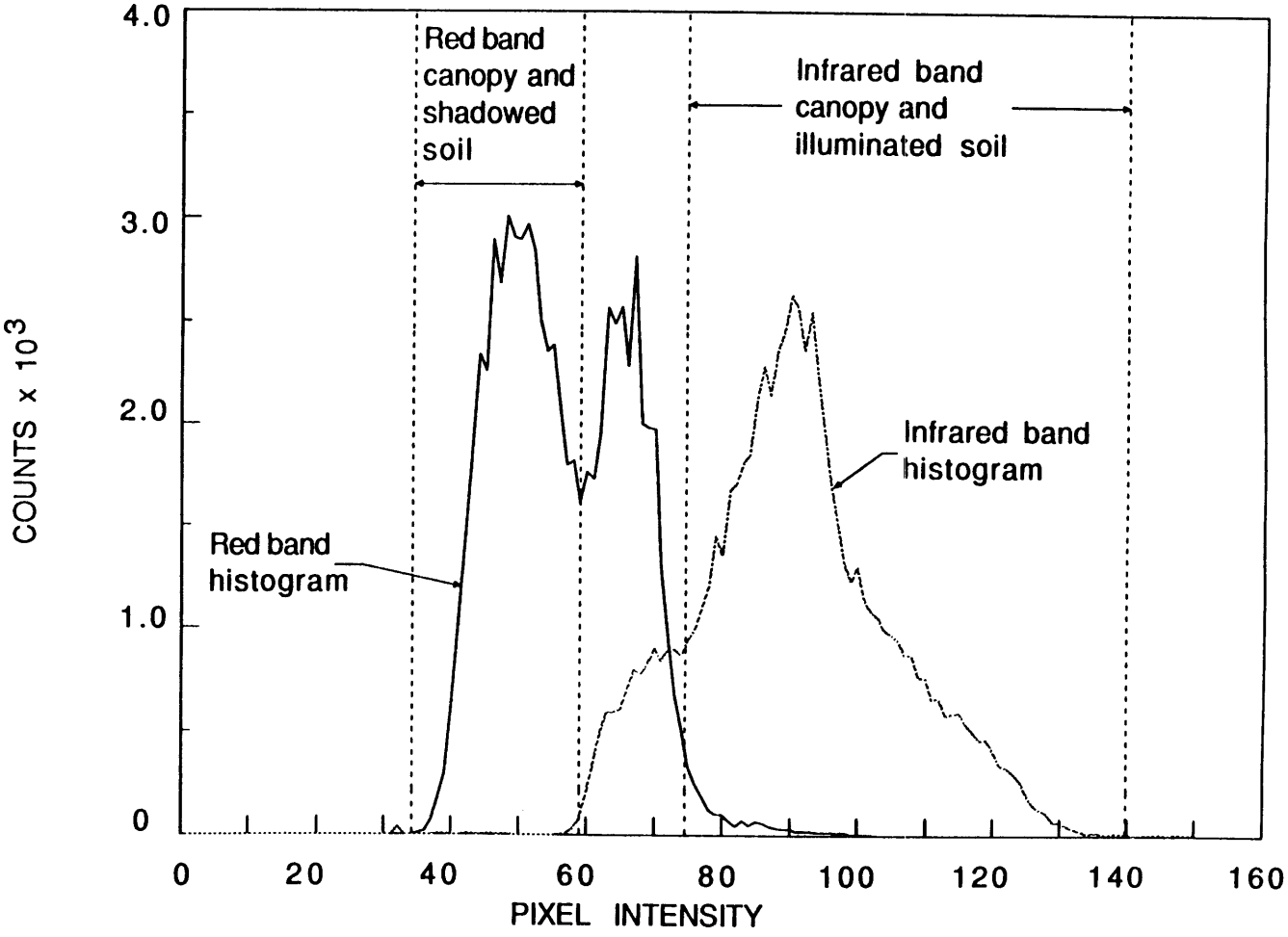

Figure 8.7 Histograms of red and infrared video images of the same semivegetated pinyon-juniper landscape.

8.2.3 Estimation of Subpixel Canopy Cover

As in the previous cases, the first step was to plot the entire set of observations in the red–infrared space as shown in Figure 8.8. The resulting scattergram, now in terms of voltages, possesses an overall triangular shape, although not as well defined as for the simulated cases. A relatively flat base does exist, however, the top of the scattergram is somewhat rounded and does not possess a fully developed "tasseled cap" shape. The reason for this lack of definition is that, unlike the simulated scenes, the watershed does not possess a full range of combinations of fractional vegetation cover and soil reflectance.

The second step in the inversion procedure was to conceptualize the pinyon–juniper landscape as Poisson distributed spheres resting on a flat surface. The spherical trees are assumed to exhibit a constant bulk reflectance in each band, $R_m(\lambda)$, which accommodates both illuminated and shadowed portions of the canopy. Soil reflectance is variable and can be shadowed or illuminated. The total reflectance of any pixel is thus given by

$$R(\lambda) = m\, R_m(\lambda) + g_S\, R_{g_S}(\lambda) + g_I R_{g_I}(\lambda,\underline{x}) \tag{8.7}$$

The geometric similarity assumption allows η to be estimated directly from Table 6.1, Item (iv). The value of η was calculated to be 0.294 based on an estimated solar zenith angle of 30.25 degrees, obtained using Iqbal (Chapter 1, 1983). The mean tree diameter is on the order of several meters, thus,

$$S_P = \frac{1300}{0.294 A_t} >> 10 \tag{8.8}$$

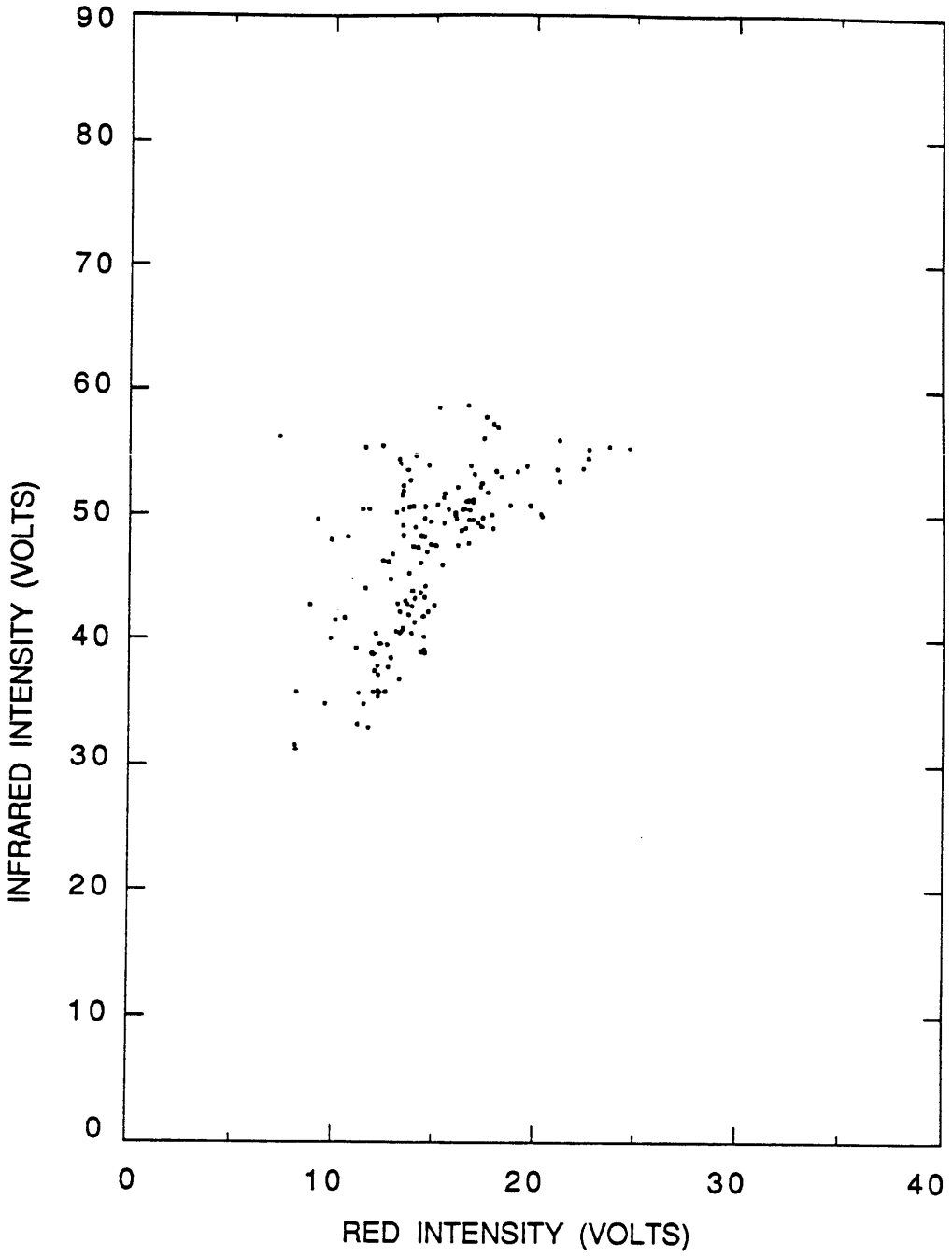

Figure 8.8 Red-infrared scattergram of pinyon-juniper watershed, aerial data.

and the assumption of a large sampling scale ratio is made.

Next, the mean and variance of the soil background radiance (expressed in terms of voltage) were calculated by fitting a straight line through approximately 20 pixels located at the bottom of the scattergram (Figure 8.9), and by estimating the moments of those pixels. The pixels do not fall completely on a straight line since they contain small amounts of green and senesced grasses, in addition to the bare soil. The estimated values of the soil moments are provided in Table 8.3.

According to the method for $S_P >> 10$, the inversion procedure next requires the identification of sets of pixels lying in a band parallel to the soil line. The sample moments of those pixels are then used to estimate g_I using (6.20). However, in the present example, the number of pixels in any given line is too small to compute sample moments, and a slightly different approach must be taken, requiring two steps. First, instead of choosing subsets of pixels lying parallel to the soil line, the entire ensemble of pixels (except those associated with the soil line) were analyzed simultaneously in order to obtain overall estimates of vegetation reflectance and fractional cover statistics for the watershed. The analysis required (6.17), (7.8) and approximate relations for the mean (7.5) and variance (7.6) based on the following order of magnitude analysis.

Since $\eta = 0.294$, then from (6.17) and (7.8) it is reasoned that $E[g_S]$ will be smaller than $E[g_I]$ and $E[m]$ for $m < 0.5$. Since $R_{g_S}(\lambda)$ is likely to be less than $R_m(\lambda)$ and $E[R_{g_I}(\lambda)]$, the product, $E[g_S]R_{g_S}(\lambda)$, will also be small compared to the other two terms in (7.5). The mean reflectance can thus be approximated by

$$E[R(\lambda)] \simeq E[m]R_m(\lambda) + E[g_I]\ E[R_{g_I}(\lambda)] \tag{8.9}$$

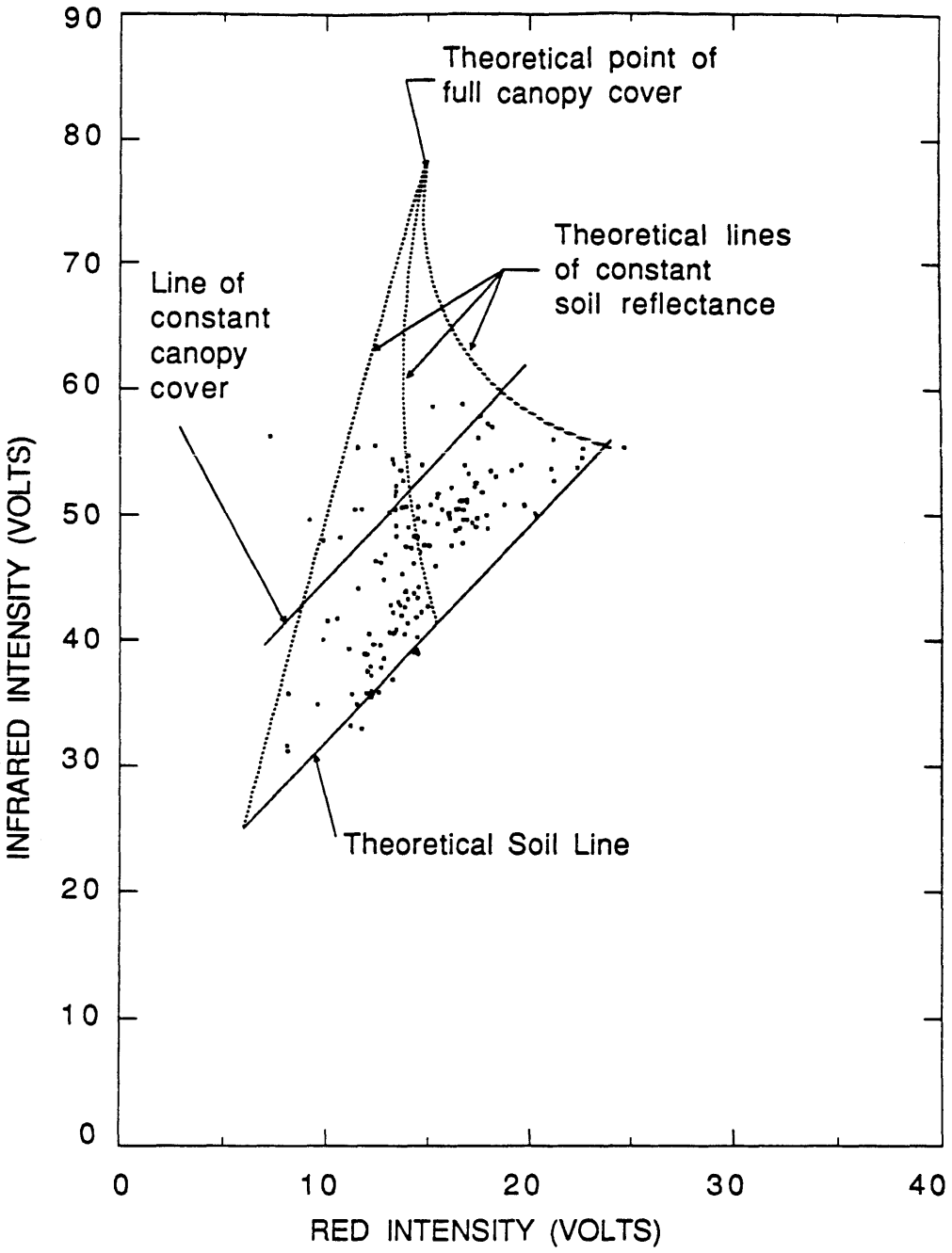

Figure 8.9 Interpretation of red-infrared scattergram for pinyon-juniper landscape, aerial data.

Table 8.3

Estimated Mean Subpixel Parameters

Pinyon–Juniper Watershed, Aerial Data

Parameter	Estimated Value
$R_m(\lambda_{RED})$	15.4 volts
$R_m(\lambda_{IR})$	79.3 volts
$E[R_{gI}(\lambda_{RED})]$	15.5 volts
$E[R_{gI}(\lambda_{IR})]$	41.3 volts
$VAR[R_{g_I}(\lambda_{RED})]$	21.4 volts^2
$VAR[R_{g_I}(\lambda_{IR})]$	64.3 volts^2
θ_z	30.25°
η	0.294
mean fractional canopy cover of watershed	0.23
A_p	1300 meters^2
Soil line equation	$R_{g_I}(\lambda_{IR}) = 1.72\ R_{g_I}(\lambda_{RED}) + 14.69$

Similar reasoning allows one to neglect the shadow terms in (7.6). Further, since g_S is small in this case, it follows from (7.9) that

$$\text{VAR}[m] \simeq \text{VAR}[g_I] \tag{8.10}$$

Substituting (8.10) into (7.6), neglecting the shadow terms, and rearranging yields

$$\text{VAR}[R(\lambda)] \simeq \left[E[g_I]^2 + \text{VAR}[g_I]\right]\text{VAR}[R_{g_I}(\lambda)] + \left[R_m(\lambda) - E[R_{g_I}(\lambda)]\right]^2 \text{VAR}[g_I] \tag{8.11}$$

Thus, the seven equations (6.17), (7.8), (8.10), (8.9), (8.11) (the latter two written for both bands) were solved simultaneously to obtain estimates of $R_m(\lambda_{RED})$, $R_m(\lambda_{IR})$, E[m], $E[g_I]$, $E[g_S]$, VAR[m] and $\text{VAR}[g_I]$ for the entire ensemble of pixels covering the watershed. Those results are provided in Table 8.3.

Finally, in order to obtain estimates of fractional cover on a pixel–by–pixel basis, equations (6.7), (6.24), (6.19) (with $g_S R_{g_S}(\lambda)$ neglected) and (7.15) were combined to yield

$$R(\lambda_{IR}) = \alpha R(\lambda_{RED}) + [R_m(\lambda_{IR}) - R_m(\lambda_{RED})]m + \gamma(1 - m)^{\eta+1} \tag{8.12}$$

Equation (8.12) was solved explicitly for m for each pixel, that is, for each paired observation $(R(\lambda_{RED}), R(\lambda_{IR}))$ in the data set. The computer programs necessary for the above analysis are provided in Appendix D.

The results of the analysis are graphically displayed in Figures 8.9, 8.10, and 8.11 and Table 8.4. Figure 8.8 indicates that the theoretical canopy–soil

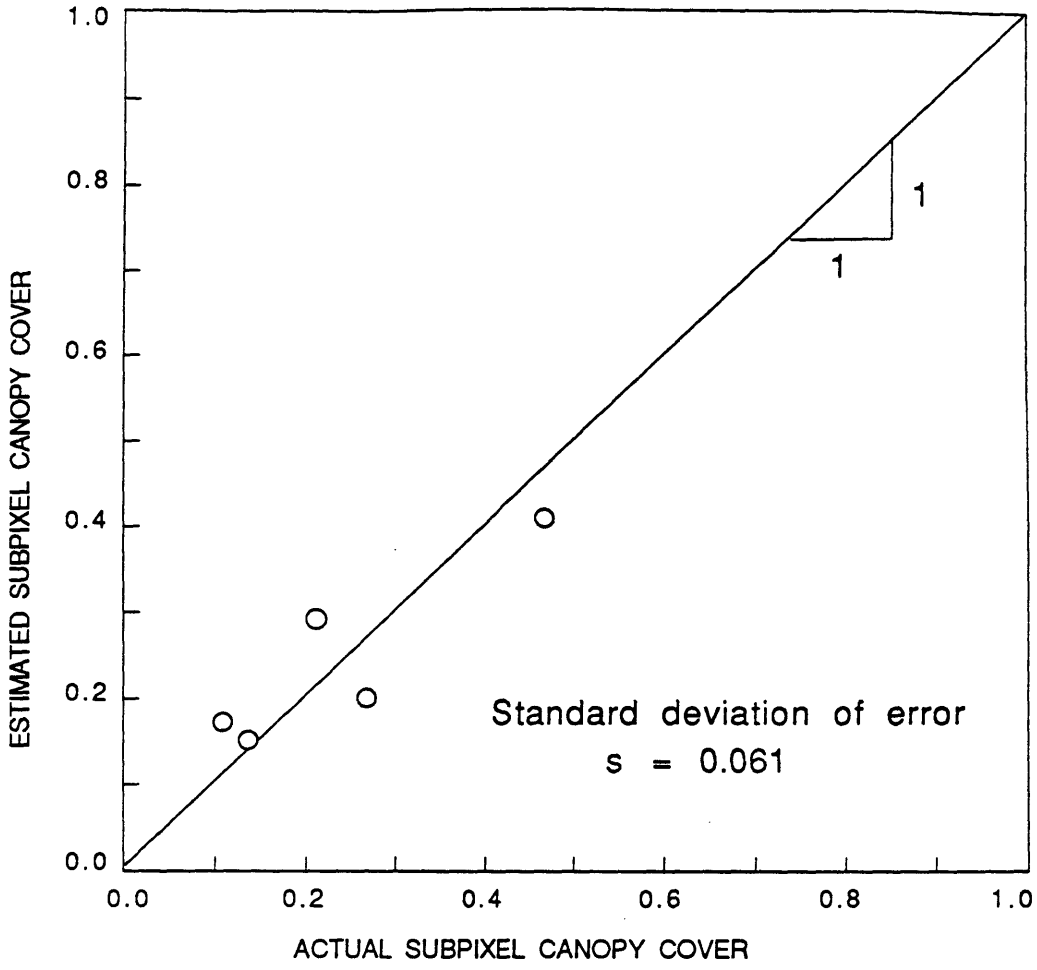

Figure 8.10 Estimated subpixel canopy cover versus ground truth obtained from video for pinyon-juniper watershed.

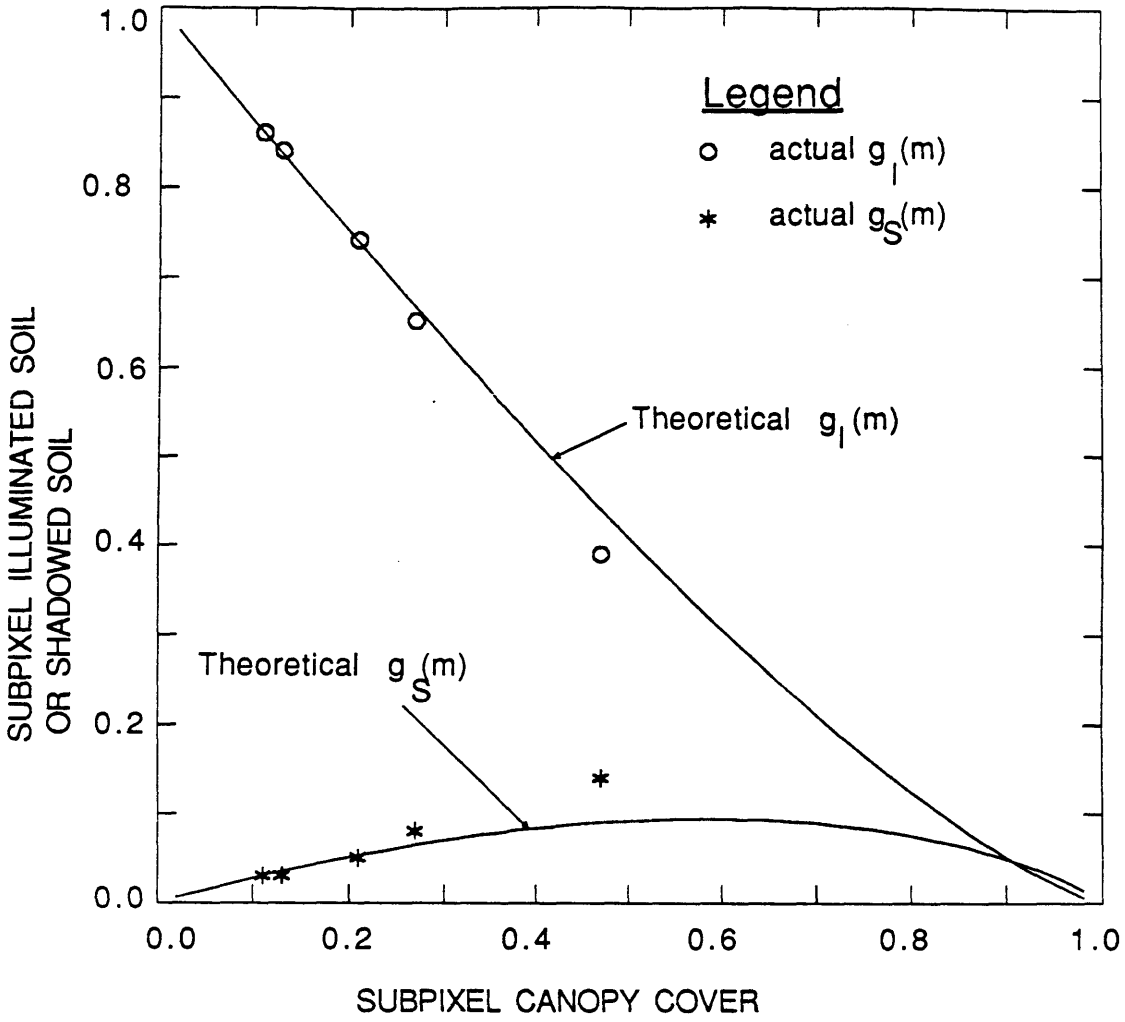

Figure 8.11 Comparison of estimated values of illuminated and shadowed soil cover to the actual ground truth obtained from video for the pinyon-juniper watershed, aerial data.

Table 8.4

Comparison of
Estimated and Actual Fractional Canopy Cover
for Pinyon-Juniper Watershed, Aerial Data

Time of Acquisition (hours)	m		g_I		g_S	
	Act.	Est.	Act.	Est.	Act.	Est.
10.2924	0.47	0.41	0.39	0.50	0.14	0.09
10.2942	0.21	0.29	0.74	0.65	0.05	0.07
10.3078	0.27	0.20	0.65	0.75	0.09	0.05
10.3113	0.11	0.17	0.86	0.79	0.04	0.04

reflectance model and the parameter estimates of Table 8.3 lead to a "triangular" interpretation of the actual red-infrared scattergram. That interpretation stems directly from the following pair of equations obtained from combining (6.24) and (8.7) and neglecting the shadow term,

$$R(\lambda_{RED}) = m\, R_m(\lambda_{RED}) + (1 - m)^{\eta+1}\, R_{g_I}(\lambda_{RED}) \tag{8.13}$$

$$R(\lambda_{IR}) = m\, R_m(\lambda_{IR}) + (1 - m)^{\eta+1}\, R_{g_I}(\lambda_{IR}) \tag{8.14}$$

For instance, the apex of the triangle in Figure 8.8 occurs at full canopy cover ($m = 1$) in which (8.13) and (8.14) reduce to

$$R(\lambda_{RED}) = R_m(\lambda_{RED}) \tag{8.15}$$

$$R(\lambda_{IR}) = R_m(\lambda_{IR}) \tag{8.16}$$

The base of the scattergram occurs for bare soil ($m = 0$) in which (8.13) and (8.14) become

$$R(\lambda_{RED}) = R_{g_I}(\lambda_{RED}) \tag{8.17}$$

$$R(\lambda_{IR}) = R_{g_I}(\lambda_{IR}) \tag{8.18}$$

and where (8.17) and (8.18) are related by the soil line equation given in Table 8.3.

Lines of constant canopy cover indicated in Figure 8.9 are obtained by setting m constant in (8.13) and (8.14) and letting $R_{g_I}(\lambda)$ vary according to the soil line equation. In a similar manner, lines of constant soil reflectance are

established by selecting one pair of $R_{g_I}(\lambda_{RED})$ and $R_{g_I}(\lambda_{IR})$ (one point on the soil line), and letting m range from 0.0 to 1.0 in (8.13) and (8.14). Three such lines are drawn in Figure 8.9 representing three different soil background reflectances.

Finally, Figures 8.10 and 8.11 and Table 8.4 show a comparison, for five pixels, of the estimated fractional covers with the actual ground truth estimates obtained from the video. Figure 8.10 contains a plot of the estimated values canopy cover versus the ground truth values (s = 0.061). Figure 8.11 contains a graph of both the estimated theoretical curves of $g_I(m)$ and $g_S(m)$ and the ground truth values. The good agreement between estimated values and the ground truth in both figures supports the applicability of this method for estimating subpixel fractional cover of semivegetated scenes, at least for the pinyon–juniper landscape.

8.3 Pinyon–Juniper Watershed: Landsat Thematic Mapper Data

This example investigates the fractional cover of the same watershed used in the previous case, except that Landsat TM data are used instead of aerial observations. Also, a different version of the inverse procedure is used due to the nature of the scattergram.

8.3.1 Landsat Thematic Mapper Data

The Landsat TM data used in this analysis were extracted from Scene ID Number Y504771733XO, obtained on June 21, 1985. The scene was purchased from EOSAT, Lanham, Maryland. The data were ordered with standard radiometric corrections that remove possible sensor error according to EOSAT procedures, and with an original pixel size of 30 meters. That size, the same as

the raw data, was selected in order to eliminate resampling, and hence unnecessary distortion to the DN values of the original data.

The month of June was selected as it is normally a dry period of the year when there are few clouds and the atmosphere is clear. That dryness enhances the analysis due to the relatively high contrast between the reflectances of the conifer canopy and the ground, which contains bare soil and senesced grasses. However, since that dryness can also increase the aerosol count in the lower atmosphere and thus the diffuse radiance. It was decided to select an image in which those atmospheric effects were minimal.

Since there was no practical means to estimate aerosol density over the Beaver Creek Basin for the archived TM images, the selection of the specific scene was made on the basis of an indirect and qualitative assessment of the cloudiness, image clarity, and soil moisture for the available TM scenes which were taken in the month of June. Cloudiness was assessed by comparing the microfiches of several scenes, made available by the EROS Data Center, Sioux Falls, South Dakota, and then selecting those which appeared to be the clearest. Next, the precipitation and climatic records of nearby meteorological stations for the months April through June were examined for each of those scenes in order to select the lowest precipitation, and thus by association, a low soil moisture for the period up to and including the time of acquisition. Although the above approach yielded perhaps the clearest of all available images for the month of June and provided some assurance that the soil was relatively dry, it did not provide any quantitative information on important properties such as optical thickness and diffuse radiance. Those quantities can best be obtained using ground–based instrumentation during the time of acquisition.

The Beaver Creek watershed was visually identified on the original scene and extracted using the General Image Processing Software (GIPS) developed by Peter Ford at the Center for Space Research, M.I.T. The watershed was located within a rectangular area covering 30 (vertical) by 29 (horizontal) pixels, or a total of 870 pixels.

8.3.2 Red–Infrared Scattergrams

Two scattergrams from the original scene are plotted in Figures 8.12 and 8.13, respectively, in terms of the satellite DN values. Figure 8.12 includes a large region covering 235 sq. km. containing several watersheds and a variety of vegetation types and densities. It possesses a typical triangular shape with a curved top and flat base, characteristic of semivegetated regions. The lower left portion of the scattergram, somewhat detached from the main part, can be shown using topographic maps to represent principally water bodies and regions with extensive shadows such as cliffs and gorges. The soil line was thus defined from the locus of pixels at the base of the major portion of the scattergram as shown in Figure 8.12. The mean and variance of the soil line are given in Table 8.5.

The portion of the scattergram associated with only the small Beaver Creek watershed is outlined on Figure 8.12 and also plotted separately in Figure 8.13. That scattergram is located entirely within the lower portion of the large scattergram and does not possess a triangular shape nor a flat base. Thus, no soil line could be discerned on the basis of the pixels located within the Beaver Creek Watershed.

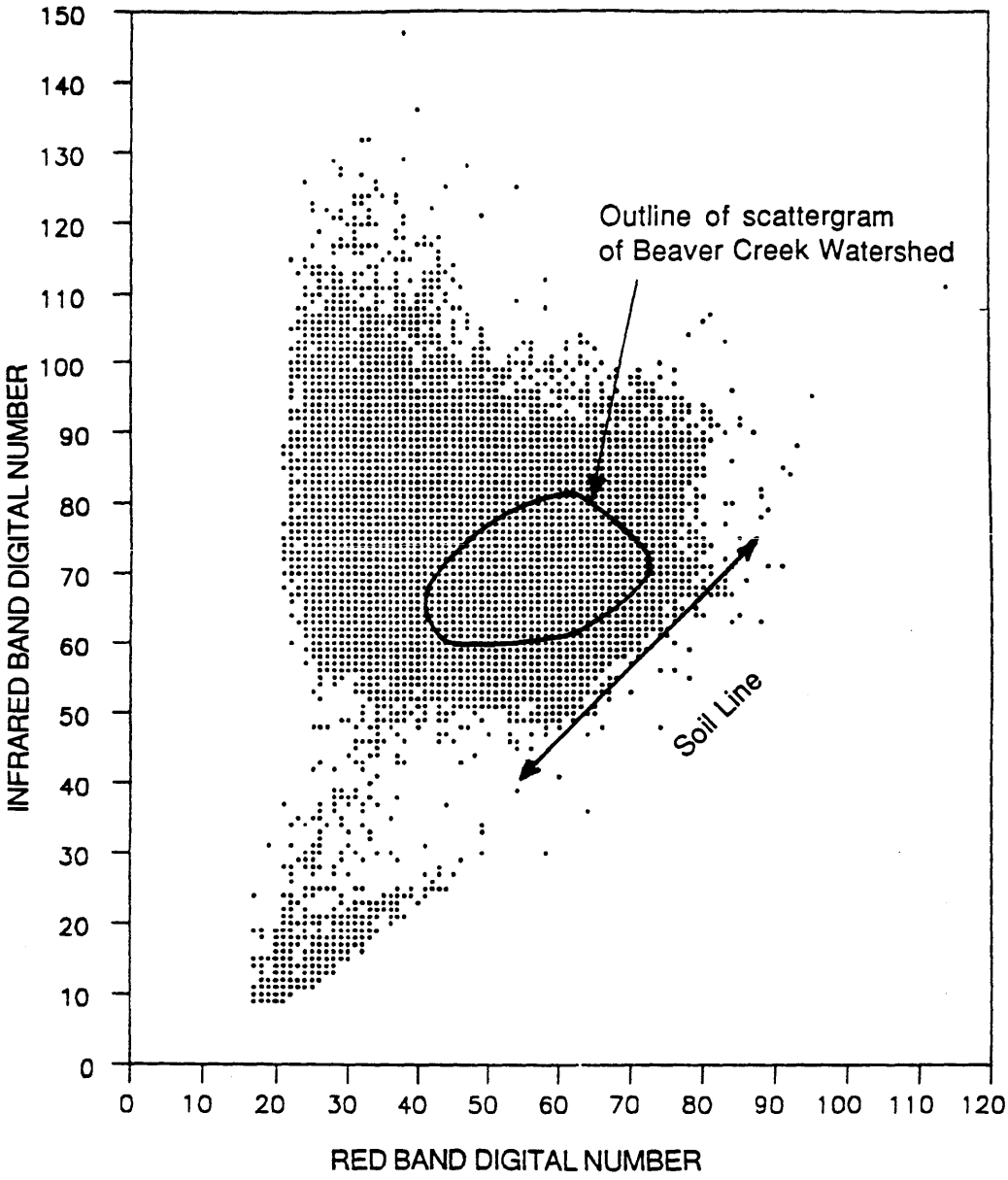

Figure 8.12 Red–infrared scattergram of 235 sq. km region encompassing Beaver Creek Watershed, Landsat TM data.

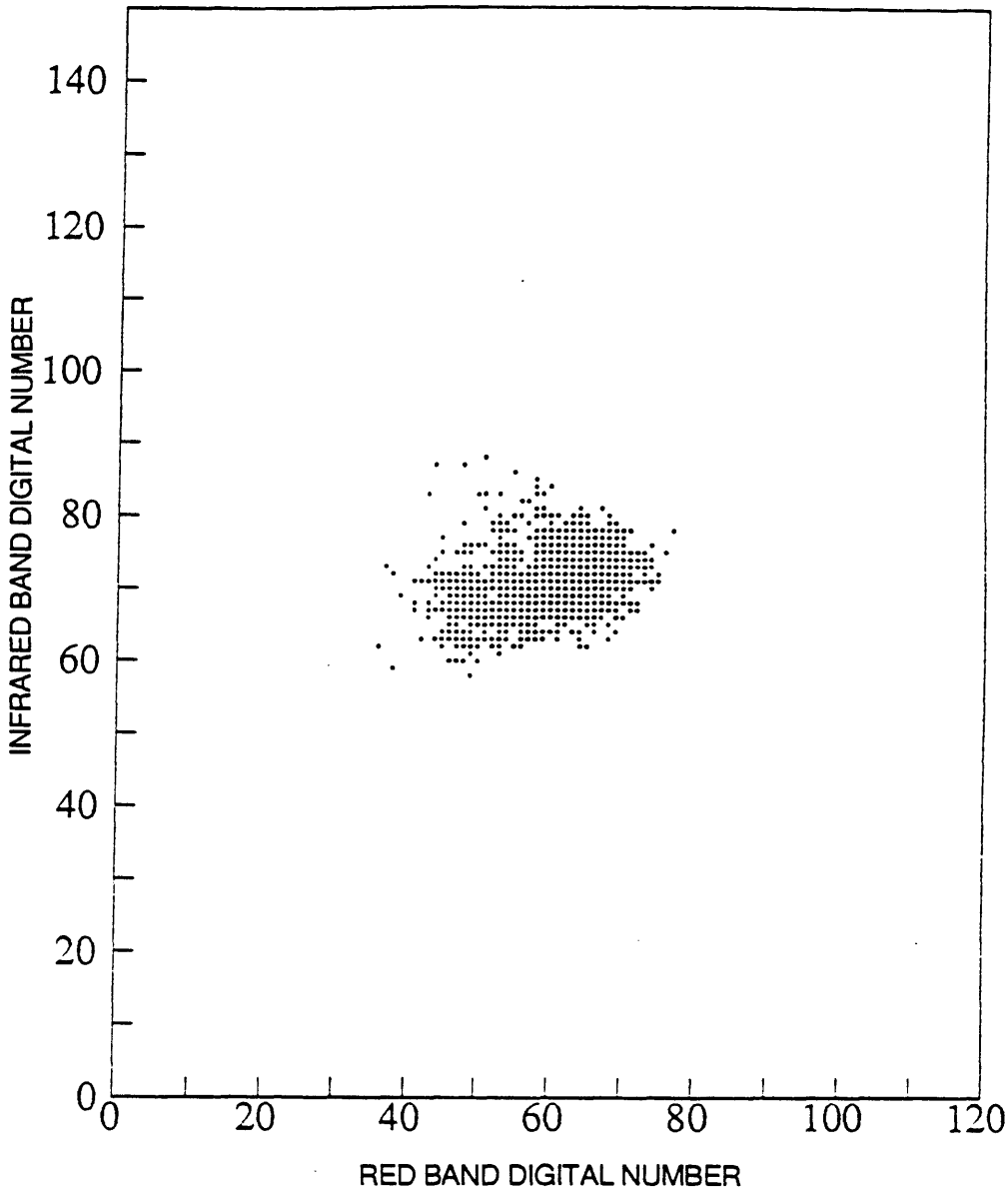

Figure 8.13 Red–infrared scattergram of Beaver Creek Watershed, Landsat TM data.

Table 8.5

Estimated Mean Subpixel Parameters
of Beaver Creek Watershed,
Landsat TM Data

Solar Zenith Angle, θ = 27.5 degrees
Similarity Parameter, η = 0.241

Percent Diffuse Radiation:		0	10	20	30
Quantity	Units				
$l'(\lambda_{RED})$	DN	0	6	12	18
$l'(\lambda_{IR})$	DN	0	6	12	18
m	-	0.25	0.23	0.21	0.17
g_I	-	0.70	0.72	0.75	0.79
g_S	-	0.05	0.05	0.04	0.04
$R'_m(\lambda_{RED})$	DN	40	30	18	1
$R'_m(\lambda_{IR})$	DN	119	116	114	123
$E[R'_{g_I}(\lambda_{RED})]$	DN	69.5	63.5	57.5	51.5
$E[R'_{g_I}(\lambda_{IR})]$	DN	56.8	50.8	44.8	38.8

Scene Parameters

$E[DN(\lambda_{RED})] = 58.8$ $\quad VAR[DN(\lambda_{RED})] = 54.2$

$E[DN(\lambda_{IR})] = 69.5$ $\quad VAR[DN(\lambda_{IR})] = 16.1$

Soil Line Parameters

$E[DN(\lambda_{RED})] = 69.5$ $\quad VAR[DN(\lambda_{RED})] = 141.6$

$E[DN(\lambda_{IR})] = 56.8$ $\quad VAR[DN(\lambda_{IR})] = 161.3$

Slope, $\alpha = 1.03$

Intercept, $\beta = -15.4$

8.3.3 Estimation of Subpixel Canopy Cover

The inverse procedure used in this example was the same as that used for aerial case, except that the moment equations were written in terms of the DN values which include atmospheric effects. Further, the soil line, which could not be defined from the Beaver Creek scattergram, was assumed to be the same as that of the larger image.

As in the aerial case, the Pinyon–Juniper landscape was assumed to consist of Poisson distributed spheres. The similarity parameter, η, was calculated to be 0.241 using Table 6.1, Item (iv), and an estimated solar zenith angle of 27.5 degrees (after Iqbal, 1983, Chapter 1). The Sampling Scale Ratio for Poisson distributions, equation (6.23), yields

$$S_P = 700/0.241A_t >> 10 \tag{8.19}$$

and thus a large Sampling Scale Ratio was assumed, allowing one to use (6.24) in the analysis.

The analysis assumed that the atmosphere was horizontally homogeneous, that the landscape was regionally homogeneous (no sharp contrasts in landscape reflectance), and that the vegetation reflectance was constant in both wavelengths. Further, since η is small, the shadow terms were neglected as previously argued in (8.9) and (8.11). Under those assumptions, the expected value and variance of the entire ensemble of pixels in the scattergram can be written in terms of the satellite DN values using equation (6.31) and (6.32), respectively, or,

$$E[DN(\lambda,\underline{x})|m] = mR'_m(\lambda) + g_I E[R'_{g_I}(\lambda,\underline{x})] + l'_d(\lambda) \tag{8.20}$$

and

$$\text{VAR}[DN(\lambda,\underline{x})\,|\,m] \;=\; \text{VAR}\Big[mR'_m(\lambda) + g_I R'_{g_I}(\lambda,\underline{x})\Big] \tag{8.21}$$

where $R'_m(\lambda)$ and $R'_{g_I}(\lambda,\underline{x})$ are "effective" reflectances of the vegetation and soil as previously used in Sections 4.3 and 6.3, and $l'_d(\lambda)$ is the backscattered solar radiation term (or simply a calibration coefficient) characteristic of that scene.

The soil line equations can be obtained by conditioning (8.20) and (8.21) along m = 0, or

$$E[DN(\lambda,\underline{x})\,|\,m = 0] \;=\; E[R'_{g_I}(\lambda,\underline{x})] + l'_d(\lambda) \tag{8.22}$$

and

$$\text{VAR}[DN(\lambda,\underline{x})\,|\,m = 0] \;=\; \text{VAR}\Big[R'_{g_I}(\lambda,\underline{x})\Big] \tag{8.23}$$

It is noted that the calibration constant is included in the expected value of the soil line, and thus mean values of the soil reflectance can not be determined explicitly as in the previous examples. The variance equation can be expanded, analogous to (8.11), by inserting (8.10) into (8.21) and rearranging, or,

$$\text{VAR}[DN(\lambda)] \simeq \Big[E[g_I]^2 + \text{VAR}[g_I]\Big]\text{VAR}[R'_{g_I}(\lambda)] + \Big[R'_m(\lambda) - E[R'_{g_I}(\lambda)]\Big]^2 \text{VAR}[g_I] \tag{8.24}$$

The number of unknowns include the fractional cover variables, m, g_I, g_S, $\text{VAR}[g_I]$, the reflectance quantities, $R'_m(\lambda_{red})$, $R'_m(\lambda_{IR})$, $E[R'_{g_I}(\lambda_{red})]$,

$E[R'_{g_I}(\lambda_{IR})]$, $VAR[R'_{g_I}(\lambda_{red})]$, $VAR[R'_{g_I}(\lambda_{IR})]$, and the atmospheric coefficients, $l'_d(\lambda_{red})$ and $l'_d(\lambda_{IR})$, for a total of twelve. The equations available to solve the problem include i) the mean and variance of the observations, (8.20 and 8.24), written for both bands, ii) the mean and variance of the soil line equation, (8.22) and (8.23) written for both bands, and iii) the cover relationship $g_I(m)$ or (6.24), and (8.6) for a total of ten. Thus, the inclusion of the diffuse radiation terms results in two more unknowns than equations.

There are several ways in which the diffuse terms can be estimated without actual atmospheric measurements. One method is to recognize that observations over areas of approximiately zero reflectance (i.e. deep clear water bodies) consist principally of the diffuse radiance (Lillesand and Kiefer, 1987). A second approach is to use observations of two additional visible bands over pixels in which the reflectance is assumed independent of wavelength. By assuming an aerosol distribution, it may be possible to estimate optical depths and diffuse radiation by examining the relative intensity of the two bands (Liou, 1983). A third approach is to develop two additional independent equations using the moment analysis, such as the use of the cross–spectral covariance or two separate conditional lines.

Since it was not possible to verify the estimated diffuse radiation using any approach, it was decided to simply assume a range of values and to compare the results as a function of those assumed values. In general, for optical depths of about 0.1 or less and surface reflectances of about 0.3, it can be argued that the backscattered diffuse radiation ranges from about 10 to 30 percent of the total radiation observed by the nadir–viewing satellite, depending on the wavelength. Scattering is likely to be greater at smaller wavelengths (i.e. blue) due to the combined effect of both Rayleigh and aerosol scattering. In the red and infrared regions, aerosol scattering is likely to contribute the most to the total optical

thickness (Liou, 1983).

The above set of equations (8.20, 8.24, 8.22, 8.23, and 6.24) written, when applicable, for both wavelengths, were solved assuming that the backscattered solar radiation term, $l'_d(\lambda)$, equaled 0, 10, 20, and 30 percent of the mean DN value of all the pixels in the watershed. For example, since the mean value in the red and infrared bands equaled 58.8 and 69.5 DN's, respectively, then for the 20 percent case, the backscattered radiation was assumed to be 12 DN's. For simplicity, both bands were assumed to possess the same diffuse radiance, ignoring wavelength dependency.

The solution to the above set of equations was found by minimizing the error between the theoretical moments and the actual moments in the same manner as for the aerial case. However, it was observed that in a few instances, two or three minimum values were obtained thus yielding two or three possible solutions. In all cases, the two additional possible solutions occurred at extreme values of m (very large, 0.90, or very small, 0.05) that were clearly inappropriate and thus they were not selected as the best estimate. That choice was supported by an a priori knowledge that the vegetation cover of the region was neither extremely dense nor sparse. However, future investigations would not necessarily benefit from such knowledge.

The results of the analysis are provided in Table 8.5 and Figure 8.14. Table 8.5 indicates that the estimates of fractional cover are about 0.20, in good agreement with field observations (about 25 percent). The results are moderately sensitive to the relative magnitude of the diffuse radiation. The greatest value, m = 0.25, is estimated when no diffuse radiation is assumed. The estimate gradually decreases to m = 0.17 for the case with 30 percent diffuse radiation.

Figure 8.14 shows the hypothetical data spaces of the 0 and 20% diffuse

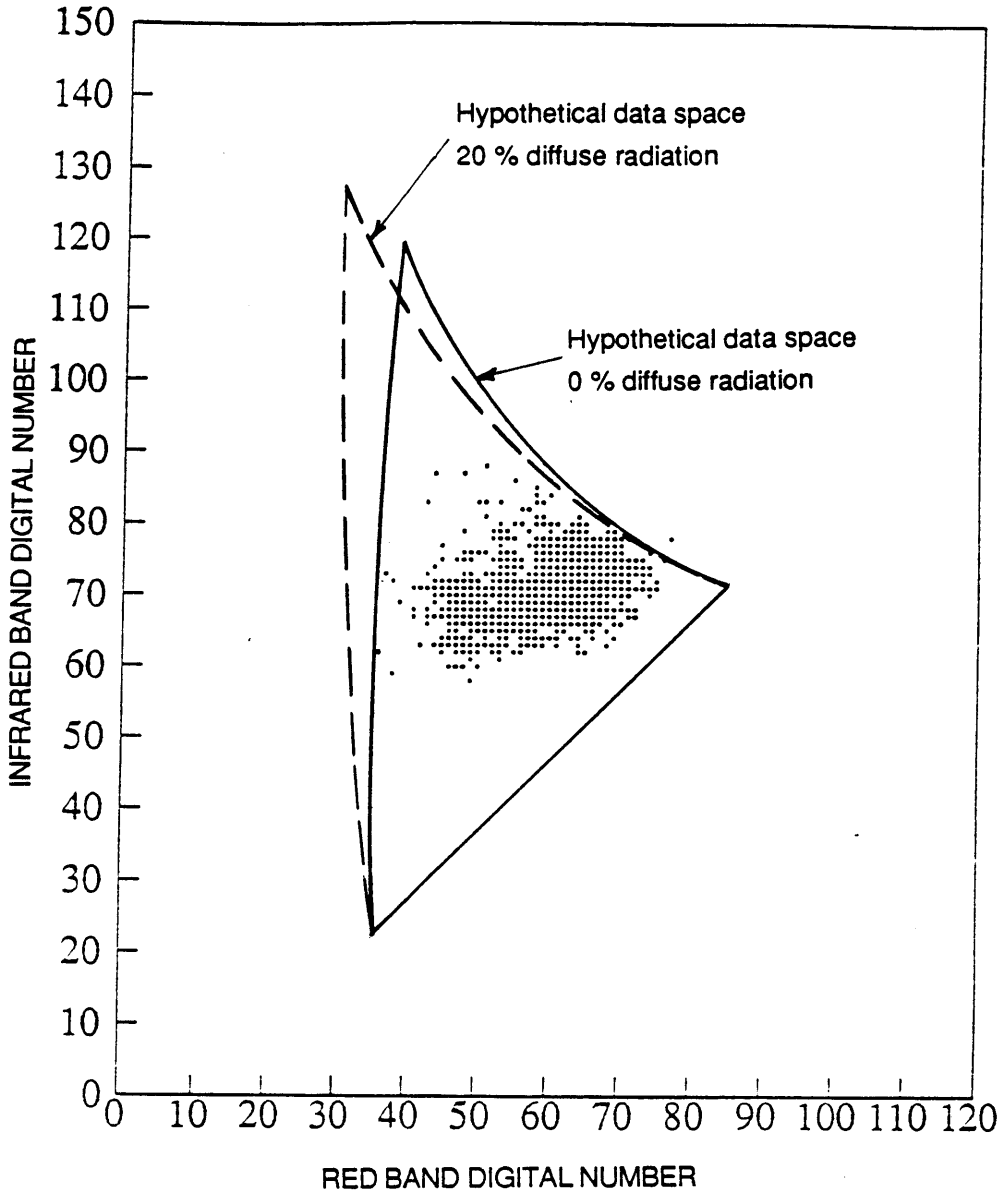

Figure 8.14 Hypothetical red–infrared data space for different amounts of backscattered diffuse radiation.

radiation cases, as compared to the actual scattergram. The hypothetical space for the 0% case was obtained in the same manner as the aerial case using (8.13) through (8.18), except that $R(\lambda)$ was replaced by $DN(\lambda)$, and the component reflectances were replaced by the effective reflectances. The data space for the 20% case was obtained using the same procedure, except that the assumed values of diffuse radiation were added to those equations. The results indicate that the peak of the 20% case is located further from the soil line than the 0% case. Since the positions of the actual scattergram and soil line do not change, the estimate of fractional cover is directly related to the relative position of the hypothetical peak. As the peak moves further away from the soil line, the estimate of fractional cover decreases.

An alternative way of plotting the 20% case is to use (8.13) through (8.18) as described above without adding the diffuse terms. The "adjusted" data space would be identical in size and shape as the 20% case plotted in Figure 8.14, but the entire space would be shifted 12 units downward and 12 units to the left.

While the overall results of the analysis provide analytically reasonable quantities, they indicate the increasing difficulty in the ability to estimate fractional vegetation cover when the diffuse component becomes large. Of particular concern is the rapid decrease in the estimated vegetation reflectance with increasing diffuse radiation. When the diffuse component is at 30 percent, the vegetation signal is only (1)(0.17)/18, or about one one–hundredth of the magnitude of the diffuse term. The signal to noise ratio is thus very small and even relatively minor perturbations in atmospheric effects would violate the assumption of horizontal homogeneity. Thus, accurate inversion for vegetation properties under conditions of moderate diffuse radiation seems unlikely.

Chapter 9

SUMMARY

9.1 Principal Conclusions

The research in this report has demonstrated that it is theoretically feasible to estimate spatially–variable bulk properties of semivegetated landscapes at subpixel scales for optically–thin atmospheres using only one set of multispectral observations without ground truth, at least for a limited range of landscapes. The approach relies on the physically–based conceptualization of landscapes as stochastic–geometric reflecting surfaces, which can possess variability in both the geometry of the shape and spatial distribution of the plants, as well the vegetation and soil background reflectance. The degree to which subpixel parameters can be retrieved depends on several factors including knowledge of the structure of the landscape, the number of landscape variables, the magnitude of the Sampling Scale Ratio, and the ability to identify groups of pixels within the red–infrared scattergram which possess common attributes.

An important feature of the inverse procedure is that it takes advantage of the multispectral nature of the data by solving equations associated with both the red and infrared wavelengths simultaneously. It thus extends the work of others (Otterman, 1984; Li and Strahler, 1985) who have inverted geometric models using only one band and assumed reflectances. The methodology offers a physically–based alternative to current practices which are highly empirical.

The reflectance model and inverse technique are primarily applicable to regional scale hydrologic investigations where the parameterization of numerous plant and soil properties is not feasible nor of practical importance at such large

scales. By absorbing the variability of such properties into a few bulk plant and soil variables, an inherent tradeoff is made between the amount of physical detail which can be modeled or estimated, and the size of the region which can be investigated. The technique relies on the existence of a large number of pixels possessing a wide range of soil and vegetation. Thus, when only a few pixels are available, or when the entire scene is homogeneous, a different version than those presented above should be considered.

The inverse method has been tested only on idealized simulated scenes and one conifer watershed using both aerial and satellite data. Good results were achieved in the case of Beaver Creek despite some major assumptions including the Poisson distribution of the trees, constant vegetation reflectance, especially for the infrared band, similar soil reflectance for the soil line and the semivegetated areas, and the neglect of shadow contributions for small η. Further, the procedure had to be adapted to each case based on the shape of the scattergram and the limited knowledge of the landsurface. While those algorithms worked well for both the idealized and actual cases, their general applicability to other semivegetated landscapes is unknown. Thus, further testing is warranted on a wide range of other types of semivegetated landscapes in order to validate and improve upon the methodology presented in this report.

The landscape reflectance simulation model developed in this research has been shown to be an effective mechanism for investigating the sensitivity of landsurface variability on the behavior of multispectral data acquired at scales representative of current satellite pixels. That feature provides a useful alternative to the toilsome and expensive task of understanding variability in actual scenes by obtaining simultaneous ground truth for a large number of pixels. By sequentially altering different variables into the simulations, valuable insight on the

multispectral behavior of actual images can be obtained. Modeling of the landscape is facilitated through the introduction of the non–dimensional similarity parameter, η, which generalizes the results without constraining them to any one geometric shape or solar angle.

A principal finding from the simulations has been the recognition of the correlation which develops among fractional canopy cover, shadow, and illuminated soil background with increasing pixel scale. The analytical formulation of the $g_I(m)$ relationships for different spatial distributions (Figures 7.8, 8.4, and 8.11), based on either deterministic or statistical reasoning, has facilitated the solution of the inverse problem by eliminating one or two unknown parameters. That correlation has been shown to be a principal mechanism that contributes to the evolution of the tasseled cap of red–infrared scattergrams of semivegetated landscapes.

The moments of the reflectance equations have been expanded in terms of the moments of the individual variates of the stochastic–geometric reflectance model for the purpose of solving the inverse problem: The estimation of subpixel parameters given only the red–infrared scattergram and limited assumptions on the structure of the scene. The inverse procedure involves equating those analytical moments to the actual moments of the image, and solving the equations simultaneously, without the need for ground truth.

Knowledge of the relationship between the physical structure of the landscape and the shape and structure of the scattergram has been shown to facilitate the inverse problem in at least two manners. First, it provides a mechanism for identifying pixels with common attributes, especially for cases with large Sampling Scale Ratios. Second, it allows the formulation of additional moment equations, conditioned on those common attributes, which are often much

simpler than the general moment equations required for cases with small Sampling Scale Ratios.

The exact formulation of the inverse procedure depends on several factors related to the structure of the landscape and to the interpretation of the red–infrared scattergram. There is no single recipe that can be listed that accommodates all situations. However, several general steps common to the solution of most of the inverse examples given in this report are as follows:

i) All the radiometric observations for a particular region are plotted in the red–infrared data space.

ii) A narrow band of pixels lying at the base of the scattergram is selected as representative of the soil background line, and the reflectance moments of that ensemble of pixels are computed.

iii) The solar zenith angle is computed based on the time of overpass.

iv) If possible, an assumption is made on the bulk geometric shape of the plants on the landscape. The similarity parameter, η, is then calculated based on the plant shape and solar zenith angle. If the shape is unknown, then η may have to be included as an unknown in the analysis.

v) The Sampling Scale Ratio is determined based on the scale of the pixel, the similarity parameter, and an assumed value of the horizontal scale of the tree. This calculation is only an order of magnitude estimate and an exact value of the tree size is not required.

vi) For small Sampling Scale Ratios, the inverse problem is solved using the full set of moment equations. Their number and complexity will depend on the number of assumptions one is willing to make on the structure of the landscape. In some examples, the moment equations can be simplified by neglecting relatively small terms, such as the shadow terms when η is small. In general, only the

moments of the fractional cover types for the entire ensemble of pixels can be retrieved for small Sampling Scale Ratios.

vii) For large Sampling Scale Ratios, several conditional moments can be written for pixels with common attributes, identified through ones knowledge of the shape and structure of the scattergram. In general, for cases in which vegetation reflectance can be assumed constant, pixels of equal vegetation amount will orient themselves parallel to the soil line. In such cases fractional cover can be estimated on a pixel–by–pixel basis.

The case studies indicate that the idealized tasseled–cap scattergram is not always realized due to limited combinations of soil and vegetations properties. However, inversion can still be achieved if a representative soil line is identified.

Finally, the analysis of the Thematic Mapper data indicates that subpixel canopy cover can be estimated on a pixel–by–pixel basis without specifying the absolute magnitudes of the soil and vegetation reflectances, even when there exists a small backscattered diffuse component. That conclusion is limited to cases with horizontally–homogeneous atmospheres and regions of low contrast. Preliminary results indicate that neglecting the diffuse radiation component tends to overestimate the mean fractional cover of the region.

9.2 Future Research

There are several directions in which future research can proceed. First, there is a need to understand the sensitivity of the present conclusions to the various assumptions required for inversion. That can best be achieved with the aid of the simulation model. The model can be extended to include other factors including different spatial distributions of plant spacing and soil reflectance,

atmospheric effects, and other similarity values. Inversion techniques can then be applied to the new set of scenes. A further extension which would improve the flexibility of the model is the incorporation of topographic effects, for instance, in conjunction with U.S.G.S. digital elevation maps.

A more rigorous analysis of the effects of diffuse radiation, both surface reflected and solar backscattered, is warranted in order to understand its effect on both the structure of the scattergram and the estimation of subpixel properties. For the inverse procedure, it might be possible to include the diffuse terms as unknowns into the analysis. The limits to which the coupled landsurface–atmosphere radiation model is applicable needs to be defined in terms absolute values of the principal surface and atmospheric properties, such as optical depth, landsurface reflectance, and solar zenith angle.

An important application of the reflectance model is the understanding of the physical basis of common vegetation indices. Although the vegetation indices are very empirical, they are nonetheless widely used by scientists for the assessment of vegetation amount. The simulation model can be used to generate common indices to investigate the sensitivity of subpixel variability on the shape of vegetation indices, in a manner similar to that used in the present report for the understanding of red–infrared scattergrams.

The original motivation for the development of the present research was to define landscape properties necessary for the application of the equilibrium hypotheses noted in Section 1.1, specifically with regard to estimating soil hydraulic properties. The analysis of the Beaver Creek vegetation in this report, together with additional data already collected (Jasinski, 1987), provide the necessary input to complete that study.

Appendix A

Red–Infrared Data Spaces of Simple Hypothetical Semivegetated Scenes

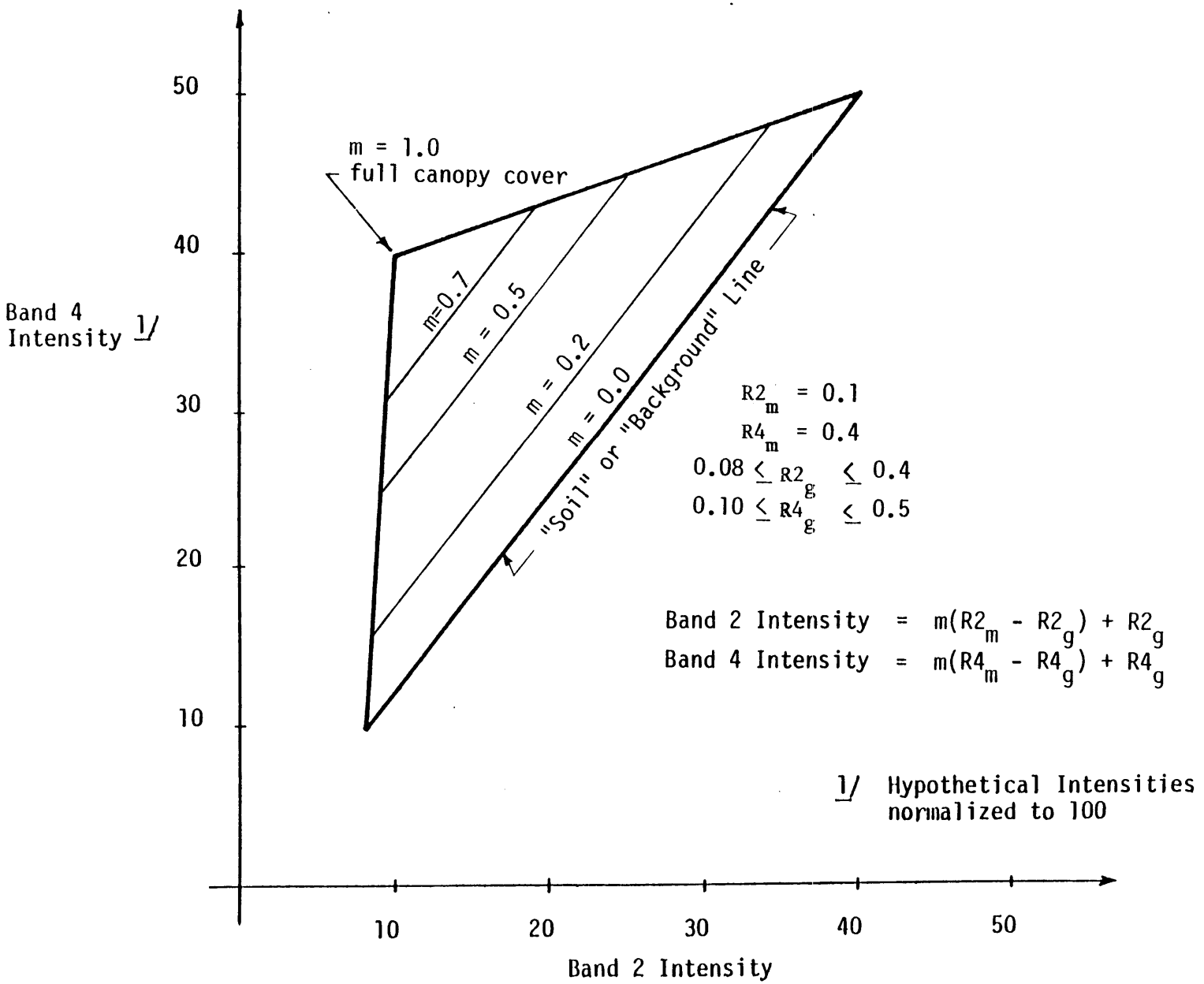

Figure A.1 Hypothetical red–infrared space of constant vegetation reflectance landscape.

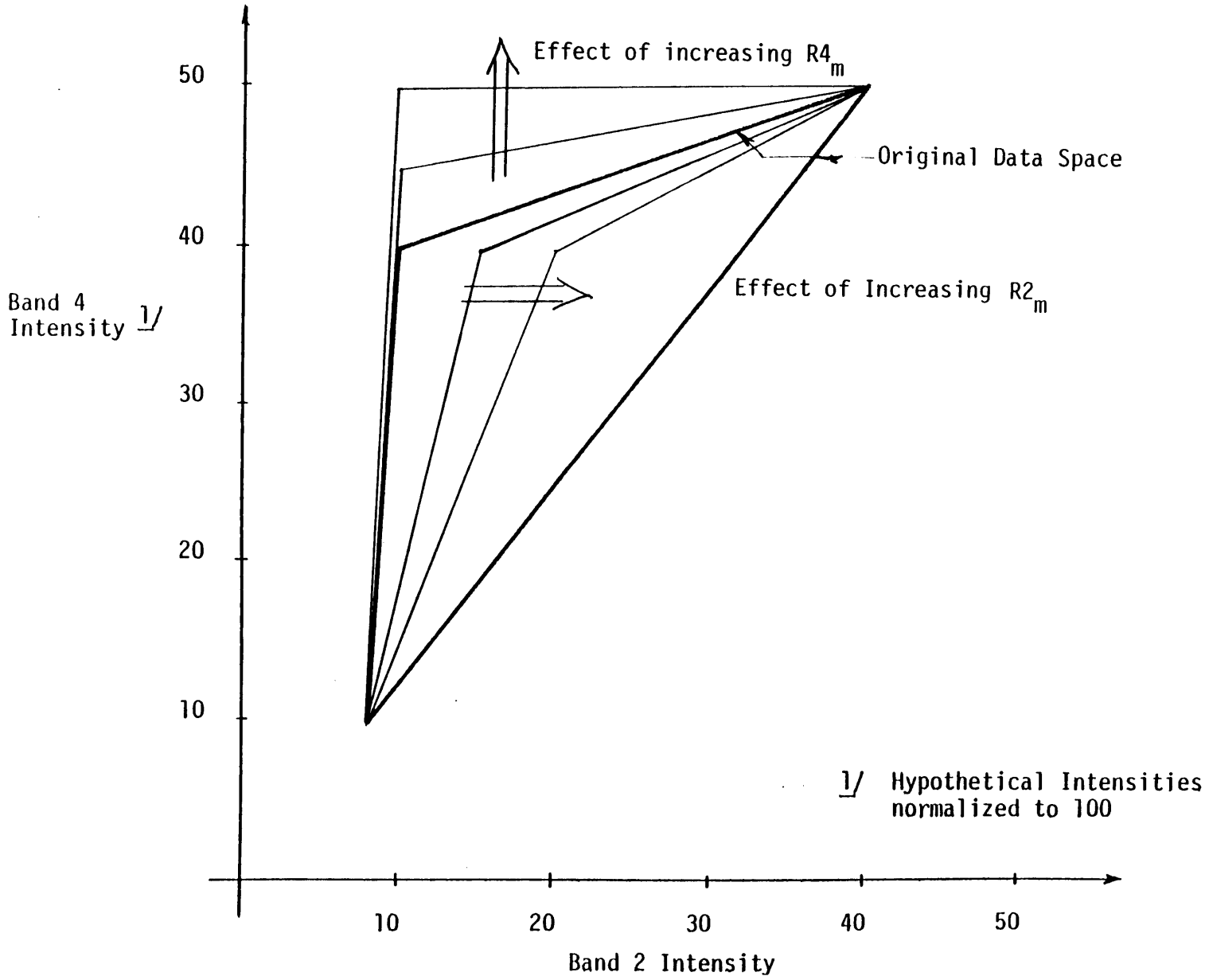

Figure A.2 Effect of increasing vegetation reflectance on hypothetical red–infrared space.

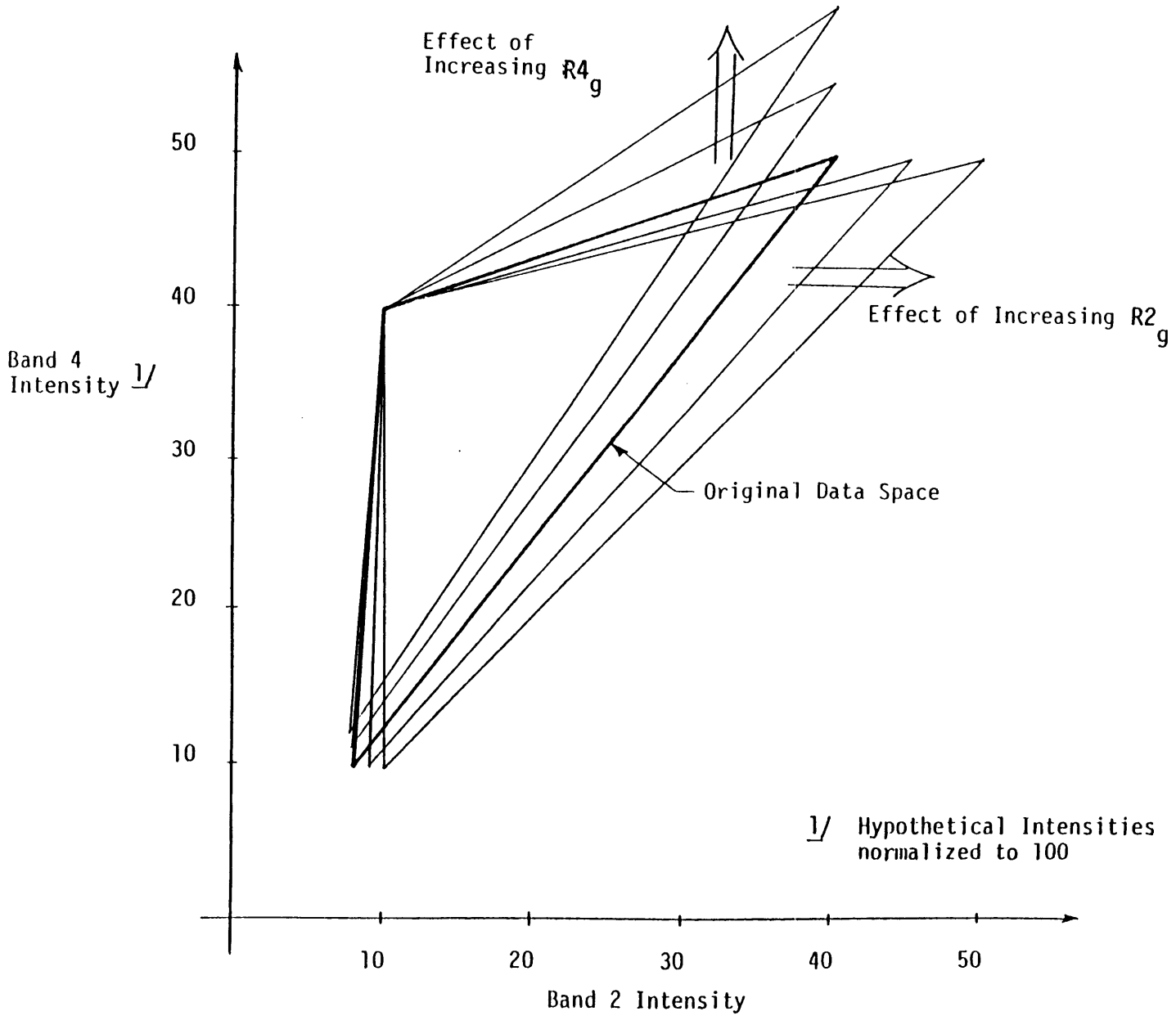

Figure A.3 Effect of increasing soil reflectance on hypothetical red–infrared space.

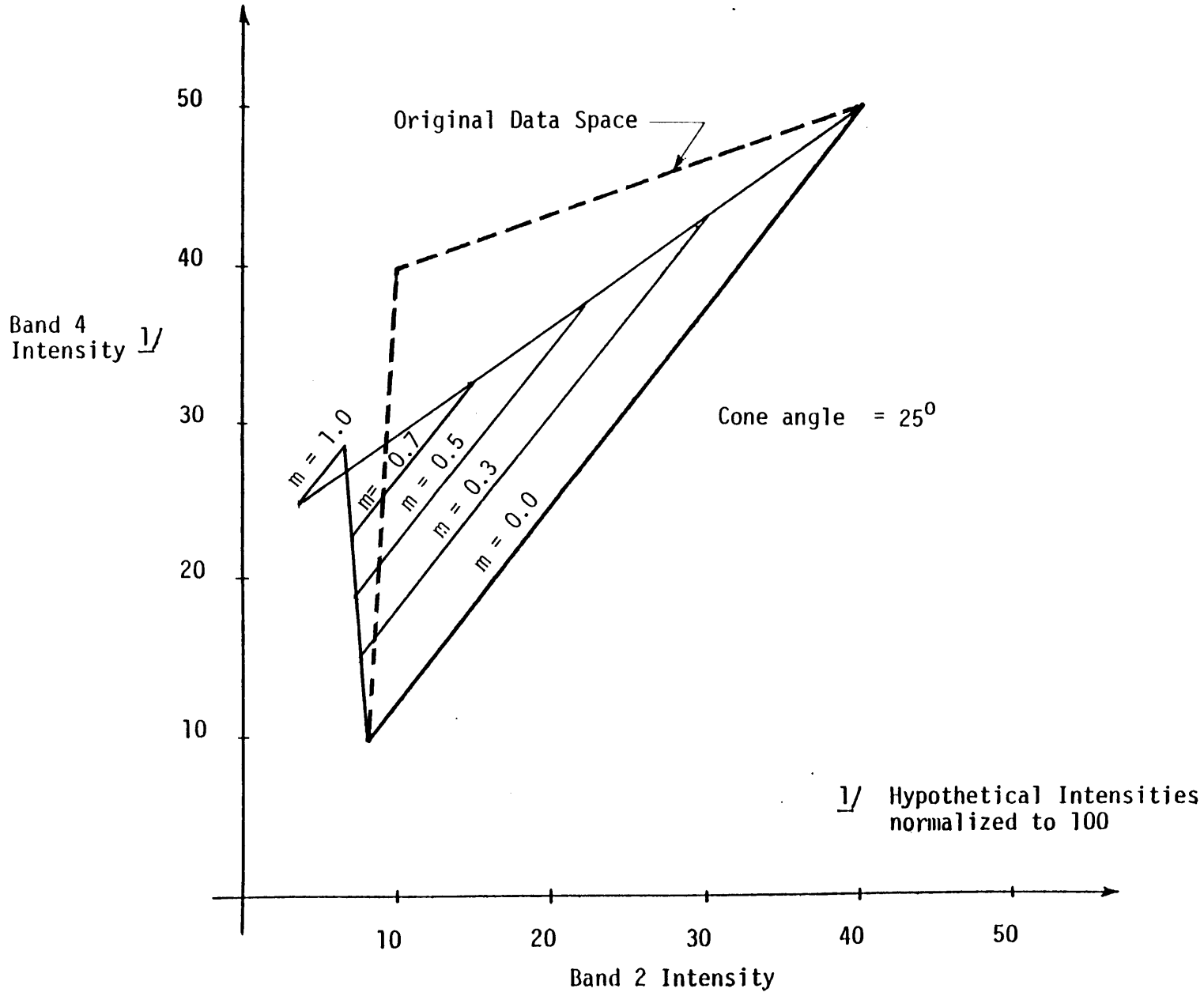

Figure A.4 Effect of shadows cast by cones on hypothetical red–infrared space.

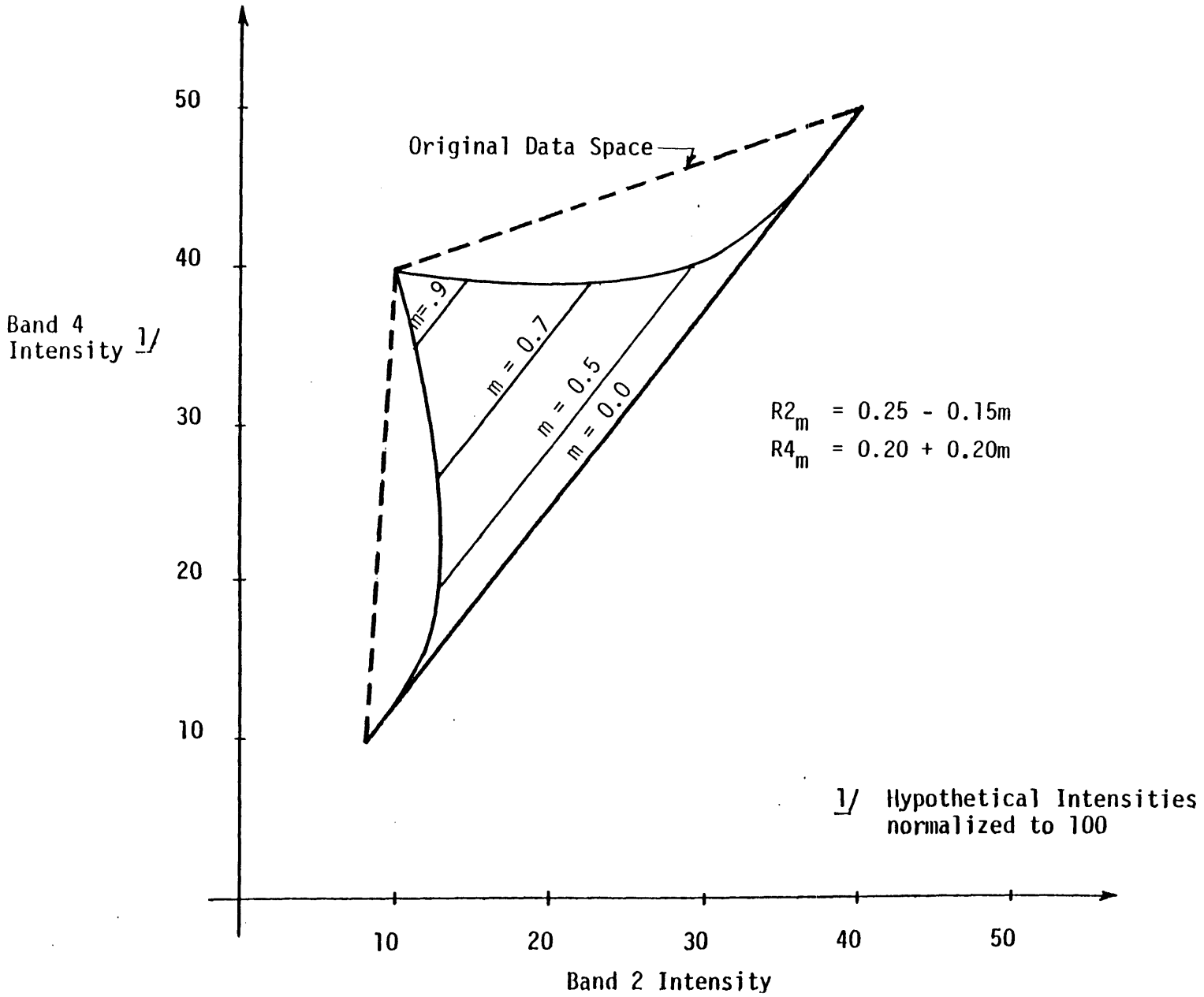

Figure A.5 Effect of variable vegetation reflectance on hypothetical red–infrared space.

Appendix B

Analysis of Landsat 2 Multispectral Scanner Data for the Taos Study Area

During the early stages of this research, several linear regressions were conducted between formulas using Landsat 2 MSS data and fractional cover estimated from aerial photography, for a region centered over Taos, New Mexico. That analysis was conducted prior to the development of the canopy–soil reflectance model and inverse procedures presented in the main portion of this report. The results of those linear regressions are presented in this appendix. Details of the work were reported by Jasinski and Eagleson (1986).

It is noted at the outset that the correlation coefficients of the regression analyses were low and the results of the regressions were considered inconclusive due to a variety of reasons. The primary reasons included i) uncertainty in the quality of the MSS data, which had gone through several preprocessings including at least two resamplings, ii) problems in registering a given Landsat pixel to a particular location on the aerial photograph, and iii) difficulties in estimating fractional cover using the color aerial photographs. Nonetheless, some insights were gained and a summary of the regression analyses is provided below.

B.1 Site Description

The Taos Study Area is outlined in Figure B.1. The land includes a wide variation in surface relief, ranging from flat plains to rolling foothills, to detached high ridges. Elevation ranges from 6,000 to 10,000 feet. Vegetation tends to follow the topography. The lower flats are covered with blue grama and

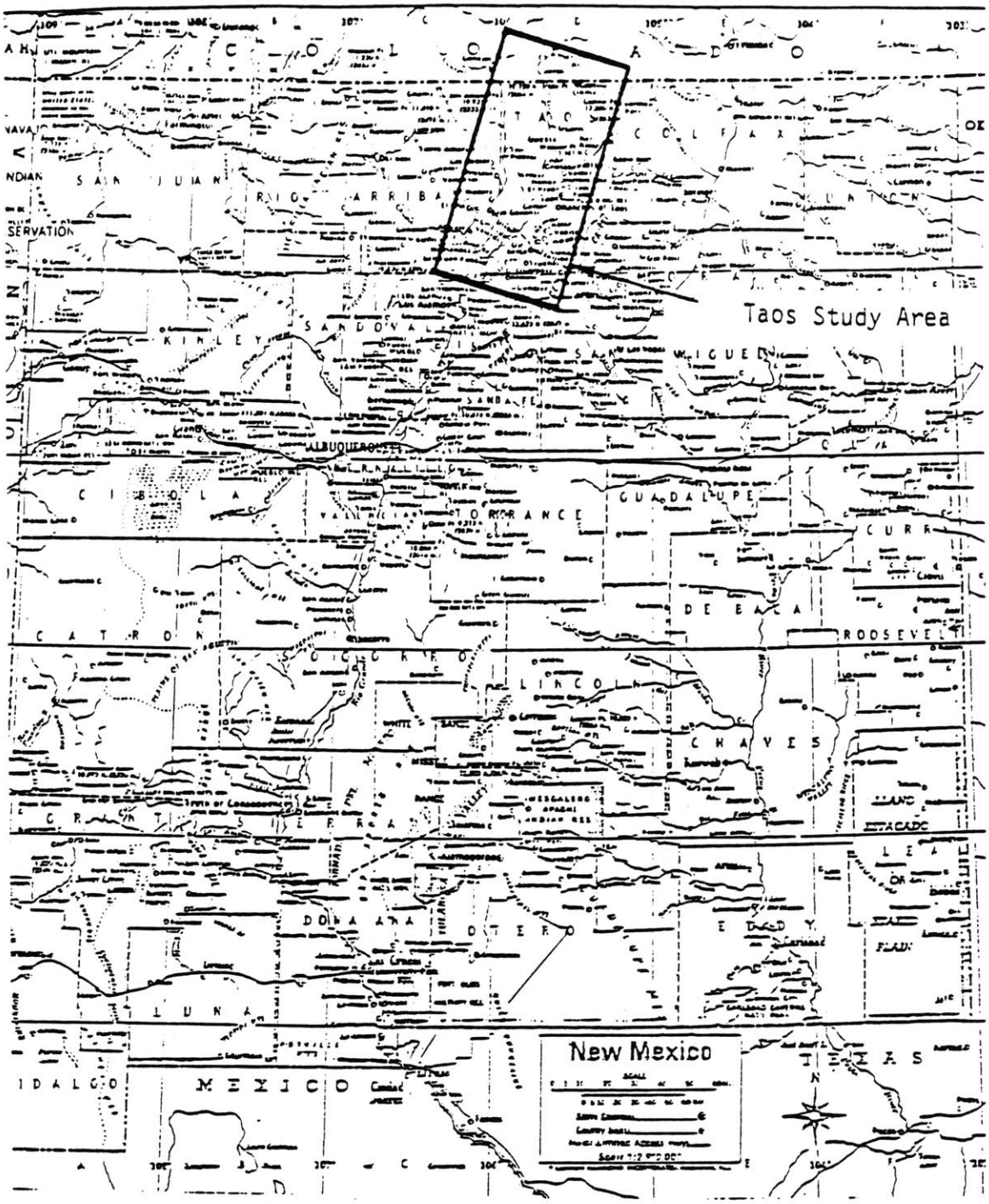

Figure B.1 Location Map, Taos Study Area.

wheatgrass grasslands, and snakeweed, rabbitbrush and sagebrush shrublands. Pinyon–juniper woodlands are found in the rolling foothills. At the higher elevations, there is ponderosa pine, spruce, fir and aspen. Percent cover ranges from nearly 0 to 100 percent, with the majority of the area 40 to 60 percent covered. At least two trends in percent vegetation cover can be readily observed. They are, first, a decreased percent vegetation cover with decreasing altitude, and second, a less dense cover on south–facing slopes compared to north facing slopes at the same elevation.

B.2 Aerial and Satellite Data

The database consisted of Landsat MSS data, and 1:3000 aerial photographs, supplied by the Bureau of Land Management, Branch of Remote Sensing, Denver, Colorado and the Bureau of Land Management, Taos Resource Area Office, Taos, New Mexico (Work, 1983).

Landsat Data. The Landsat scene used for this analysis was derived from an original Landsat MSS scene, Number 21608–16562, on June 18, 1979. The scene included some preprocessing by BLM in addition to that routinely supplied by the EROS Data Center on original CCTs. The processing consisted of 1) the removal of certain radiometric and electronic anomalies known as line drops and banding by filtering, 2) the removal of minor geometric distortions which were inherent in the data, and 3), the registration of the Landsat data to a Universal Transverse Mercator (UTM) map projection using a resampled 100 meter square pixel. Since the regression procedure worked on a pixel–by–pixel basis, correct registration was of paramount importance. Landsat data were fitted to the UTM grid by visual inspection through the use of color slides of Landsat segments projected directly onto USGS topographic maps.

Aerial Photography. Approximately eighty color aerial photographs at about 1:3000 nominal scale were borrowed from the Bureau of Land Management, Taos Resource Area Office, Taos, New Mexico for the current study. Those were taken on June 16, 1981 using a relatively low flying aircraft with a nine inch square format and a six inch focal lens.

Photographs were selected to represent a broad range of vegetation cover and to exclude agricultural and urban areas. Because of the random nature of the photograph locations, the eighty photographs were distributed over twenty different USGS quadrangles.

Photograph analysis included several steps. First, photographs were visually registered to the UTM grid by comparing topographic features of the photograph to those of the USGS map. Next, the photograph was divided into pixels 100 meters square using a clear overlay and the center eight pixels were selected from each photograph. Each pixel at 1:3000 scale was about 1 to 1–1/2 inches square and contained a random vegetation cover interspersed with soil background.

Fractional vegetation cover for each pixel were analyzed using an image analyzer connected to a video camera. Percent cover was determined by selecting for each pixel the threshold "grey level" associated with only the vegetation cover and then computing the total area below (darker than) the threshold level. The procedure worked satisfactorily for pixels which contain distinct vegetation and soil characteristics. The error of the canopy cover estimate for such cases, which represent roughly one half of the over 100 pixels analyzed to date, was several percent. For pixels containing dark soils or significant shadows, error was estimated to be roughly ±10 percent. Roughly twenty percent of the pixels analyzed fit into the latter category.

B.3 Regression with Normalized Difference Vegetation Index

This analysis consisted of regressing the NDVI with ground truth obtained from the aerial photographs. Two variations of this approach were tested. A total of 116 pixels were used. The first variation involved using the NDVI defined in terms of actual integer DN values instead of reflectances. The second approach used actual radiances computed using conversion factors described by Markham and Barker (1986). The results are provided in Table B.1 below and shown on Figures B.2 and B.3.

Table B.1

Normalized Vegetation Index
versus Percent Cover

NVDI Variation	m	R^2
$VI_{DN} = \frac{2\times DN_4 - DN_2}{2\times DN_4 + DN_2}$	$m = 1.99\ VI_{DN} + 0.95$	0.61
$VI_R = \frac{R_4 - R_2}{R_4 + R_2} \times 100$	$m = 3.06\ VI_R - 111$	0.58

The results indicate that for both variations, about 60% of the change in NDVI can be explained in terms of percent vegetation cover.

B.4 Regression Using Direct Beam Equation

Assuming that the landscape consists of only two cover types, soil and vegetation, equation (4.10) can be rewritten,

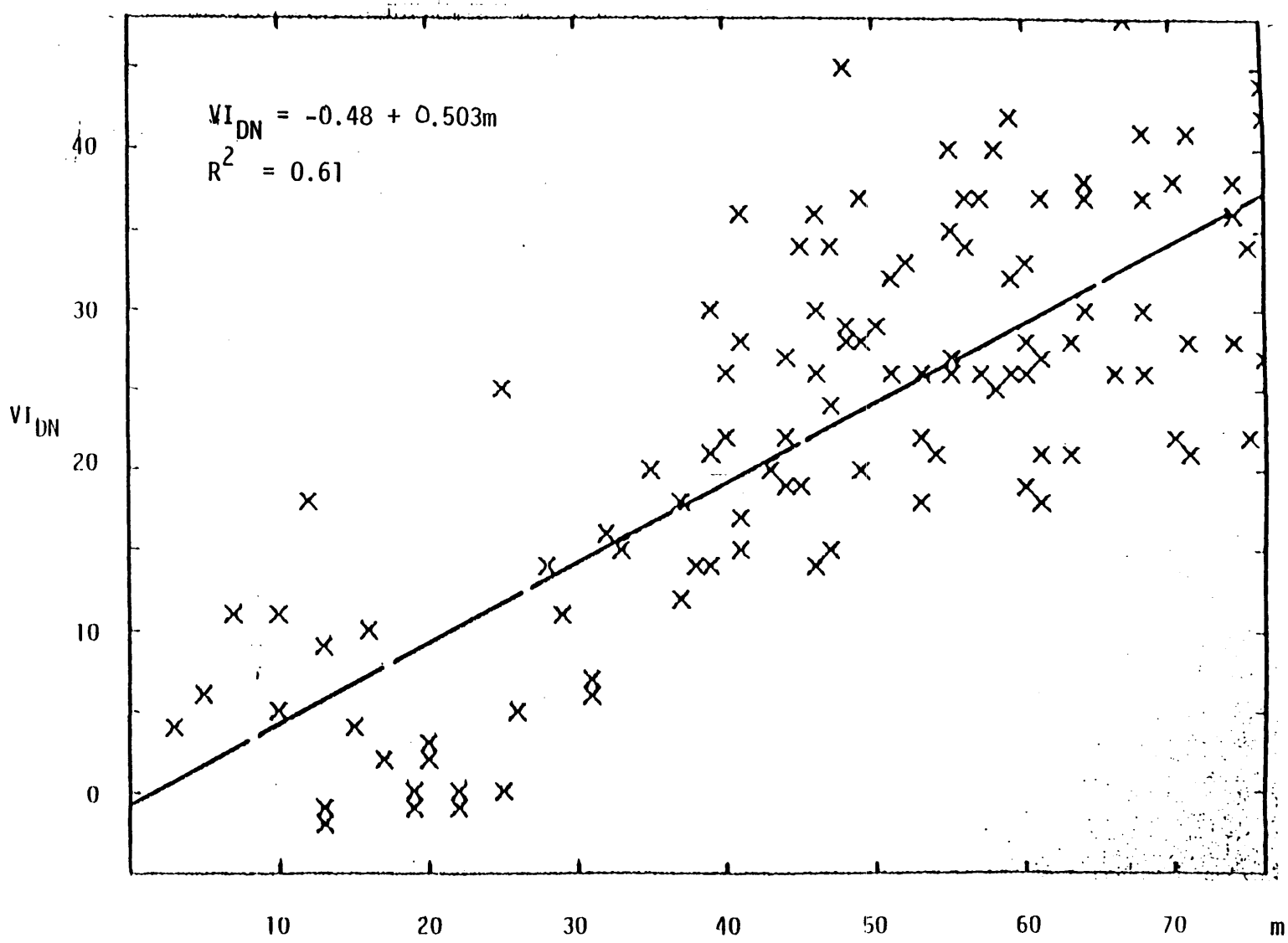

Figure B.2 $NDVI_{DN}$ versus percent green canopy cover.

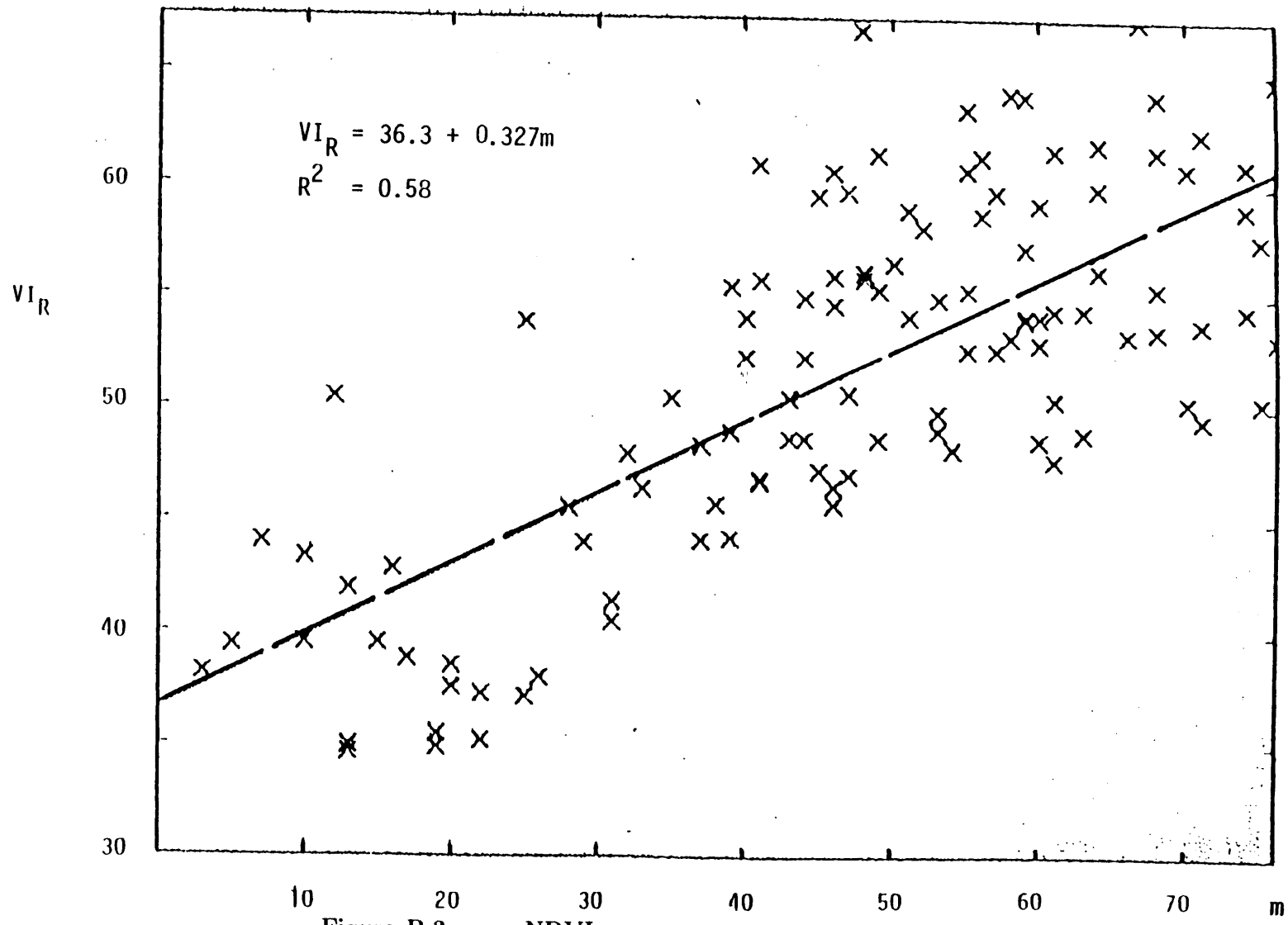

Figure B.3 $NDVI_R$ versus percent green canopy cover.

$$m = \left[\frac{L}{L'} - R_g\right]/[R_m - R_g] \qquad (B.1)$$

For constant reflectances, m is thus linearly related to the observed direct beam radiance or the DN values. With this in mind several linear regressions were carried out with m as the dependent variable and the DNs as independent variables. The results are shown in Figures B.4 and B.5 and summarized in Table B.2,

Table B.2

Summary of Linear Regressions

Direct Beam Equation

Regression Equations	R^2
$m = 126 - 199DN2$	0.53
$m = 377 - 138DN4$	0.10
$m = 120 - 197DN2 \cos \beta$	0.53
$m = 143 - 189DN2/\cos\theta$	0.42

where DN2 and DN4 represent MSS bands 2 and 4, respectively.

Variations of the above direct beam equation include accounting for changes in zenith angle due to topographic slope. For surfaces with average slope β, the equation (B.1) can be rewritten

$$m = \left[\frac{L\cos\beta}{L'} - R_g\right]/[R_m - R_g] \qquad (B.2)$$

Zenith angle effects can be included by

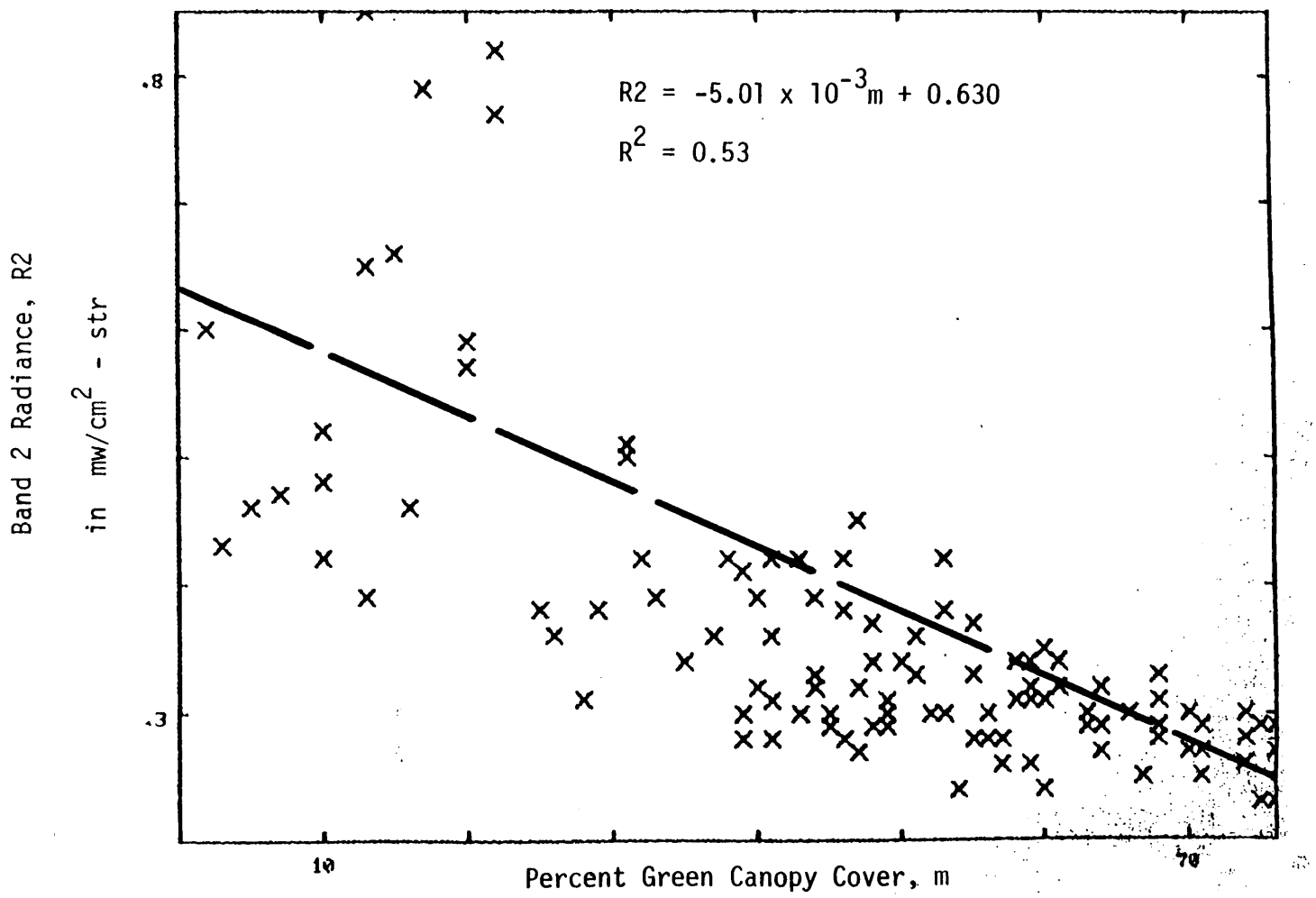

Figure B.4 Band 2 versus percent green canopy cover.

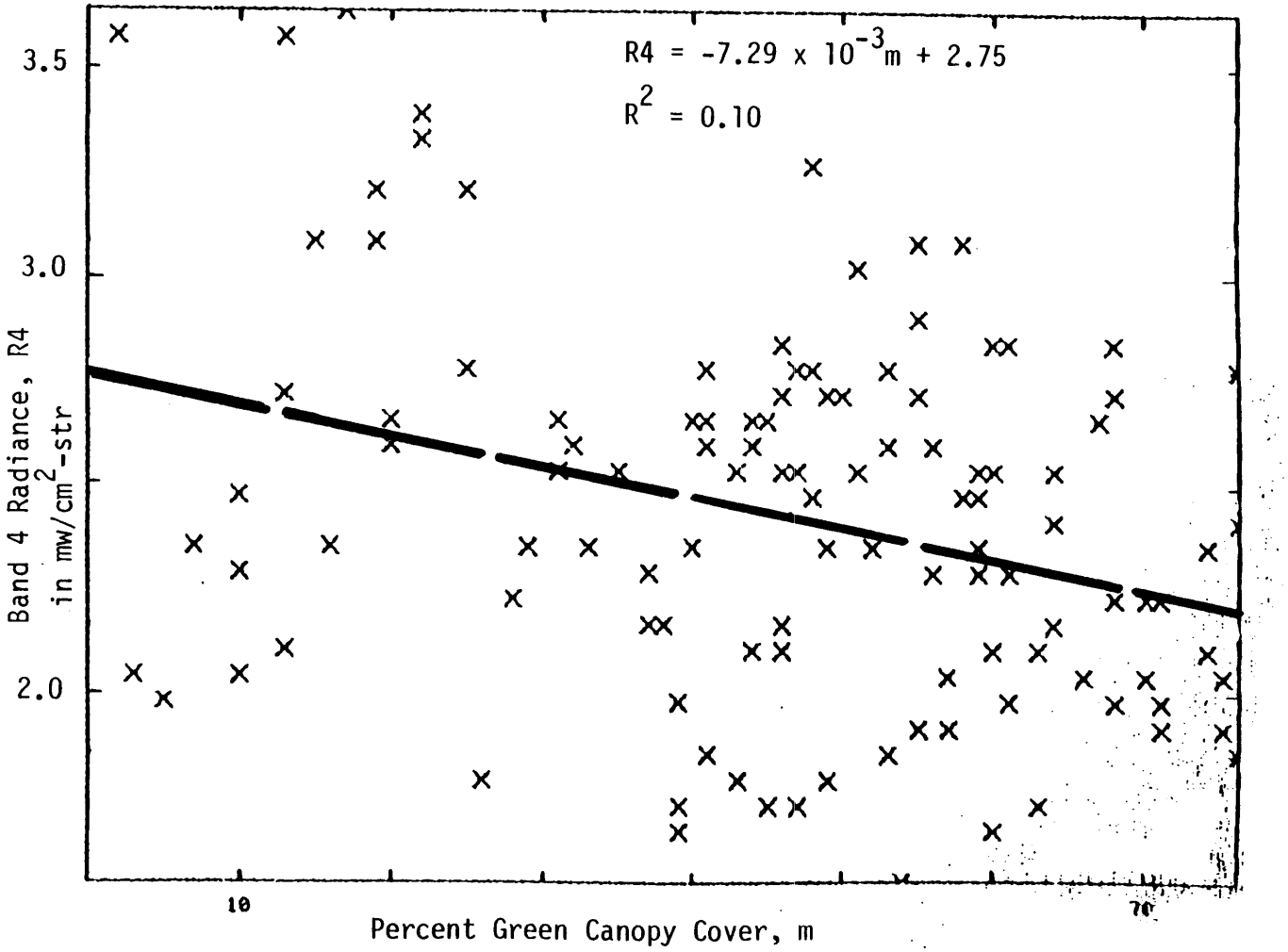

Figure B.5 Band 4 versus percent green canopy cover.

$$m = \left[\frac{L\cos\beta}{L'\cos\theta} - R_g\right]/[R_m - R_g] \qquad (B.3)$$

where β is the ground slope, measured from USGS 7.5–minute topographic maps. Zenith angle was computed using the following formula from Iqbal (1983),

$$\begin{aligned}\text{Cos}\ \theta = &(\sin\phi\cos\beta - \cos\phi\sin\beta\cos\gamma)\sin\delta \\ &+ (\cos\phi\cos\beta + \sin\phi\sin\beta\cos\gamma)\cos\delta\cos\omega \\ &+ (\cos\delta\sin\beta\sin\gamma\sin\omega)\end{aligned} \qquad (B.4)$$

where

δ = solar declination

ω = hour angle

γ = surface azimuth angle

β = average slope of pixel

Solar declination and hour angle were estimated from the time of Landsat overpass.

The results of the linear regression including the ground slope and zenith angle corrections were also poor, as indicated on Figures B.6 and B.7, and on Table B.2. Although part of the explanation for the poor correlation may simply be due to the bidirectional reflection characteristics of the soil, a more likely explanation may also simply be the inaccuracies introduced by measuring small distances off the topographic maps. At the 1:24000 scale, pixels are less than 0.2 cm^2 in area and small inaccuracies in measurement or pixel registration can cause serious error in the regression analysis.

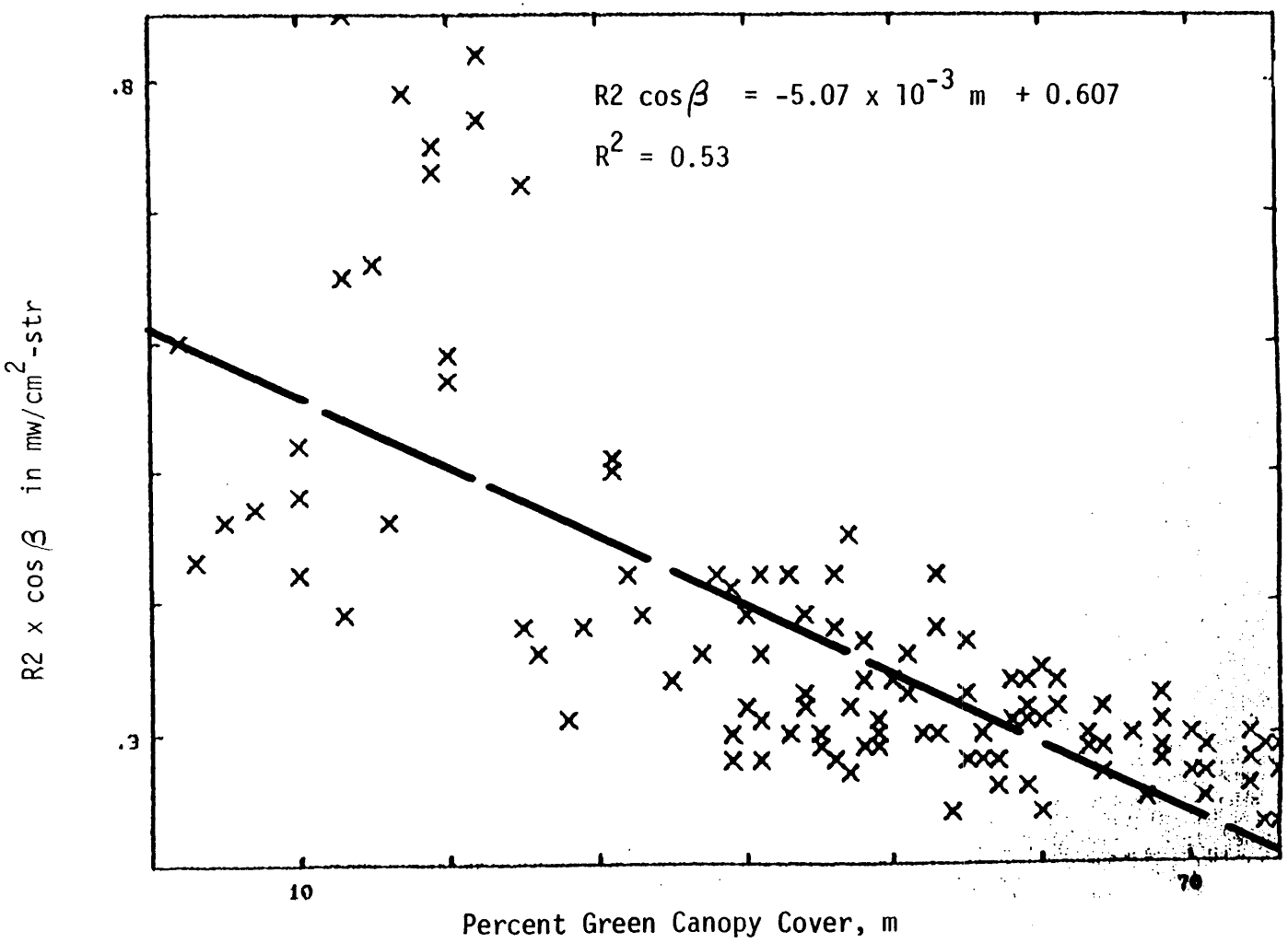

Figure B.6 Band 2·cosβ versus percent green canopy cover.

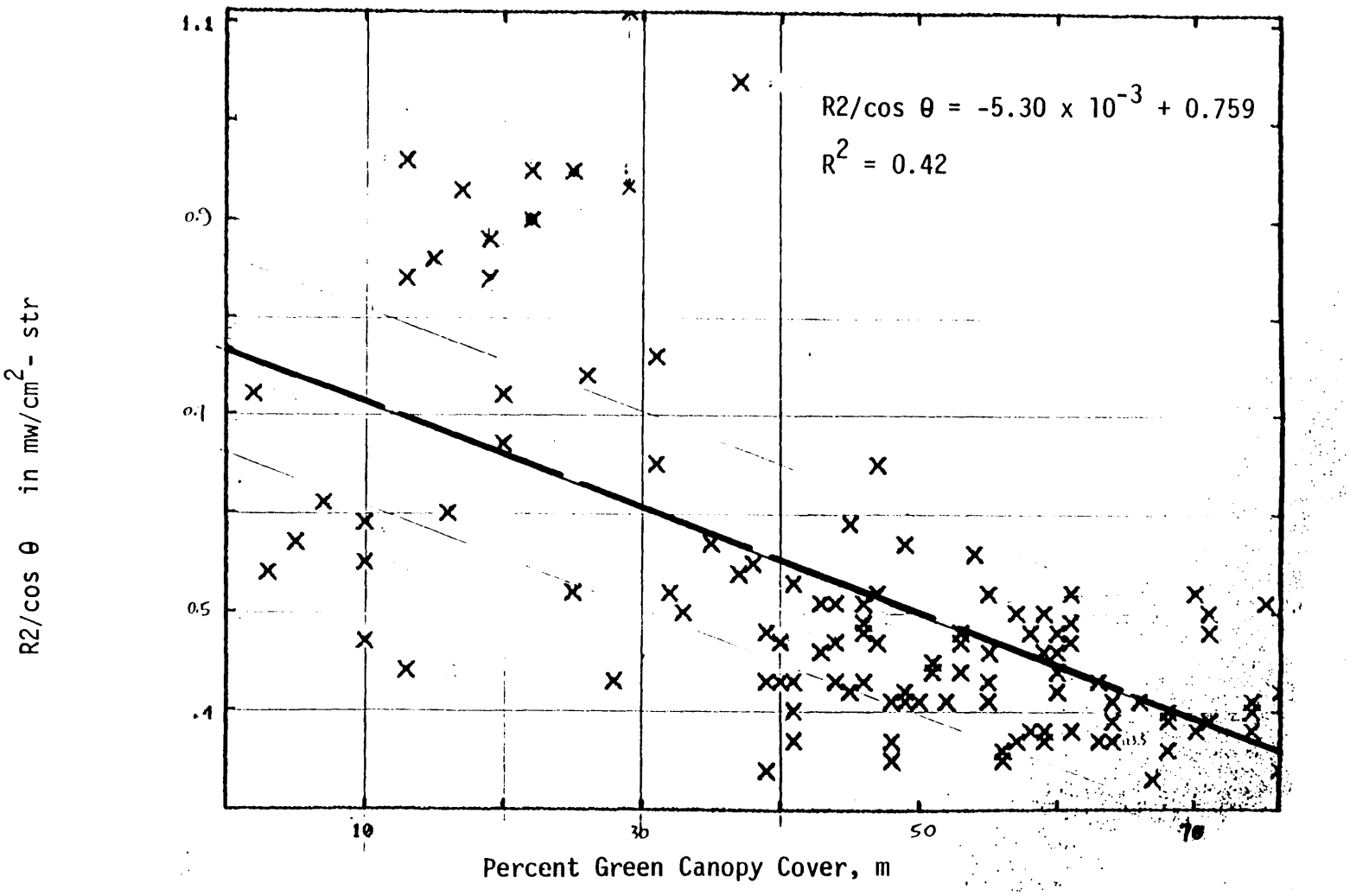

Figure B.7 Band 2/cosθ versus percent green canopy cover.

B.5 Regression with Kauth–Thomas Indices

The Kauth–Thomas greenness and brightness indices were computed and then regressed with actual percent cover obtained from the aerial photographs. The results are shown in Table B.3. They indicate, contrary to expectation, that brightness appears to explain more of the variation in m than greenness.

Table B.3

Regressions with Kauth–Thomas Indices

Index	R^2
Greenness, GU	0.24
Brightness, BI	0.39

The regression analyses yielded,

$$m = 10.47 + 0.14\ GI \qquad (B.4)$$

$$m = 82.82 - 0.48\ BI \qquad (B.5)$$

B.6 Multiple Linear Regression

Multiple linear regressions were carried out with the same data set as in previous cases with percent cover as the dependent variable and the MSS band observations as independent variables. The two cases examined were m vs. DN1 and DN2, and m vs. DN1, DN2, DN3 and DN4. Once regression coefficients were obtained, theoretical percent cover obtained from the multiple linear regression analysis was regressed with actual percent cover in order to compare correlation

coefficients with other methods. The results for the second case are shown on Figure B.8 (for regression with four bands) and summarized on Table B.4.

Table B.4

Results of Multiple Linear Regression

Regression Equation	R^2
$m = -2.25\ DN2 + 0.70\ DN4 + 74.97$	0.53
$m = -2.07\ DN1 - 0.62\ DN2 + 0.20\ DN3 + 0.63\ DN4 + 72.25$	0.58

As expected, there is negative correlation with the visible bands and positive with the near infrared. It is also noted that the addition of bands 1 and 3 only contributes an increase of 0.05 in R^2.

B.7 Regression Using Linear Distances in the Red–Infrared Scattergram

The fractional cover of a given pixel estimated from the aerial photographs, m_g, was regressed with estimate of m based on the pixel's location in the red–infrared scattergram plotted in Figure B.9 (An expanded version of Figure 1.6). The procedure consisted of the following:

1) All data points within the segment were plotted.

2) Envelope lines are drawn along the three sides of the triangular data space. The soil line was drawn as a straight line emanating from the origin. (For the assumption of no shadows and constant vegetation reflectivities, all sides of the triangle must be drawn straight.)

3) Along the soil line, m was assumed equal to zero. Likewise, at the top of the triangle, m was assumed equal to one.

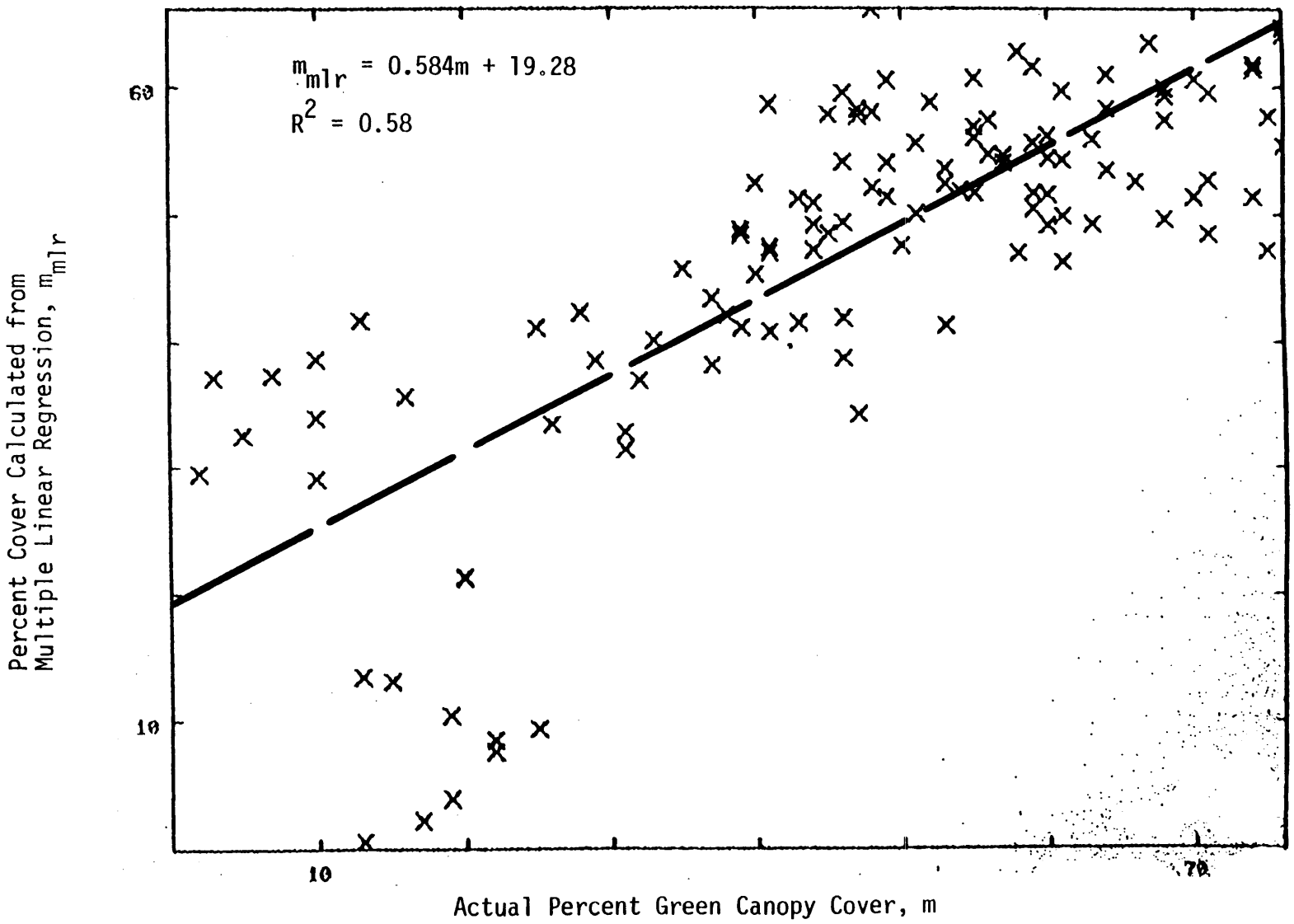

Figure B.8 Percent cover from multiple linear regression, m_g, versus actual percent cover, m.

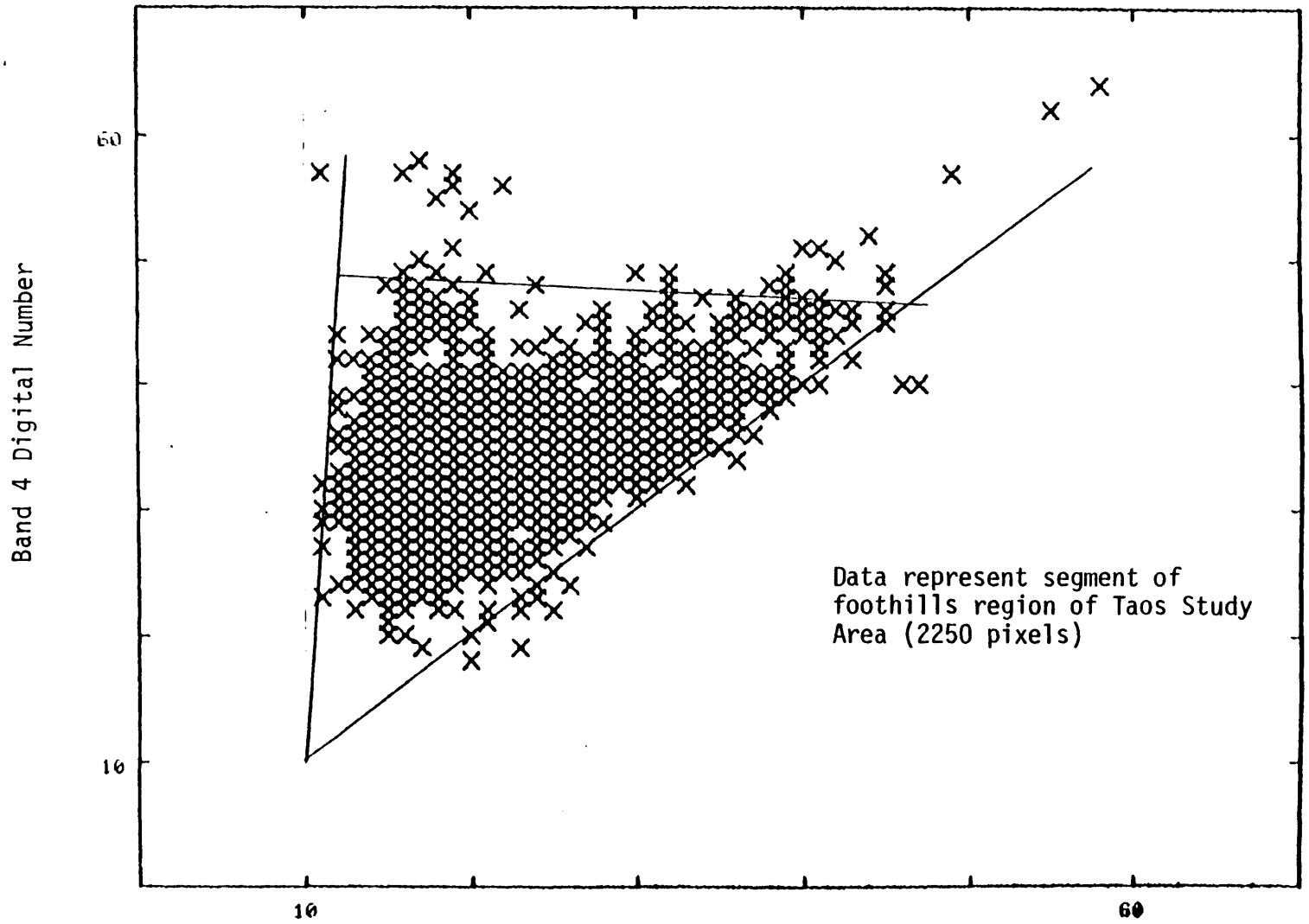

Figure B.9 Data plot of MSS Band 4 versus Band 2.

4) For constant vegetation reflectivity, m was assumed linearly related to the distance between the top and base of the triangle. For example, for a point exactly halfway between the top and the base, m was assumed equal to 50% cover.

The graphical results are shown in Figure B.10, which for clarity, includes only the data points with ground truth, and not the full scattergram. The R^2 value resulting from the regression of m_g with m was 0.34.

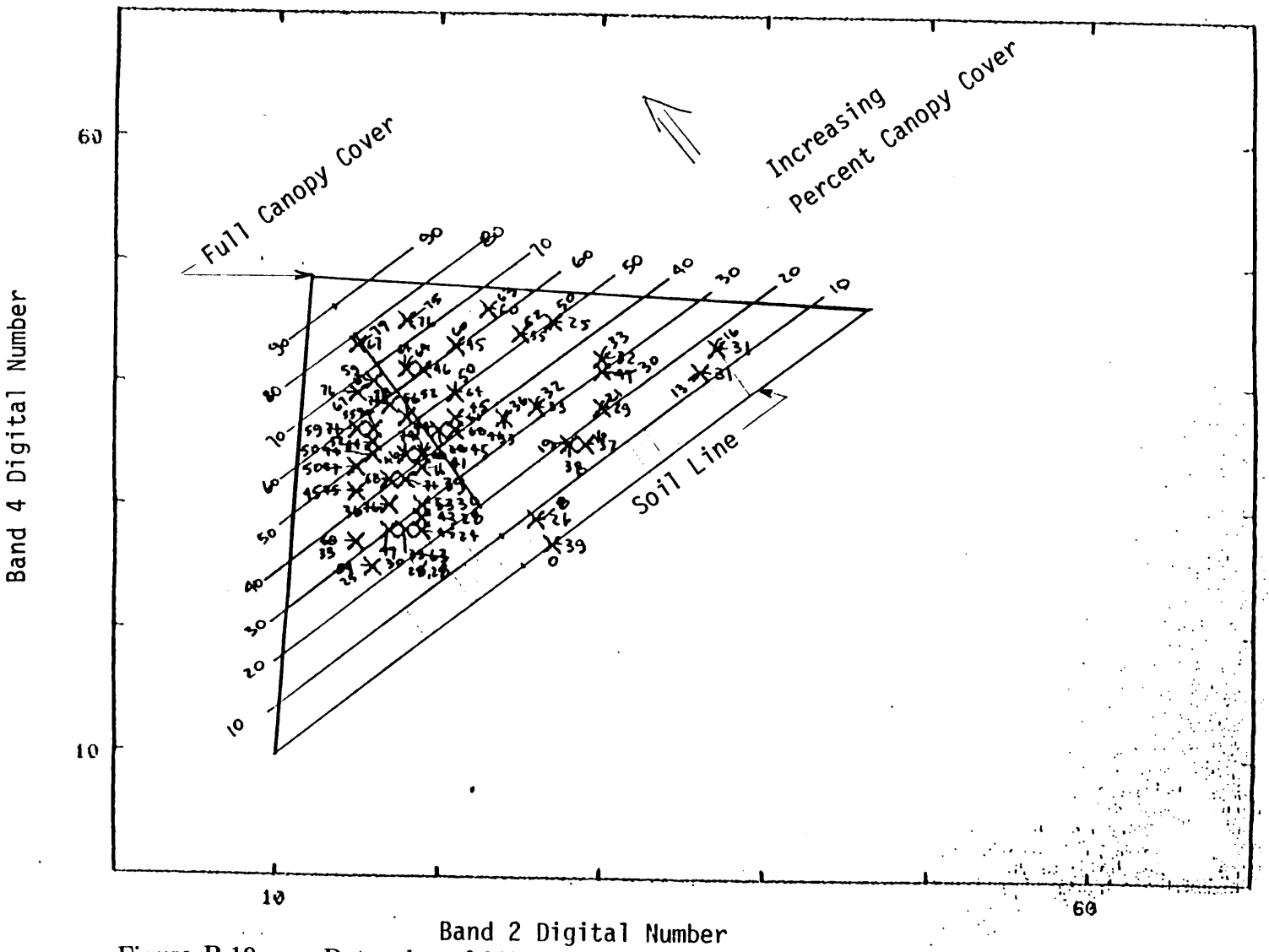

Figure B.10 Data plot of MSS Band 4 versus Band 2 for pixels with ground truth.

Appendix C

Derivation of Equations

This appendix describes the derivation and assumptions of the following equations presented in the main text:

C1.) General Reflectance Moment Equations

- C1.1) Mean Reflectance
- C1.2) Variance of Reflectance
- C1.3) Cross–Spectral Covariance
- C1.4) Spatial Covariance of Reflectance

C2.) Reflectance Moment Equations: Case V, Method 2

- C2.1) Mean Reflectance
- C2.2) Variance of Reflectance

C3.) Geometric Similarity Formula for Poisson Distributions

C1. General Reflectance Moment Equations

The reflectance equation is

$$R(\lambda,\underline{x}) = \sum_i f_i(\underline{x})\ R_i(\lambda,\underline{x}) \tag{4.1}$$

where the terms are defined in Section 4.1.

C1.1 Mean Reflectance

Considering all the terms in (4.1) as random variables, the mean reflectance in its most general form is

$$E[R(\lambda,\underline{x})] = \sum_i E[f_i(\underline{x})\ R_i(\lambda,\underline{x})] \tag{C1.1}$$

Using the identity

$$E[xy] = COV[x,y] + E[x]\ E[y] \tag{C1.2}$$

equation C1.1 can be expanded

$$E[R(\lambda,\underline{x})] = \sum_i \left[E[f_i(\underline{x})]\ E[R_i(\lambda,\underline{x})] + COV[f_i(\underline{x}),\ R_i(\lambda,\underline{x})]\right] \tag{C1.3}$$

Assuming that the fractional cover, $f_i(\underline{x})$ is independent of the reflectance of that fractional cover, $R_i(\lambda,\underline{x})$, the above equation becomes,

$$E[R(\lambda,\underline{x})] = \sum_i E[f_i(\underline{x})]\ E[R_i(\lambda,\underline{x})] \tag{C1.4}$$

which is the same as (6.1).

C1.2 Variance of Reflectance

The variance of (4.1) in its most general form is

$$\text{VAR}[R(\lambda,\underline{x})] = \sum_i \text{VAR}[f_i(\underline{x})\ R_i(\lambda,\underline{x})]$$

$$+ \sum_{i\neq j}\sum \text{COV}\Big[[f_i(\underline{x})\ R_i(\lambda,\underline{x})],\ [f_j(\underline{x})\ R_j(\lambda,\underline{x})]\Big] \qquad \text{(C1.5)}$$

If $f_i(\underline{x})$ and $R_i(\lambda,\underline{x})$ are independent, the first term on the right hand side of the above equation can be written

$$\sum_i \text{VAR}[f_i\underline{x})\ R_i(\lambda,\underline{x})] = \sum_i\Big[E[f_i(\underline{x})]^2\ \text{VAR}[R_i(\lambda,\underline{x})]$$

$$+ E[R_i(\lambda,\underline{x})]^2\ \text{VAR}[f_i(\underline{x})]$$

$$+ \text{VAR}[f_i(\underline{x})]\ \text{VAR}[R_i(\lambda,\underline{x})]\Big] \qquad \text{(C1.6)}$$

If it is further assumed that the reflectances are independent of each other, the second term on the right hand side of (C1.5) becomes

$$\sum_{i\neq j}\sum \text{COV}\Big[[f_i(\underline{x})\ R_i(\lambda,\underline{x})],\ [f_j(\underline{x})\ R_j(\lambda,\underline{x})]\Big]$$

$$= \sum_{i\neq j}\sum R_i(\lambda,\underline{x})\ R_j(\lambda,\underline{x})\ \text{COV}[f_i(\underline{x}),\ f_j(\underline{x})] \qquad \text{(C1.7)}$$

Combining C1.6 and C1.7 yields the variance equation given in (6.2).

C1.3 Cross–Spectral Covariance

The cross–spectral covariance can be expanded using C1.2 as

$$\text{COV}[R(\lambda,\underline{x}),\ R(\lambda_2,\underline{x})]$$

$$= E[R(\lambda_1,\underline{x})\ R(\lambda_2,\underline{x})] - E[R(\lambda_1,\underline{x})]E[R(\lambda_2,\underline{x})] \qquad \text{(C1.8)}$$

Inserting (4.1) into (C1.8) yields

$$\begin{aligned}
&\text{COV}[R(\lambda_1,\underline{x}),\ R(\lambda_2,\underline{x})] \\
&\quad = E\left[\left[\sum_i f_i(\underline{x})\ R_i(\lambda_1,\underline{x})\right]\left[\sum_j f_j(\underline{x})\ R_j(\lambda_2,\underline{x})\right]\right] \\
&\quad - E\left[\sum_i f_i(\underline{x})\ R_i(\lambda_1,\underline{x})\right]\ E\left[\sum_j f_j(\underline{x})\ R_j(\lambda_2,\underline{x})\right]
\end{aligned} \tag{C1.9}$$

Assuming that the fractional covers, $f_i(\underline{x})$, are independent of the reflectances, $R_i(\lambda,\underline{x})$ yields

$$\begin{aligned}
&\text{COV}[R(\lambda_1\underline{x}),\ R(\lambda_2\underline{x})] \\
&\quad = \sum_i \sum_j E[R_i(\lambda_1,\underline{x})\ R_j(\lambda_2,\underline{x})]\ E[f_i(\underline{x})\ f_j(\underline{x})] \\
&\quad - \sum_i \sum_j E[R_i(\lambda_1,\underline{x})\ E[R_j(\lambda_2,\underline{x}]\ E[f_i(\underline{x})]\ E[f_j(\underline{x})]
\end{aligned} \tag{C1.10}$$

Applying (C1.2) to $E[f_i(\underline{x})\ f_j(\underline{x})]$ and to $E[R_i(\lambda_1,\underline{x})\ R_j(\lambda_2,\underline{x})]$ and inserting into (C1.10) yield

$$\begin{aligned}
&\text{COV}[R(\lambda_1,\underline{x}),\ R(\lambda_2,\underline{x})] \\
&\quad = \sum_i \sum_j \left[\text{COV}[R_i(\lambda_1,\underline{x}),\ R_j(\lambda_2\underline{x})] + E[R_i(\lambda_1,\underline{x})]\ E[R_j(\lambda_2,\underline{x})]\right] \cdot \\
&\qquad\qquad \left[\text{COV}[f_i(\underline{x}),f_j(\underline{x})] + E[f_i(\underline{x})]\ E[f_j(\underline{x})]\right] \\
&\quad - \sum_i \sum_j E[R_i(\lambda_1,\underline{x})]\ E[R_j(\lambda_2,\underline{x})]\ E[f_i(\underline{x})]\ E[f_j(\underline{x})]
\end{aligned} \tag{C1.11}$$

Cancelling terms of opposite sign yields

$$\text{COV}[R(\lambda_1,\underline{x}),\ R(\lambda_2,\underline{x})]$$

$$= \sum_i \sum_j \Big[\text{COV}[R_i(\lambda_1,\underline{x}),\ R_j(\lambda_2,\underline{x})]\ \text{COV}[f_i(\underline{x}),\ f_j(\underline{x})]$$

$$+ \text{COV}[R_i(\lambda_1,\underline{x}),\ R_j(\lambda_2,\underline{x})]\ E[f_i(\underline{x})]\ E[f_j(\underline{x})]$$

$$+ E[R_i(\lambda_1,\underline{x})]\ E[R_j(\lambda_2,\underline{x})]\ \text{COV}[f_i(\underline{x}),\ f_j(\underline{x})]\Big] \qquad \text{(C1.12)}$$

When i = j, then

$$f_i(\underline{x})\ f_j(\underline{x}) = f_i^2(\underline{x}) \qquad \text{(C1.13)}$$

and,

$$\text{COV}[f_i(\underline{x}),\ f_j(\underline{x})] = \text{VAR}[f_i(\underline{x})] \qquad \text{(C1.14)}$$

Assuming there is no cross–spectral covariance between the reflectances of different cover types, then

$$\text{COV}[R_i(\lambda_1,\underline{x}),\ R_j(\lambda_2,\underline{x})] = 0 \qquad \text{for } i \neq j \qquad \text{(C1.15)}$$

Separating the summation in C1.12 into portions representing i = j and i ≠ j, and inserting C1.13, C1.14, and C1.15 yields,

$$\text{COV}[R(\lambda_1,\underline{x})\ R(\lambda_2,\underline{x})]$$

$$= \sum_i \Big[E[f_i(\underline{x})]^2\ \text{COV}[R_i(\lambda_1,\underline{x}),\ R_i(\lambda_2,\underline{x})]$$

$$+ \text{VAR}[f_i(\underline{x})]\ E[R_i(\lambda_1,\underline{x})]\ E[R_i(\lambda_2,\underline{x})]\Big]$$

$$+ \sum_{i\neq j} \sum E[R_i(\lambda_1,\underline{x})]\ E[R_j(\lambda_2,\underline{x})]\ \text{COV}[f_i(\underline{x}),\ f_j(\underline{x})] \qquad \text{(C1.16)}$$

which is the same as that given in (6.3).

C1.4 Spatial Covariance of Reflectance

The spatial covariance of the total reflectance between two pixels located at $\underline{x}$ and $\underline{x}'$ can be written

$$\mathrm{COV}_x[R(\lambda,\underline{x}),\ R(\lambda,\underline{x}')] = \mathrm{COV}_x\left[\left[\sum_i f_i(\underline{x})\ R_i(\lambda,\underline{x})\right],\ \left[\sum_j f_j(\underline{x}')R_j(\lambda,\underline{x}')\right]\right] \quad \text{(C1.17)}$$

where i and j represent cover types. The above can be expanded

$$\begin{aligned}\mathrm{COV}_x[R(\lambda,\underline{x}),(\lambda,\underline{x}')] \quad &= E\left[\left[\sum_i f_i(\underline{x})\ R_i(\lambda,\underline{x})\right]\left[\sum_j f_j(\underline{x}')\ R_j(\lambda,\underline{x}')\right]\right] \\ &\quad - E\left[\sum_i f_i(\underline{x})\ R_i((\lambda,\underline{x})\right]\ E\left[\sum_j f_j(\underline{x}')\ R_j((\lambda,\underline{x}')\right] \quad \text{(C1.18)}\end{aligned}$$

The first term on the right hand side of (C1.18) can be rewritten

$$\begin{aligned}&E\left[\left[\sum_i f_i(\underline{x})\ R_i(\lambda,\underline{x})\right]\left[\sum_j f_j(\underline{x}')\ R_j(\lambda,\underline{x}')\right]\right] \\ &\qquad = E\left[\sum_i\sum_j f_i(\underline{x})\ f_j(\underline{x}')\ R_i(\lambda,\underline{x})\ R_j(\lambda,\underline{x}')\right] \quad \text{(C1.19)}\end{aligned}$$

Assuming the fractional covers are independent of the reflectances, then (C1.19) becomes

$$\begin{aligned}&E\left[\sum_i\sum_j f_i(\underline{x})\ f_j(\underline{x}')\ R_i(\lambda,\underline{x})\ R_j(\lambda,\underline{x}')\right] \\ &\qquad = \sum_i\sum_j E\left[f_i(\underline{x})\ f_j(\underline{x}')\right]\ E\left[R_i(\lambda,\underline{x})\ R_j(\lambda,\underline{x}')\right] \quad \text{(C1.20)}\end{aligned}$$

The same assumption allows the second term on the right hand side of (C1.18) to be written

$$E\Big[\sum_i f_i(\underline{x})\ R_i(\lambda,\underline{x})\Big]\ E\Big[\sum_j f_j(\underline{x}')\ R_j(\lambda,\underline{x}')\Big]$$

$$= \sum_i E[f_i(\underline{x})]\ E[R_i(\lambda,\underline{x})]\ \sum_j E[f_j(\underline{x}')]\ E[R_j(\lambda,\underline{x}')] \qquad \text{(C1.21)}$$

Equations (C1.20) and (C1.21) can be rearranged and combined to yield

$$\text{COV}_x[R(\lambda,x),\ R(\lambda,\underline{x}')] =$$

$$\sum_i \sum_j \Big[E[f_i(\underline{x})\ f_j(\underline{x}')]\ E[R_i(\lambda,\underline{x})\ R_j(\lambda,x')]$$

$$- E[f_i(\underline{x})]\ E[f_j(\underline{x}')]\ E[R_i(\lambda,\underline{x})]\ E[R_j(\lambda,\underline{x}')]\Big]$$

Using the identity given in (C1.2),

$$E[f_i(\underline{x})\ f_j(\underline{x}')] = \text{COV}_x[f_i(\underline{x}),\ f_j(\underline{x}')] + E[f_i(\underline{x})]\ E[f_j(\underline{x}')] \qquad \text{(C1.23)}$$

$$E[R_i(\lambda,\underline{x})\ R_j(\lambda,\underline{x}')] = \text{COV}_x[R_i(\lambda,\underline{x}),\ R_j(\lambda,\underline{x}')]$$

$$+ E[R_i(\lambda,\underline{x})]\ E[R_j(\lambda,\underline{x}')] \qquad \text{(C1.24)}$$

Inserting (C1.23) and (C1.24) into (C1.22) yields

$$\text{COV}_x[R(\lambda,\underline{x}),\ R(\lambda,\underline{x}')] =$$

$$\sum_i \sum_j \Big[\{\text{COV}_x[f_i(\underline{x}),\ f_j(\underline{x}')] + E[f_i(\underline{x})\ f_j(\underline{x}')]\} \cdot$$

$$\{\text{COV}_x[R_i(\lambda,\underline{x}),\ R_j(\lambda,\underline{x}')] + E[R_i(\lambda,\underline{x})]\ E[R_j(\lambda,\underline{x}')]\}$$

$$- E[f_i(\underline{x})]\ E[f_j(\underline{x}')]\ E[R_i(\lambda,\underline{x})]\ E[R_j(\lambda,\underline{x}')]\Big] \qquad \text{(C1.25)}$$

which is the same as (C6.4).

C2. Reflectance Moment Equations for Case V – Method 2

The reflectance moment equations for Case V, Method 2, can be derived from equations (6.1) through (6.4). The notation is changed to that of equation (5.1), or

$$R(\lambda,\underline{x}) = m_I R_{m_I}(\lambda,\underline{x}) + m_s R_{m_s}(\lambda,\underline{x}) + g_I R_{g_I}(\lambda,\underline{x}) + g_s R_{g_s}(\lambda,\underline{x})$$

where i = 1 (in equation (4.1)) designates illuminated vegetation, i = 2 designates shadowed vegetation, i = 3 designates illuminated soil background, and i = 4 designates soil background shadowed by vegetation.

C2.1 Mean Reflectance

In this example $m_s = 0$, and $R_m(\lambda)$ and $R_{g_s}(\lambda)$ are assumed constant throughout space. The mean reflectance equation is thus

$$E[R(\lambda,\underline{x})] = E[m]\, R_m(\lambda) + E[g_s]\, R_{g_s}(\lambda) + E[g_I]\, E[R_{g_I}(\lambda,\underline{x})] \qquad (C2.1)$$

C1.2.2 Variance of Reflectance

In this case it is recognized that the variance of all the constant reflectance terms equals zero, or

$$\text{VAR}[R_m(\lambda)] = \text{VAR}[R_{g_s}(\lambda)] = 0 \qquad (C2.2)$$

The variance equation in (6.2) becomes

$$
\begin{aligned}
\text{VAR}[R(\lambda,\underline{x})] = {} & E[g_I]^2 \text{ VAR}[R_{g_I}(\lambda,\underline{x})] \\
& + R_m(\lambda)^2 \text{ VAR}[m] + E[R_{g_I}(\lambda,\underline{x})]^2 \text{ VAR}[g_I] \\
& + \text{VAR}[g_I] \text{ VAR}[R_{g_I}(\lambda,\underline{x})] \\
& + R_{g_S}(\lambda)^2 \text{ VAR}[g_S] \\
& + 2E[R_m(\lambda)] \, E[R_{g_I}(\lambda,\underline{x})] \, \text{cov}[m,g_I] \\
& + 2E[R_m(\lambda)] \, E[R_{g_S}(\lambda)] \, \text{COV}[m,g_S] \\
& + 2E[R_{g_I}(\lambda,\underline{x})] \, E[R_{g_S}(\lambda)] \, \text{COV}[g_I,g_S] \qquad \text{(C2.3)}
\end{aligned}
$$

In order to reduce the number of unknowns, all the covariance terms will be expressed in terms of $\text{COV}[m,g_S]$. For instance,

$$
\begin{aligned}
\text{COV}[m,g_I] &= \text{COV}[m,\, 1 - m - g_S] \\
&= E[m(1 - m - g_S)] - E[m] \, E[1 - m - g_S] \\
&= E[m - m^2 - mg_S] - E[m] + E[m]^2 + E[m] \, E[g_S] \\
&= E[m] - E[m^2] - E[mg_S] - E[m] + E[m]^2 + E[m] \, E[g_S] \\
&= -\left[E[m^2] + E[m]^2\right] - \left[E[mg_S] - E[m] \, E[g_S]\right] \\
&= -\text{VAR}[m] - \text{COV}[m,g_S] \qquad \text{(C2.4)}
\end{aligned}
$$

Following a similar expansion as above for $\text{COV}[g_I,g_S]$, and inserting those covariance expressions into (C2.3) yields the variance expression given in (7.6).

The cross–spectral covariance, given in (7.7), can be obtained in a similar manner as for the variance.

C3. Geometric Similarity Formula for Poisson Distributions

This section derives the geometric similarity equation for Poisson distributions given in (6.17). Assume that a flat surface of area A_p is covered with a random number of flat two–dimensional figures of arbitrary shape and size with mean area a. Assume that the figures can overlap one another, and that the centers of the figures are Poisson distributed in space with density ρ. The expected area that is covered, A_c, can be shown to be (Kellerer, 1983),

$$E[A_c|\rho] = A_p[1 - \exp(-a\rho)] \tag{C3.1}$$

letting $f = A_c/A_p$ then

$$E[f|\rho] = [1 - \exp(-a\rho)] \tag{C3.2}$$

for trees or plants with projected mean area A_t, the expected fractional area covered is

$$E[m|\rho] = [1 - \exp(-A_t\rho)] \tag{C3.3}$$

when the mean shadow cast by an individual tree, S_t, is defined,

$$S_t = \eta A_t \tag{C3.4}$$

then the expected fraction of plant and shadow is

$$\begin{aligned} E[(m + g_s)|\rho] &= \left[1 - \exp[-\rho(A_t + S_t)]\right] \\ &= \left[1 - \exp[-\rho(\eta + 1)\ A_t]\right] \end{aligned} \tag{C3.5}$$

Assuming that the plant canopy overlaps the shadow (that is, there is no shadowed canopy), then

$$E[m_s] = 0$$

From (5.7),

$$E[g_I] = 1 - \left[E[m] + E[g_s]\right] \qquad \text{(C3.6a)}$$

Inserting C3.5 into the above,

$$\begin{aligned} E[g_I] &= \exp[-\rho(\eta + 1)A_t] \\ &= \left[\exp[-\rho A_t]\right]^{\eta+1} \end{aligned} \qquad \text{(C3.6b)}$$

Inserting C3.3 into the above yields

$$E[g_I] = \left[1 - E[m]\right]^{\eta+1} \qquad \text{(C3.7)}$$

which is the same as equation (6.17).

Appendix D

Computer Programs

D1.) Canopy–Soil Reflectance Simulation Model

D2.) Inverse Procedure for Case II

D3.) Inverse Procedure for Case V, Method 1

D4.) Inverse Procedure for Case V, Method 2:

- i) Estimate Soil Background Cover
- ii) Estimate η

D5.) Inverse Procedure for Beaver Creek:

- i) Estimate Bulk Parameters for Entire Scene
- ii) Estimate Bulk Parameters for Each Pixel

```
C
C              CANOPY-SOIL REFLECTANCE SIMULATION MODEL
C
C                                   BY
C
C                            MICHAEL F. JASINSKI
C          PARSONS LABORATORY FOR WATER RESOURCES AND HYDRODYNAMICS
C                            M.I.T, Room 48-212
C                            Cambridge, MA 02139
C                             Tel. 617-253-5483
C
C  This program simulates the reflectance of a sparse canopy
C  consisting of trees superposed on a soil background.  Total
C  reflectance is calculated at each grid point or pixel.
C  The output files are "CAN14.OUT" (printer) and "C14BPL.DAT"
C  (plotter).
C  Version 14: computes visible and infrared reflectances,
C              percent canopy, and percent shadow for four
C              levels of aggregation (1,5,10,30).  Includes
C              calculation of percent canopy for
C              each pixel.  Includes soil variability determined
C              from Turning Bands Model (calculated previously).
C              For soil reflectance (ASSIGN SOILREF.OUT = FOR002).
C              Assumes relationship between tree vis/ir reflectances.
C              Increases dimensions to 150x150.
C              Includes inhibitory field, ie.e nonoverlapping
C              of trees. Trees positioned at center of one meter
C              pixels. Includes shadows as an option. Version 14
C              reorganizes the sequence of calculations of
C              reflectance and shadows. If elevations are to
C              be read then ASSIGN ELEV0_05.OUT FOR001. For
C              shadows to be read, ASSIGN VEGREF.OUT FOR003.
C  Variables:
C      X1,X2  -  tree center coordinates
C      RNODE  -  actual reflectance at a given node, finest resolution
C      RAGNODE-  aggregated reflectance at a given node
C      PCTV   -  actual percent vegetation at a given pixel, finest
C                resolution (range 0 - 1.0)
C      PCTVAG -  aggregated percent vegetation at a given node
C      PCTS   -  percent shadow in a given pixel (range 0 - 1.0)
C      PCTSAG -  aggregated percent shadow
C      THGT   -  height of given tree
C      TREF   -  reflectance of a given tree
C      ETREF  -  expected value of tree reflectance
C      ETHGT  -  expected value of tree height
C      TDIA   -  diameter of a given tree
C      VARREF -  variance of reflectance
C      NVI    -  normalized vegetation index
C      MREF   -  mean of reflectance
C      IBAND  -  number of reflectance bands
C      IAG    -  highest level of aggregation
C      ISHAD  -  control parameter for shadow computation
C                (0 = no shadows computed, 1 = compute shadows)
C      IELEV  -  control parameter for elevation computation
C                (0 = compute elevations, 1 = read elevations)
C      IVREF  -  control parameter for vegetation reflection
C                computation (0 = compute, 1 = read from file)
C      IVDIA  -  control parameter for special case of tree
```

```
C                diameter = 1 pixel (0 = dia  not equal to
C                one pixel, 1 = dia equal to 1 pixel)
C      VREF   -  vegetation reflectance distribution

C  Last revised:  1/7/88

       REAL     X1(20000),X2(20000),RNODE(2,150,150),TDIA(20000),
     &          TREF(2,20000),ELEV(-10:150,150),
     &          LAM,ETDIA,ETREF(2),STREF(2),THGT(20000),
     &          MREF(2),RAGNODE(2,150,150),
     &          DIST_SQ,DIST(150),
     &          PCTV(150,150),PCTVAG(150,150),ALPHA,THETA,PCTS(150,150),
     &          PCTSAG(150,150),PCTVI(150,150),PCTVIAG(150,150),
     &          PCTGS(150,150),PCTGSAG(150,150),NVI(150,150),S1,S2,
     &          PCTVS(150,150),PCTVSAG(150,150),VREF(150,150),V1,V2

       INTEGER NUM,IDIM,IBAND,IA,IAG,IELEV,ISHAD,IVREF,IVDIA

       OPEN(10,FILE='CAN14.IN',STATUS='OLD')
       OPEN(11,FILE='CAN14.OUT',STATUS='NEW',FORM='FORMATTED')
       OPEN(13,FILE='C14BPL.DAT',STATUS='NEW',CARRIAGECONTROL='LIST')

C  Input model parameters

       READ(10,*) IBAND
       READ(10,*) IDIM,IAG
       READ(10,*) IELEV,ISHAD
       READ(10,*) IVREF,IVDIA
       READ(10,*) V1,V2
       READ(10,*) S1,S2
       READ(10,*) LAM
       READ(10,*) ALPHA, THETA
       READ(10,*) ETHGT,STHGT
       READ(10,*) ETREF(1),STREF(1)
       READ(10,*) ETREF(2),STREF(2)

C  Call RANGEN to generate tree locations, heights, and diameters

       CALL RANGEN(IELEV,IDIM,LAM,ALPHA,ETHGT,STHGT,X1,X2,
     &             THGT,TDIA,NUM,IBAND,ELEV)

C  Call OUTPAR to write inputted parameters and number of trees.

       CALL OUTPAR(LAM,ALPHA,THETA,ETHGT,STHGT,ETREF,STREF,IBAND,NUM)

C  Call ELEVA to compute elevation of tree at each node.

       CALL ELEVA(ISHAD,IELEV,IDIM,NUM,ELEV,ALPHA,X1,X2,THGT,TDIA)

C  Call OUTEL to print elevation at each node.

       CALL OUTEL(IDIM,ELEV)

C  Call REFLEC to compute the reflectance at each node (before
C  shadow subroutine).

       CALL REFLEC(IDIM,NUM,X1,X2,TDIA,ETREF,STREF,S1,S2,
     &             TREF,RNODE,IBAND,PCTV,IVREF,IVDIA,VREF,V1,V2)
```

```
C  Call SHADOW to compute shadowed pixels (reflectivity = 0.0).

       CALL SHADOW(ISHAD,IDIM,ALPHA,THETA,ETHGT,STHGT,
     &             RNODE,ELEV,IBAND,PCTS,PCTV,PCTVI,PCTGS)

C  Compute average reflectance for increasing levels of aggregation

       DO 100 IAGR = 1,4
          IA = 1
          IF (IAGR.EQ.2) THEN
             IA =  5
          ENDIF
          IF (IAGR.EQ.3) THEN
             IA = 10
          ENDIF
          IF (IAGR.EQ.4) THEN
             IA = 30
          ENDIF
          IF (IA.LT.2) THEN
             CALL OUTREF(IDIM,NUM,RNODE,IA,
     &                   IBAND,PCTV,PCTS)
             CALL OUTPLOT(IDIM,RNODE,IA,IAG,IBAND,PCTV,PCTVI,
     &                    PCTVS,PCTS,PCTGS,ELEV)
          ELSE
             CALL AGGREG(IDIM,RNODE,RAGNODE,IA,IBAND,PCTV,PCTVAG,
     &                   PCTS,PCTSAG,PCTVI,PCTVIAG,PCTGS,PCTGSAG)

C  call OUTREF to print array of reflectances and subpixel
C  components at each node.

             CALL OUTREF(IDIM,NUM,RAGNODE,IA,
     &                   IBAND,PCTVAG,PCTSAG)
             CALL OUTPLOT(IDIM,RAGNODE,IA,IAG,IBAND,PCTVAG,
     &                    PCTVIAG,PCTVSAG,PCTSAG,PCTGSAG,ELEV)
          ENDIF

C  Subroutine to summarize statistics of subpixel percentages

       CALL OUTPCT(IDIM,IA,RAGNODE,PCTVAG,PCTVIAG,PCTSAG,PCTGSAG)

  100  CONTINUE
       STOP
       END

C  -------------------------------------------------------------
C  -------------------------------------------------------------
C  This subroutine aggregates the reflectance values and subpixel
C  percentages up to the level IA

       SUBROUTINE AGGREG(IDIM,RNODE,RAGNODE,IA,IBAND,PCTV,PCTVAG,
     &                   PCTS,PCTSAG,PCTVI,PCTVIAG,PCTGS,PCTGSAG)
       REAL RNODE(2,150,150),RAGNODE(2,150,150),PCTV(150,150),
     & PCTVAG(150,150),PCTS(150,150),PCTSAG(150,150),PCTVI(150,150),
     & PCTVIAG(150,150),PCTGS(150,150),PCTGSAG(150,150)
       INTEGER IDIM,IA,IBAND,IX,IY

C  Initialize variables
```

```
      IX = 0
      IY = 0
      DO 50 I = 1,IDIM
         DO 50 J = 1,IDIM
            DO 60 IB = 1,IBAND
               RAGNODE(IB,I,J) = 0.
60          CONTINUE
            PCTVAG(I,J) = 0.
            PCTSAG(I,J) = 0.
            PCTVIAG(I,J) = 0.0
            PCTGSAG(I,J) = 0.0
50    CONTINUE

C  Compute aggregated matrix

      DO 100 I = 1,IDIM-IA+1,IA
         IX = IX + 1
         DO 110 J = 1,IDIM-IA+1,IA
            IY = IY + 1
            DO 120 I1 = 1,IA
               DO 120 J1 = 1,IA
                  DO 130 IB = 1,IBAND
                    RAGNODE(IB,IX,IY) = RAGNODE(IB,IX,IY) +
     &                                  RNODE(IB,I+I1-1,J+J1-1)/(IA**2)
130               CONTINUE
                  PCTVAG(IX,IY) =  PCTVAG(IX,IY) +
     &                             PCTV(I+I1-1,J+J1-1)/(IA**2)
                  PCTSAG(IX,IY) =  PCTSAG(IX,IY) +
     &                             PCTS(I+I1-1,J+J1-1)/(IA**2)
                  PCTVIAG(IX,IY) = PCTVIAG(IX,IY) +
     &                             PCTVI(I+I1-1,J+J1-1)/(IA**2)
                  PCTGSAG(IX,IY) = PCTGSAG(IX,IY) +
     &                             PCTGS(I+I1-1,J+J1-1)/(IA**2)

120         CONTINUE
110      CONTINUE
         IY = 0
100   CONTINUE
      RETURN
      END

C  ---------------------------------------------------------
C  ---------------------------------------------------------
C  Subroutine RANGEN samples from appropriate random
C  distributions to generate tree center locations,
C  then tree heights and diameters.

C  Variables:
C        RAD      -  radius of tree
C        NUM      -  number of trees
C        SECNDS   -  MICROVAX function returns time in sec.
C        GGUBFS   -  IMSL uniform random number generator
C        GGNML    -  IMSl normal random number generator

      SUBROUTINE RANGEN(IELEV,IDIM,LAM,ALPHA,ETHGT,STHGT,
     &                  X1,X2,THGT,TDIA,NUM,IBAND,ELEV)
      REAL      LAM,ETHGT,STHGT,MDIA,ELEV(-10:150,150),
```

```
     &            RADIUS,OMEGA,TDIA(20000),THGT(20000),
     &            X1(20000),X2(20000),MHGT,
     &            GGUBFS,SECNDS,R(1),OVERLAP
       INTEGER NR,IBAND,IX1(20000),IX2(20000)
       DOUBLE PRECISION   SEED
       SAVE SEED
       PARAMETER(PI=3.14159)

C  Zero variables.

       RADIUS = 0.0
       NUM    = 0
       NR = 1

C  If(IELEV=1) then read elevations computed outside
C  this program.
       IF(IELEV.GT.0.5) THEN
            READ(1,*)
          DO 200 J=1,IDIM
             READ(1,*) (ELEV(I,J),I= -10,0)
             READ(1,*) (ELEV(I,J),I=   1,25)
             READ(1,*) (ELEV(I,J),I=  26,50)
             READ(1,*) (ELEV(I,J),I=  51,75)
             READ(1,*) (ELEV(I,J),I=  76,100)
             READ(1,*) (ELEV(I,J),I= 101,125)
             READ(1,*) (ELEV(I,J),I= 126,150)
  200     CONTINUE
          DO 210 J=1,IDIM
             DO 210 I=-10,IDIM
                IF(ELEV(I,J).GT.0.0) THEN
                   NUM = NUM + 1
                   THGT(NUM) = ELEV(I,J)
                   X1(NUM) = I
                   X2(NUM) = J


                   TDIA(NUM) = 1.0
                ENDIF
  210     CONTINUE
       GO TO 110
       ENDIF

C  Obtain seed from internal clock.

       SEED = SECNDS(0.0) + 10000.

C  Generate tree centers.....................................
C  Simulate 2-D Poisson Process
C  Source:  Cox, Point Processes
C  Method:  generate variable X = PI*(R2**2 - R1**2) from
C           exponential distribution, and angle,
C           OMEGA, from uniform distribution on 0,2PI

C  To obtain exponential deviate, X, from U uniform (0,1):
C           X = (-1/R)*LOG(U);
C          where f(x) = R * exp(R*x)
C  GGUBFS(SEED)  -  IMSL uniform random number generator
```

```
C  Maximum radius of tree location equal to extent of field
C  plus ten times tree diameter.

C  Maximum radius is SQRT(2)*IDIM/2 + 3*RMAX

       RADMAX = 3.*(ETHGT*(TAN(ALPHA*6.283/360))*2.) + 106.1
  10   RADIUS = SQRT((-(1./LAM)*LOG(GGUBFS(SEED)))/PI
     &                                        + RADIUS*RADIUS)

C  If radius exceeds extent of field return to main program.

       IF(RADIUS.GT.RADMAX)GO TO 20
       IF(NUM.GE.20000)GO TO 20

C  Increment tree number, generate angular coordinate.

       NUM = NUM+1
       OMEGA = GGUBFS(SEED) * 2. * PI

       IX1(NUM) = RADIUS * COS(OMEGA) + 75.
       IX2(NUM) = RADIUS * SIN(OMEGA) + 75.

C  Put tree at center of pixel by truncating to integer value.

       X1(NUM) = IX1(NUM)
       X2(NUM) = IX2(NUM)

C  Generate tree height (normal distribution).....
C  Set bounds for acceptable range of heights(1-10 meters only).

       CALL GGNML(SEED,NR,R)
       THGT(NUM) = ETHGT + (STHGT*R(1))
       IF(THGT(NUM).LT.0.) THEN
         THGT(NUM) = 1.0
       ENDIF
       IF(THGT(NUM).GT.10.0) THEN
         THGT(NUM) = 9.9
       ENDIF
       MHGT = MHGT + THGT(NUM)

C  Compute tree diameter.....

       TDIA(NUM) = THGT(NUM)*TAN(ALPHA*6.283/360)*2
       MDIA = MDIA  + TDIA(NUM)

C  Compute inhibitory field. If tree locations overlap
C  then no tree is generated (Decrement tree NUM).

       IMAX = MIN(NUM,500)
       ITEST = 0.
       IF(IMAX.LT.2) GO TO 600
       DO 600 IT = 1,IMAX-1
       IF(ITEST.GT.0.1) GO TO 600
       DIST_TR = SQRT((X1(NUM) - X1(NUM-IT))**2 +
     &           (X2(NUM) - X2(NUM-IT))**2)
       OVERLAP = ((TDIA(NUM)+TDIA(NUM-IT))/2) - DIST_TR
       IF(OVERLAP.GT.0.1) THEN
         NUM = NUM-1
```

```
        ITEST = 1.0
      ENDIF
  600 CONTINUE
      IF(ITEST.GT.0.1) GO TO 10

      GO TO 10

   20 MHGT = MHGT/NUM
      MDIA = MDIA/NUM
  110 RETURN
      END

C  ------------------------------------------------------------
C  ------------------------------------------------------------
C  Subroutine ELEVA calculates the elevation at each pixel based
C  on the tree center height and cone angle.  Ground surface is
C  assumed flat and horizontal at elev = 0.0.

      SUBROUTINE ELEVA(ISHAD,IELEV,IDIM,NUM,ELEV,
     &                 ALPHA,X1,X2,THGT,TDIA)

      REAL ELTEMP,ELEV(-10:150,150),ALPHA,X1(20000),X2(20000),
     &     THGT(20000),TDIA(20000),XX,YY
      INTEGER IDIM,NUM,ITDIA,X11,X22

C  If (IELEV=1) then use elevations computed outside this program
C  and skip this subroutine

      IF(IELEV.GT.0.5) GO TO 110

C  Initialize pixels at 0.0 elevation.

      DO 20 I= -10,IDIM
         DO 20 J= 1,IDIM
            ELEV(I,J) = 0.0
  20  CONTINUE

C  If (ISHAD=0) then above initializations stand and skip
C  the rest of this subroutine

      IF(ISHAD.LT.0.5) GO TO 110

      TANCON = TAN(ALPHA*6.283/360)

C  Iteration to compute elevation

      DO 100 N=1,NUM
         ITDIA = TDIA(N)
         DO 50 I=-ITDIA,ITDIA
            DO 50 J=-ITDIA,ITDIA

C  Find nearest integer pixel by truncating

               X11 = X1(N) + I
               X22 = X2(N) + J
               IF(X11.GT.IDIM .OR. X11.LT.-10) GO TO 50
               IF(X22.GT.IDIM .OR. X22.LT.1) GO TO 50
```

```
C  Compute elevation based on distance from tree center

                ELTEMP = THGT(N) - SQRT(((X11-X1(N))**2) +
     &                     ((X22-X2(N))**2))/TANCON

C  For overlapping tree canopies, take highest canopy

                IF(ELTEMP.LT.ELEV(X11,X22)) THEN
                  GO TO 50
                ELSE
                  ELEV(X11,X22) = ELTEMP
                ENDIF
  50        CONTINUE
  100   CONTINUE
  110   RETURN
        END

C  ------------------------------------------------------------
C  ------------------------------------------------------------
C  Subroutine OUTEL prints the elevation of each pixel
        SUBROUTINE OUTEL(IDIM,ELEV)

        REAL ELEV(-10:150,150)
        INTEGER IDIM
        WRITE(11,800)
  800   FORMAT(//,2X,'Pixel elevation in meters',/)
        DO 850 J=1,30
           WRITE(11,870) (ELEV(I,J),I=1,15)
  850   CONTINUE
  870   FORMAT(15F6.2)
        RETURN
        END

C  ------------------------------------------------------------
C  ------------------------------------------------------------
C  Subroutine REFLEC computes reflectance at each node based
C  on superposition of trees on soil background.

C  Variables:
C     DIST_SQ - square of distance from node to tree center

        SUBROUTINE REFLEC(IDIM,NUM,X1,X2,TDIA,ETREF,STREF,S1,S2,
     &                    TREF,RNODE,IBAND,PCTV,IVREF,IVDIA,VREF,V1,V2)

        REAL  X1(20000),X2(20000),TDIA(20000),ETREF(2),STREF(2),
     &        TREF(2,20000),RNODE(2,150,150),DIST_SQ,PCTV(150,150),
     &        SECNDS,R(1),MREF(2),VREF(150,150),V1,V2,S1,S2
        INTEGER IDIM,NUM,INUM,NR,IVREF,IVDIA,IX1,IX2
        DOUBLE PRECISION SEED
        SAVE SEED

        SEED = SECNDS(0.0) + 10000.
        NR = 1

C  Initialize percent vegetation

        DO 15 I = 1,IDIM
           DO 15 J = 1,IDIM
```

```
            PCTV(I,J) = 0.
 15     CONTINUE

C  Soil distribution obained from the TURNING BANDS model
C  computed outside this program.  Just read input here.

       DO 40 I=1,IDIM
             READ(2,*)  (RNODE(1,I,J),J=  1,15)
             READ(2,*)  (RNODE(1,I,J),J= 16,30)
             READ(2,*)  (RNODE(1,I,J),J= 31,45)
             READ(2,*)  (RNODE(1,I,J),J= 46,60)
             READ(2,*)  (RNODE(1,I,J),J= 61,75)
             READ(2,*)  (RNODE(1,I,J),J= 76,90)
             READ(2,*)  (RNODE(1,I,J),J= 91,105)
             READ(2,*)  (RNODE(1,I,J),J=106,120)
             READ(2,*)  (RNODE(1,I,J),J=121,135)
             READ(2,*)  (RNODE(1,I,J),J=136,150)

C  Infrared soil reflectance linearly related to visible reflectance

             DO 40 J=1,IDIM
             IF(RNODE(1,I,J).LT.0.05) THEN
               RNODE(1,I,J) = 0.05
             ENDIF
             RNODE(2,I,J) = (S1*RNODE(1,I,J)) + S2
 40     CONTINUE

C  If (IVREF.EQ.1) then read visible tree reflectance distribution
C  from outside this program and assign reflectance at tree centers

       IF(IVREF.GT.0.5) THEN
          DO 200 I=1,IDIM
             READ(3,*)  (VREF(I,J),J=  1,15)
             READ(3,*)  (VREF(I,J),J= 16,30)
             READ(3,*)  (VREF(I,J),J= 31,45)
             READ(3,*)  (VREF(I,J),J= 46,60)
             READ(3,*)  (VREF(I,J),J= 61,75)
             READ(3,*)  (VREF(I,J),J= 76,90)
             READ(3,*)  (VREF(I,J),J= 91,105)
             READ(3,*)  (VREF(I,J),J=106,120)
             READ(3,*)  (VREF(I,J),J=121,135)
             READ(3,*)  (VREF(I,J),J=136,150)
 200      CONTINUE
          DO 250 IN=1,NUM
             IX1 = X1(IN)
C   (can't handle negatives in some arrays)
             IF(IX1.LT.1.0) GO TO 250
             IX2 = X2(IN)
             TREF(1,IN) = VREF(IX1,IX2)

C  Assume IR tree reflectance logrithmicly related to VIS reflectance

             TREF(2,IN) = (V1*TREF(1,IN)) + V2

 250  CONTINUE
      GO TO 270
      ENDIF
```

```
C  In general, generate tree reflectance (normal distribution) for
C  each tree. Revision of 7/21/87 assumes linear relation (therefore
C  same random relation) between visible and infrared reflectances.
C  Therefore only one random number is generated for both reflectances.

C       DO 60 IB = 1,IBAND
        DO 60 INUM = 1, NUM
          CALL GGNML(SEED,NR,R)
          IB = 1
          TREF(IB,INUM) = ETREF(IB) + (STREF(IB)*R(1))
          MREF(IB) = MREF(IB) + TREF(IB,INUM)
          IB = 2
          TREF(IB,INUM) = ETREF(IB) + (STREF(IB)*R(1))
          MREF(IB) = MREF(IB) + TREF(IB,INUM)
  60    CONTINUE

  270   CONTINUE

C  The next algorithm assigns tree reflectances to all grid
C  nodes within the tree canopy area.  Node coordinates are
C  located at centers of unit pixels.

C  If tree diameter is equal to one grid, then pixel reflectance
C  equals tree reflectance only at that grid; skip following
C  time-consuming calculation

       IF(IVDIA.GT.0.5) THEN
         DO 295 I=1,NUM
            IX1 = X1(I)
            IF(IX1.LT.1.0) GO TO 295
            IX2 = X2(I)
            DO 290 IB=1,IBAND
               RNODE(IB,IX1,IX2)= TREF(IB,I)
  290       CONTINUE
            PCTV(IX1,IX2) = 1.0
  295    CONTINUE
       GO TO 280
       ENDIF

       DO 10 I = 1,NUM
          X11 = X1(I)
          X22 = X2(I)
          DO 20 J = 1,IDIM
              DO 20 K = 1,IDIM
                  Z1 = J
                  Z2 = K

                  DIST_SQ = (X11 - Z1)**2 + (X22 - Z2)**2
                  IF ((TDIA(I)/2).GE.SQRT(DIST_SQ)) THEN

C  It's assumed that reflectance of the overlap portion
C  of two trees is equal to the latter generated tree.

                     DO 50 IB=1,IBAND
                       RNODE(IB,J,K) = TREF(IB,I)
  50                   CONTINUE
                       PCTV(J,K) = 1.0
                   ENDIF
```

```
  20      CONTINUE
  10    CONTINUE
  280   RETURN
        END

C  ------------------------------------------------------------
C  ------------------------------------------------------------
C  Subroutine to compute shadows cast by trees.  Sun is
C  assumed directly from west (left of page).

        SUBROUTINE SHADOW(ISHAD,IDIM,ALPHA,THETA,ETHGT,STHGT,
     &                    RNODE,ELEV,IBAND,PCTS,PCTV,PCTVI,PCTGS)

        REAL ALPHA,THETA,ETHGT,STHGT,RNODE(2,150,150),
     & ELEV(-10:150,150),TANCON,TANSUN,PCTS(150,150),
     & PCTV(150,150),PCTVI(150,150),PCTGS(150,150)
        INTEGER ISHAD,IMAX,IBAND

C  Initialize variables.

        DO 100 I=1,IDIM
           DO 100 J=1,IDIM
              PCTS(I,J) = 0.
              PCTVI(I,J) = PCTV(I,J)
              PCTGS(I,J) = 0.
  100   CONTINUE

C  If there are no shadows (ISHAD = 0.0), above initializations
C  stand and rest of algorithm can be skipped.

        IF(ISHAD.LT.0.5) GO TO 60

        TANCON = TAN(ALPHA*6.283/360)
        TANSUN = TAN((90-THETA)*6.283/360)
        IMAX   = (ETHGT + (5*STHGT))/TANSUN

        DO 50 J = 1,IDIM
           DO 50 I = IDIM,1,-1
              DO 40 IN = 1,IMAX
                 IF((I-IN).LT.-10) GO TO 40
                 IF((((ELEV((I-IN),J)) - ELEV(I,J))/IN).GE.TANSUN) THEN
                      RNODE(1,I,J) = 0.0
                      RNODE(2,I,J) = 0.0

C  Initialize percent shadow

                      PCTS(I,J)    = 1.0
                      IF(PCTV(I,J).GE.0.95) THEN
                        PCTVI(I,J) = 0.0
                      ELSE
                        PCTGS(I,J) = 1.0
                      ENDIF
                 ENDIF
  40          CONTINUE
  50    CONTINUE
  60    RETURN
        END
```

```
C  ------------------------------------------------------------
C  ------------------------------------------------------------
C  This subroutine prints the reflectances at each node
C  and a summary of the statistics

      SUBROUTINE OUTREF(IDIM,NUM,RNODE,IA,
     &                  IBAND,PCTV,PCTS)
      REAL   RNODE(2,150,150),
     &       LAG,DIST,PCTV(150,150),PCTS(150,150)
      INTEGER IDIM,NUM,IBAND,IA,ITAU,IMAX,IMIN
      ITAU = IDIM/IA
      IMAX = 15
      IMIN = MIN(IMAX,ITAU)
      WRITE(11,805) IA
 805  FORMAT(//,'--------------------
     &----------------------------------------------------
     &--------'/,26X,'Level of aggregation =',I4)
      DO 810 IB = 1,IBAND
         WRITE(11,815) IB
 815     FORMAT(//,2X,'Pixel reflectance: Band number =',I4,/)
         DO 830 J=1,IMIN
            WRITE(11,850) (RNODE(IB,I,J), I=1,IMIN)
 830     CONTINUE
 850     FORMAT(15F6.2)
 810  CONTINUE
      WRITE(11,845) 'Percent vegetation'
 845  FORMAT(//,2X,A,/)
      DO 840 J =1,IMIN
         WRITE(11,850) (PCTV(I,J),I=1,IMIN)
 840  CONTINUE
      WRITE(11,845) 'Percent shadow'
      DO 842 J =1,IMIN
         WRITE(11,850) (PCTS(I,J),I=1,IMIN)
 842  CONTINUE

      RETURN
      END

C  ------------------------------------------------------------
C  ------------------------------------------------------------
C  This subroutine writes inputted storm parameters and
C  number of trees generated.

      SUBROUTINE OUTPAR(LAM,ALPHA,THETA,ETHGT,STHGT,
     &                  ETREF,STREF,IBAND,NUM)
      REAL LAM,ALPHA,THETA,ETHGT,STHGT,ETREF(2),STREF(2)
      INTEGER IBAND,NUM
      WRITE(11,860) 'CANOPY MODEL: VERSION 11',
     &              'LAMB','ALPH','THET','E[THGT]','S[THGT]',
     &              'E[REF_VIS]','S[REF_VIS]','E[REF_IR]','S[REF_IR]'
 860  FORMAT(//,2X,A,/,2X,A,2X,A,2X,A,2X,A,2X,A,2X,A,1X,A,2X,A,2X,A,2X,A)
      WRITE(11,870) LAM,ALPHA,THETA,ETHGT,STHGT,
     &      (ETREF(IB),STREF(IB),IB=1,IBAND)
 870  FORMAT(/,F6.3,3F6.1,F10.3,F11.3,F12.3,F10.3,F11.3)
      WRITE(11,820) NUM
 820  FORMAT(//,2X,'Number of trees =',X,I8)
      RETURN
      END
```

```
C  ------------------------------------------------------------
C  ------------------------------------------------------------
C  This subroutine computes subpixel components
C  and arranges output for use in the DRAW package
C  of the microVAX II.

      SUBROUTINE OUTPLOT(IDIM,RNODE,IA,IAG,
     &              IBAND,PCTV,PCTVI,PCTVS,PCTS,PCTGS,ELEV)
      REAL RNODE(2,150,150),LAG,DIST,PCTV(150,150),
     &     PCTS(150,150),PCTVI(150,150),PCTGS(150,150),
     &     PCTG(150,150),PCTGI(150,150),PCTVS(150,150),
     &     ELEV(-10:150,150),NVI(150,150)
      INTEGER IDIM,IA,IAG,ITAU,IMAX,IMIN,IPLOTB
      ITAU = IDIM/IA
      IMAX = 15
      IMIN = MIN(IMAX,ITAU)

C Initialize variables

      DO 50 J = 1,ITAU
         DO 50 I = 1, ITAU
            PCTVS(I,J) = 0.
            PCTG(I,J)  = 0.
            PCTGI(I,J) = 0.
            NVI(I,J)   = 0.
   50 CONTINUE

C     Write header for draw files (once)

      IF(IA.GT.1) GO TO 960
      IPLOTB = 12
      WRITE(13,970) IPLOTB
  970 FORMAT('CANOPY MODEL: VERSION 14',
     & /,I4,/,'VIS_REF',/,'INF_REF',/,'M',/,'MI',/,'MS',/,'MI/M',
     & /,'MS/M',/,'G',/,'GI',/,'GS',/,'S',/,'NVI')

C Skip printing for aggregations less than 3

  960 IF (IA.LT.3) GO TO 980

C Print file or reflectance and percent vegetation
C for last aggregation.

      WRITE(13,700) IA
  700 FORMAT(/,' Level of aggregation is', I4,/)

      DO 100 J=1,ITAU
         DO 100 I=1,ITAU
            PCTVS(I,J) = PCTS(I,J) - PCTGS(I,J)
            PCTVI(I,J) = PCTV(I,J) - PCTVS(I,J)
            PCTG(I,J)  = 1.0 - PCTV(I,J)
            PCTGI(I,J) = PCTG(I,J) - PCTGS(I,J)
            RSUM       = RNODE(2,I,J) + RNODE(1,I,J)
            IF(RSUM.EQ.0.0) THEN
              NVI(I,J) = 0.0
              GO TO 150
            ENDIF
```

```
            NVI(I,J)    = (RNODE(2,I,J) - RNODE(1,I,J))/RSUM

C Correction for zero-divide (at low aggregations)

  150       IF(PCTV(I,J).LT.0.0001) THEN
              PCTV(I,J) = .0001
            ENDIF

            WRITE(13,200) 100*RNODE(1,I,J),100*RNODE(2,I,J),
     &                    100*PCTV(I,J),100*PCTVI(I,J),
     &                    100*PCTVS(I,J),100*PCTVI(I,J)/PCTV(I,J),
     &                    100*PCTVS(I,J)/PCTV(I,J),100*PCTG(I,J),
     &                    100*PCTGI(I,J),100*PCTGS(I,J),
     &                    100*PCTS(I,J),100*NVI(I,J)
  100   CONTINUE
  200   FORMAT(12F8.3)

  980   RETURN
        END

C -----------------------------------------------------------------
C -----------------------------------------------------------------
C Subroutine to summarize statistics of the subpixel percentages.
        SUBROUTINE OUTPCT(IDIM,IA,RNODE,PCTV,PCTVI,PCTS,PCTGS)

        REAL PV,PVI,PVS,PG,PGS,PGI,PS,PCTV(150,150),PCTS(150,150),
     &       PCTVI(150,150),PCTGS(150,150),RNODE(2,150,150),NNVI
        INTEGER IDIM,IA,IMAX,IMIN

        IMAX = 15
        ITAU = IDIM/IA
        IMIN = MIN(IMAX,ITAU)

        PV  = 0.
        PVI = 0.
        PGS = 0.
        R1  = 0.
        R2  = 0.
        PS  = 0.

        DO 100 I=1,ITAU
           DO 100 J=1,ITAU
              PV  = PV + PCTV(I,J)/(ITAU**2)
              PVI = PVI + PCTVI(I,J)/(ITAU**2)
              PGS = PGS + PCTGS(I,J)/(ITAU**2)
              R1  = R1 + RNODE(1,I,J)/(ITAU**2)
              R2  = R2 + RNODE(2,I,J)/(ITAU**2)
              PS  = PS + PCTS(I,J)/(ITAU**2)
              IF((RNODE(2,I,J) + RNODE(1,I,J)).EQ.0.0) THEN
                NNVI = 0.0
                GO TO 100
              ENDIF
              NNVI = NNVI + ((RNODE(2,I,J)-RNODE(1,I,J))/
     &                       (RNODE(2,I,J)+RNODE(1,I,J)))/(ITAU**2)
  100   CONTINUE

C  Correction for zero divide
```

```
      IF(PV.LT.0.0001) THEN
         PV = 0.0001
      ENDIF

      WRITE(11,210) ' Subpixel component averages','R1','R2',
     &  'M','MI','MS','MI/M','MS/M','G','GI','GS','S','NVI'
210   FORMAT(//,'-----------------------------------------
     &-----------------------------',/,A,/,4X,A,4X,A,5X,A,4X,A,4X,
     &A,2X,A,2X,A,5X,A,4X,A,4X,A,5X,A,4X,A,//)

      PG = 1-PV
      PGI = PG - PGS
      WRITE(11,200) R1,R2,PV,PVI,PV-PVI,PVI/PV,(PV-PVI)/PV,
     &              PG,PGI,PGS,PS,NNVI

200   FORMAT(2F6.3,9F6.3,F7.2)
      RETURN
      END
```

```
C
C              INVERSE PROCEDURE FOR CASE II
C                    (Program M_II.FOR)
C
C  Program to compute mean,st. dev., min, and max of a group of
C  data from a DRAW output file for a specified line of R1 and R2
C  in the red-IR scattergram, identified by slop A, intercept, B,
C  and Bandwidth BANDWIDTH.  Program computes
C  estimate of percent vegetation cover, PM_EST,from simulations
C  and compares it to mean of actual percent cover, PM_MEAN.

        REAL RNODE(2),PM_ACT,BIGIR,SMALLIR,BIGVS,SMALLVS,
     &                SMALLPM,BIGPM,
     &               RIR_SUM,MEANIR,SDEV_VSSL,SDEV_IRSL,
     &               RIRSQ_SUM,RVS_SUM,MEANVS,RVSSQ_SUM,
     &               BANDWIDTH,A,B,CVPARM(10),
     &               PM_EST_VS,PM_EST_IR,PARM,MACT(300),
     &               PM_MEAN,PM_SDEV,PM_SUM,PM_SSQ,NUM
        INTEGER NN,NUMPAIRS
        OPEN(10,FILE='M_II.IN',STATUS='OLD')
C       ASSIGN INPUT DRAW FILE TO FOR011
        OPEN(12,FILE='M_II.OUT',STATUS='NEW')
        OPEN(13,FILE='M_IIL.OUT',STATUS='NEW')

        SMALLIR = 500.0
        SMALLVS = 500.0
        SMALLPM = 500.0
        NUM  = 0.0
        RIR_SUM = 0.0
        RIRSQ_SUM = 0.0
        RVS_SUM = 0.0
        RVSSQ_SUM = 0.0
        PM_SSQ = 0.0
        PM_SUM = 0.0
        NN = 0

C  Read input parameters
        READ(10,*) NUMPAIRS,A,B,BANDWIDTH,PARM
C  Read sdev of soil line
        READ(10,*) SDEV_VSSL,SDEV_IRSL
C  Skip header
        READ(11,300) IPLOT
  300   FORMAT(/,I4,////////////)
C  Iterate for each data pair
        DO 100 I = 1,NUMPAIRS
           READ(11,*) (RNODE(K),K=1,2), (CVPARM(J),J=1,10)
           PM_ACT = CVPARM(PARM)
C  Compute perpendicular distance between a chosen point and
C  the line RIR = A*RVIS + B

           AP = TAN(-(3.142/2 - ATAN(A)))
           BP = RNODE(2) - (AP*RNODE(1))
           RVS = (B - BP)/(AP - A)
           RIR = A*RVS + B
           DIS =SQRT((RIR-RNODE(2))**2 + (RVS - RNODE(1))**2)
C       WRITE (5,*) AP,BP,RIR,RVS,DIS

           IF(DIS.GT.BANDWIDTH) GO TO 100
```

```
                NUM = NUM + 1.0
                NN = NN  + 1
                MACT(NN) = PM_ACT
C Sum IR data
               RIR_SUM    = RIR_SUM + RNODE(2)
               RIRSQ_SUM = RIRSQ_SUM + (RNODE(2)**2)
               BIGIR = MAX(BIGIR,RNODE(2))
               SMALLIR = MIN(SMALLIR,RNODE(2))
C Sum Visible data
               RVS_SUM    = RVS_SUM + RNODE(1)
               RVSSQ_SUM = RVSSQ_SUM + (RNODE(1)**2)
               BIGVS = MAX(BIGVS,RNODE(1))
               SMALLVS = MIN(SMALLVS,RNODE(1))
C  Sum percent canopy cover
               PM_SUM    = PM_SUM + PM_ACT
               PM_SSQ    = PM_SSQ + PM_ACT**2
               BIGPM = MAX(BIGPM,PM_ACT)
               SMALLPM = MIN(SMALLPM,PM_ACT)
  100  CONTINUE
       MEANIR = RIR_SUM/NUM
       SDEVIR = SQRT((RIRSQ_SUM - NUM*(MEANIR**2))/(NUM-1))
       MEANVS = RVS_SUM/NUM
       SDEVVS = SQRT((RVSSQ_SUM - NUM*(MEANVS**2))/(NUM-1))
       PM_MEAN = PM_SUM/NUM
       PM_SDEV = SQRT((PM_SSQ - NUM*(PM_MEAN**2))/(NUM-1))
C  Write input and output parameters
       WRITE(12,210) 'NUM','A','B','BANDWIDTH',NUM,A,B,BANDWIDTH
       WRITE(5,210) 'NUM','A','B','BANDWIDTH',NUM,A,B,BANDWIDTH
  210  FORMAT(5X,A,7X,A,7X,A,2X,A,/,F8.0,2F8.3,F10.3)
C  Write summary of reflectance statistics
       WRITE(12,200) 'BAND','MEAN','SDEV','SD/MN','MAX','MIN',
     &           'IR',MEANIR,SDEVIR,SDEVIR/MEANIR,BIGIR,SMALLIR,
     &           'VIS',MEANVS,SDEVVS,SDEVVS/MEANVS,BIGVS,SMALLVS
       WRITE(5,200) 'BAND','MEAN','SDEV','SD/MN','MAX','MIN',
     &           'IR',MEANIR,SDEVIR,SDEVIR/MEANIR,BIGIR,SMALLIR,
     &           'VIS',MEANVS,SDEVVS,SDEVVS/MEANVS,BIGVS,SMALLVS
  200  FORMAT(/,4X,A,4X,A,4X,A,3X,A,5X,A,5X,A,//,
     &        6X,A,5F8.2,/,5X,A,5F8.2)
C  Compute canopy cover using variances
C  COMPUTE E{GI}

       PM_EST_VS = 100*(1 - (SDEVVS/SDEV_VSSL))
       PM_EST_IR = 100*(1 - (SDEVIR/SDEV_IRSL))


C  Write summary of canopy cover statistics
       WRITE(*,301) 'M_ACT','SDEV','M_EST(VIS)','M_EST(IR)',
     &              PM_MEAN, PM_SDEV, PM_EST_VS, PM_EST_IR
       WRITE(12,301) 'M_ACT','SDEV','E[M]_(VIS)','E[M]_(IR)',
     &              PM_MEAN, PM_SDEV, PM_EST_VS, PM_EST_IR
  301  FORMAT(/,5X,A,6X,A,2X,A,3X,A,/,2F10.2,2F12.2)
       DO 120 K=1,NN
         WRITE(13,302) K, MACT(K), PM_EST_VS, PM_EST_IR
  120  CONTINUE
  302  FORMAT(I8,3F8.2)
       STOP
       END
```

```
C
C            INVERSE PROCEDURE FOR CASE V, METHOD 1
C                  (VB2 PARVO2.FOR)
C
C   Estimates parameters from moment analysis
C   Three unknowns, EM, ETA, AT

      REAL EM,EM_MIN,EM_MAX,DEM,VM,
     &     EGI,EGS,VGI,CMGS,CMGS_MIN,CMGS_MAX,DCMGS,DCM,
     &     AT,AT_MIN,AT_MAX,DAT,AP,
     &     Y1,Y2,Y3,Y(3),F,FMIN,X1,X2,X3,
     &     ERGI(2),VRGI(2),SER(2),SVR(2),SCR1CR2,RV(2),
     &     NDELTA,M_SAM,CMGS_SAM,CMGS_MIN_INIT,CMGS_MAX_INIT,
     &     EM_MIN_INIT,EM_MAX_INIT,AT_MIN_INIT,AT_MAX_INIT,
     &     FPRINT(10),ATPRNT(10),W1,W2,W3,A1,A2,
     &     ETA,ETA_MIN,ETA_MAX,DETA
      INTEGER LEVEL, IDELTA

C     ASSIGN FOR010.DAT MOMENT.DAT
      OPEN(11, FILE='PARVL.IN',STATUS ='OLD')
      OPEN(12, FILE='PARV.OUT',STATUS ='NEW')


      READ(11,*) LEVEL, NDELTA, IDELTA
      READ(11,*) EM_MIN_INIT, EM_MAX_INIT
      READ(11,*) AT_MIN_INIT,AT_MAX_INIT
      READ(11,*) ETA_MIN_INIT,ETA_MAX_INIT
C  Weighting constants for minimization
      READ(11,*) W1,W2,W3
C  Read correlation coefficients
      READ(11,*) A1,A2
      READ(11,*) A3,A4
      READ(11,*) A5,A6
      DO 800 NDAT = 1,8

C  Read fixed parameters and sample moments
       CALL READDAT(AP,M_SAM,CMGS_SAM,ERGI,VRGI,SER,SVR,SCR1R2)
C  Initialize
       EMF = 100.00
       ATF = 100.00
       CMGSF = 100.00
       FMIN = 10000000000.00
       EM_MIN = EM_MIN_INIT
       EM_MAX = EM_MAX_INIT
       AT_MIN = AT_MIN_INIT
       AT_MAX = AT_MAX_INIT
       ETA_MIN = ETA_MIN_INIT
       ETA_MAX = ETA_MAX_INIT

       M_SAM = M_SAM*0.0100
       CMGS_SAM = CMGS_SAM*0.000100
       WRITE(5,460) 'M_SAMPLE =',M_SAM, 'COV(M,GS) =', CMGS_SAM
       WRITE(12,460) 'M_SAMPLE =',M_SAM, 'COV(M,GS) =', CMGS_SAM
 460   FORMAT(//,2(3X,A,F9.5))
       WRITE(5,440) 'EM','AT','ETA','CMGS','Y1','Y2','Y3','FMIN'
       WRITE(12,440) 'EM','AT','ETA','CMGS','Y1','Y2','Y3','FMIN'
 440   FORMAT(6X,A,6X,A,5X,A,6X,A,3(10X,A),7X,A)
```

```
C  Iterate over MAX and MIN values
       DO 600 IT = 1,LEVEL
            DEM = (EM_MAX - EM_MIN)/NDELTA
            DAT = (AT_MAX - AT_MIN)/NDELTA
            DETA = (ETA_MAX - ETA_MIN)/NDELTA
            EM = EM_MIN
            DO 500 IT1 = 1,IDELTA
               EM = EM + DEM
               AT = AT_MIN
               DO 510 IT2=1,IDELTA
                  AT = AT + DAT
                  ATPRNT(IT2) = AT
                  ETA = ETA_MIN
                  DO 520 IT3=1,IDELTA
                     ETA = ETA + DETA

C  Call minimization routine

                     CALL FUNCT(EM,AT,CMGS,Y,F,AP,ETA,ERGI,VRGI,
     &                SER,SVR,SCR1R2,EGI,EGS,VM,VGI,RV,W1,W2,W3,
     &                A1,A2,A3,A4,A5,A6,ITER)
                     FPRINT(IT3) = MIN(999.900,F)

                     IF(F.LT.FMIN) THEN
                      FMIN = F
                      EMF = EM
                      ATF = AT
                      CMGSF = CMGS
                      EGIF = EGI
                      EGSF = EGS
                      ETAF = ETA
                      Y1 = Y(1)
                      Y2 = Y(2)
                      Y3 = Y(3)
                      VMF = VM
                      VGIF = VGI
                      RV1F = RV(1)
                      RV2F = RV(2)

                     ENDIF
  520             CONTINUE
  510          CONTINUE
  500       CONTINUE
            WRITE(5,430) EMF,ATF,ETAF,CMGSF,Y1,Y2,Y3,FMIN
            WRITE(12,430) EMF,ATF,ETAF,CMGSF,Y1,Y2,Y3,FMIN
  430       FORMAT(3F8.5,F10.5,3(X,F11.6),X,F10.6)
            ITER = 0
C  Change MAX and MIN values

           EM_MAX = EMF + 0.4D0*(EM_MAX - EM_MIN)
           EM_MIN = EMF - 0.4D0*(EM_MAX - EM_MIN)
C           EM_MAX = EMF + DEM
C           EM_MIN = EMF - DEM
            IF(EM_MIN.LT.0.00) THEN
             EM_MIN = 0.000
            ENDIF
            IF(EM_MAX.GT.1.00) THEN
             EM MAX = 1.000
```

```
            ENDIF
            AT_MAX = ATF + 0.400*(AT_MAX - AT_MIN)
            AT_MIN = ATF - 0.400*(AT_MAX - AT_MIN)
            IF(AT_MIN.LT.0.00) THEN
             AT_MIN = AT_MIN_INIT
            ENDIF
            ETA_MAX = ETAF + 0.400*(ETA_MAX - ETA_MIN)
            ETA_MIN = ETAF - 0.400*(ETA_MAX - ETA_MIN)
            IF(ETA_MIN.LT.0.00) THEN
             ETA_MIN = ETA_MIN_INIT
            ENDIF
  600    CONTINUE

         WRITE(5,450) 'EM','EGI','AT','ETA','VM','VGI','CMGS','RV1',
     &      'RV2',EMF,EGIF,ATF,ETAF,VMF,VGIF,CMGSF,RV1F,RV2F
         WRITE(12,450) 'EM','EGI','AT','ETA','VM','VGI','CMGS','RV1',
     &      'RV2',EMF,EGIF,ATF,ETAF,VMF,VGIF,CMGSF,RV1F,RV2F
  450    FORMAT(5X,A,4X,A,5X,A,4X,A,7X,A,6X,A,6X,A,2(7X,A),/,4(F7.3),
     &         2(F9.6),F10.6,2F10.3)

  800    CONTINUE
         STOP
         END

C-----------------------------------------------------------------------
         SUBROUTINE FUNCT(EM,AT,CMGS,Y,F,AP,ETA,ERGI,VRGI,
     &          SER,SVR,SCR1R2,EGI,EGS,VM,VGI,RV,W1,W2,W3,
     &          A1,A2,A3,A4,A5,A6,ITER)
         REAL Y(3),ER(2),VR(2),CR1R2,EM,EGS,EGI,
     &       VM,VGS,VGI,W1,W2,W3,A1,A2,A3,A4,A5,A6,
     &       ERGI(2),VRGI(2),RV(2),CMGS,SER(2),SVR(2),SCR1R2,
     &       AP,F,ETA,AT,AST,DUM,CORR,CST

         EGI  =  (1.00 - EM)**(ETA + 1.00)
         EGS  =  1.00 - EM - EGI
         EGSGI = 1 - EM
         X = 2.3/((AP/AT)**1.50)
         VM  = (X*EGSGI) +
     &        (EGSGI**2.00)*((EGSGI**(-AT/AP))*(1.00-X)-1.00)
         AST =  AT*(1.00 + ETA)
         X = 2.300/((AP/AST)**1.500)
         VGI = (X*EGI) +
     &        (EGI**2.00)*((EGI**(-AST/AP))*(1.00 - X) - 1.00)

C Compute correlation BT/ M AND GS
         IF(EM.LE.0.10) THEN
         A1 = A1
         A2 = A2
         GO TO 160
         ENDIF
         IF(EM.LE.0.65) THEN
         A1 = A3
         A2 = A4
         GO TO 160
         ENDIF
         A1 = A5
         A2 = A6
  160    CORR = A1 - EM*A2
```

```
C  ESTIMATE CORRELATION BY ITERATION
       EMIN = 1000
       IF(CORR.GE.0.0) THEN
         CMGS = 0.0
       ELSE
         CMGS = -.03
       ENDIF
C
C  Option to compute CMGS by empirical formula (not used)
C      IF(EM.GT.0.48.AND.EM.LT.0.81) THEN
C         E = EM*100
C         CMGS = 51.34 - 1.957*E + 0.0176*(E**2) + 0.00003092*(E**3)
C         CMGS = CMGS/10000
C         GO TO 355
C       ENDIF

C  Solution by solving quadratic expression

       DO 350 IC = 1,300
          CMGS = CMGS + 0.0001
          ELEFT = (CMGS**2)
     &             - (VGI-VM)*(2*VM*(CORR**2))/2
          ERIGHT = -CMGS*(2*VM*(CORR**2))
          DIFF = ABS(ELEFT - ERIGHT)
          EMIN = MIN(DIFF,EMIN)
          IF(EMIN.EQ.DIFF) THEN
            CM_ACT = CMGS
          ENDIF
  350  CONTINUE
         CMGS = CM_ACT
  355  CONTINUE

C Compute minimization bt/ theoretical and sample reflecctance moments
       DO 100 M=1,2
         RV(M) = (SER(M) - EGI*ERGI(M))/EM
         IF(RV(M).LT.0.0) THEN
           RV(M) = 0.00
         ENDIF

         VR(M) = (RV(M)**2)*VM  +  (EGI**2)*VRGI(M)
     &           +  (ERGI(M)**2)*VGI  +  VGI*VRGI(M)
     &           -  2*RV(M)*ERGI(M)*(VM + CMGS)
  100  CONTINUE

       CR1R2  = RV(1)*RV(2)*VM
     &         - (RV(1)*ERGI(2) + RV(2)*ERGI(1))*(VM + CMGS)
     &         + (EGI**2)*VRGI(1)  +  VGI*(VRGI(1) + ERGI(1)*ERGI(2))

       NN = NN + 1
C       IF(NN.EQ.10) THEN
C          WRITE(5,420) RV(1),RV(2),VR(1),VR(2),CR1R2
C          WRITE(5,420) (Y(J),J=1,5), VM,F
C         WRITE(5,410) 'RV1','RV2','EM','AT','CMGS',
C     &                 RV(1),RV(2),EM,AT,CMGS
C  410    FORMAT(7X,A,7X,A,8X,A,8X,A,6X,A,/,4F10.3,F10.6)
  420    FORMAT(7E10.2)
```

```
C          NN = 0
C        ENDIF
         Y(1) = (VR(1)/SVR(1) - 1)**2
         Y(2) = (VR(2)/SVR(2) - 1)**2
         Y(3) = (CR1R2/SCR1R2 - 1)**2
         F  =  (W1*Y(1)) + (W2*Y(2)) + (W3*Y(3))
C        WRITE(5,420) (Y(J),J=1,3),F

         RETURN
         END
C
-----------------------------------------------------------------------
         SUBROUTINE READDAT(AP,M_SAM,CMGS_SAM,
     &                          ERGI,VRGI,SER,SVR,SCR1R2)
         REAL AP,ERGI(2),VRGI(2),SER(2),SVR(2),SCR1CR2,
     &       CR1R2,M_SAM,CMGS_SAM
         INTEGER IND

         IF(IND.GT.0) GO TO 100
C  Read fixed parameters

         READ(11,*) AP
         READ(10,*) ERGI(1), ERGI(2), VRGI(1), VRGI(2)

C  Read sample moments
  100    READ(10,*) M_SAM,CMGS_SAM,SER(1),SER(2),SVR(1),SVR(2),SCR1R2

         IND = 1

         RETURN
         END
```

```
C              INVERSE PROCEDURE FOR CASE V, METHOD 2
C
C              a.)  ESTIMATE SOIL BACKGROUND COVER, GI
C                   (VB1 G_V.FOR)
C
C  Program to compute mean,st. dev., min, and max of a DRAW output
C  file for a specified line of R1 and R2 and also compute
C  estimate of percent ILLUMINATED GROUND cover, PGIV_EST, for Case V
C  simulations and compare it to mean of actual percent cover, PGIV_MEAN.

        REAL RNODE(2),PGIV_ACT,BIGIR,SMALLIR,BIGVS,SMALLVS,
     &                 SMALLPGIV,BIGPGIV,
     &                RIR_SUM,MEANIR,SDEV_VSSL,SDEV_IRSL,
     &                RIRSQ_SUM,RVS_SUM,MEANVS,RVSSQ_SUM,
     &                BANDWIDTH,A,B,CVPARM(10),
     &                PGIV_EST_VS,PGIV_EST_IR,PARM,
     &                PGIV_MEAN,PGIV_SDEV,PGIV_SUM,PGIV_SSQ,NUM,
     &                MACT(100),MESTVS,MESTIR
        INTEGER NUMPAIRS,NN
        OPEN(10,FILE='G_V.IN',STATUS='OLD')
C       ASSIGN INPUT FILE TO FOR011
        OPEN(12,FILE='G_V.OUT',STATUS='NEW')
        OPEN(13,FILE='G_VL.OUT',STATUS='NEW')
        SMALLIR = 500.0
        SMALLVS = 500.0
        SMALLPGIV = 500.0
        NUM  = 0.0
        RIR_SUM = 0.0
        RIRSQ_SUM = 0.0
        RVS_SUM = 0.0
        RVSSQ_SUM = 0.0
        PGIV_SSQ = 0.0
        PGIV_SUM = 0.0
        NN = 0
C  Read input parameters
        READ(10,*) NUMPAIRS,A,B,BANDWIDTH,PARM
C  Read sdev of soil line  and ETA
        READ(10,*) SDEV_VSSL,SDEV_IRSL
        READ(10,*) ETA
C  Skip header
        READ(11,300) IPLOT
  300   FORMAT(/,I4,////////////)
C  Iterate for each data pair
        DO 100 I = 1,NUMPAIRS
           READ(11,*) (RNODE(K),K=1,2), (CVPARM(J),J=1,10)
           PGIV_ACT = CVPARM(PARM)
C  Compute perpendicular distance between a chosen point and
C  the line RIR = A*RVIS + B
            AP = TAN(-(3.142/2 - ATAN(A)))
            BP = RNODE(2) - (AP*RNODE(1))
            RVS = (B - BP)/(AP - A)
            RIR = A*RVS + B
            DIS =SQRT((RIR-RNODE(2))**2 + (RVS - RNODE(1))**2)
C       WRITE (5,*) AP,BP,RIR,RVS,DIS
            IF(DIS.GT.BANDWIDTH) GO TO 100
               NUM = NUM + 1.0
               NN = NN + 1
               MACT(NN) = CVPARM(1)
```

```
C Sum IR data
              RIR_SUM   = RIR_SUM + RNODE(2)
              RIRSQ_SUM = RIRSQ_SUM + (RNODE(2)**2)
              BIGIR = MAX(BIGIR,RNODE(2))
              SMALLIR = MIN(SMALLIR,RNODE(2))
C Sum Visible data
              RVS_SUM   = RVS_SUM + RNODE(1)
              RVSSQ_SUM = RVSSQ_SUM + (RNODE(1)**2)
              BIGVS = MAX(BIGVS,RNODE(1))
              SMALLVS = MIN(SMALLVS,RNODE(1))
C  Sum percent canopy cover
              PGIV_SUM   = PGIV_SUM + PGIV_ACT
              PGIV_SSQ   = PGIV_SSQ + PGIV_ACT**2
              BIGPGIV = MAX(BIGPGIV,PGIV_ACT)
              SMALLPGIV = MIN(SMALLPGIV,PGIV_ACT)
  100  CONTINUE
       MEANIR = RIR_SUM/NUM
       SDEVIR = SQRT((RIRSQ_SUM - NUM*(MEANIR**2))/(NUM-1))
       MEANVS = RVS_SUM/NUM
       SDEVVS = SQRT((RVSSQ_SUM - NUM*(MEANVS**2))/(NUM-1))
       PGIV_MEAN = PGIV_SUM/NUM
       PGIV_SDEV = SQRT((PGIV_SSQ - NUM*(PGIV_MEAN**2))/(NUM-1))
C  Write input and output parameters
       WRITE(12,210) 'NUM','A','B','BANDWIDTH',NUM,A,B,BANDWIDTH
       WRITE(5,210) 'NUM','A','B','BANDWIDTH',NUM,A,B,BANDWIDTH
  210  FORMAT(5X,A,7X,A,7X,A,2X,A,/,F8.0,2F8.3,F10.3)
C  Write summary of reflectance statistics
       WRITE(12,200) 'BAND','MEAN','SDEV','SD/MN','MAX','MIN',
     &          'IR',MEANIR,SDEVIR,SDEVIR/MEANIR,BIGIR,SMALLIR,
     &          'VIS',MEANVS,SDEVVS,SDEVVS/MEANVS,BIGVS,SMALLVS
       WRITE(5,200) 'BAND','MEAN','SDEV','SD/MN','MAX','MIN',
     &          'IR',MEANIR,SDEVIR,SDEVIR/MEANIR,BIGIR,SMALLIR,
     &          'VIS',MEANVS,SDEVVS,SDEVVS/MEANVS,BIGVS,SMALLVS
  200  FORMAT(/,4X,A,4X,A,4X,A,3X,A,5X,A,5X,A,//,
     &        6X,A,5F8.2,/,5X,A,5F8.2)
C  Compute canopy cover using variances
C  COMPUTE E{GI}
              XGIVS = (SDEVVS/SDEV_VSSL)
              XGIIR = (SDEVIR/SDEV_IRSL)
       PGIV_EST_VS = 100*(XGIVS)
       PGIV_EST_IR = 100*(XGIIR)
C  Compute M based on assumed value of ETA
              MESTVS = 100*(1 - (XGIVS**(1/(ETA+1))))
              MESTIR = 100*(1 - (XGIIR**(1/(ETA+1))))
C  Write summary of canopy cover statistics
       WRITE(5,301) 'GI_ACT','SDEV','G_EST(VIS)','G_EST(IR)',
     &              PGIV_MEAN, PGIV_SDEV, PGIV_EST_VS, PGIV_EST_IR
       WRITE(12,301) 'GI_ACT','SDEV','E[GI]_(VIS)','E[GI]_(IR)',
     &              PGIV_MEAN, PGIV_SDEV, PGIV_EST_VS, PGIV_EST_IR
  301  FORMAT(/,5X,A,6X,A,2X,A,3X,A,/,2F10.2,2F12.2)
       DO 130 J=1,NN
         WRITE(13,430) J,MACT(J),MESTVS,MESTIR
  430       FORMAT(I8,4F8.2)
  130  CONTINUE
       STOP
       END
```

```
C
C                    INVERSE PROCEDURE FOR CASE V, METHOD 2
C
C                    b.)  ESTIMATE ETA
C                         (ETA.FOR)
C
C  Program to estimate ETA for large S by selecting
C  four conditional lines.
C  Use input from M_II.FOR to obtain R(I) and GI(I), RSOIL is
C  average reflectance of Soil Line.

      REAL ETA,ETA_INIT,M(4),GI(4),GS(4),R(4),RSOIL,
     &     LHS,RHS
      OPEN(12,FILE='ETA.IN',STATUS='OLD')
      OPEN(13,FILE='ETA.OUT',STATUS='NEW')

      READ(12,*) RSOIL
      READ(12,*) (R(I),I=1,4)
      READ(12,*) (GI(I),I=1,4)
      READ(12,*) NETA,ETA_INIT,DEL_ETA
      ETA = ETA_INIT

      WRITE(5,400) 'A','B','C','D','ETA','A-C','B-D','LHS-RHS'
      WRITE(13,400) 'A','B','C','D','ETA','A-C','B-D','LHS-RHS'
  400 FORMAT(4(6X,A),3(6X,A),2X,A,/)

C  Iterate over ETA
      DO 100 J=1,NETA
        ETA = ETA + DEL_ETA

C  Compute GS and M
        DO 110 I=1,4
          M(I) = 1.0 - ((GI(I))**(1/(ETA+1.0)))
          GS(I) = 1.0 - M(I) - GI(I)
  110   CONTINUE
C  Compute LHS
          A =  ((R(1)/M(1)) - (R(2)/M(2)))/
     &         ((GS(1)/M(1)) -(GS(2)/M(2)))
          B =  ((R(3)/M(3)) - (R(4)/M(4)))/
     &         ((GS(3)/M(3)) -(GS(4)/M(4)))
        LHS = A - B
C  Compute RHS
          C =  (((GI(1)/M(1)) - (GI(2)/M(2)))/
     &          ((GS(1)/M(1)) - (GS(2)/M(2))))*RSOIL
          D =  (((GI(3)/M(3)) - (GI(4)/M(4)))/
     &          ((GS(3)/M(3)) - (GS(4)/M(4))))*RSOIL
         RHS = C - D

      DIFF1 = A-C
      DIFF2 = B-D
      QUO =  LHS/RHS
      WRITE(5,410) A,B,C,D,ETA,DIFF1,DIFF2,(LHS-RHS)
      WRITE(13,410) A,B,C,D,ETA,DIFF1,DIFF2,(LHS-RHS)
  100 CONTINUE
  410 FORMAT(4(X,F6.1),4(X,F8.4))
      STOP
      END
```

```
C
C          INVERSE PROCEDURE FOR BEAVER CREEK
C          a.) ESTIMATE BULK PARAMETERS FOR ENTIRE SCENE
C              (M_BCA.FOR)
C
C    Estimates parameters of entire data set from moment analysis
C    8 unknowns, M,GI,GS,RVRED,RVIR,RSRED,RSIR,RGRED,RGIR

        REAL M,GI,GS,RVRED,RVIR,RSRED,RSIR,RGRED,RGIR,SDGRED,SDGIR,
     &       TIME,REF(5),
     &       RIR_SUM,MEANIR,MAXIR,MINIR,RIRSQ_SUM,
     &       RRED_SUM,MEANRED,MAXRED,MINRED,RREDSQ_SUM,
     &       BANDWIDTH,A,B,VARRED,VARIR,F1,AETA

        INTEGER N,NUM,I1,I2,NREF,NDAT

C       ASSIGN FOR010.DAT BC623B2.OUT
        OPEN(11, FILE='M_BC.IN',STATUS ='OLD')
        OPEN(12, FILE='M_BC.OUT',STATUS ='NEW')
C        OPEN(13, FILE='SL_BC.OUT',STATUS='NEW')

        NS = 7
C        WRITE(13,442) 'M_BC, SOIL LINE',NS,'NUM','TIME',
C     &                'BLU','GRN','RED','NIR','TMP'
  442   FORMAT(2X,A,/,I4,7(/,2X,A))
        MINIR = 500
        MINRED = 500
        NUM  = 0
        RIR_SUM = 0
        RIRSQ_SUM = 0
        RRED_SUM = 0
        RREDSQ_SUM = 0

C  Read fixed parameters and soil line parameters
        READ(11,*) NREF
        READ(11,*) NDAT
        READ(11,*) I1,I2
        READ(11,*) ALPHA,GAMMA
        READ(11,*) F1, AETA
        READ(11,*) RGRED,RGIR,SDGRED,SDGIR
        READ(11,*) A,B,BANDWIDTH

C    Skip header
        READ(10,*)
        READ(10,*) ICOL
        DO 100 I=1,ICOL
          READ(10,*)
  100   CONTINUE

C    Read reflectance data
        DO 110 I=1,NDAT

          READ(10,*) N,TIME,(REF(J),J=1,NREF)

C  Compute conditional moments of arbitrary line, A*RRED + B
C  Compute linear relation between RIR and RVS, RIR = A*RVIS + B
C  Select data pairs
```

```
C New Version
          AP = TAN(-(3.142/2-ATAN(A)))
          BP = REF(I2) - (AP*REF(I1))
          RVS = (B-BP)/(AP-A)
          RIR = A*RVS + B
          DIS = SQRT((RIR-REF(I2))**2 + (RVS-REF(I1))**2)
          IF(DIS.GT.BANDWIDTH) GO TO 110
          NUM = NUM + 1
C          WRITE(13,441) NUM,TIME,(REF(K),K=1,NREF)
  441        FORMAT(3X,I5,2X,F10.4,5(X,F6.2))
C Sum IR data
             RIR_SUM    = RIR_SUM + REF(I2)
             RIRSQ_SUM = RIRSQ_SUM + (REF(I2)**2)
             MAXIR = MAX(MAXIR,REF(I2))
             MINIR = MIN(MINIR,REF(I2))
C Sum Visible data
             RRED_SUM    = RRED_SUM + REF(I1)
             RREDSQ_SUM = RREDSQ_SUM + (REF(I1)**2)
             MAXRED  = MAX(MAXRED ,REF(I1))
             MINRED = MIN(MINRED,REF(I1))
  110  CONTINUE
       MEANIR = RIR_SUM/NUM
       SDEVIR = SQRT(RIRSQ_SUM/NUM - (MEANIR**2))
       MEANRED = RRED_SUM/NUM
       SDEVRED = SQRT(RREDSQ_SUM/NUM - (MEANRED**2))
C  Write input and output of conditional line parameters
       WRITE(12,210) 'NUM','A','B','BANDWIDTH','E[GI_RED]','E[GI_IR]',
     &  'SD[GI_RED]','SD[GI_IR]',NUM,A,B,BANDWIDTH,RGRED,RGIR,
     &  SDGRED,SDGIR
       WRITE(5,210) 'NUM','A','B','BANDWIDTH','E[GI_RED]','E[GI_IR]',
     & 'SD[GI_RED]','SD[GI_IR]',NUM,A,B,BANDWIDTH,RGRED,RGIR,
     &  SDGRED,SDGIR
  210  FORMAT(5X,A,7X,A,7X,A,2X,A,X,A,2X,A,X,A,X,A,/,
     &         I8,2F8.2,F10.3,4F10.3)
       WRITE(12,200) 'BAND','MEAN','SDEV','SD/MN','MAX','MIN','ETA',
     &           'IR',MEANIR,SDEVIR,SDEVIR/MEANIR,MAXIR,MINIR,AETA,
     &           'RED',MEANRED,SDEVRED,SDEVRED/MEANRED,MAXRED ,MINRED
       WRITE(5,200) 'BAND','MEAN','SDEV','SD/MN','MAX','MIN','ETA',
     &           'IR',MEANIR,SDEVIR,SDEVIR/MEANIR,MAXIR,MINIR,AETA,
     &           'RED',MEANRED,SDEVRED,SDEVRED/MEANRED,MAXRED,MINRED
  200  FORMAT(/,4X,A,4X,A,4X,A,3X,A,5X,A,5X,A,5X,A,//,
     &         6X,A,6F8.3,/,5X,A,5F8.3)
C
C-------------------------------------------------------------
C      Compute parameters of scene
C-------------------------------------------------------------

C  Call minimization routine
       CALL EST(IB,AETA,F1,RGRED,RGIR,SDGRED,SDGIR,MEANRED,MEANIR,
     &            SDEVRED,SDEVIR,M,GI,GS,
     &            RVRED,RVIR,RSRED,RSIR)

C  Write estimate values
        WRITE(5,450) 'M','GI','GS','RV_RED','RV_IR','RS_RED','RS_IR',
     &         M,GI,GS,RVRED,RVIR,RSRED,RSIR
        WRITE(12,450) 'M','GI','GS','RV_RED','RV_IR','RS_RED','RS_IR',
     &         M,GI,GS,RVRED,RVIR,RSRED,RSIR
  450  FORMAT(/,9X,A,8X,A,8X,A,4X,A,5X,A,4X,A,5X,A,/,3(F10.3),
```

```
     &        2(F10.3),2F10.3)

       STOP
       END

C-----------------------------------------------------------------------
       SUBROUTINE EST(IB,AETA,F1,RGRED,RGIR,SDGRED,SDGIR,MEANRED,MEANIR,
     &             SDEVRED,SDEVIR,M,GI,GS,
     &             RVRED,RVIR,RSRED,RSIR)

       REAL AETA,F1,RGRED,RGIR,SDGRED,SDGIR,MEANRED,MEANIR,SDEVRED,
     &             SDEVIR,M,GI,GS,
     &             RVRED,RVIR,RSRED,RSIR

       GI = 0.00
       DIFMIN=100000.
       DO 500 I=1,99
          GI = GI + 0.01
          EXP = 1.0/(1.0 + AETA)
          M = 1.0 - GI**(EXP)
          GS = 1.0 - GI - M
          RVRED = (MEANRED - (GI*RGRED))/(M + (F1*GS))
          RVIR = (MEANIR - (GI*RGIR))/(M + (F1*GS))
          VARRED = SDEVRED**2
          VARIR = SDEVIR**2
          VARGRED = SDGRED**2
          VARGIR = SDGIR**2
          VAR_IR_EST =(GI**2)*VARGIR + (((RVRED-RGRED)/(RVIR-RGIR))**2)
     &                 *((VARRED**2) - (GI**2)*VARGRED)
          DIFF = ABS(VARIR - VAR_IR_EST)
          DIFMIN = MIN(DIFF,DIFMIN)
          IF(DIFF.EQ.DIFMIN) THEN
            GI_EST = GI
            EM_EST = M
            GS_EST = GS
            RVRED_EST = RVRED
            RVIR_EST = RVIR
          ENDIF
  500  CONTINUE
            GI = GI_EST
            M = EM_EST
            GS = GS_EST
            RVRED = RVRED_EST
            RVIR = RVIR_EST
       RETURN
       END
```

```
C
C          INVERSE PROCEDURE FOR BEAVER CREEK
C          b.) ESTIMATE BULK PARAMETERS FOR EACH PIXEL
C              (M_BC2.FOR)
C
C    Estimates M directly for each pixel in a conditional parallel line
C    Assumes Rgs = 0.0

        REAL M,GI,RVRED,RVIR,RGRED,RGIR,
     &       TIME,REF(5),
     &       BANDWIDTH,A,B,VARRED,VARIR,F1,AETA

        INTEGER N,NUM,I1,I2,NREF,NDAT

C       ASSIGN FOR010.DAT BC623B3A.OUT
        OPEN(11, FILE='M_BC2.IN',STATUS ='OLD')
        OPEN(12, FILE='M_BC2.OUT',STATUS ='NEW')

        NS = 7
        NUM  = 0

C  Read fixed parameters and soil line parameters
        READ(11,*) NREF
        READ(11,*) NDAT
        READ(11,*) I1,I2
        READ(11,*) ALPHA,GAMMA
        READ(11,*) F1, AETA
        READ(11,*) RGRED,RGIR,SDGRED,SDGIR
        READ(11,*) A,B,BANDWIDTH
        READ(11,*) RVRED,RVIR


C    Skip header
        READ(10,*)
        READ(10,*) ICOL
        DO 100 I=1,ICOL
          READ(10,*)
  100   CONTINUE
         NNCOL = 9
         WRITE(5,*) 'M_BC2 ESTIMATES'
         WRITE(5,*) NNCOL
         WRITE(5,450) 'N','TIME','RED','IR','E[M]','E[GI]','E[GS]',
     &                'Rg[RED]','Rg[IR]'
         WRITE(12,*) 'M_BC2 ESTIMATES'
         WRITE(12,*) NNCOL
         WRITE(12,450) 'N','TIME','RED','IR','E[M]','E[GI]','E[GS]',
     &                 'Rg[RED]','Rg[IR]'
   450   FORMAT(7X,A,/,4X,A,/,5X,A,/,6X,A,/,4X,A,/,3X,A,/,3X,
     &         A,/,X,A,/,2X,A)
C    Read reflectance data

        DO 110 I=1,NDAT
          READ(10,*) N,TIME,(REF(J),J=1,NREF)
          RED = REF(3)
          RIR = REF(4)
          EM = 0.0
          DIF_MIN=500
          DO 120 J=1,100
```

```
            EM = EM + 0.01
            RIR_TEST = (ALPHA*RED) + ((RVIR-RVRED)*EM)
     &                   + GAMMA*((1-EM)**(AETA+1))
            DIFF = ABS(RIR_TEST-RIR)
            DIF_MIN = MIN(DIFF,DIF_MIN)
            IF(DIFF.EQ.DIF_MIN) THEN
              RIR_EST = RIR_TEST
              RED_EST = RED
              EM_EST = EM
              GI_EST = (1-EM)**(AETA+1)
              GS_EST = 1 - EM - GI_EST
              RG_IR_EST = (RIR - (RVIR*EM))/GI_EST
              RG_RED_EST = (RED - (RVRED*EM))/GI_EST
            ENDIF
  120     CONTINUE
C  Write estimate values
          WRITE(5,460) N,TIME,RED_EST,RIR_EST,EM_EST,GI_EST,GS_EST,
     &                 RG_RED_EST,RG_IR_EST
         WRITE(12,460) N,TIME,RED_EST,RIR_EST,EM_EST,GI_EST,GS_EST,
     &                 RG_RED_EST,RG_IR_EST
  110   CONTINUE
  460   FORMAT(I8,F8.4,7(F8.3))

        STOP
        END
```

Appendix E

References

American Society of Photogrammetry, *Manual of Remote Sensing*, The Sheridan Press, 1983.

André, J. C., J. P. Goutorbe, and A. Perrier, "HAPEX–MOBILHY: a hydrologic atmospheric experiment for the study of water budget and evaporation flux at the climatic scale," *Bulletin of the American Meteorological Society, 67*, pp 138–144, 1986.

Bowers, S. A. and R. J. Hanks, "Reflection of radiant energy from soils," *Science, 100*(2), pp. 130–138, 1965.

Bugnolo, "On the question of multiple scattering in the troposphere," *Journal of Geophysical Research, 65*(3), pp. 879–884, 1960.

Camillo, P., "A canopy reflectance model based on an analytical solution to the multiple scattering equation," *Remote Sensing of Environment, 23*, pp. 453–477, 1987.

Camillo, P. J., R. J. Gurney, and T. J. Schmugge, "A soil and atmospheric boundary layer model for evapotranspiration and soil moisture studies," *Water Resources Research*, 1983.

Carlson, T. N., "Regional–scale estimates of surface moisture availability and thermal inertia using remote thermal measurements," *Remote Sensing of Environment, 1*, pp. 197–247, 1986.

Chahine, M. T., "Interaction mechanisms within the atmosphere," Chapter 5, in *Manual of Remote Sensing*, American Society of Photogrammetry, pp. 165–230, 1983.

Chandrasekhar, S., *Radiative Transfer*, Dover Publications, New York, 1960.

Chen, J., Kubelka–Munk equations in vector–matrix forms and the solution for bidirectional vegetative canopy reflectance, *Applied Optics, 24*(3), pp. 376–382, 1985.

Chhikara, R. S., Effect of mixed (boundary) pixels on crop proportion estimation, *Remote Sensing of Environment, 14*, pp. 207–218, 1984.

Choudhury, B. J., "Relationships between vegetation indices, radiation absorption and net photosynthesis evaluated by a sensitivity analysis," *Remote Sensing of Environment, 22*, pp. 209–233, 1987.

Cierniewski, J., "A model for soil surface roughness influence on the spectral response of bare soils in the visible and near–infrared range," *Remote Sensing of Environment, 23*, pp 97–115, 1987.

Clary, W. P., M. B. Baker, Jr., P. F. O'Connel, T. N. Johnsen, Jr., R. E. Campbell, *Effects of Pinyon–Juniper Removal on Natural Resource Products and Uses in Arizona*, U.S.D.A. Forest Service Research Paper RM–128, 1974.

Colwell, J. E., Vegetation canopy reflectance, *Remote Sensing of Environment*, *3*, pp. 175–183, 1974.

Crist, E. P., The thematic mapper tasseled cap—a preliminary formulation, in *Machine Processing of Remotely Sensed Data Symposium*, pp. 357–364, 1983.

Crist, E. P. and R. C. Cicone, A physically–based transformation of thematic mapper data, *IEEE Trans. on Geoscience and Remote Sensing*, *GE–22*(3), pp. 256–263, 1984.

Curran, P., Multispectral photographic remote sensing of vegetation amount and productivity, *Proc. Fourteenth International Symp. on Remote Sensing of Environment*, Ann Arbor, MI, pp. 623–637, 1980.

Dave, J. V., Effect of atmospheric conditions on remote sensing of a surface nonhomogeneity, *Photogrammetric Engineering and Remote Sensing*, *46*(9), pp. 1173–1180, September 1980.

Dickinson, R. E., "Modelling evapotranspiration for three–dimensional global climate models, in *Climate Processes and Climate Sensitivity*, Geophysical Monograph No. 29, Ed. by J. E. Hansen and T. Takahashi, American Geophysical Union, Washington, D.C., pp. 73–91, 1984.

Dickinson, R. E., Land surface processes and climate–surface albedos and energy balance, in *Advances in Geophysics*, *25*, pp. 305–353, 1983.

Diggle, P. J., *Statistical Analysis of Spatial Point Patterns*, Academic Press, New York, 1983.

Dozier, J., A method for satellite identification of surface temperature fields of subpixel resolution, *Remote Sensing of Environment*, *11*, pp. 221–229, 1981.

Eagleson, P. S. (Editor), *Land Surface Processes in Atmospheric General Circulation Models*, Cambridge University Press, 1982.

Eagleson, P. S., "The emergence of global–scale hydrology," *Water Resources Research*, *22*(9), pp 65–145, 1986.

Eagleson, P. S., and R. I. Segarra, "Water–limited equilibrium of savanna vegetation systems, *Water Resources Research*, *21*(10), pp 1483–1493, 1985.

Eagleson, P. S. and M. F. Jasinski, "Use of Landsat images of vegetation cover to estimate effective hydraulic properties of soils," Final Technical Report on NAG 5–510, August 1988.

Eagleson, P. S., Ecological optimality in water–limited natural soil–vegetation systems, 1. Theory and hypothesis, *Water Resources Research, 18*(2), pp. 325–340, 1982.

Eagleson, P. S. and T. E. Tellers, Ecological optimality in water–limited natural soil vegetation systems, 2. Tests and applications, *Water Resources Research, 18*(2), pp. 341–354, 1982.

Elvidge, C. D. and R. J. P. Lyon, Influence of rock–soil spectral variation on the assessment of green biomass, *Remote Sensing of Environment, 17*, pp. 265–279, 1985.

Ezra, C. E., L. R. Tinney, and R. D. Jackson, Effect of soil background on Vegetation discrimination using Landsat data, *Remote Sensing of Environment, 16*, pp. 233–242, 1984.

Freden, S. C. and F. Gordon, Jr., "Landsat satellites," Chapter 12, in *Manual of Remote Sensing*, American Society of Photogrammetry and Remote Sensing, pp. 517–570, 1983.

Garwood, F., "The Variance of the overlap of geometrical figures with reference to a bombing problem," *Biometrika 34* (I and II), pp 1–17, 1947.

Gates, D. M., *Remote Sensing*, National Academy of Sciences, p. 224, 1970.

Gerstl, A. W. and A. Zardecki, Coupled atmosphere/canopy model for remote sensing of plant reflectance features, *Applied Optics, 24*(1), pp. 94–103, 1985.

Goel, N. S. and D. E. Strebel, Inversion of canopy reflectance models for estimating agronomic variables. I. Problem definition and initial results using the Suits model, *Remote Sensing of Environment, 13*, pp. 487–507, 1983.

Goel, N. S., D. E. Strebel, and R. L. Thompson, Inversion of vegetation canopy reflectance models for estimating agronomic variables. II. Use of angle transforms and error analysis as illustrated by Suits' model, *Remote Sensing of Environment, 14*, pp 77–111, 1984a.

Goel, N. S. and R. L. Thompson, Inversion of vegetation canopy reflectance models for estimating agronomic variables. III. Estimation using only canopy reflectance data as illustrated by the suits model, *Remote Sensing of Environment, 15*, 223–236, 1984a.

Goel, N. S., and R. L. Thompson, Inversion of vegetation canopy reflectance models for estimating agronomic variables. IV. Total inversion of the SAIL Model, *Remote Sensing of Environment, 15*, pp. 237–253, 1984b.

Goel, N. S. and R. L. Thompson, Inversion of vegetation canopy reflectance models for estimating agronomic variables. V. Estimation of leaf area index and average leaf angle using measured canopy reflectances, *Remote Sensing of Environment, 16*, pp. 69–85, 1984c.

Gurney, R. J., and P. J. Camillo, "Modelling daily evapotranspiration using remotely sensed data," *Journal of Hydrology, 69*, pp. 305–324, 1984.

Hall, F. G., "Remote sensing of vegetation at regional scales," *Proceedings of the Society of Photo–Optical Instrumentation Engineering, 475*, pp. 81–96–1984.

Hall, F. G., P. J. Sellers, D. E. Strebel, K. F. Hvernmrich, S. J. Goetz, B. L. Blad, J. R. Irons, and B. L. Markham, "An evaluation of remote sensing in the estimation of surface energy balance – results from FIFE year two *EOS Transactions*, American Geophysical Union, No. 15, p. 344, 1989.

Horwitz, H. M., R. F. Nalepka, P. D. Hyde, and J. P. Morgenstern, Estimating the proportions of objects within a single resolution element of a multispectral scanner, *Proceedings of the 6th International Symposium on Remote Sensing of Environment*, Willow Run Labs, The University of Michigan, Ann Arbor, pp. 1307–1320, 1971.

Huete, A. R., "A soil–adjusted vegetation index (SAVI), "*Remote Sensing of Environment, 25*, pp. 295–309, 1988.

Huete, A. R., R. D. Jackson and D. F. Post, "Spectral response of a plant canopy with different soil backgrounds, *Remote Sensing of Environment, 17*, pp. 37–53, 1985.

Huete, A. R., D. F. Post, and R. D. Jackson, Soil spectral effects on 4–space vegetation discrimination, *Remote Sensing of Environment, 15*, pp. 155–165, 1984.

Iqbal, M., *An Introduction to Solar Radiation*, Academic Press, 1983.

Jackson, R. D., R. J. Reginato, P. J. Pinter, and S. B. Idso, "Plant canopy information extraction from composite scene reflectance of row crops," *Applied Optics, 18*(22), pp. 3775–3782, 1979.

Jackson, R. D., M. S. Moran, P. N. Slater and S. F. Biggar, "Field Calibration of Reference Reflectance Panels," *Remote Sensing of Environment, 22*, pp. 145–158, 1987.

Jasinski, M. J., "Parameterization of natural semi–arid landscapes using satellite multispectral imagery; Part I: subpixel resolution of vegetation density; Part II: estimation of soil hydraulic properties," Doctoral Proposal, Department of Civil Engineering, Massachusetts Institute of Technology, February 12, 1987.

Jasinski, M. F., and P. S. Eagleson, "The structure of red–infrared scattergrams of semivegetated Landscapes," *IEEE Transactions on Geoscience and Remote Sensing, 27*(4), pp. 441–451, 1989.

Jasinski, M. F. and P. S. Eagleson, Feasibility of using Landsat images of vegetation cover to estimate effective hydraulic properties of soils, *Annual Technical Report on NASA Grant #5–510*, 1986.

Kaufman, Y. J., "Solution of the equation of radiative transfer for remote sensing over nonuniform surface reflectivity," *Journal of Geophysical Research*, 87(C6), pp. 4137–4147, 1982.

Kauth, R. J. and G. S. Thomas, "The Tasselled Cap – A graphic description of the spectral–temporal development of agricultural crops as seen by Landsat," *Proc. of the Symp. on Machine Processing of Remotely Sensed Data*, Purdue Univ., W. Lafayette, IN, pp. 4B41–4B51, 1976.

Kellerer, A. M. , "On the number of clumps resulting from the overlap of randomly placed figures in a plane," *Journal of Applied Probability, 20*, pp. 126–135, 1983.

Kimes, D. S., J. M. Norman, and C. L. Walthall, "Modeling the Radiant Transfers of Sparse Vegetation Canopies," *IEEE Transactions on Geoscience and Remote Sensing*, GE–23(5), pp. 695–704, 1985.

Kondratyev, K. Y. A., *Radiation in the Atmosphere*, Academic Press, 1969.

Lang, A. R. G., X. Yuegin, and J. M. Horman, Crop structure and the penetration of direct sunlight, *Agriculture and Forest Meteorology, 35*, pp. 83–101, 1985.

Lennington, R. K., C. T. Sorenson, and R. P. Heydon, A mixture model approach for estimating crop areas from Landsat data, *Remote Sensing of Environment, 14*, pp. 197–206, 1984.

Li, X. and A. H. Strahler, Geometric–optical modeling of a conifer forest canopy, *IEEE Trans. on Geoscience and Remote Sensing, GE–23*(5), pp. 705–721, 1985.

Lillesand, T. M., and R. W. Kiefer, *Remote Sensing and Image Interpretation*, 2nd Edition, John Wiley and Sons, New York, 1987.

Liou, K. N., *An Introduction to Atmospheric Radiation*, International Geophysics Series, Volume 26, Academic Press, New York, 1980.

Manabe, S., Climate and the Ocean Circulation: I, The atmospheric circulation and the hydrology of the earth's surface, *Monthly Weather Review, 97*, pp. 739–744, 1969.

Mantoglou, A., and J. L. Wilson, "The turning bands method for simulation of random fields using line generation by a spectral method," *Water Resources Research, 18*(5), pp. 1379–1394, 1982.

Markham, B. L. and J. L. Barker, "Landsat MSS and TM Post–Calibration Dynamic Ranges, Exoatmospheric Reflectance, and At–Satellite Temperature," EOSAT Landsat Technical Note, pp. 3–8, August, 1986.

McCloy, K. R., The response characteristics of vegetation in Landsat MSS digital data, *Remote Sensing of Environment, 10*, pp. 185–190, 1980.

Meador, W. E. and W. R. Weaver, Two–stream approximations to radiative transfer in planetary atmospheres: A unified description of existing methods and a new improvement, *Journal of Atmospheric Sciences, 37*, pp. 630–643, March 1980.

Monsi, M. and T. Saeki, Über den Lichtfaktor in den Pflanzengesellschafter und seine Bedeutung für die Stoffproduktion, *Jpn. Journal of Botany, 14*(1), pp. 22–52, 1953.

Mood, A. M., and F. A. Graybill, *Introduction to the Theory of Statistics*, McGraw–Hill, New York, 1963.

Moran, Susan, Personal communications, 1988.

Musick, H. B., Assessment of Landsat multispectral scanner spectral indices for monitoring arid rangeland, *IEEE Trans. Geosci. and Remote Sensing, GE–22*(6), pp. 512–519, 19 .

Myers, V. I., Remote sensing applications in agriculture, in *Manual of Remote Sensing*, American Society of Photogrammetry, Ch. 33, pp. 2111–2228, 1983.

Nalepka, R. F., H. M. Horwitz, and P. D. Hyde, Estimating proportions of objects from multispectral data, *Willow Run Labs Technical Report No. 31650–73–T*, The University of Michigan, Ann Arbor, MI, 1972.

NASA, *Earth System Science, A Program for Global Change*, Report of the Earth System Sciences Committee, NASA Advisory Council, Washington, D.C., January, 1988.

Otterman, J, Single–scattering solution for radiative transfer through a turbid atmosphere, *Applied Optics, 17*(21), pp. 3431–3438, November 1978.

Otterman, J., and R. S. Fraser, Adjacency effects on imaging by surface reflection and atmospheric scattering: cross radiance to zenith, *Applied Optics, 18*(16), pp. 2852–2859, August 1979.

Otterman, J., S. Ungar, Y. Kaufman, and M. Podolak, Atmospheric effects on radiometric imaging from satellites under low optical thickness conditions, *Remote Sensing of Environment, 9*, pp. 115–129, 1980.

Otterman, J., Reflection from soil with sparse vegetation, *Advances in Space Res., 1*, pp. 115–119, 1981.

Otterman, J., Albedo of a forest modeled as a plane with dense protrusions, *J. of Climate and Applied Meteorology, 23*, pp. 297–307, February, 1984.

Otterman, J. and G. H. Weiss, Reflection from a field of randomly located vertical protrusions, *Applied Optics, 23*(12), pp. 1931–1936, 1984.

Perry, C. R., Jr., and L. F. Lautenschlager, Functional equivalence of spectral vegetation indices, *Remote Sensing of Environment, 14*, pp. 169–182, 1984.

Pierce, L. L. , and R. G. Congalton, "A methodology for mapping forest latent heat flux densities using remote sensing," *Remote Sensing of Environment, 24*, pp. 405–418, 1988.

Price, J. C., "On the use of satellite data to infer surface fluxes at meteorological scales, *Journal of Applied Meteorology, 21*, pp. 1111–1122.

Reginato, R. J., Jackson, R. D., and P. J. Pinter, Jr., "Evapotranspiration calculated from remote multispectral and ground station meteorological data," *Remote Sensing of Environment, 18*, pp. 75–89, 1985.

Reyna, E. and G. D. Badhwar, Inclusion of specular reflectance in vegetative canopy models, *IEEE Trans. on Geoscience and Remote Sensing, GE–23*(5), pp. 731–736, 1985.

Richardson, A. J. and C. L. Wiegand, Distinguishing vegetation from soil background information, *Photogrammetric Engineering and Remote Sensing, 43*(12), pp. 1541–1552, 1977.

Richardson, A. J., C. L. Wiegand, H. W. Gausman, J. A. Cuellar, and A. H. Gerbermann, "Plant, soil and shadow reflectance components of row crops," *Photogrammetric Engineering and Remote Sensing, 41*(11), pp. 1401–1407, 1975.

Rind, D., "The Influence of vegetation on the hydrologic cycle in a global climate model, in *Climate Processes and Climate Sensitivity*, Geophysical Monograph Number 29, Eds. J. E. Hansen and T Takahashi, American Geophysical Union, Washington, D.C., pp 73–91, 1984.

Rosenberg, N. H., B. L. Blad, and S. B. Verma, *Microclimate, The Biological Environment*, 2nd Edn., Wiley–Interscience, 1983.

Rosenthal, W. D., B. J. Blanchard, and A. J. Blanchard, Visible infrared/ – microwave agriculture classification, biomass, and plant height algorithms, *IEEE Trans. on Geoscience and Remote Sensing, GE–23*(2), pp. 84–90, 1985.

Ross, J., *The Radiation Regime and Architecture of Plant Stands*, Dr. W. Junk, Publishers, The Hague, 1981.

Schmugge, T. J., "Remote sensing of soil moisture: Recent advances," *IEEE Transactions on Geoscience and Remote Sensing*, GE–21, pp. 336–344, 1983.

Sellers, P. J., "Canopy reflectance, photosynthesis and transpiration," *International Journal of Remote Sensing, 6*(8), pp. 1335–1372, 1985.

Sellers, P. J., Hall, F. G., Asrar, G., Strebel, D. E. , and R. E. Murphy, "The first ISLSCP field experiment (FIFE)," *Bulletin of the American Meteorological Society, 69*(1), 1988.

Sellers, P. J., Mintz, Y., Sud, Y. C., and A. Dalcher, "A simple biosphere model (SiB) for use within general circulation models," in *Journal of the Atmospheric Sciences, 43*(6), pp. 505–531, 1986.

Simmer, C., and S. A. W. Gerstl, Remote sensing of angular characteristics of canopy reflectances, *IEEE Transactions on Geoscience and Remote Sensing, GE-23*(5), pp. 648–658, 1985.

Skidmore, E. L., J. D. Dickerson and H. Schimmelpfennig, "Evaluating surface–soil water content by measuring reflectance," *Soil Sci. Soc. Amer. Proc., 39*, pp. 238–242, 1975.

Slater, P. N., *Remote Sensing Optics and Optical Systems*, Addison–Wesley, Reading, Massachusetts, 1980.

Smith, J. A., Matter–energy interaction in the optical region, *Manual of Remote Sensing*, American Society of Photogrammetry, Ch. 3, pp. 61–113, 1983.

Smith, M. D. , P. E. Johnson, and J. B. Adams, "Quantitative Determination of Mineral Types and Abundances from Reflectance from Reflectance Spectra Using Principal Components Analysis," *Proc. 15th Lunar and Planetary Science Conference, Part 2, J. of Geoph. Res., Vol. 20*, Supplement, pp. C797–C804, 1985.

Strahler, A. H., and Li Xiaowen, An invertible coniferous forest canopy reflectance model, *Proc. of Fifteenth International Symposium on Remote Sensing of Environment*, Ann Arbor, MI, pp. 1237–1244, 1981.

Strebel, D. E., H. S. Goel and K. J. Ranson, Two–dimensional leaf orientation distributions, *IEEE Transactions on Geoscience and Remote Sensing, GE-23*(5), pp. 640–647, 1985.

Suits, G. H., Calculation of the directional reflectance of a vegetation canopy, *Remote Sensing of Environment, 2*, pp. 117–125, 1972.

Taconet, O., Carlson, T., Bernard, R., and D. Vidal–Madjar, "Evaluation of a surface/vegetation parameterization using satellite measurements of surface temperature," *Journal of Climate and Applied Meteorology, 25*, pp. 1752–1767, 1986.

Theis, S. W., B. J. Blanchard and R. W. Newton, Utilization of vegetation indices to improve soil moisture estimates over agricultural lands, *IEEE Trans. on Geoscience and Remote Sensing, GE-22*(6), pp. 490–495, 1984.

Tsang, L., Kong, J. A., and R. T. Shin, *Theory of Microwave Remote Sensing*, John Wiley and Sons, New York, 1985.

Tucker, C. J. and L. D. Miller, Soil spectra contributions to grass canopy spectral reflectance, *Photogrammetric Engineering and Remote Sensing, 43*(6), pp. 721–726, 1977.

Tucker, C. J., C. Vanpraet, E. Boerwinkel, and A. Gaston, Satellite remote sensing of total dry matter production in the Senegalese Sahel, *Remote Sensing of Environment, 14*, pp. 461–474, 1983.

Ungar, S. G., and E. Bryant, Fanning: A classification algorithm for mixture landscapes applied to landsat data of Maine forests, *Proceedings of the Fifteenth International Symposium on Remote Sensing of Environment*, Ann Arbor, Michigan, May 1981, pp. 113–120, 1981.

van de Griend, A. A., and J. H. van Boxel, "Water and surface energy balance model with a multilayer canopy representation for remote sensing purposes," *Water Resources Research*, *25*(5), pp. 949–971, 1989.

Vanderbilt, V.C. and L. Grant, Plant canopy specular reflectance model, *IEEE Transactions on Geoscience and Remote Sensing*, *GE–23*(5), pp. 722–730, 1985.

Vanmarcke, E., *Random Fields: Analysis and Synthesis*, *MIT Press*, *Cambridge*, *MA*, *1983.*

Verhoef, W. and N. J. J. Bunnik, Influence of crop geometry on multispectral reflectance determined by use of canopy reflectance models, *Proceedings of the International Colloquium on Signatures of Remotely Sensed Objects*, Avignon, pp. 273–290, 1981.

Walthall, C. L., J. M. Norman, J. M. Welles, G. Campbell, and B. L. Blad, Simple equation to approximate the bidirectional reflectance from vegetative canopies and bare soil surfaces, *Applied Optics*, *24*(3), pp. 383–387, 1983.

Washington, W. M., and C. L. Parkinson, *An Introduction to Three–Dimensional Climate Modelling*, University Science Books, California 1986.

Whittaker, R. H., *Communities and Ecosystems*, 2nd Edition, Macmillan Publishing Co., New York, 1975.

Woodcock, C. E., *Understanding spatial variation in remotely sensed imagery*, Ph.D. Dissertation, University of California, Santa Barbara, 1985.

Work, E. A., Application of the Earth Resources Technology Satellite for monitoring the breeding habitat of migratory waterfowl in the glaciated prairies, M. S. Thesis, University of Michigan, 1974.

Work, E. A., Taos resource area remote sensing project, *Final Report,* Bureau of Land Management, Branch of Scientific Systems Applications, Denver, CO, 1983.